MICROSTRUCTURAL, METAMORPHIC AND EXPERIMENTAL CONSTRAINTS ON DIFFERENTIAL STRESS AND TEMPERATURE IN THE MIDDLE CRUST

Thesis by

Steven B. Kidder

In Partial Fulfillment of the Requirements

for the Degree of

Doctor of Philosophy

California Institute of Technology

Pasadena, California

2012

(Defended November 16, 2011)

ACKNOWLEDGEMENTS

I wish to thank the members of my thesis advisory committee: First my thesis advisor, Jean-Philippe Avouac, who had the great idea of doing grain-size piezometry in Taiwan, then followed through with encouragement, support of all varieties, patience, and room to make it my own. I thank Jason Saleeby for his generosity, guidance and support throughout my time at Caltech, and Brian Wernicke and Joann Stock for making a special effort in their teaching that makes their classes memorable, inspiring and informative. I thank John Eiler for his clear, concise feedback and availability at key moments during my time at Caltech.

Support outside of Caltech was essential for this work. I thank John Platt at USC for letting me sit in on his fantastic microstructure class, inviting me on field trips, and for sponsoring Pasadena Rheological Society meetings at his home. John's enthusiasm and insights inspired and improved numerous aspects of this work. I also thank Greg Hirth for hosting me during an invaluable semester at Brown University. John and Greg's willingness to work outside of institutional boundaries allowed me to pursue my interest in microstructures and rheology. Their support has made this thesis possible. Yu-Chang Chan at Academia Sinica enabled the field elements of this project possible, and recruited great field assistants: Chih-Tung Chen, Chung Huang, Shiao An-You, Yong Chi-Kai. I thank Eric Goergen and Linda Chernak at Brown University for patient laboratory instruction. Jan Tullis provided helpful advice and feedback on a number of occasions. Numerous conversations with Whitney Behr defined and motivated various aspects of this work. I thank Christian Teyssier, Michelle Markley and Ben Holtzman for introducing me to microstructures when I was an undergraduate at the University of Minnesota. Discussions with Martine Simoes helped clarify the thermal history of the Hsüehshan range.

Chi Ma, Yunbin Guan and Scott Sitzman provided patient training with the SEM, SIMS and EBSD. Marion Le Voyer provided helpful comments on an early draft of chapter 1. Heather Steele helped with innumerable logistical issues. Jeremy Boyce provided helpful training for analysis of SIMS data. I thank Adrienne Walser for her friendship and helpful edits of proposals and drafts over the years.

Financial support for the thesis work was provided by the Gordon and Betty Moore Foundation through Caltech's Tectonics Observatory.

I thank my parents for taking my sister and me on family vacations to the mountains every summer, and for their constant support and enthusiasm. I thank my sister Jennifer for providing a quiet place to work this summer at her home in Port Angeles, WA.

I'm especially grateful for the friends I've made and spent time with while at Caltech: Willy Amidon, Agatha Beins, Magali Bonifacie, Dan Bower, Mia Brasco Miller, Robinson Cecil, Melanie Channon, Alan Chapman, Kelly Chapman, Steve Chemtob, Linda Chernak, Stacy Dacheux, Sarah Danielson, Ruben Diaz, Nick Dygert, Rita Economos, Eric Flewelling, Gina Gage, Crystal Gammon, Eric Goergen, David Goldspy, Ana Gonzales, Catherine Grose, Emily Hamecher, Eric Hansen, Amy Hofmann, James Hollingworth, Ravi Kanda, Anna Kochersperger, Carissa Kostopoulos, Alison Kudlow, Alexis Lantz, Nina Lin, Michelle Markley, Andrew Matzen, Vali Memeti, Robyn Morrison, Elisabeth Nadin, Krista Olson, Ryan Petterson, Elizabeth Salud, Eva Sanchez, Michelle Selvans, Sam Solomon, Bec Ulrich, Yu Wang, Ying Wang and Linda Wei.

Finally I thank my wife, Robin Wisser Kidder, for her encouragement, love, support, feedback, and help with figures.

ABSTRACT

Because shear stress drives plate tectonics and causes earthquakes, important objectives in the Earth Sciences include quantifying stress magnitudes and variability in space and time, and developing and improving tools to do so. This thesis addresses both objectives. In the first chapter I demonstrate that the Titanium-in-quartz thermobarometer (“TitaniQ”) can be used to accurately record deformation temperatures under greenschist facies conditions. In the second chapter, an experimental study, I show that the relationship between recrystallized grain size and flow stress (the “recrystallized grain size paleopiezometer”) can be used to determine the stress history of dynamically recrystallized quartz under non steady state conditions. In the third chapter I apply the paleopiezometer in Taiwan’s Hsüehshan range and compare results to independent constraints (e.g. critical taper theory and potential energy considerations). This analysis demonstrates: 1) the piezometer is accurate to within a factor of two or better under conditions at the brittle-ductile transition; 2) piezometric results are consistent with recent flow laws for quartz; 3) the activation energy of naturally deformed quartzite is >133 kJ/mol, consistent with experimental determinations; and 4) Peak differential stress in the Hsüehshan range was ~210 MPa at temperature ~300°C. Our results indicate hydrostatic fluid pressure and a low friction coefficient of ~0.38 within the Taiwan wedge. Integrated crustal strength in Taiwan is $1.5\text{-}2.1*10^{12}$ N/m, consistent with the force needed to support the topography of the range. The final chapter investigates stress levels on the Vincent thrust in the San Gabriel Mountains, California by constructing a numerical model of the initiation of flat slab subduction. A model inversion demonstrates that previously hypothesized high stresses are not required to explain inverted metamorphism along the fault.

TABLE OF CONTENTS

LIST OF FIGURES

Introduction

Chapter 1

Chapter 2

Chapter 3

Chapter 4

LIST OF TABLES

Chapter 1

Chapter 2

Chapter 3

INTRODUCTION

The rheology of rocks governs the seismic cycle along faults, continuous deformation, (e.g. mountain building and coupling between deformation and erosion), and plate tectonic rates and behavior. The rheological laws governing crustal deformation are most commonly inferred from laboratory experiments (e.g. Brace and Kohlstedt, 1980) or the modeling of geodetic strain (e.g. due to postseismic relaxation or surface load variations (e.g. Bürgmann and Dresen, 2008)). There is general agreement that ductile deformation obeys some power-law relationship and that temperature and fluid content are the most important governing parameters (e.g. Kohlstedt et al., 1995), however estimates of crustal rheology vary widely. Experimentally derived flow laws are created by deforming monomineralic quartz or feldspar aggregates at strain rates many orders of magnitude larger than occur in nature. Extrapolating these flow laws to crustal strain rates, compositions and temperatures involves substantial uncertainties (e.g. Molnar, 1992). Inferring crustal rheology from geodetic data is not straightforward either (Bruhat et al., 2011; Cavalie et al., 2007; Cohen, 1999; Fialko, 2004; Godard et al., 2004; Kaufmann and Amelung, 2000; Montesi, 2004; Perfettini et al., 2005; Savage, 2000). For example, crustal deformation models constrained by surface deformation are often non-unique because afterslip and distributed viscous deformation often jointly contribute to postseismic deformation.

In this thesis I explore how crustal flow parameters, in particular stress, temperature and strain rate, can be estimated from exhumed rock samples. I place a particular emphasis on quantifying stresses experienced by rocks using the recrystallized grain size piezometer in quartz (e.g. Mercier et al., 1977; Passchier and Trouw, 2005; Twiss, 1977). The size of recrystallized grains has been used previously to estimate differential stress levels in ancient deformation zones (Behr and Platt, 2011; Dunlap et al., 1997; Hacker et al., 1992; Hacker et al., 1990; Hirth et al., 2001; Kohlstedt and Weathers, 1980; Kuster and Stöckhert, 1998; Ord and Christie, 1984; Prior et al., 1990; Stipp et al., 2002; Stipp et al., 2010; Stockhert et al., 1999; Zulauf, 2001), however its widespread use has been restricted in part due to unknown uncertainties stemming from the extrapolation of laboratory-derived grain-size stress relationships to natural conditions and a poor theoretical understanding of the phenomenon.

The extraction of rheological information from rocks deformed in the crust is an elusive goal (e.g. Talbot, 1999). In the first three chapters of this thesis I address a number of uncertainties inherent in such efforts. In the first chapter I demonstrate that trace levels of titanium in quartz can be used to accurately estimate deformation temperatures under greenschist facies conditions. The second chapter is a laboratory-based exploration of the effect of changing stress levels on grain-size stress relationships. In the third chapter I demonstrate that the recrystallized grain size piezometer in quartz yields accurate estimates of paleostress levels in Taiwan. Chapters one and three are based in Taiwan because, as an active tectonic setting, geological and geodetic observations can be combined there to place tight independent constraints on rheological parameters. In the fourth chapter I apply a numerical modeling approach to estimate stress levels at a classic locality in Southern California based on the effect of strain heating on metamorphism.

OVERVIEW OF THE GEOLOGY OF TAIWAN

Taiwan results from the collision of the Luzon volcanic arc (Philippine sea plate), with the Chinese continental margin (Eurasian plate) at a rate of ~ 9 cm/yr (Sella et al., 2002). Figure 1 shows the main tectonic provinces exposed in the orogen in cross sectional view (a corresponding map of Taiwan can be found in chapter 1). From west to east these are: 1) the Coastal Plain, a generally flat-lying sequence of Miocene and younger foreland basin sediments. 2) the Western Foothills, the youngest portion of the Taiwan mountain belt comprising passive margin clastic sedimentary rocks and overlying syn-tectonic sediments ("molasse"). The Western Foothills localize nearly all the active shortening in Taiwan (Simoes and Avouac, 2006), including the deformation associated with the Chelungpu thrust which produced the 1999 Chi Chi earthquake (magnitude 7.6, figure 1). 3) The Hsüehshan range comprises Eocene-Miocene sandstones and slates deposited during rifting and opening of the South China Sea. The Hsüehshan range interupts Taiwan's generally eastward-increasing trend in metamorphic grade and isotopic ages (Simoes et al., 2012), and is envisaged as a pop-up structure placing higher grade metamorphic rocks west of the Lishan fault against the lower grade Backbone range (Clark et al., 1993). 4) The Backbone range is comprised of Eocene and Miocene slates. The Hsüehshan range and Backbone range together comprise Taiwan's "slate belt." 5) The Tananao Schist is the oldest tectonic province exposed in Taiwan and comprises uplifted, pre-Tertiary, Eurasian basement. The Tananao schist can be split into the high-temperature Tailuko belt in the west, and the low temperature-higher pressure Yuli belt in the east. 6) The longitudinal valley is a basin overlying the plate boundary between the Eurasian basement and cover and the accreted arc complex to the east. 7) the Coastal range is the onland equivalent of the Luzon volcanic arc and comprises Miocene and younger volcanic rocks, turbiditic volcaniclastic rocks, and ophiolitic melange.

FIGURE CAPTIONS

Figure 1. Crustal-Scale cross section of the Taiwan moutain belt based on surface geology (sedimentary basins, structures, and metamorphism), seismic profiles, crustal tomography, and regional seismicity (unpublished figure by Yu-Chang Chan, 2005 reproduced here with permission). No vertical exageration.

REFERENCES

Behr, W. M., and Platt, J. P., 2011, A naturally constrained stress profile through the middle crust in an extensional terrane: Earth and Planetary Science Letters, v. 303, no. 3-4, p. 181-192.

Brace, W. F., and Kohlstedt, D. L., 1980, Limits on lithospheric stress imposed by laboratory experiments: Journal of Geophysical Research, v. 85, no. B11, p. 6248-6252.

Bruhat, L., Barbot, S., and Avouac, J.-P., 2011, Evidence for postseismic deformation of the lower crust following the 2004 Mw6.0 Parkfield earthquake: Journal of Geophysical Research, v. 116, no. B8.

Bürgmann, R., and Dresen, G., 2008, Rheology of the lower crust and upper mantle: Evidence from rock mechanics, geodesy, and field observations: Annu. Rev. Earth Planet. Sci., v. 36, p. 531-567.

Cavalie, O., Doin, M.-P., Lasserre, C., and Briole, P., 2007, Ground motion measurement in the Lake Mead area, Nevada, by differential synthetic aperture radar interferometry time series analysis: Probing the lithosphere rheological structure: Journal of Geophysical Research, v. 112, no. B03403, doi: 10.1029/2006JB004344.

Clark, M. B., Fisher, D. M., Lu, C.-Y., and Chen, C.-H., 1993, Kinematic analyses of the Hsüehshan range, Taiwan: A large-scale pop-up structure: Tectonics, v. 12, no. 1, p. 205-217.

Cohen, S. C., 1999, Numerical models of crustal deformation in seismic zones: Adv. Geophys., v. 41, p. 134-231.

Dunlap, W., Hirth, G., and Teyssier, C., 1997, Thermomechanical evolution of a ductile duplex: Tectonics, v. 16, no. 6, p. 983-1000.

Fialko, Y., 2004, Evidence of fluid-filled upper crust from observations of postseismic deformation due to the 1992 M(w)7.3 Landers earthquake: Journal of Geophysical Research-Solid Earth, v. 109, no. B8.

Godard, V., Cattin, R., and Lave, J., 2004, Numerical modeling of mountain building: interplay between erosion law and crustal rheology: Geophysical Research Letters, v. 31, no. L23607, p. doi:10.1029/2004GL021006.

Hacker, B. R., Yin, A., Christie, J. M., and Davis, G. A., 1992, Stress Magnitude, Strain Rate, and Rheology of Extended Middle Continental-Crust Inferred from Quartz Grain Sizes in the Whipple Mountains, California: Tectonics, v. 11, no. 1, p. 36-46.

Hacker, B. R., Yin, A., Christie, J. M., and Snoke, A. W., 1990, Differential Stress, Strain Rate, and Temperatures of Mylonitization in the Ruby Mountains, Nevada - Implications for the Rate and Duration of Uplift: Journal of Geophysical Research-Solid Earth and Planets, v. 95, no. B6, p. 8569-8580.

Hirth, G., Teyssier, C., and Dunlap, W. J., 2001, An evaluation of quartzite flow laws based on comparisons between experimentally and naturally deformed rocks: International Journal of Earth Sciences (Geol Rundsch), v. 90, p. 77-87.

Kaufmann, G., and Amelung, F., 2000, Reservoir-induced deformation and continental rheology in vicinity of Lake Mead, Nevada: Journal of Geophysical Research-Solid Earth, v. 105, no. B7, p. 16341-16358.

Kohlstedt, D. L., Evans, B., and Mackwell, S. J., 1995, Strength of the Lithosphere - Constraints Imposed by Laboratory Experiments: Journal of Geophysical Research-Solid Earth, v. 100, no. B9, p. 17587-17602.

Kohlstedt, D. L., and Weathers, M. S., 1980, Deformation-Induced Microstructures, Paleopiezometers, and Differential Stresses in Deeply Eroded Fault Zones: Journal of Geophysical Research, v. 85, no. Nb11, p. 6269-6285.

Kuster, M., and Stöckhert, B., 1998, High differential stress and sublithostatic pore fluid pressure in the ductile regime — microstructural evidence for short-term post-seismic creep in the Sesia Zone, Western Alps: Tectonophysics, v. 1998, no. 303, p. 263-277.

Mercier, J. C. C., Anderson, D. A., and Carter, N. L., 1977, Stress in Lithosphere - Inferences from Steady-State Flow of Rocks: Pure and Applied Geophysics, v. 115, no. 1-2, p. 199-226.

Molnar, P., 1992, Brace-Goetze strength profiles, the partitioning of strike-slip and thrust faulting at zones of oblique convergence, and the stress-heat flow paradox of the San Andreas fault, *in* Evans, B., and Wong, T.-F., eds., Fault mechanics and transport properties of rocks, Volume International Geophysics Series volume 51: San Diego, Academic Press Inc., p. 524.

Montesi, L. G. J., 2004, Controls of shear zone rheology and tectonic loading on postseismic creep: Journal Of Geophysical Research-Solid Earth, v. 109, no. B10.

Ord, A., and Christie, J. M., 1984, Flow stresses from microstructures in mylonitic quartzites of the Moine Thrust zone, Assynt area, Scotland: Journal of Structural Geology, v. 6, no. 6, p. 639-654.

Passchier, C. W., and Trouw, R. A. J., 2005, Microtectonics, 2nd edition.

Perfettini, H., Avouac, J. P., and Ruegg, J. C., 2005, Geodetic displacements and aftershocks following the 2001 Mw=8.4 Peru earthquake: Implications for the mechanics of the earthquake cycle along subduction zones: Journal of Geophysical Research-Solid Earth, v. 110, no. B9.

Prior, D. J., Knipe, R. J., and Handy, M. R., 1990, Estimates of the rates of microstructural changes in mylonites: Deformation mechanisms, rheology and tectonics, Geological Society Special Publications, 54, p. 309-319.

Savage, J. C., 2000, Viscoelastic-coupling model for the earthquake cycle driven from below: J. Geophys. Res., v. 105, no. B11, p. 25,525-525,532.

Sella, G. F., Dixon, T. H., and Mao, A. L., 2002, REVEL: A model for Recent plate velocities from space geodesy: Journal of Geophysical Research-Solid Earth, v. 107, no. B4, p. -.

Simoes, M., and Avouac, J. P., 2006, Investigating the kinematics of mountain building in Taiwan from the spatiotemporal evolution of the foreland basin and western foothills: Journal of Geophysical Research, v. 111, no. B10, p. 1-25.

Simoes, M., Beyssac, O., and Chen, Y.-G., 2012, Late Cenozoic metamorphism and mountain building in Tawain: a review: Journal of Asian Earth Sciences, v. In Press.

Stipp, M., Stunitz, H., Heilbronner, R., and Schmid, S. M., 2002, Dynamic recrystallization of quartz: correlation between natural and experimental conditions: Deformation Mechanisms, Rheology and Tectonics: Current Status and Future Perspectives, v. 200, p. 171-190.

Stipp, M., Tullis, J., Scherwath, M., and Behrmann, J. H., 2010, A new perspective on paleopiezometry: Dynamically recrystallized grain size distributions indicate mechanism changes: Geology, v. 38, no. 8, p. 759-762.

Stockhert, B., Brix, M. R., Kleinschrodt, R., Hurford, A. J., and Wirth, R., 1999, Thermochronometry and microstructures of quartz - a comparison with experimental flow laws and predictions on the temperature of the brittle-plastic transition: Journal of Structural Geology, v. 21, no. 3, p. 351-369.

Talbot, C. J., 1999, Can field data constrain rock viscosities?: Journal of Structural Geology, v. 21, p. 949-957.

Twiss, R. J., 1977, Theory and Applicability of a Recrystallized Grain-Size Paleopiezometer: Pure and Applied Geophysics, v. 115, no. 1-2, p. 227-244.

Zulauf, G., 2001, Structural style, deformation mechanisms and paleodifferential stress along an exposed crustal section: constraints on the rheology of quartzofeldspathic rocks at supra- and infrastructural levels (Bohemian Massif): Tectonophysics, v. 332, p. 211-237.

Figure 1

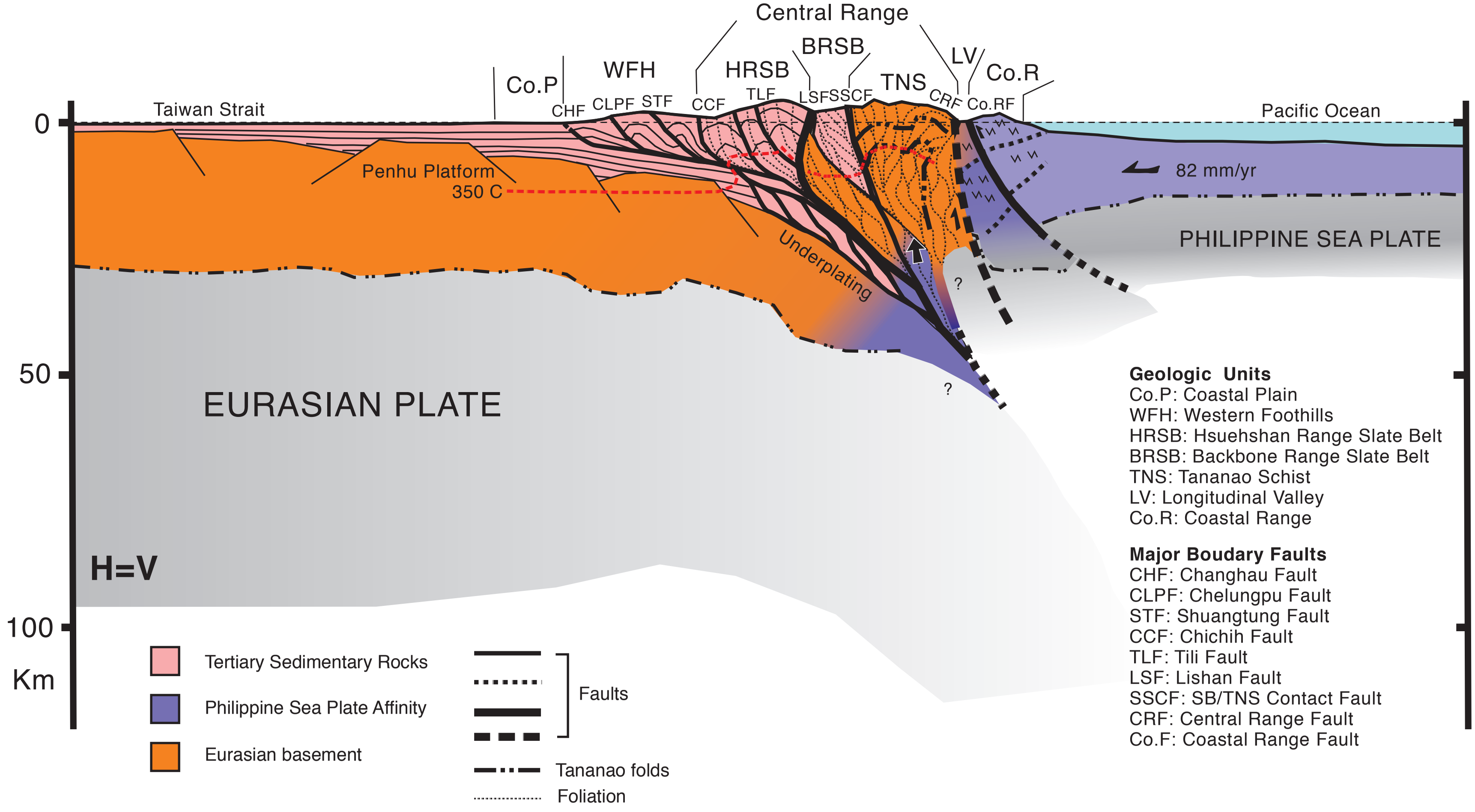
Central Range
Co.P
WFH
HRSB
BRSB
TNS
LV
Co.R
CHF
CLPF
STF
CCF
TLF
LSF
SSCF
CRF
Co.RF
Taiwan Strait
Pacific Ocean
Penhu Platform
350 C
82 mm/yr
Underplating
?
?
PHILIPPINE SEA PLATE
EURASIAN PLATE
H=V
0
50
100
Km
Tertiary Sedimentary Rocks
Philippine Sea Plate Affinity
Eurasian basement
Faults
Tananao folds
Foliation
Geologic Units
Co.P: Coastal Plain
WFH: Western Foothills
HRSB: Hsuehshan Range Slate Belt
BRSB: Backbone Range Slate Belt
TNS: Tananao Schist
LV: Longitudinal Valley
Co.R: Coastal Range
Major Boudary Faults
CHF: Changhau Fault
CLPF: Chelungpu Fault
STF: Shuangtung Fault
CCF: Chichih Fault
TLF: Tili Fault
LSF: Lishan Fault
SSCF: SB/TNS Contact Fault
CRF: Central Range Fault
Co.F: Coastal Range Fault

CHAPTER 1

Application of titanium-in-quartz thermobarometry to greenschist facies veins and recrystallized quartzites in the Hsüehshan range, Taiwan

Steven Kidder[1], Jean-Philippe Avouac[1], Yu-Chang Chan[2]

[1]*California Institute of Technology, Pasadena, CA, United States*
[2]*Academia Sinica, Taipei, Taiwan*

Submitted to *Solid Earth*

ABSTRACT

The accuracy, reliability and best practices of Ti-in-quartz thermobarometry ("TitaniQ") in greenschist facies rocks have not been established. To address these issues we measured Ti concentrations in rutile-bearing samples of moderately deformed, partially recrystallized quartzite and vein quartz from Taiwan's Hsüehshan range. The spread of Ti concentrations of recrystallized grains in quartzite correlates with recrystallized grain size. Recrystallized quartz (grain size ~300 μm) that formed during early deformation within the biotite stability field shows a marked increase in intermediate Ti-concentration grains (~1-10 ppm) relative to detrital porphyroclasts (Ti ~ 0.1-200 ppm). Fine recrystallized quartz (~5% of the samples by area, grain size ~10–20 μm) has a further restricted Ti concentration peaking at 0.8–2 ppm. This trend suggests equilibration of Ti in recrystallized quartz with a matrix phase during deformation and cooling. Vein emplacement and quartzite recrystallization are independently shown to have occurred at 250–350 °C and 300–410 °C respectively, lithostatic pressure ~5 kbar, and hydrostatic fluid pressure. Estimates of the accuracy of TitaniQ at these conditions depend on whether lithostatic or fluid pressure is used in the TitaniQ calibration. Using lithostatic pressure, Ti concentrations predicted by the Thomas et al. (2010) TitaniQ are within error of Ti concentrations measured by SIMS. If fluid pressure is used, predicted temperatures are ~30-40 °C too low. TitaniQ has potential to yield accurate PT information for vein emplacement and

dynamic recrystallization of quartz at temperatures as low as ~250 °C, however clarification of the relevant pressure term and further tests in rutile-present rocks are warranted.

INTRODUCTION

Titanium-in-quartz thermobarometry (referred to hereafter as TitaniQ; Huang and Audétat, 2012; Thomas et al., 2010; Wark and Watson, 2006) has significant potential as a tool for constraining pressure and temperature of deformation independently of major-element exchange thermobarometers. TitaniQ is based on the temperature- and pressure-dependent substitution of Ti for Si in quartz in the presence of rutile or other Ti-bearing phases. Previous workers have found reasonable consistency between TitaniQ and traditional thermobarometry in metamorphic rocks at temperatures above ~500 °C (Grujic et al., 2011; Menegon et al., 2011; Pennacchioni et al., 2010; Rusk et al., 2008; Spear and Wark, 2009; Storm and Spear, 2009); though see also (Kawasaki and Osanai, 2008; Raimondo et al., 2011). At lower temperatures results are less clear: Kohn and Northrup (2009), Peterman and Grove (2010), Rasmussen et al. (2011), and Behr and Platt (2011) used TitaniQ to estimate temperatures as low as 280 °C in some samples (although the accuracy of these results has not systematically been verified with independent PT constraints). Alternatively, Grujic et al. (2011) found that Ti concentrations in quartz in low-temperature mylonites were not reset during dynamic recrystallization, and Behr and Platt (2011) found both significantly higher and lower Ti-concentrations than expected in more than a third of their mylonites. These results are all challenged by Huang and Audétat (2012), who found a crystallization-rate dependence of the thermobarometer and claim that temperatures should be 100 °C (or more) higher than those calculated in the above-cited examples. We note below however that crystallization rate did not affect Ti concentration in the experiments of Thomas et al. (2010), calling into question the results of Huang and Audétat (2012).

The above studies raise significant questions regarding the use of TitaniQ for estimating temperature and pressure in greenschist facies rocks: Does quartz dynamically recrystallized at low temperatures equilibrate with respect to Ti concentration? If so, how do results depend on timescale, strain, and lithology? Does equilibration depend on recrystallization mechanism

(Grujic et al., 2011)? How well does TitaniQ perform when extrapolated >400 °C beyond its experimental calibration?

In many of the above studies, as well as the volcanic applications of TitaniQ (e.g. Wilson et al., 2012), rutile is absent and the activity of Ti is a major source of uncertainty. In this study we analyze Ti concentrations in vein quartz in rutile-bearing rocks and dynamically recrystallized quartz in rutile-bearing quartzite. Samples were obtained from the Hsüehshan range in central Taiwan, and we show that recrystallization and vein emplacement there took place within a relatively restricted range of PT conditions within the greenschist facies. We show that quartz recrystallized at low temperatures can equilibrate with respect to Ti in short time scales with little strain, and that the calibration of Thomas et al. (2010) predicts measured Ti concentrations well.

GEOLOGIC BACKGROUND

Taiwan's Hsüehshan range (Figs. 1 and 2) is comprised of lithofied coarse- to medium-grained sands and muds deposited in the Chinese continental margin during early Tertiary rifting (Ho, 1988). Hsüehshan range strata experienced minor extensional deformation and associated quartz veining during rifting (Clark et al., 1993; Tillman et al., 1992). An unconformity near the latitude of the study area at ~6.5 Ma separates these passive margin rocks from a foreland overlap sequence and marks the onset of collision of the Luzon volcanic arc with the Chinese continental margin (Lin et al., 2003). In the Hsüehshan range, deformation associated with collision is marked by upright folds (e.g. Fig. 3), subvertical cleavage, and pressure shadows indicative of co-axial deformation and horizontal compression (Clark et al., 1993; Tillman and Byrne, 1995).

Metamorphism throughout the Hsüehshan range is greenschist facies, with highest reported temperatures of ~475 °C reached near the core of the Tachien anticline (Fig. 2, Beyssac et al., 2007) based on Raman spectroscopy of carbonaceous material ("RSCM," Fig. 2c). Temperatures were at or near peak conditions at the onset of deformation. Beyssac et al. (2007) suggested that peak temperatures were acquired under "static" conditions prior to collision since peak temperatures based on traditional metamorphic phase equilibria are lower than those indicated by RSCM (Beyssac et al., 2007) and deformation facilitates metamorphic recrystallization but has relatively little effect on RSCM. Beyssac et al. (2007) and Chen et al. (2011) additionally point to a correlation between RSCM temperature and stratigraphic depth in uplifted strata as evidence that collisional-deformation postdated peak metamorphic conditions. We provide evidence below that temperatures were at least ~400 °C in the core of the Tachien anticline at the onset of deformation. Potential PT paths and available thermochronologic data are depicted in Fig. 4.

METHODS

Thin sections were made from 50 samples of quartzite and quartz veins. Eight representative samples were selected for further study. The eight were polished, cleaned with isopropyl alcohol and coated with ~30 nm Au. Ti concentrations in quartz were analyzed on the Cameca 7f Secondary Ion Mass Spectrometer (SIMS) at the California Institute of Technology using a $^{16}O^{-}$ primary ion beam. In the first of four sessions we used a beam current of 4–5 nA, a mass resolving power of ~3000, and analyzed masses ^{27}Al, ^{28}Si, ^{40}Ca, ^{47}Ti, ^{48}Ti, ^{49}Ti and ^{56}Fe. In the remaining sessions we used a beam current of 7–30 nA, a mass resolving power of ~4000, and analyzed masses ^{27}Al, ^{30}Si, ^{44}Ca, ^{47}Ti and ^{49}Ti. Prior to each analysis we rastered for 60 s over a 50 × 50 μm area. We used a field aperture of 100 μm to avoid surface contamination. In an early set of (discarded) analyses using a 400 μm aperture, Ti counts in samples containing less than ~1 ppm Ti steadily decreased over >1200 s and failed to reach Ti concentrations later found using a 100 μm aperture. No temporal decay in Ti-contamination was evident using the 100 μm aperture. Effective spot size using the small aperture is 8–10 μm.

Raw data were minimally filtered. We inspected and compared trends in element ratios for each analysis and removed 11 spots (of 560 total) that could be shown with reasonable certainty to have intersected non-quartz phases. This judgment call was made when two or three trace elements at the same spot were highly irregular or when high Ti concentration coincided with petrographic evidence that the beam encountered non-quartz phases. Because of the difficulty in confidently distinguishing micro- or nano-inclusions encountered in a SIMS analysis from quartz (which could contain fine-scale compositional anomalies), we did not filter out occasional mass cycles with anomalous trace element contents. Instead, all mass cycles were used to estimate Ti-concentrations. Our approach was to minimize subjective biases introduced by picking outliers, and use median estimates and standard errors to estimate mean values and uncertainties since these statistics are better suited for noisy data than the arithmetic mean and standard deviation.

Analyses that are likely to have intersected grain boundaries or cracks are noted in appendix 2. We carried out a few test analyses of cracks in large, low-Ti quartz grains to determine whether they yield anomalous Ti concentrations (e.g., due to contamination during polishing). These analyses showed no higher Ti concentrations than adjacent quartz. Based on this, and the difficulty in fine-grained recrystallized zones of establishing whether or not an analysis intersected a grain boundary, we did not discard analyses that may have intersected grain boundaries.

We used a regression line constrained through the origin (Fig. 5) to calculate Ti concentrations using National Institute of Standards (NIST) glasses 610 and 612 (434 ± 15 and 44 ± 5 ppm TiO2 respectively, Jochum et al., 2005). To account for matrix effects between quartz and NIST glass, we used the correction factor determined by Behr et al. (2010). While such corrections could potentially change over time and under different SIMS environments, we note that the Behr et al. (2011) analyses were carried out on the same SIMS used in this study and that measured Ti/Si ratios for NIST glasses for the two studies are within error. The robustness of the correction factor is additionally suggested by its reproducibility using the same glasses and quartz standards on the SIMS at Arizona State University (W. Behr, personal communication, 2011). To check the Behr et al. (2010) correction factor, in our third analytical session we analyzed an experimentally synthesized, Ti-doped quartz (sample "Qtip 17" from Thomas et al., 2010) which has light and dark sector zones in CL images and independently known Ti concentrations of 53 ± 3 and 40 ± 2 ppm, respectively. We measure similar Ti concentrations of 56.0 ± 1 and 47.6 ± 1 ppm, respectively, using the NIST glass as standards. A regression line based on these results instead of the NIST glasses would shift our results only ~10 °C lower. As a Ti-blank, we used Herkimer “Diamond,” a natural quartz containing <6 ppb Ti (Kohn and Northrup, 2009). Our analyses of this natural blank gave apparent concentrations of 15 ± 20 and 31 ± 42 ppb in session 1. The higher beam current used in later sessions however allowed us to resolve an apparent concentration of ~4–5 ± 2 ppb in the blank, consistent with previous work (Kohn and Northrup, 2009). No blank correction was made since these values are minimal and consistent with the expected Ti concentration of Herkimer diamond estimated by Kohn and Northrup (2009).

The TitaniQ calibration of Wark and Watson (2006) was based on experiments carried out at a uniform pressure of 10 kbar. Later experiments by Thomas et al. (2010) found a significant pressure dependence captured by the expression

$$RT \ln X_{TiO_2}^{quartz} = -60952 + 1520 \cdot T(K) - 1741 \cdot P(kbar) + RT \ln a_{TiO_2} \qquad (1)$$

where R is the gas constant 8.3145 J/K, T is temperature in Kelvin, $X_{TiO_2}^{quartz}$ is the mole fraction of TiO_2 in quartz, and a_{TiO_2} is the activity of TiO_2 in the system. Huang and Audétat (2012) found that Ti concentrations in experimentally grown quartz additionally correlate with crystallization rate, and present the relationship

$$\log Ti(ppm) = -0.2794.3\ /T - 660.53 \cdot (P^{0.35}/T) + 5.6459 \qquad (2)$$

based on their slowest experiments, with T given in Kelvin and P in kbar. Unless otherwise noted, TitaniQ temperature reported in the paper are based on the Thomas et al. (2010) calibration.

Because metamorphic mineral assemblages observed in the Hsüehshan range are not amenable to independent quantitative geobarometry (Beyssac et al., 2007), we assume that pressure and temperature for each analysis are linked by a geothermal gradient of 25 ± 5 °/km (91 °/kbar assuming a crustal density of 2.8 g/cm^3). This geothermal gradient is broadly consistent with the change of 25–30 °/km in RSCM temperature with stratigraphic depth in the study area (Beyssac et al., 2007), the thermal history modeled by Simoes et al. (2007) for deep exposures of the Hsüehshan range prior to 4 Ma (Fig. 6), and the average thermal gradient in exploration wells in Taiwan (Zhou et al., 2003). The uncertainty in the estimate of the geothermal gradient of +5 or – 5 °/km would alter a temperature estimate of ~300 °C by - 10 or + 17 °C respectively (Fig. 6). We used a Ti activity of 1.0 since the quartzites, wall rocks of veins, and some veins themselves (see table 1) contain rutile.

Data for samples and standards are reported in appendix 2 and appendix 1 respectively. We averaged titanium concentrations based on $^{47}Ti/^{30}Si$ and $^{49}Ti/^{30}Si$ measurements to calculate reported temperatures (the average $^{47}Ti/^{49}Ti$ of all the data is 1.37 ± 0.01, within error of natural occurrence 1.375 ± 0.006; De Laeter et al., 2003). The uncertainties in temperature and pressure given in appendix 2 are dominated by analytical precision, but also include negligible uncertainties related to analyses of standards and the above mentioned correction factor of Behr et al. (2010). Median temperatures for recrystallized quartzite, unrecrystallized veins, and recrystallized veins are given in table 1. The 1 sigma and standard errors given in table 1 reflect only the standard deviation of the pooled analyses for a given vein or recrystallized fraction. Systematic errors resulting from uncertainty in the TitaniQ calibration and geotherm estimate are also given in table 1. By “fully recrystallized” we refer to areas with a fairly uniform recrystallized grain size, i.e. places where the beam intersected only unambiguously new grains with clear grain boundaries (no subgrains). Sorting of unrecrystallized and recrystallized quartz analyses was done under the petrographic microscope following SIMS analyses but without knowledge of the Ti content of the spots.

Cathodoluminescence (CL) images were acquired on a Zeiss 1550 VP field emission scanning electron microscope at Caltech. Photons were collected using a variable-pressure secondary electron detector operated at high vacuum, 30 kV accelerating voltage and 7 nA beam current.

RESULTS

Description of Samples

Sampled quartz veins are generally >99% quartz with occasional fragments of wall rock, chlorite, carbonate, illmenite, rutile, fluid inclusions and pressure solution seams. The wall rock of all the veins contains rutile; the presence or absence of rutile in veins is indicated in table 1. The veins were collected from slate, muddy siltstone, and fine- to coarse-grained quartzites, and have thicknesses ranging from 100 μm to 25 mm (table 1). Based on the orientation criteria of Tillman et al. (1992), we sampled veins that were emplaced both before and during collision (table 1). In three of the vein samples, crosscutting relationships described below allow us to discriminate sequential information about the timing of veining and dynamic recrystallization.

Two quartzite samples (148d and 148j) were chosen for intensive analysis. They have a wide range of initial grain size: fine-grained layers have detrital grains as small as 100 µm, while coarser layers contain grains commonly as large as 3 mm. The quartzite contains ~60%–80% quartz (detrital grains of quartz, quartzite, chert and quartz schist), along with lithic fragments (predominantly volcanics and slate), detrital feldspar and mica, and metamorphic chlorite and biotite (Figs. 7 and 8). The quartzites are moderately deformed with a minimum axial strain of 0.32 (Chapter 3). Foliation in the quartzites is defined by the near-vertical, NNE-SSW striking orientation of flattened porphyroclasts and subgrains (Figs. 2 and 7). This fabric is indistinguishable in orientation from the collisional fabrics in neighboring slates (figure 2, Clark et al., 1993; Fisher et al., 2002; Tillman and Byrne, 1995).

Throughout the Hsüehshan range, quartzites and quartz veins are dynamically recrystallized with a fine grain size of 4–22 µm (e.g. Figs. 9 and 10; Chapter 3). Recrystallization is focused along grain boundaries and occupies only 5%–10% of the samples, allowing at least rough outlines of original detrital grains to be established in thin section. Porphyroclasts (remnants of both detrital quartz grains and coarse vein quartz grains) are irregularly flattened, have serrated grain boundaries, strong undulose extinction, contain irregular subgrains of variable size, and occasionally contain deformation lamellae (Figs. 9, 10, 11). These features indicate a classification in the low temperature “bulge” recrystallization regime (Stipp et al., 2002b; Stipp et al., 2010), a rough analogue to the experimental dislocation creep “regime 1” of Hirth and Tullis (1992).

In the core of the Hsüehshan range, the bulging recrystallization is the latest phase of dynamic recrystallization and overprints coarser recrystallized grains (~100-400 µm), which we refer to as “midsized” grains. The midsized grains (and subgrains of similar size) have a strong, oblate shape preferred orientation with long axes parallel to foliation (Figs. 7, 10, 11). While collisional deformation is clearly responsible for the shape preferred orientation of the midsized grains, their formation during collision is only confirmed by comparison with undeformed Tachien and

Paileng quartzites to the east and west of the Tachien anticline where this grain size fraction is rare. The size of the midsized grains falls at the boundary between recrystallized grains interpreted to have formed by subgrain rotation recrystallization and grain boundary migration recrystallization (Stipp et al., 2010). It is likely that both processes were active since subgrains are abundant with similar size and orientation as fully recrystallized midsized grains, and petrographic evidence for migration of grain boundaries at a scale of 50–60 μm across interpreted detrital boundaries is also common (Fig. 11).

Independent Constraints on Temperature

The grey field shown in Fig. 2c depicts the range indicated by independent constraints on temperature for dynamic recrystallization. In the case of samples 148d and 148j this constraint brackets the formation of the fine recrystallized grains overprinting the midsized grains discussed above.

Peak Temperature Constraints

RSCM analyses (Beyssac et al., 2007) reflect peak temperature conditions and therefore serve as maximum temperature constraints for deformation. The spatial distribution of RSCM data from Beyssac et al. (2007) is plotted as grey diamonds in Fig. 2c. Systematic errors associated with the RSCM calibration are ~± 50 °C (Beyssac et al., 2004).

Minimum Temperature for Dynamic Recrystallization

The formation of dynamically recrystallized quartz grains requires a minimum temperature of 250–300 °C (Dresen et al., 1997; Dunlap et al., 1997; Stipp et al., 2002b; Stöckhert et al., 1999; van Daalen et al., 1999; Voll, 1976).

Structural Constraints on Quartz Vein Emplacement Temperature

Structural observations indicate that eight of the veins we analyzed were emplaced at temperatures above those required for dynamic recrystallization (i.e. >250–300 °C). The other six veins, including pre-collisional veins, have emplacement temperatures constrained only by the peak conditions indicated by RSCM (samples with blue and orange bars in Fig. 12 extending off the chart on the left). The structural constraints for the eight veins emplaced at >250–300 °C are based on the observation that the Hsüehshan range was at or near peak temperatures conditions at the onset of collision and followed a relatively monotonic cooling path thereafter (Fig. 4). By showing that these veins formed during collision, but prior to cooling below temperatures where dynamic recrystallization does not occur, we constrain their emplacement temperatures between 250 °C and peak conditions.

In sample 123b, a slate, cross-cutting relationships indicate that a vein ("vein 2") cut a strongly deformed "vein 1" following a period of deformation in which vein 1 was heavily recrystallized and transposed into a vertical, collision-related cleavage (Fig. 9a). Vein 1 formed during either stages 1, 2, or 3 on Fig. 4b. Vein 2 must have been emplaced after collision but before cooling below 250 °C (i.e. during stage 3 in Fig. 4) because it shows minor dynamic recrystallization itself but also cuts a collisional fabric.

The veins in samples 004 and 131 were sampled from the hinge zones of anticlines (e.g. Fig. 3; Fig. 4 of Chapter 3) formed during collision (Tillman and Byrne, 1995). The veins formed during folding since they are concentrated in the hinge zone and have a conjugate symmetry about the fold axis (Fig. 3). Dynamic recrystallization of the veins indicates that they were emplaced prior to cooling below 250 °C.

Microfabric Constraints on Maximum Deformation Temperature

An additional constraint on deformation temperature can be derived using the quartz deformation mechanism map of Stipp et al. (2002a). The map links the transitions between the three laboratory-based dislocation creep regimes in quartz (Hirth and Tullis, 1992) with similar microstructures found in well-constrained natural settings, and delineates boundaries in temperature-strain rate space between the regimes. Maximum bulk strain rate in the quartzite samples was ~6.3 x 10^{-14} s^{-1} (Chapter 3), yielding a maximum likely temperature for bulging recrystallization of ~360 °C. Uncertainties associated with this approach are significant but unquantified; we assume a value of ± 50 °C in Fig. 2c (i.e. the upper limit of the grey field is drawn at 410 °C).

Flow Law Constraint on Deformation Temperature

The late, overprinting dynamic recrystallization in the core of the Tachien anticline (samples 148d and 148j, grain size ~13–15 µm) is coarser grained than in the region to the west where the vein samples were collected (grain size ~7–12 µm; Chapter 3). The recrystallized grain size piezometer of Stipp and Tullis (2003) indicates differential stresses of ~75 MPa for the Tachien anticline quartzites and ~110 MPa for the samples west of the Tili fault (Chapter 3). This stress difference indicates a higher deformation temperature in the anticline core if we assume a standard dislocation creep flow law for quartzite a. We estimate a minimum temperature difference of ~50 °C by using the flow law for quartzite of Hirth et al. (2001), the above stress values, and assume the same strain rate in the two areas. The uniform strain rate assumption makes the estimate a minimum, since strain rates were probably slower in the west where the rocks show less total strain. Minimum deformation temperatures for samples 148d and 148j were thus ~300 °C (the minimum temperature of 250 °C required for dynamic recrystallization, plus 50 °C).

Ti concentrations

Veins

Ti contents for each sampled vein are shown in Fig. 12. Unrecrystallized portions of veins (unfilled bars in Fig. 12) have titanium concentrations of ~0.2–1.0 ppm. Fully recrystallized vein quartz (filled bars in Fig. 12) have equivalent or slightly higher Ti concentrations, however in no sample is the difference in Ti concentration between recrystallized and primary vein quartz significant at a 2-sigma level (table 1).

Quartzites

A high density of analyses (N = 459) in two quartzites samples from the core of the Tachien anticline was designed to: 1) establish potential differences in Ti concentration between undeformed remnant detrital grains and recrystallized grains (Figs. 10, 13, 14), 2) monitor potential changes in Ti concentration in quartz interpreted to have recrystallized via grain boundary migration (e.g. Figs. 11, 15), and 3) analyze quartz at various distances from the rims of porphyroclasts to document whether systematic changes in Ti content occur toward grain rims (Fig. 16). As shown in the histogram of detrital Ti concentrations in Fig. 13, unrecrystallized quartz shows a wide range of Ti concentrations from ~0.1 to ~200 ppm which we interpret, given slow diffusion rates of Ti in quartz (Cherniak et al., 2007), to reflect the diverse origins of the detrital quartz grains. Midsized grains have a range similar to the detrital grains, but with a higher proportion of analyses in the range ~1-10 ppm. Fully recrystallized grains from the latest deformation phase are represented by bars filled in black in Fig. 13 and peak in the range of 0.8–2 ppm.

DISCUSSION

Effect of dynamic recrystallization on Ti concentration in quartz

Titanium concentrations in quartz changed during recrystallization in the studied quartzites. Fine recrystallized grains mantling high Ti detrital quartz grains have lower Ti concentrations (Fig. 10). Early “midsized” recrystallized grains have modified Ti concentration distributions relative to detrital grains (Fig. 7): only 20% of detrital grain analyses have intermediate Ti concentrations (1-15 ppm) while 45% of the Ti analyses of the midsized grains fall in this range. It is clear from Fig. 14 that the trend towards intermediate Ti concentrations with reduced grain size continues to the finest grain fraction.

Do these changes represent equilibration of quartz and a Ti-bearing phase or phases? Or do they simply represent homogenization of quartz to an average composition, or incomplete loss of Ti from quartz without equilibration? The pattern of decreasing range of Ti-concentration with reduced grain size in Fig. 14 suggests that as recrystallization progressively reduced grain size, Ti-concentrations in quartz both decreased in areas that originally had high Ti-concentrations, and increased in areas that initially had low Ti-concentration. We conclude that Ti was not simply evacuated from quartz, but shifted toward an intermediate value. This value, ~1-2 ppm for the finest grain size fraction, is not simply an average concentration of initial Ti concentrations in detrital quartz grains, as we estimate a spatially averaged initial Ti concentration of the detrital grains was at least 10–20 ppm. We suggest that these changes in Ti concentration in recrystallized quartz reflect equilibration between quartz and at least one other phase.

In contrast to the quartzites, recrystallization of quartz in the studied veins was not associated with significant shifts in Ti concentration (Fig. 12). This observation is discussed further below.

Mechanisms of Ti-Mobility

We suggest that changes in Ti concentration in quartz in our samples occurred predominantly during grain boundary migration. During grain boundary migration, quartz is dissolved along one side of a grain boundary and precipitates with a new orientation on the other side (e.g. Urai et al., 1977). This process provides the opportunity for exchange of trace elements between minerals and grain boundary fluids. When such exchange occurs, gradients in trace element concentration along grain boundaries can increase, thereby increasing their mobility. Grain boundary migration was clearly active in our quartzite samples as evidenced by the offset of crystallographic grain boundaries from interpreted detrital grains boundaries (as marked by opaque and non-quartz phases, see e.g. Fig. 11). Typical migration distances range up to ~50 μm and are common, occurring 10–20 times per thin section. Figure 11 demonstrates one such location where, mean Ti concentration in an interpreted recrystallized area is 14 ± 7 ppm versus 34 ± 2 ppm Ti in unrecrystallized host grain. Figure 15 compiles the results of 6 such sites where large-scale grain boundary migration is suspected. A shift to lower average Ti concentrations in the recrystallized areas is apparent. A similar conclusion was also reached by Grujic (2011) who found reset Ti in mylonitized quartz veins recrystallized at temperatures above ~540 °C.

Although predicted characteristic diffusion distances for Ti in quartz based on experimentally-based diffusion coefficients (Cherniak et al., 2007) are exceedingly small under the deformation conditions experienced by the Hsüehshan range (~0.001 μm in 2.5 m.y. at 300 °C), it is possible that diffusion processes could play a roll in changing Ti concentrations (e.g. the affect of high dislocation densities and strain on diffusion in quartz is unknown). We would expect diffusion to be expressed by systematic, gradual shifts in Ti-concentration along grain rims. Porphyroclasts occasionally show indications of such behavior, e.g. the black-circled SIMS analyses in Fig. 10, and the slight convergence in Fig. 16 to intermediate Ti concentrations at distances of 5-20 μm. While intriguing, these limited observations are insufficient to unequivocally point to diffusion, and we suggest that diffusion of Ti was probably not a significant process in the sample we studied.

While we find grain boundary migration a likely mechanism for resetting Ti in quartz in the early mid-sized grains, the fine grain size associated with the latest phase of deformation prevents a similar analysis of these grains. We note that the fine grains classify within the grain boundary bulging regime of Stipp et al. (2002b; 2010)(Figs. 9, 10 and 11; Chapter 3), and hypothesize that Ti concentrations in the fine grains were reset in essentially the same fashion as we propose above for the midsized grains, i.e. migration and precipitation of Ti along migrating grain boundaries.

Bias and uncertainty of TitaniQ thermobarometry at low temperatures

A major uncertainty associated with Ti-in-quartz thermobarometry in greenschist facies rocks is the potential loss of accuracy associated with extrapolating trends from laboratory calibrations to quartz crystallized or recrystallized at temperatures many hundreds of degrees below laboratory conditions. A rough estimate of the goodness of fit of our results can be made by comparing the TitaniQ predictions of Thomas et al. (2010) and Huang and Audétat (2012) with the independent constraints depicted in Figs. 2, 12, and 13. The fit can be quantified if we assume that the TitaniQ thermometer is systematically biased by ΔT and that errors are normally distributed with a variance σ^2. We can then estimate ΔT and σ from their probability distributions computed from the estimated TitaniQ temperatures (T_o) and independent constraints on temperature T_{min} and T_{max} using:

$$\rho_i(\sigma, \Delta T) = \alpha \int_{Tmin}^{Tmax} \frac{1}{\sqrt{2\pi\sigma}} \exp\left(-\frac{(T - T_o - \Delta T)^2}{2\sigma^2}\right) dT$$

where ρ is probability, T_o is a TitaniQ temperature estimate, T is temperature, and α is a normalization factor. The product of the probabilities ρ of a group of analyses yields a probability density function in $\sigma - \Delta T$ space. The results of pooled analyses for vein emplacement (using only the eight veins with minimum and maximum constraints on temperature) and quartzite recrystallization are given in Table 2. For vein emplacement we estimate a bias of -22 °C +8/-6 (67% confidence interval) and 80 °C +8/-6 using the Thomas et al. (2010) and Huang and Audétat (2012) calibrations respectively. For quartzite recrystallization we calculate biases of 12 °C and 136 °C. The larger bias associated with the Huang and Audétat (2012) relationship may result from non-equilibrium effects in their experiments. The growth rate dependence they describe did not occur in the experiments of Thomas et al. (2010), whose experimental results vary significantly in grain size (<10 μm -1 mm) and therefore growth rate, with similar Ti concentrations in crystals of various sizes in any given experiment (J. Thomas, personal communication, 2012).

The bias values calculated above using the Thomas et al. (2010) calibration are small, and considering the multiple sources of potential error, there is good accord between our results and the Thomas et al. (2010) calibration. We believe the difference in estimated bias between the veins and quartzites results in part from the higher concentration of high Ti outliers in recrystallized quartzites (note the skew of the distribution of the fully recrystallized grains in Fig. 13). This is probably due to a combination of incomplete equilibration from initial conditions (detrital grains in the Tachien sandstone are dominantly high Ti) and a higher concentration of impurities in the quartzite than the veins. While a more “hands on” approach to filtering anomalous SIMS cycles and potential outliers would reduce this difference, it would introduce a set of judgment calls needed to distinguish “real” quartz analyses and analyses of inclusions.

There is no reliable procedure for distinguishing between inclusions and a high impurity concentration, and *ad hoc* procedures to do so reduce the ability to make meaningful comparisons between studies.

Constraints on Hsüehshan range deformation conditions and timing

The thermomechanical model of Simoes et al. (2007) required two phases of deformation to match thermochronologic and metamorphic constraints in the Hsüehshan range. The early phase is characterized by slow uplift and erosion rates throughout the orogenic wedge, and the second by underplating and increased uplift rates in the Hsüehshan range. Geologic evidence also suggests a two-phase evolution of the Hsüehshan range, with early deformation characterized by penetrative horizontal compression responsible for over 30 km of shortening (Fisher et al., 2002), and later deformation marked by out of sequence thrusts (Tillman and Byrne, 1996). We suggest that the two-phases proposed by the different researchers are equivalent. This constrains the timing of the upright folding, subvertical cleavage, and strain markers described by Clark et al. (1993) and Tillman and Byrne (1995) to before ~4 Ma, the timing of phase two onset in the model of Simoes et al. (2007). This age constraint is consistent with observations of dislocation creep in quartzite associated with compressional deformation (this study; Tillman and Byrne, 1995), since this deformation mechanism could not be active following cooling through the zircon fission track closure temperature of ~200–260 °C at 2.6–2.9 Ma (figure 3; Liu et al., 2001). The second phase of deformation may continue to the present-day, where little or no internal shortening in the Hsüehshan range is observed (Simoes and Avouac, 2006).

Previous studies of the Hsüehshan range have documented deformation under retrograde conditions (Clark et al., 1993) and concluded that peak metamorphism of the Hsüehshan range occurred “statically,” prior to collision (Beyssac et al., 2007). In the course of our study we have noted features from the core of the Tachien anticline indicating that compressional deformation began while temperatures were at or near peak conditions. First, metamorphic biotite, originally noted by Yen (1973), grew in pressure shadows oriented consistently with compressional deformation (Fig. 8). Secondly, the presence of systematically oriented midsized recrystallized grains and subgrains, and the migration of grain boundaries in the quartzite samples across distances of 50–60 μm (e.g. Fig. 11) is indicative of high-temperature grain-boundary migration recrystallization (Stipp et al., 2002a). These features indicate temperatures of at least ~400 °C (Bucher and Grapes, 2011; Stipp et al., 2002a) at the onset of collision ~6.5 Ma (Lin et al., 2003), somewhat warmer than modeled by Simoes et al. (2007; Fig. 4, 6). This early high-temperature deformation may have resulted from thickening at the toe of the orogenic wedge under ambient PT conditions prior to significant motion on the decollement beneath the Hsüehshan range.

Recommendations for future TitaniQ studies

We suggest that quartzites are generally more likely to be reset during dynamic recrystallization than vein quartz. Grujic et al. (2011) found that Ti concentrations did not change during bulging recrystallization in mylonitic veins recrystallized at similar PT conditions as the Hsüehshan range quartzites, despite much higher strains in their rocks. We note similar behavior in the Hsüehshan range veins (Fig. 12, although here it also possible that PT conditions were constant during veining and recrystallization). The lack of resetting of Ti in recrystallized vein quartz may result from an absence or scarcity of Ti-bearing phases in veins. In the quartzite we studied, Ti-bearing phases are nearly always <200 μm from recrystallized quartz. Rutile, while present in some of our veins, is rare, and the nearest source of Ti is often wall rock several mm distant (table 1). Future studies on veins can test this hypothesis by analyzing quartz at various distances from vein edges.

As a new technique, the applicability of TitaniQ thermobarometry is debated (e.g. Thomas and Watson, 2012; Wilson et al., 2012), and further field-based tests in well-constrained localities are warranted before Ti-concentrations in quartz can be confidently interpreted in te16 of PT conditions. Many previous studies have focused on Ti-undersaturated systems, and considerable effort has been expended attempting to simultaneously determine Ti activity and test TitaniQ (e.g. Grujic et al., 2011; Wilson et al., 2012). A priority for the next phase of field-based TitaniQ studies should be the deconvolution of these two sources of uncertainty by carrying out studies in rocks containing rutile.

An additional uncertainty in Ti-in-quartz thermobarometry not previously discussed, is the possibility that the relevant pressure term in the TitaniQ equation is fluid pressure rather than lithostatic pressure as has previously been assumed (though not stated, e.g. Behr and Platt, 2011; Grujic et al., 2011). In many situations these pressure te16 are equal, e.g. magmas, deep crustal rocks, and the experimental capsules used to calibrate TitaniQ. Near the brittle-ductile transition however, fluid pressure may often be sub-lithostatic (e.g. Behr and Platt, 2011; Kuster and Stöckhert, 1998; Townend and Zoback, 2000). In the Hsüehshan range, differential stress estimates require nearly hydrostatic fluid pressure, since effective pressure ($P_{lithostatic}$ - P_{fluid}) must be greater than differential stress in order for dislocation creep and dynamic recrystallization to occur (Kohlstedt et al., 1995). Vein quartz certainly fo16 in the presence of fluid, and fluids may also be present along grain boundaries during grain boundary migration (e.g. Hippertt, 1994; Mancktelow and Pennacchioni, 2004; Urai et al., 1977). It is possible that Ti concentrations in quartz in these settings are a function of fluid pressure rather than lithostatic pressure. Were this the case, temperatures based on Thomas et al. (2010) would be ~30-40 °C lower than calculated above. Used with fluid pressure, the Huang and Audétat (2012) equation would give results more consistent with the independent constraints above, however this combination significantly overpredicts temperature in higher grade rocks where fluid pressures were likely lithostatic (e.g. the data presented by Storm and Spear, 2009). Considering the importance of fluid pressure in the crust (e.g. Townend and Zoback, 2000), further exploration of the sensitivity of TitaniQ to different types of pressure is warranted.

CONCLUSIONS

1) Collisional deformation of quartzites in the core of the Tachien anticline began at temperatures >400 °C, and was accommodated in part by high temperature grain boundary migration recrystallization, then by bulging recrystallization as deformation continued at lower temperatures. Quartz recrystallization and penetrative deformation occurred between ~6.5 and 4 Ma.
2) Equilibration of Ti in dynamically recrystallized quartz occurred in <2.5 m.y., during moderate deformation (axial strain ~0.32) at temperatures ~300 °C.
3) If Ti concentrations are sensitive to lithostatic pressure, as commonly assumed, the TitaniQ calibration of Thomas et al. (2010) predicts Ti concentrations in vein quartz and recrystallized quartzite within error of independently known deformation conditions in the Hsüehshan range, whereas the more recent equation from Huang and Audétat (2012) overpredicts temperatures by ~100 °C.
4) If instead Ti concentrations are a function of fluid pressure, the Thomas et al. (2010) calibration underpredicts temperatures in the Hsüehshan range by ~30-40 °C.

FIGURE LEGENDS AND TABLE TITLES

Figure 1. Shaded relief map of Taiwan showing simplified tectonic provinces modified after Ho (1988): FB, foreland basin; WF, western foothills; HR, Hsüehshan range; BS, Backbone slates; TC, Pre-Tertiary Tananao complex; LV, Longitudinal Valley; CoR, Coastal Range; LZ, Luzon Volcanic Arc. Study area is located within the box labeled Fig. 2. Plate convergence rate (white arrow) is taken from Sella et al. (2002).

Figure 2. A: Geologic map of a portion of the Hsüehshan range based on Tillman and Byrne (1995) and Ho (1988) showing rock units, major structures and sample locations. B: Composite cross section based on Tillman and Byrne (1995) showing their strain ellipse data from slates and our foliation analyses from quartzites. C: TitaniQ temperature estimates (Thomas et al., 2010) on individual veins and independent temperature constraints are plotted relative to location on the cross section. Grey diamonds are peak temperatures from Raman spectroscopy of carbonaceous material ("RSCM"). RSCM and microstructural-based constraints discussed in the text limit quartz recrystallization to the area shaded in grey. TitaniQ estimates for vein emplacement temperatures with independent maximum and minimum temperature constraints are shown in purple. Dynamic recrystallization temperatures of quartzites and veins are shown in blue.

Figure 3. Anticline within the Chiayang formation, and location of sample 131g. The outcrop is dominantly quartzite, with minor slate interbeds. Insets show examples of conjugate veins concentrated in the hinge zone of the anticline.

Figure 4. Constraints on temperature-time history and possible cooling paths for (A) the deepest exposed levels of the Hsüehshan range where quartzites 148d and 148j were sampled, and (B) the cooler region to the west where the remainder of samples were collected. Cooling rates since ~3 Ma are well constrained at ~90 °/m.y. by zircon fission track (Liu et al., 2001), zircon U-Th-He (Beyssac et al., 2007), and white mica K-Ar data (Tsao, 1996). Note that the x-axis is compressed by a factor of 10 between 30 and 8 Ma. The dashed line reproduces the results of the thermal-kinematic model of Simoes et al. (2007). The thin black lines represent cooling paths constrained by evidence of elevated temperatures at the onset of collision. Quadrants 1, 2, 3, and 4 separate

pre- and post-collision stages and stages where dynamic recrystallization (DRX) occurs (grey) or does not occur (white). Closure temperatures for K-Ar data on a set of <2 μm white mica grains span the values quoted by Tsao (1996) and a lower temperature suggested by Beyssac et al. (2007) for these data.

Figure 5. Ti content of standards vs. adjusted ^{49}Ti/^{30}Si ratios. Measured ^{49}Ti/^{30}Si ratios for NIST glasses are corrected for Si concentration (multiplied by factors of 0.7 and 0.72 for NIST 610 and 612 respectively to account for differences in silica content between quartz and NIST glass) then divided by a correction factor of 0.67 (Behr et al., 2010) to enable direct comparison with NIST glasses. The plotted regression line is constrained by the origin and data for NIST glasses only. Quartz samples Qtip-17 and a sample of Herkimer "Diamond" are plotted for comparison purposes (see text). Error bars for ^{49}Ti/^{30}Si ratios and Ti concentrations are 2σ.

Figure 6. Pressure-temperature plot showing the Thomas et al. (2010) and Huang and Audétat (2012) TitaniQ calibrations for 0.1, 1, and 10 ppm Ti; the 25 °/km geothermal gradient assumed in our calculations with ±5 °/km assumed uncertainty (gray field); the PT path for the core of the Hsüehshan range from the model of Simoes et al. (2007) (orange line) with numbers indicating ages in Ma. The geothermal gradient at 4 Ma from the thermokinematic model of Simoes et al. (2007) is shown in red.

Figure 7. Photomicrographs of sample 148d oriented with bedding horizontal and vertical tectonic foliation marked by preferred orientation of porphyroclasts and subgrains. A: unpolarized. B: Cross polarized. Locations of Figs. 10 and 11 are outlined in (A). The white circles in (B) indicate two locations dominated by "midsized" recrystallized grains as discussed in the text. FOV ~7 mm.

Figure 8. Photomicrograph of sample 148d showing growth of metamorphic biotite in strain fringes on two detrital feldspar grains in the core of the Tachien anticline. Bedding and tectonic shortening direction (WNW-ESE) are horizontal in the figure. FOV 0.9 mm.

Figure 9. Microphotographs of two samples where alternating brittle and plastic deformation can be documented. A: sample 123b showing a strongly recrystallized early vein (“vein 1”) cut and offset by a later vein (“vein 2”) outlined in yellow. Foliation (vertical in the field) is horizontal in the photograph. FOV ~12 mm. B: Photo of site 34 in sample 004, with early vein material strongly recrystallized in the upper part of the photograph. A late vein (“vein 2”) running from lower left to upper right postdates dynamic recrystallization of the earlier vein. The late vein has a lower inclusion concentration and retains some crystal facets (lower left). Undulatory extinction, subgrains, and minor dynamic recrystallization (inset) of the late vein indicate it too was deformed at temperatures >250 °C. FOV ~2.7 mm.

Figure 10. Cross-polarized microphotograph (A), cross-polarized microphotograph with mica-plate inserted (B), and CL image (C) of the same area of quartzite sample 148d. D: Graph of Ti concentrations for SIMS analyses. White lines on the images are detrital grain boundaries. Spacing of SIMS analyses is 25 μm. The five black-outlined spots in (A) are analyses where Ti concentration is notably reduced in the vicinity of grain boundaries. This trend does not hold for all grain boundaries (e.g. the edge of the top grain in the figure), but occurs more often than not. Two white-outlined spots in the grain at the top of the figure show significant reduction of Ti content along a band marked by increased visible inclusions (A and B) and lower CL intensity (C). This zone corresponds with a subgrain boundary visible under different polarization orientation.

Figure 11. Photomicrographs showing an example of a large-scale grain boundary migration. A: Image taken in plain polarized light showing outlines of three labeled detrital grains. B: Same image taken under cross-polarized light with the mica-plate inserted. A portion of the right side of grain 1 has been recrystallized with the same orientation as grain 2. Arrows indicate the interpreted direction and magnitude of grain boundary migration. C: CL image of the same area. The recrystallized portion of grain 1 in this image has a slightly darker color than either grain 1 or 2. D: Cross-polarized image showing Ti concentrations in grains 1 and 2. Ti concentrations in the recrystallized portion of grain 1 are significantly lower than the average Ti concentration of grain 1 (see text for details). Field of view: 880 μm.

Figure 12. Histograms showing Ti content of fully recrystallized grains (black fill) and unrecrystallized or incompletely recrystallized grains (white fill). Orange and blue bars at the base of the histograms indicate the range of Ti concentrations predicted by the Huang and Audétat (2012) and Thomas et al. (2010) TitaniQ calibrations respectively based on independent temperature constraints discussed in the text. The orange and blue bars are based on a geothermal gradient between 20 and 30 °/km. Temperature scale shown is based on Thomas et al. (2010) calibration assuming 25 °/km.

Figure 13. Histograms showing (A) Ti content of detrital grain remnants (white fill), (B) midsized recrystallized grains (grey fill), and (C) fully recrystallized fine-grained quartz (black fill). Orange and blue bars at the base of the histograms indicate the range of Ti concentrations predicted by the Huang and Audétat (2012) and Thomas et al. (2010) TitaniQ calibrations respectively based on independent temperature constraints discussed in the text. The orange and blue bars are based on a geothermal gradient between 20 and 30 °/km. The histogram for detrital quartz is biased by the preferential analysis of low Ti grains, and its peaks should not therefore be strictly interpreted in terms of sedimentary provenance. Temperature scale shown is based on Thomas et al. (2010) calibration assuming 25 °/km.

Figure 14. Temperature vs. grain size for all analyses in the quartzite samples.

Figure 15. Comparison of compiled Ti analyses in (A) six detrital porphyroclasts and (B) regions of the same porphyroclasts believed to have recrystallized due to grain boundary migration (GBM). An example of one such site is shown in Fig. 11. Temperature scale shown is based on Thomas et al. (2010) calibration assuming 25 °/km.

Figure 16. Ti concentration vs. distance to grain edge in porphyroclasts.

REFERENCES

Behr, W. M., and Platt, J. P., 2011, A naturally constrained stress profile through the middle crust in an extensional terrane: Earth and Planetary Science Letters, v. 303, no. 3-4, p. 181-192.

Behr, W. M., Thomas, J., and Hervig, R., 2010, Calibrating Ti concentrations in quartz on the SIMS using NIST silicate glasses with applications to the TitaniQ geothermobarometer: American Mineralogist, v. 96, no. 7, p. 1100-1106.

Beyssac, O., Bollinger, L., Avouac, J. P., and Goffé, B., 2004, Thermal metamorphism in the Lesser Himalaya of Nepal determined from Raman spectroscopy of carbonaceous material: Earth and Planetary Science Letters, v. 225, p. 233-241.

Beyssac, O., Simoes, M., Avouac, J. P., Farley, K. A., Chen, Y.-G., Chan, Y.-C., and Goffé, B., 2007, Late Cenozoic metamorphic evolution and exhumation of Taiwan: Tectonics, v. 26, no. 6, p. 1-32.

Bucher, K., and Grapes, R., 2011, Petrogenesis of Metamorphic Rocks, 8th Edition, Springer-Verlag, 428 p.:

Chen, C. T., Chan, Y. C., Lu, C. Y., Simoes, M., and Beyssac, O., 2011, Nappe structure revealed by thermal constraints in the Taiwan metamorphic belt: Terra Nova, v. 23, no. 2, p. 85-91.

Cherniak, D. J., Watson, E. B., and Wark, D. A., 2007, Ti diffusion in quartz: Chemical Geology, v. 236, no. 1-2, p. 65-74.

Clark, M. B., Fisher, D. M., Lu, C.-Y., and Chen, C.-H., 1993, Kinematic analyses of the Hsüehshan range, Taiwan: A large-scale pop-up structure: Tectonics, v. 12, no. 1, p. 205-217.

De Laeter, J. R., Bohlke, J. K., De Bievre, P., Hidaka, H., Peiser, H. S., Rosman, K. J. R., and Taylor, P. D. P., 2003, Atomic weights of the elements: Review 2000 - (IUPAC technical report): Pure and Applied Chemistry, v. 75, no. 6, p. 683-800.

Dresen, G., Duyster, J., Stockhert, B., Wirth, R., and Zulauf, G., 1997, Quartz dislocation microstructure between 7000 m and 9100 m depth from the Continental Deep Drilling Program KTB: Journal of Geophysical Research, v. 102, no. B8, p. 18,443-418,452.

Dunlap, W., Hirth, G., and Teyssier, C., 1997, Thermomechanical evolution of a ductile duplex: Tectonics, v. 16, no. 6, p. 983-1000.

Fisher, D. M., Lu, C.-Y., and Chu, H. T., 2002, Taiwan Slate Belt: Insights into the ductile interior of an arc-continent collision, *in* Byrne, T., and Liu, C. S., eds., Geology and Geophysics of an Arc-Continent Collision, Taiwan: Boulder, Colorado, Geological Society of America Special Paper 358, p. 93-106.

Grujic, D., Stipp, M., and Wooden, J. L., 2011, Thermometry of quartz mylonites: Importance of dynamic recrystallization on Ti-in-quartz reequilibration: Geochemistry Geophysics Geosystems, v. 12, no. 6.

Hippertt, J. o. F. M., 1994, Grain boundary microstructures in micaceous quartzite: significance for fluid movement and deformation processes in low metamorphic grade shear zones: The Journal of Geology, v. 102, no. 3, p. 331-348.

Hirth, G., Teyssier, C., and Dunlap, W., 2001, An evaluation of quartzite flow laws based on comparisons between experimentally and naturally deformed rocks: International Journal of Earth Sciences (Geol Rundsch), v. 90, p. 77-87.

Hirth, G., and Tullis, J., 1992, Dislocation creep regimes in quartz aggregates: Journal of Structural Geology, v. 14, no. 2, p. 145-159.

Ho, C. S., 1988, An introduction to the geology of Taiwan: explanatory text of the geologic map of Taiwan, Taipei, Taiwan, Republic of China, Central Geological Survey, Ministry of Economic Affairs, xiii, 192 p., 120 p. of plates p.:

Huang, R., and Audétat, A., 2012, The titanium-in-quartz (TitaniQ) thermobarometer: A critical examination and re-calibration: Geochimica Et Cosmochimica Acta, v. 84, p. 75-89.

Jochum, K., Nohl, U., Herwig, K., Lammel, E., Stoll, B., and Hofmann, A., 2005, GeoReM: A new geochemical database for reference materials and isotopic standards: Geostandards Newsletters, v. 22, p. 7-13.

Kawasaki, T., and Osanai, Y., 2008, Empirical thermometer of TiO2 in quartz for ultrahigh-temperature granulites of East Antarctica: Geological Society, London, Special Publications, v. 308, no. 1, p. 419-430.

Kohlstedt, D. L., Evans, B., and Mackwell, S. J., 1995, Strength of the lithosphere–constraints imposed by laboratory experiments: Journal of Geophysical Research-Solid Earth, v. 100, no. B9, p. 17587-17602.

Kohn, M. J., and Northrup, C. J., 2009, Taking mylonites' temperatures: Geology, v. 37, no. 1, p. 47-50.

Kuster, M., and Stöckhert, B., 1998, High differential stress and sublithostatic pore fluid pressure in the ductile regime — microstructural evidence for short-term post-seismic creep in the Sesia Zone, Western Alps: Tectonophysics, v. 1998, no. 303, p. 263-277.

Lin, A. T., Watts, A. B., and Hesselbo, S. P., 2003, Cenozoic stratigraphy and subsidence history of the South China Sea margin in the Taiwan region: Basin Research, v. 15, p. 453-478.

Liu, T. K., Hsieh, S., Chen, Y. G., and Chen, W. S., 2001, Thermo-kinematic evolution of the Taiwan oblique-collision mountain belt as revealed by zircon fission track dating: Earth and Planetary Science Letters, v. 186, no. 1, p. 45-56.

Mancktelow, N. S., and Pennacchioni, G., 2004, The influence of grain boundary fluids on the microstructure of quartz-feldspar mylonites: Journal of Structural Geology, v. 26, no. 1, p. 47-69.

Menegon, L., Nasipuri, P., Stünitz, H., Behrens, H., and Ravna, E., 2011, Dry and strong quartz during deformation of the lower crust in the presence of melt: Journal of Geophysical Research, v. 116, no. B10.

Pennacchioni, G., Menegon, L., Leiss, B., Nestola, F., and Bromiley, G., 2010, Development of crystallographic preferred orientation and microstructure during plastic deformation of natural coarse-grained quartz veins: Journal of Geophysical Research-Solid Earth, v. 115, p. -.

Peterman, E. M., and Grove, M., 2010, Growth conditions of symplectic muscovite plus quartz: Implications for quantifying retrograde metamorphism in exhumed magmatic arcs: Geology, v. 38, no. 12, p. 1071-1074.

Raimondo, T., Clark, C., Hand, M., and Faure, K., 2011, Assessing the geochemical and tectonic impacts of fluid-rock interaction in mid-crustal shear zones: a case study from the intracontinental Alice Springs Orogen, central Australia: Journal of Metamorphic Geology, v. 29, no. 8, p. 821-850.

Rasmussen, B., Fletcher, I. R., Muhling, J. R., Gregory, C. J., and Wilde, S. A., 2011, Metamorphic replacement of mineral inclusions in detrital zircon from Jack Hills, Australia: Implications for the Hadean Earth: Geology, v. 39, no. 12, p. 1143-1146.

Rusk, B. G., Lowers, H. A., and Reed, M., H., 2008, Trace elements in hydrothermal quartz: Relationships to cathodoluminescent textures and insights into vein formation: Geology, v. 36, no. 7, p. 547-550.

Sella, G. F., Dixon, T. H., and Mao, A. L., 2002, REVEL: A model for recent plate velocities from space geodesy: Journal of Geophysical Research-Solid Earth, v. 107, no. B4, p. -.

Simoes, M., and Avouac, J. P., 2006, Investigating the kinematics of mountain building in Taiwan from the spatiotemporal evolution of the foreland basin and western foothills: Journal of Geophysical Research, v. 111, no. B10, p. 1-25.

Simoes, M., Avouac, J. P., Beyssac, O., Goffé, B., Farley, K. A., and Chen, Y.-G., 2007, Mountain building in Taiwan: A thermokinematic model: Journal of Geophysical Research, v. 112, no. B11, p. 1-25.

Spear, F. S., and Wark, D. A., 2009, Cathodoluminescence imaging and titanium thermometry in metamorphic quartz: Journal of Metamorphic Geology, v. 27, p. 187-205.

Stipp, M., Stunitz, H., Heilbronner, R., and Schmid, S. M., 2002a, Dynamic recrystallization of quartz: correlation between natural and experimental conditions: Deformation Mechanisms, Rheology and Tectonics: Current Status and Future Perspectives, v. 200, p. 171-190.

Stipp, M., Stünitz, H., Heilbronner, R., and Schmid, S. M., 2002b, The eastern Tonale fault zone: a 'natural laboratory' for crystal plastic deformation of quartz over a temperature range from 250 to 700 °C: Journal of Structural Geology, v. 24, p. 1861-1884.

Stipp, M., and Tullis, J., 2003, The recrystallized grain size piezometer for quartz: Geophysical Research Letters, v. 30, no. 21.

Stipp, M., Tullis, J., Scherwath, M., and Behrmann, J. H., 2010, A new perspective on paleopiezometry: Dynamically recrystallized grain size distributions indicate mechanism changes: Geology, v. 38, no. 8, p. 759-762.

Stöckhert, B., Brix, M. R., Kleinschrodt, R., Hurford, A. J., and Wirth, R., 1999, Thermochronometry and microstructures of quartz--comparison with experimental flow laws and predictions on the temperature of the brittle-plastic transition: Journal of Structural Geology, v. 21, p. 351-369.

Storm, L. C., and Spear, F. S., 2009, Application of the titanium-in-quartz thermometer to pelitic migmatites from the Adirondack Highlands, New York: Journal of Metamorphic Geology, v. 27, no. 7, p. 479-494.

Thomas, J., and Watson, E., 2012, Application of the Ti-in-quartz thermobarometer to rutile-free systems. Reply to: A comment on: 'TitaniQ under pressure: the effect of pressure and temperature on the solubility of Ti in quartz': Contributions to Mineralogy and Petrology, v. in press.

Thomas, J. B., Watson, E. B., Spear, F. S., Shemella, P. T., Nayak, S. K., and Lanzirotti, A., 2010, TitaniQ under pressure: the effect of pressure and temperature on the solubility of Ti in quartz: Contributions to Mineralogy and Petrology.

Tillman, K. S., and Byrne, T. B., 1995, Kinematic Analysis of the Taiwan Slate Belt: Tectonics, v. 14, no. 2, p. 322-341.

-, 1996, Out-of-sequence thrusting in the Taiwan Slate Belt: Journal of the Geological Society of China, v. 39, p. 189-208.

Tillman, K. S., Byrne, T. B., and Lu, C.-Y., 1992, Pre-collision extensional structures from the central range, Taiwan: implications for the kinematic evolution of the South China Margin: Acta Geologica Taiwanica, v. 30, p. 11-26.

Townend, J., and Zoback, M. D., 2000, How faulting keeps the crust strong: Geology, v. 28, no. 5, p. 399-402.

Tsao, S. J., 1996, The geological significance of illite crystallinity, zircon fission-track ages and K-Ar ages of metasedimentary rocks of the Central Range [Ph.D.: National Taiwan University, 272 p.

Urai, J. L., Means, W. D., and Lister, G. S., 1977, Dynamic recrystallization of minerals, *in* Hobbs, B. E., and Heard, H. C., eds., Mineral and rock deformation: laboratory studies. The Paterson Volume. Geophysical Monograph 36: Washington, DC, American Geophysical Union, p. 161-199.

van Daalen, M., Heilbronner, R., and Kunze, K., 1999, Orientation analysis of localized shear deformation in quartz fibres at the brittle-ductile transition: Tectonophysics, v. 303, no. 1-4, p. 83-107.

Voll, G., 1976, Recrystallization of quartz, biotite and feldspars from Erstfeld to the Leventina nappe, Swiss Alps, and its geological significance: Schweizer Mineralogische und Petrographische Mitteilungen, v. 56, p. 641-647.

Wark, D. A., and Watson, B., 2006, TitaniQ: a titanium-in-quartz geothermometer: Contributions to Mineralogy and Petrology, v. 2006, no. 152, p. 743-754.

Wilson, C. J. N., Seward, T. M., Allan, A. S. R., Charlier, B. L. A., and Bello, L., 2012, A comment on: ‘TitaniQ under pressure: the effect of pressure and temperature on the solubility of Ti in quartz’, by Jay B. Thomas, E. Bruce Watson, Frank S. Spear, Philip T. Shemella, Saroj K. Nayak and Antonio Lanzirotti: Contributions to Mineralogy and Petrology, v. In Press.

Yen, T. P., 1973, The Eocene sandstones in the Hsüehshan range terrain, Northern Taiwan: Proceedings of the Geological Society of China, v. 16, p. 97-110.

Zhou, D., Yu, H.-S., Xu, H.-H., Shi, X.-B., and Chou, Y.-W., 2003, Modeling of thermo-rheological structure of lithosphere under the foreland basin and mountain belt of Taiwan: Tectonophysics, v. 374, no. 3-4, p. 115-134.

Figure 1

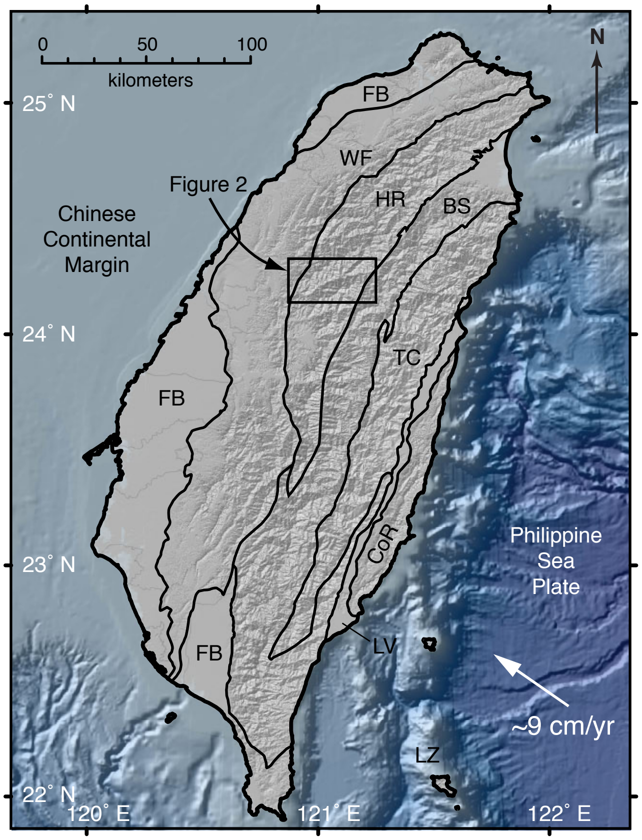
0
50
100
kilometers
N
25° N
24° N
23° N
22° N
120° E
121° E
122° E
FB
WF
HR
BS
Figure 2
Chinese Continental Margin
TC
FB
CoR
Philippine Sea Plate
LV
FB
~9 cm/yr
LZ

Figure 2

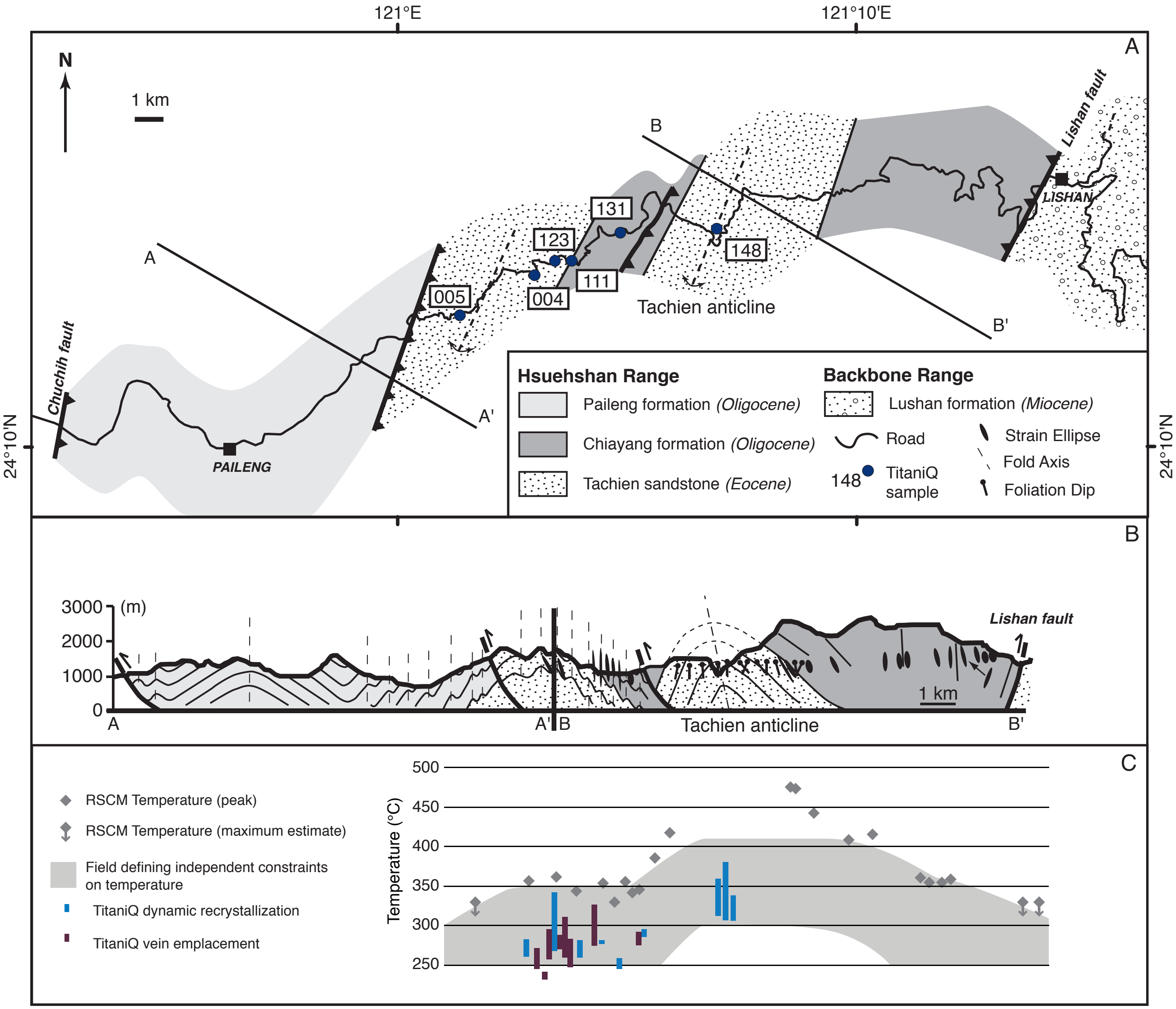
121°E
121°10'E
A
N
1 km
B
Lishan fault
LISHAN
131
123
148
005
004
111
Tachien anticline
B'
A
A'
Chuchih fault
PAILENG
24°10'N
24°10'N
Hsuehshan Range
Paileng formation (Oligocene)
Chiayang formation (Oligocene)
Tachien sandstone (Eocene)
Backbone Range
Lushan formation (Miocene)
Road
148 TitaniQ sample
Strain Ellipse
Fold Axis
Foliation Dip
B
3000 (m)
2000
1000
0
Lishan fault
1 km
A
A' B
Tachien anticline
B'
C
RSCM Temperature (peak)
RSCM Temperature (maximum estimate)
Field defining independent constraints on temperature
TitaniQ dynamic recrystallization
TitaniQ vein emplacement
Temperature (°C)
500
450
400
350
300
250

Figure 3

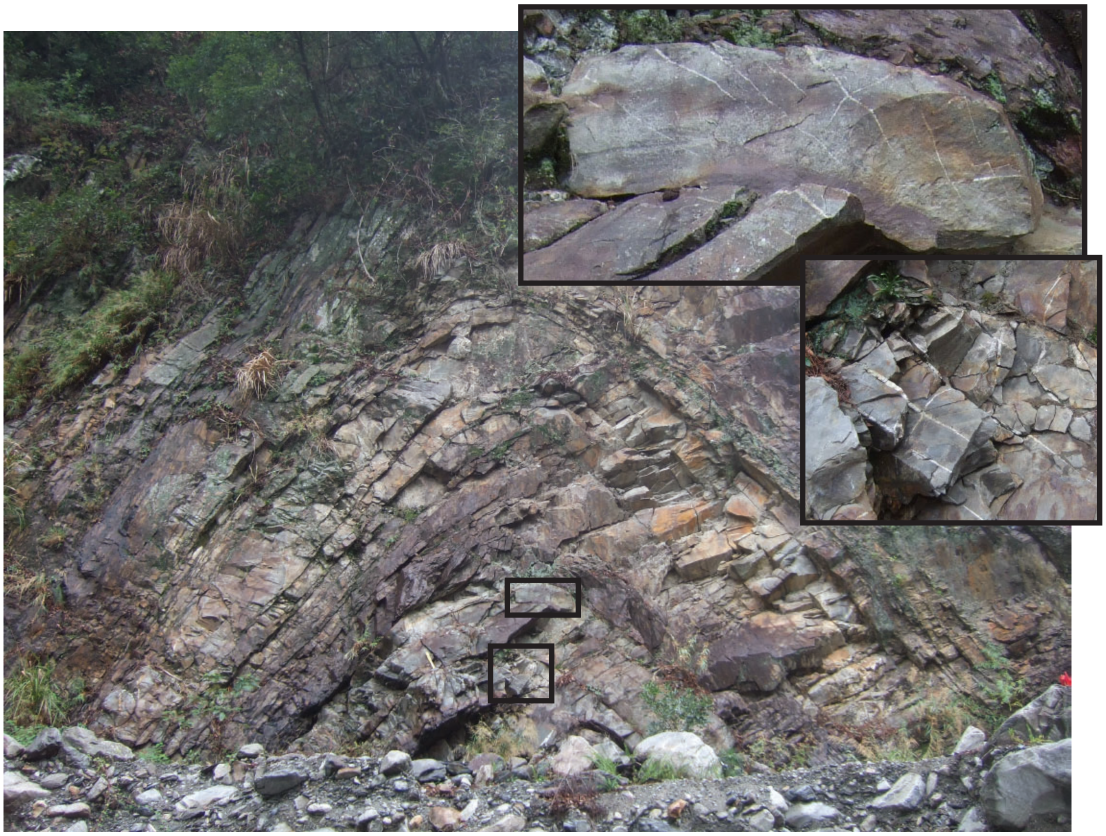

Figure 4

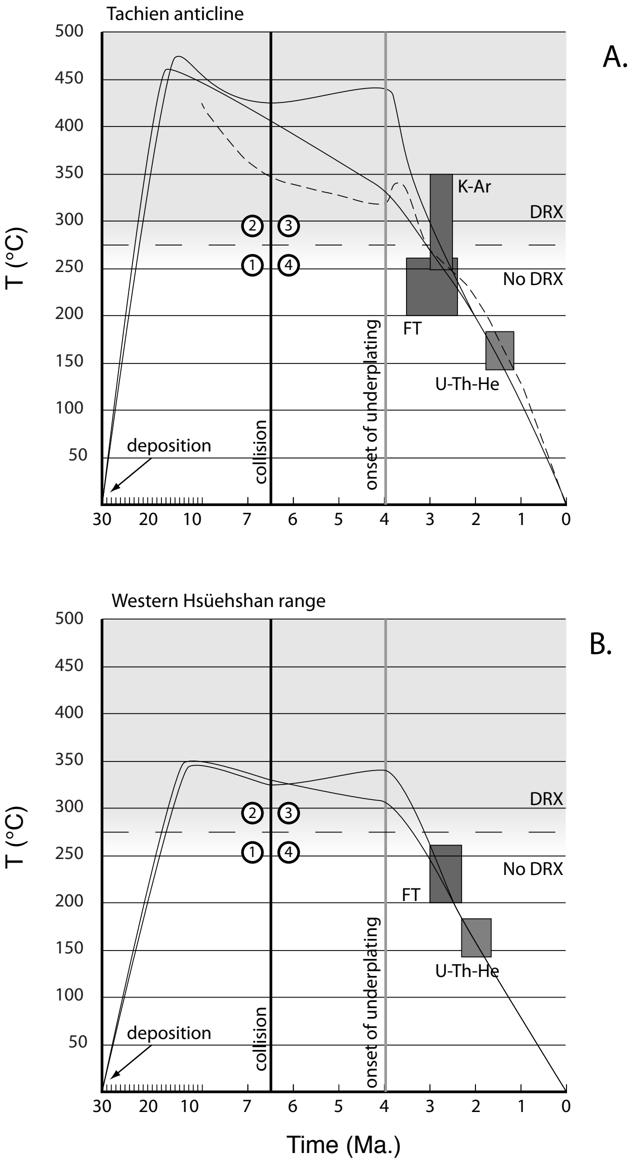
Tachien anticline
A.
500
450
400
350
300
250
200
150
100
50
T (°C)
K-Ar
DRX
No DRX
FT
U-Th-He
② ③
① ④
deposition
collision
onset of underplating
30 20 10 7 6 5 4 3 2 1 0
Western Hsüehshan range
B.
500
450
400
350
300
250
200
150
100
50
T (°C)
DRX
No DRX
FT
U-Th-He
② ③
① ④
deposition
collision
onset of underplating
30 20 10 7 6 5 4 3 2 1 0
Time (Ma.)

Figure 5

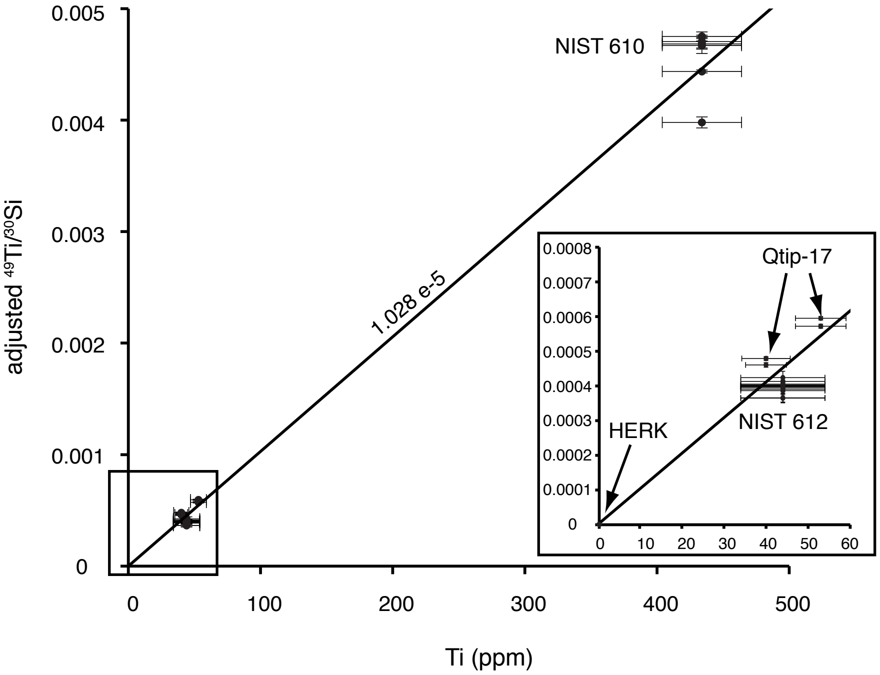
0.005
0.004
0.003
0.002
0.001
0
adjusted $^{49}Ti/^{30}Si$
NIST 610
1.028 e-5
0
100
200
300
400
500
Ti (ppm)
0.0008
0.0007
0.0006
0.0005
0.0004
0.0003
0.0002
0.0001
0
0
10
20
30
40
50
60
Qtip-17
HERK
NIST 612

Figure 6

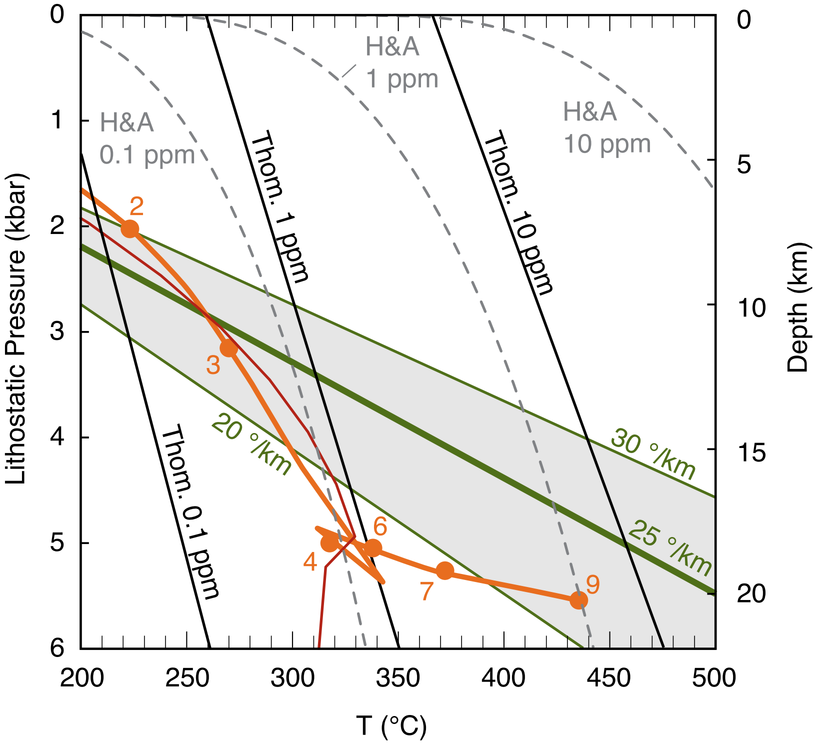
Lithostatic Pressure (kbar)
Depth (km)
T (°C)
0
1
2
3
4
5
6
200
250
300
350
400
450
500
0
5
10
15
20
H&A 0.1 ppm
H&A 1 ppm
H&A 10 ppm
Thom. 0.1 ppm
Thom. 1 ppm
Thom. 10 ppm
20 °/km
25 °/km
30 °/km
2
3
4
6
7
9

Figure 7

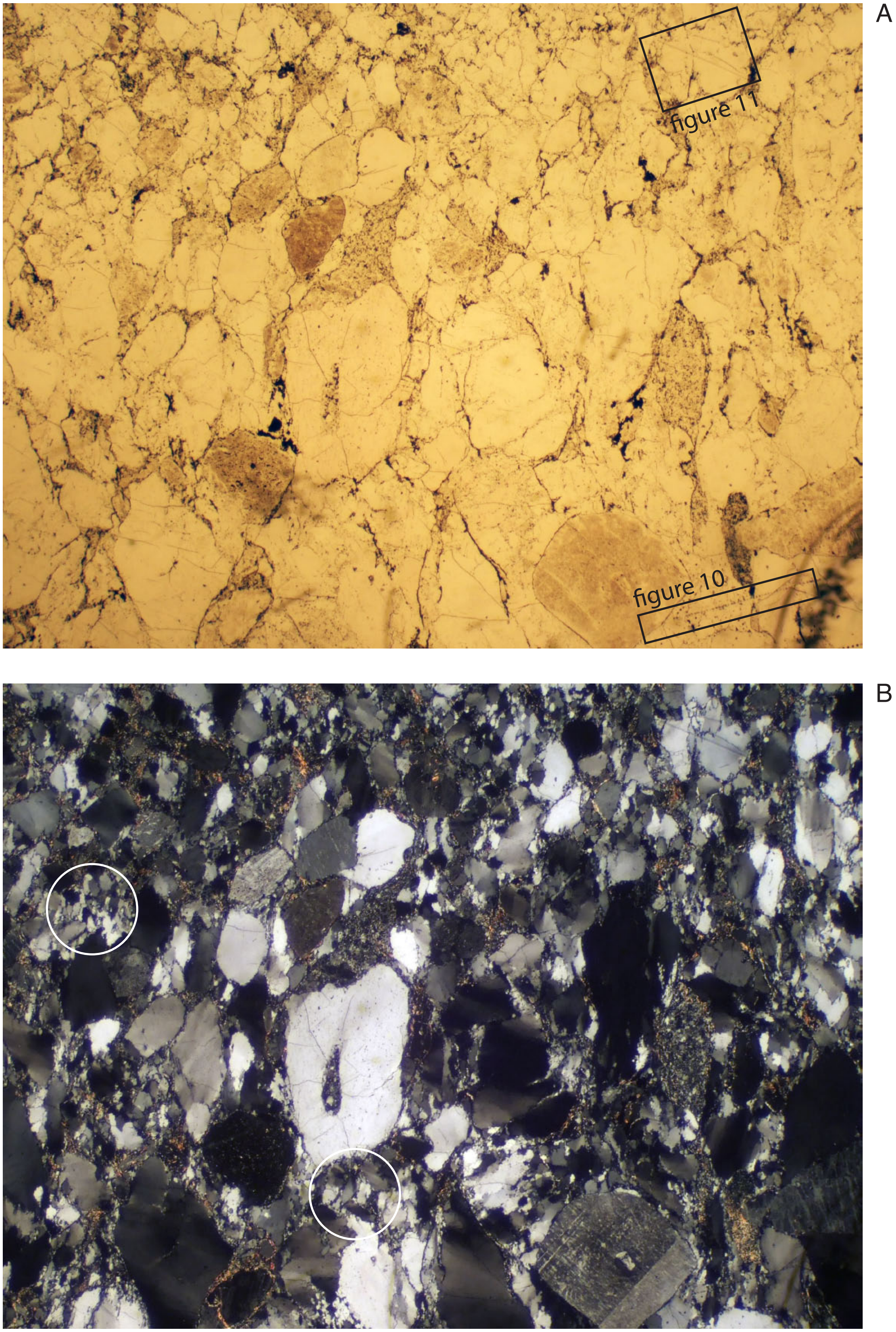

Figure 8

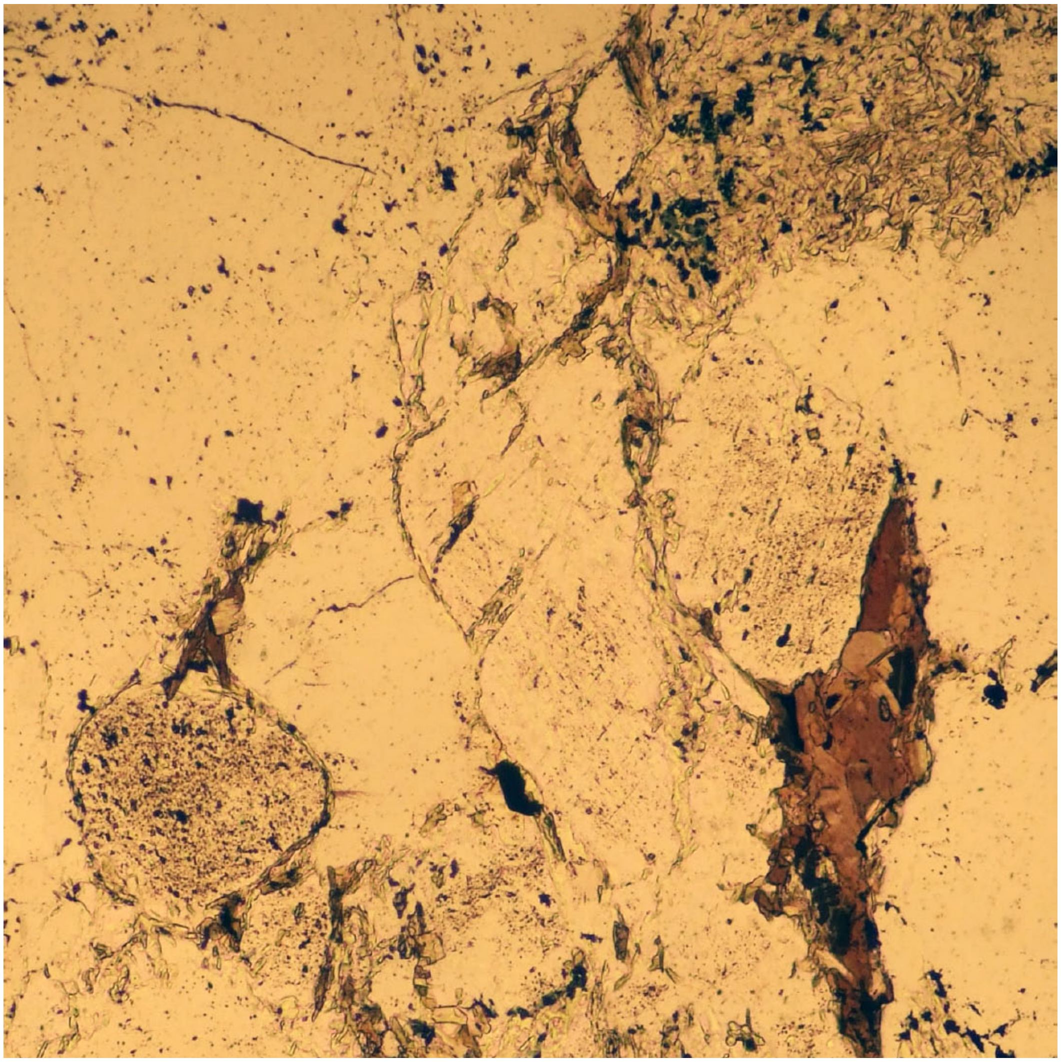

Figure 9

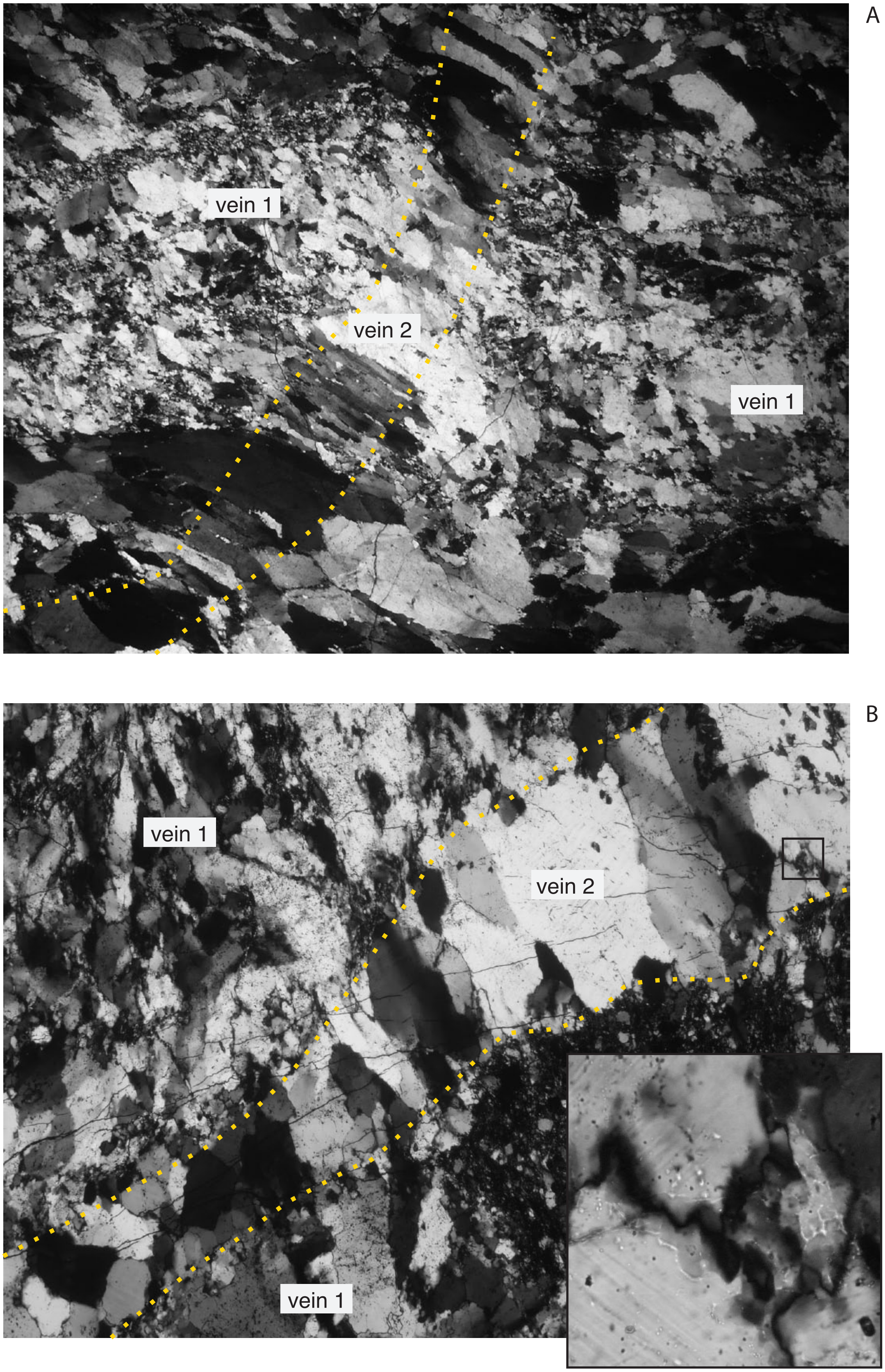

Figure 10

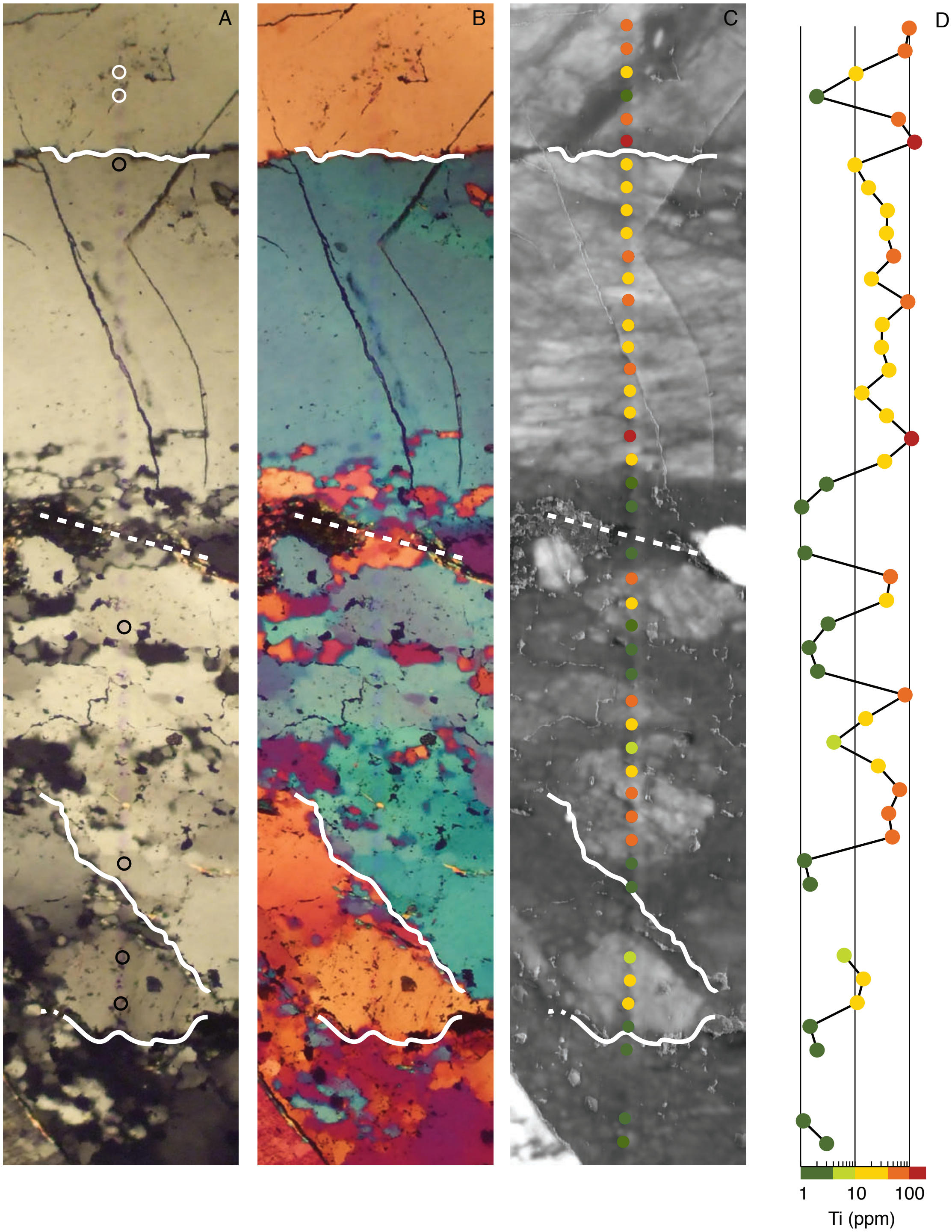

Figure 11

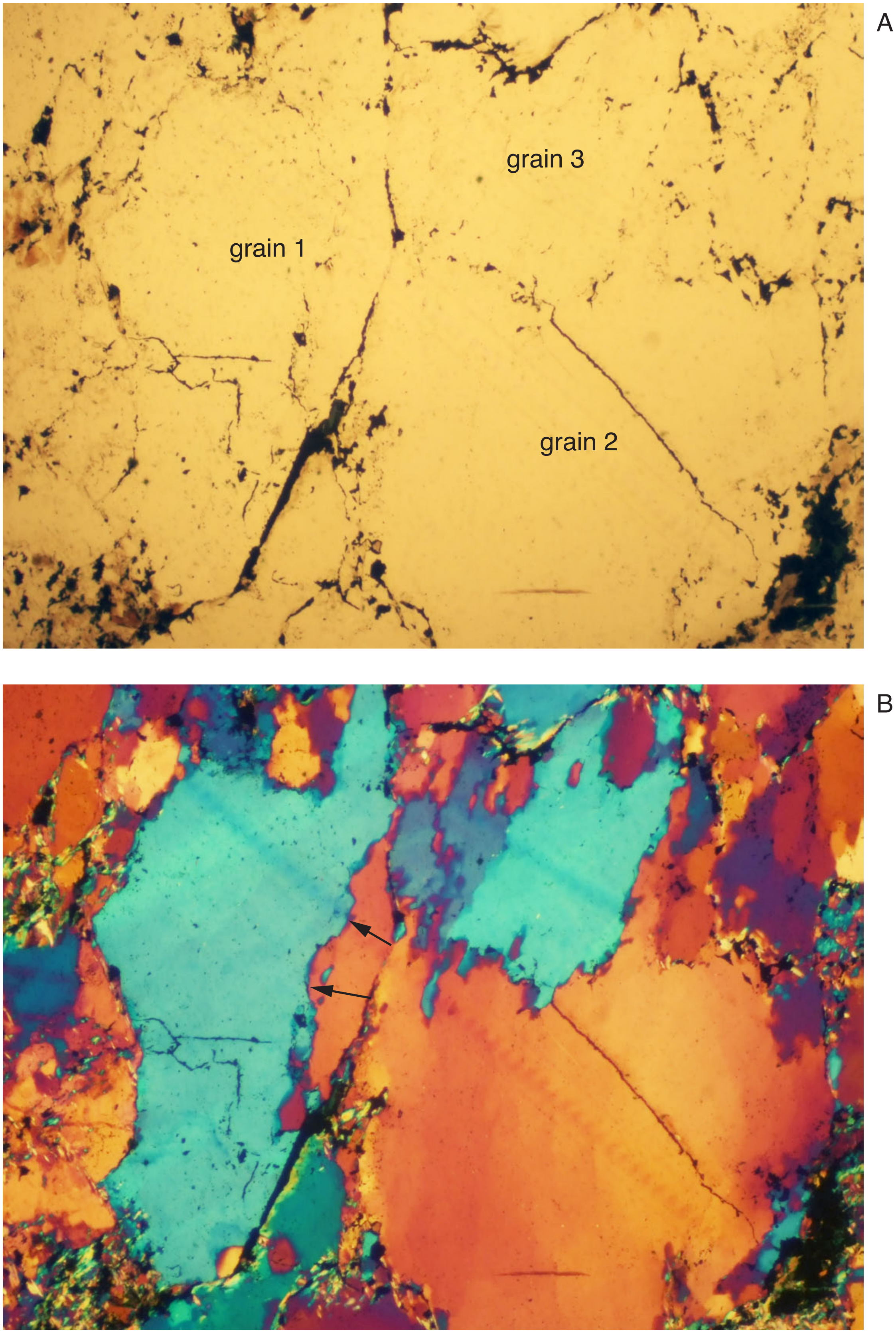

Figure 11 continued

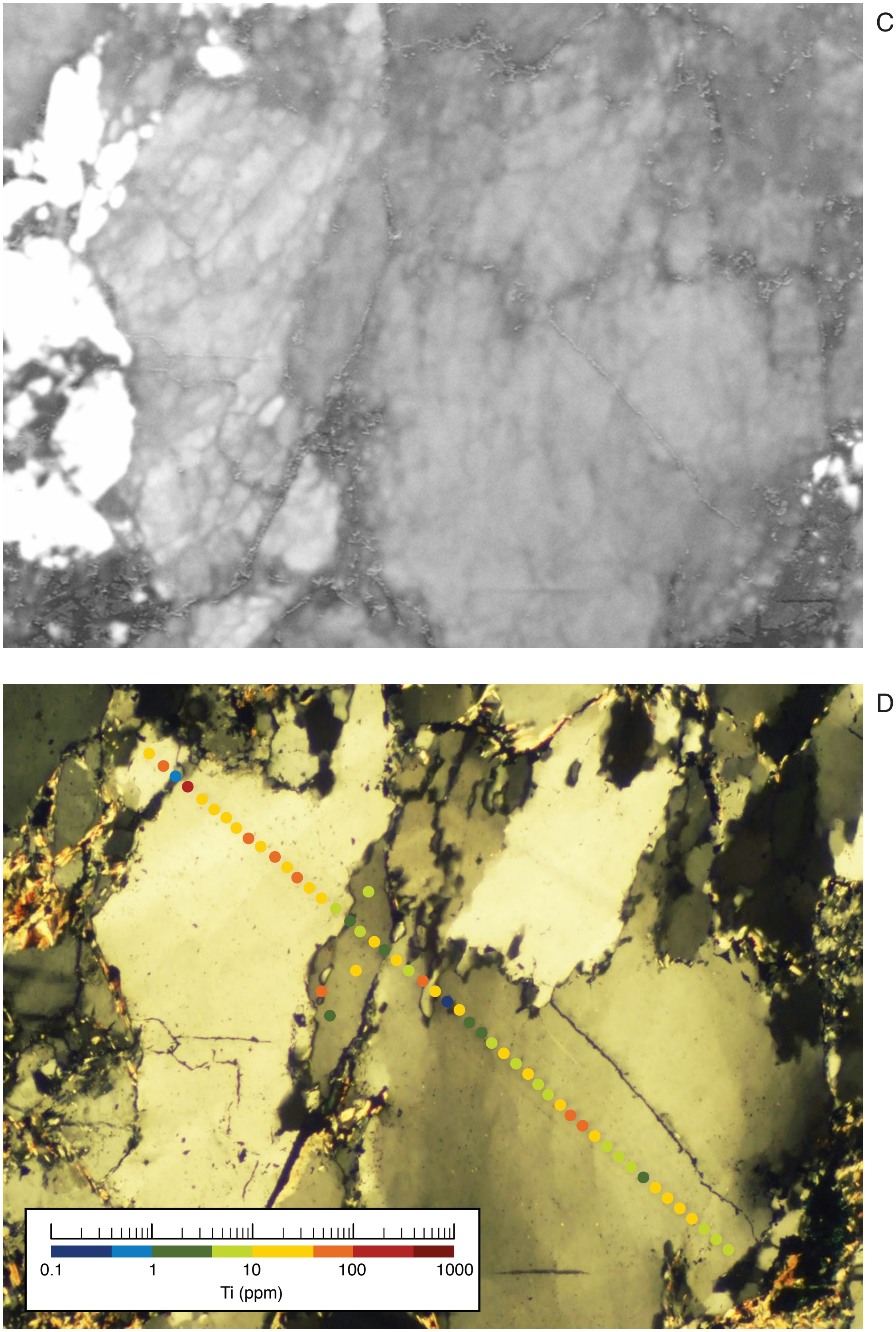

Figure 12

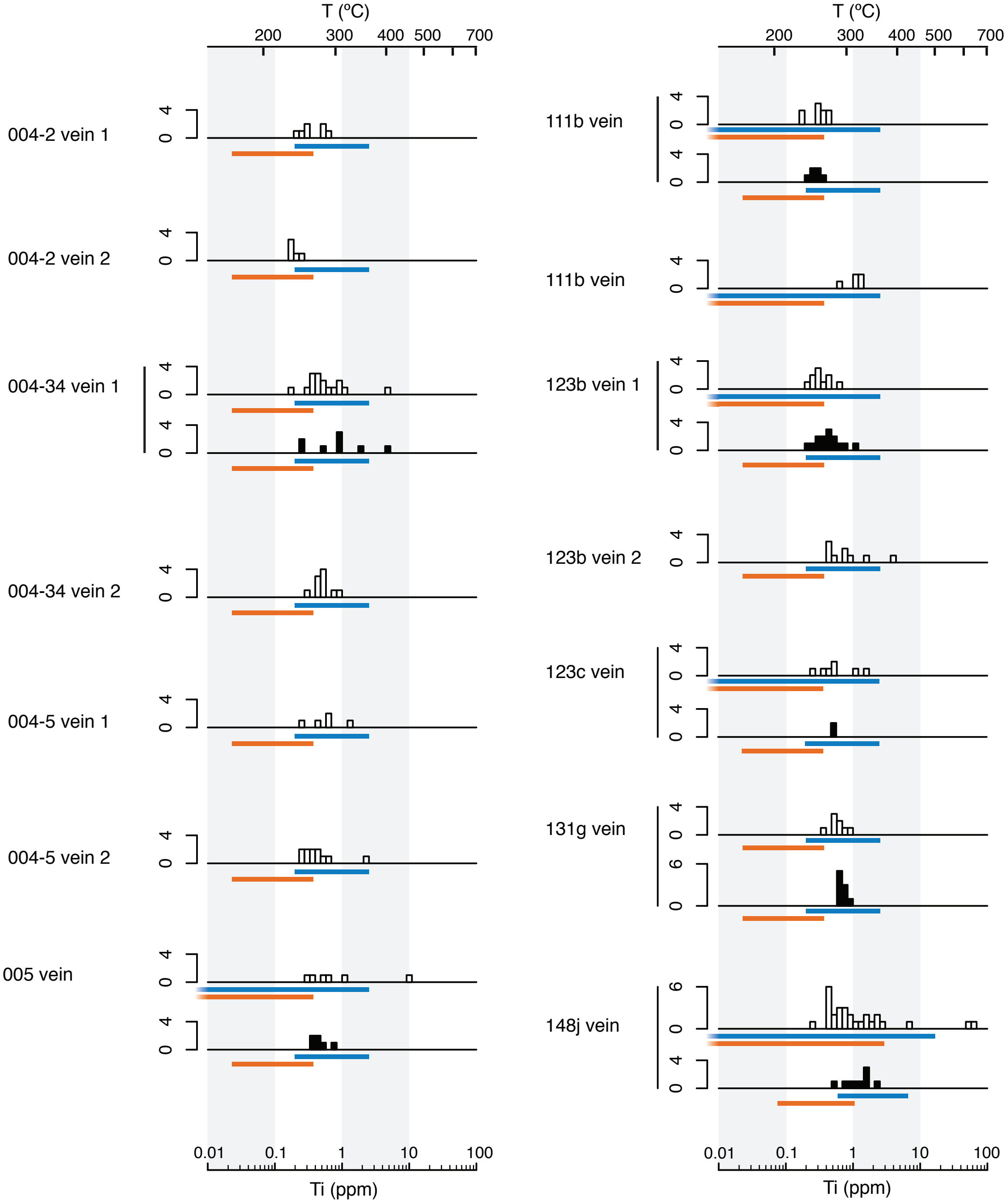
T (ºC)
200
300
400
500
700
004-2 vein 1
004-2 vein 2
004-34 vein 1
004-34 vein 2
004-5 vein 1
004-5 vein 2
005 vein
111b vein
111b vein
123b vein 1
123b vein 2
123c vein
131g vein
148j vein
0
4
6
0.01
0.1
1
10
100
Ti (ppm)

Figure 13

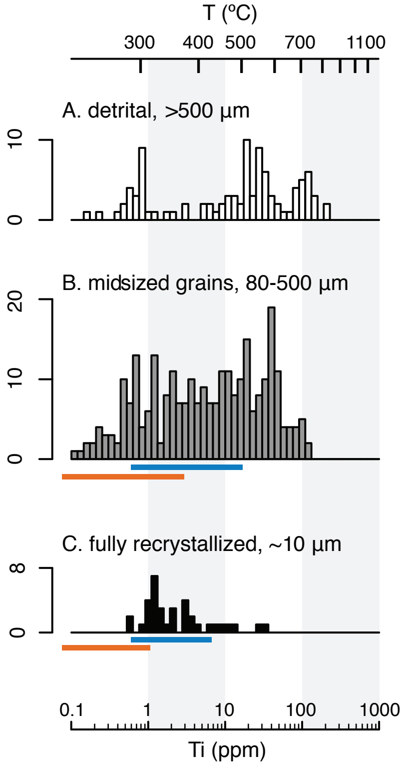
T (ºC)
300
400
500
700
1100
A. detrital, >500 µm
10
0
B. midsized grains, 80-500 µm
20
10
0
C. fully recrystallized, ~10 µm
8
0
0.1
1
10
100
1000
Ti (ppm)

Figure 14

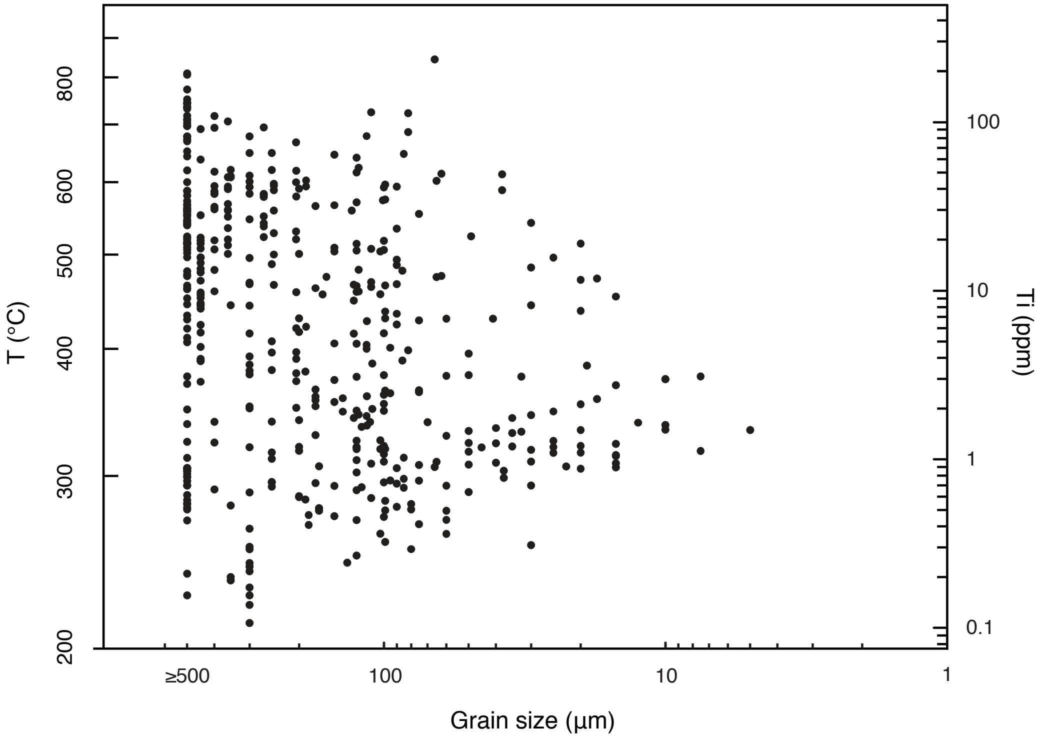
T (°C)
200
300
400
500
600
800
Ti (ppm)
0.1
1
10
100
≥500
100
10
1
Grain size (µm)

Figure 15

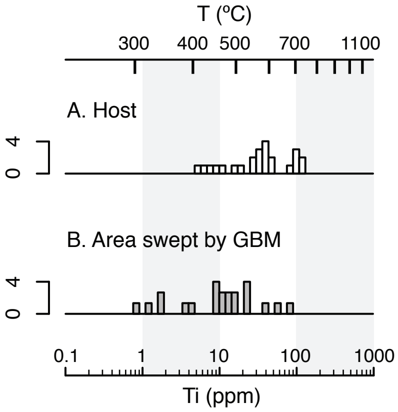
T (ºC)
300
400
500
700
1100
A. Host
0
4
B. Area swept by GBM
0
4
0.1
1
10
100
1000
Ti (ppm)

Figure 16

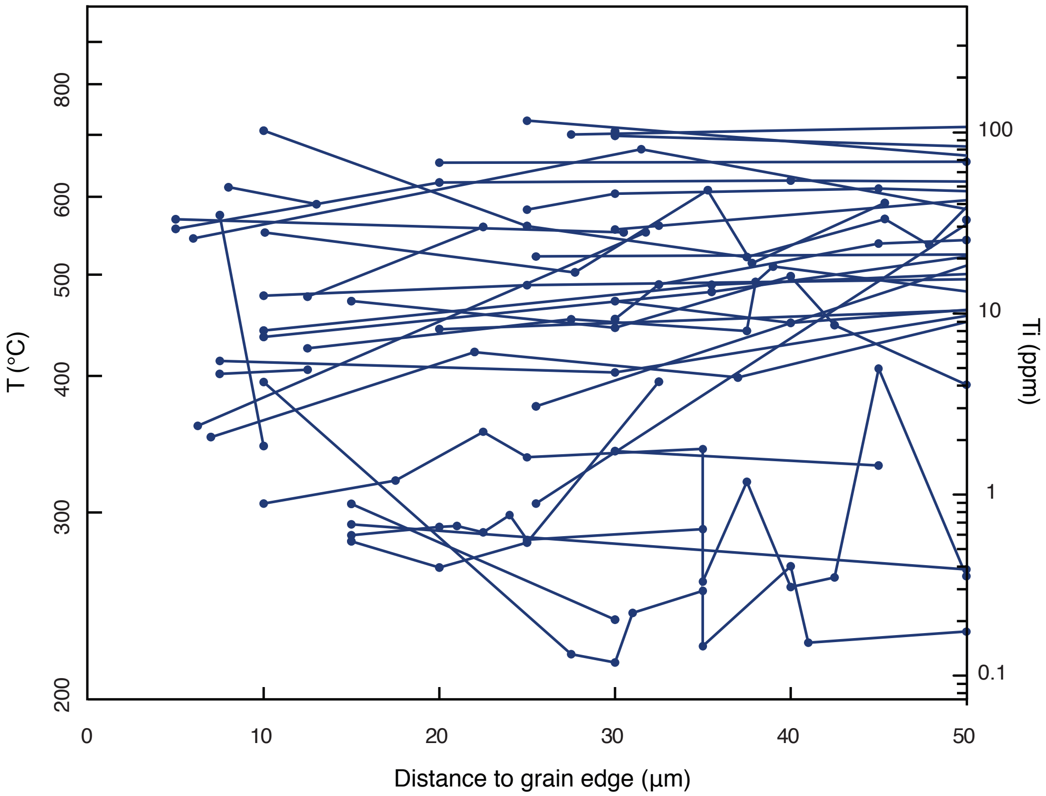
T (°C)
800
600
500
400
300
200
Ti (ppm)
100
10
1
0.1
0
10
20
30
40
50
Distance to grain edge (µm)

Table 1. Summary of results. Abbreviations: ms (metasiltstone), q (quartzite), s (slate), c (collisional), pc (pre-collisional), 1σ (random error), SE (1σ standard error), Rxl (recrystallization), sys err (systematic error due to uncertainty in the geotherm and TitaniQ calibration). “Stage” refers to the quadrants depicted in Fig. 4.

Sample/ Sample Area	Type	Rutile in vein?	Host	Width (mm)	Stage	Ti (ppm) median	mean Vein T (°C)	median Vein T (°C)	1σ	sys err	N	SE	Ti (ppm) median	Rxl T (°C) mean	Rxl T (°C) median	1σ	sys err	N	SE
004/2	vein 1, c	n	ms	0.5	1,2,3	0.32	265	258	17.7	27.2	7	6.69	-	-	-	-	-	-	-
004/2	vein 2, c	y	ms	0.5	3	0.187	238	237	5.6	26	5	2.5	-	-	-	-	-	-	-
004/34	vein 1, c	y	ms	2	1,2,3	0.484	286	276	38.1	28.1	16	9.53	0.883	306.3	305	52	30	8	18.5
004/34	vein 2, c	y	ms	0.5	3	0.515	279	279	14.3	28.3	10	4.52	-	-	-	-	-	-	-
004/5	vein 1, c	n	ms	1	1,2,3	0.591	282	286	28.7	28.6	5	12.8	-	-	-	-	-	-	-
004/5	vein 2, c	n	ms	0.1	3	0.377	272	265	29.7	27.5	11	8.95	-	-	-	-	-	-	-
005	vein, pc	y	q	5	1,2	0.544	309	282	77.6	28.4	6	31.7	0.437	275.6	272	13	28	6	5
111b/1	vein	n	q	1.1	1,2	0.307	256	257	14.1	27.1	9	4.7	0.277	252.6	252	8	27	6	3.4
111b/2	vein	n	q	5	2,3	1.122	313	317	17.1	30.4	5	7.65	-	-	-	-	-	-	-
123b	vein 1	y	s	4	1,2,3	0.303	260	256	14.5	27	10	4.59	0.426	272.2	271	21	28	14	5.48
123b	vein 2, c	n	s	25	3	0.805	303	300	39	29.5	9	13	-	-	-	-	-	-	-
123c	vein	n	q	>10	1,2,3	0.49	284	277	29.7	28.2	7	11.2	0.515	279.3	279	2	28	2	1.1
131g	vein, c	n	q	3.6	3	0.569	285	284	12.2	28.5	8	4.31	0.662	293.2	291	7	29	9	2.4
148d	q	-	-	-	-	-	-	-	-	-	-	-	1.601	365.6	336.2	69.5	31.5	35	11.7
148j	q	-	-	-	-	-	-	-	-	-	-	-	1.834	379.3	343.8	66.5	32	13	18.4
148j	vein, pc	y	q	1,9	1,2,3	0.715	330	295	93.3	29.2	28	17.6	1.237	321.5	322	24.1	30.7	9	8.0

Table 2. Estimated bias and uncertainty of TitaniQ temperature estimates for veins and quartzites based on Thomas et al. (2010) and Huang and Audetat (2012) equations. Positive values of bias indicate an overestimate by TitaniQ relative to independent constraints.

Type	**Calibration**	**ΔT**	**st. dev. (σ)**
quartzite recrystallization	Thomas	12 +16/-14	104 +18/-16
quartzite recrystallization	H&A	136 +16/-20	126 +22/-16
vein emplacement	Thomas	-22 +6/-8	52 +8/-6
vein emplacement	H&A	80 +6/-8	62 +10/-6

CHAPTER 2

Grain Size Kinetics in Experimentally Deformed Quartzite

Steven Kidder[1], Greg Hirth[2], Jean-Philippe Avouac[1]

[1]*California Institute of Technology, Pasadena, CA, United States*

[2]*Brown University, Providence, Rhode Island, United States*

ABSTRACT

Relationships between recrystallized grain size and differential stress provide a useful means of estimating paleodifferential stress in deformed rocks. Most laboratory-derived calibrations and theoretical treatments of grain-size piezometers assume steady-state deformation conditions. To assess the role of transient stress states on microstructural development, we conducted a series of twelve experiments on Black Hills Quartzite at 900°C in a Griggs apparatus. Stress was varied by changing the strain rate between values of 10^{-4}, 5×10^{-5}, 10^{-5}, 10^{-6} s^{-1}, and also by stopping the motor and allowing stress to relax. Grain size distributions were established using electron backscatter diffraction. Results indicate that grain size equilibrated to the range of changing stress conditions studied in less than ~25% strain. The experimental results are well predicted by the paleowattmeter formulation, however we do not recommend the extrapolation of this relationship to geologic conditions for quartz.

INTRODUCTION

Plastic deformation of rocks is commonly accompanied by changes in grain size (e.g. Snoke et al., 1998). There are at least two major reasons for studying such change. First, grain size reduction is associated with a reduction in strength, and therefore grain size reduction rates are key to understanding strain localization, a first-order feature of plate tectonics. Second, grain size can be used as a paleopiezometer to quantify stress levels experienced during deformation. This study focuses on the rate of change of grain size during experimentally induced dynamic recrystallization of quartz. Quartz is studied because, as the weakest of the major mineral constituents of the continental crust, it may control crustal deformation (e.g. Lowry and Pérez-Gussinyé, 2011).

The series of experiments described below investigate the response of grain size to changes in differential stress (referred to below simply as “stress”). With a few exceptions, previous laboratory experiments and theoretical treatments of grain size-stress relationships have assumed equilibrium deformation conditions (e.g. Stipp and Tullis, 2003; Twiss, 1977). Equilibrium presumably requires a mechanical and/or microstructural steady state—conditions that are only ever approximated in nature or experiments and in certain cases are demonstrably inappropriate (e.g. Nüchter and Ellis, 2010; Prior et al., 1990; Trepmann and Stöckhert, 2001; Trepmann and Stöckhert, 2003). The experiments described below allow us to quantify the rates of change of grain size following stress increases and decreases. Our results are compared to a number of theoretical and experimental predictions to help evaluate how well these conceptual tools predict grain size kinetics.

BACKGROUND

Dynamic recrystallization is a phenomenon that accompanies dislocation creep, the flow of material aided by the movement of linear defects called dislocations (e.g. Poirier, 1985). During dynamic recrystallization, the formation of new grains reduces internal strain energy associated with elevated dislocation density. Dynamic recrystallization is thought to occur by two major processes: grain boundary migration and subgrain rotation recrystallization. In experimentally deformed quartz, three dislocation creep regimes occur (Hirth and Tullis, 1992). At high stress levels (regime 1), new grains form predominantly by the migration of grain boundaries from areas of lower to higher dislocation density in response to large, intragranular dislocation density differences. Bulges are pinched, rotated or sheared off, thereby forming new grains (e.g. Stipp and Kunze, 2008). At moderate stresses (regime 2), formation of new grains is dominated by rotation recrystallization. Dislocations form low-energy arrangements known as subgrain boundaries, and continued addition of dislocations at these boundaries increases misorientation until high-angle grain boundaries form. At low stress (regime 3), grain boundary mobility is greatly enhanced such that grain boundaries rapidly sweep through grains in response to slight changes in dislocation density. While the dominance of subgrain rotation and grain boundary migration recrystallization differ in the three regimes, in reality both processes occur to some extent in all three regimes.

Previous experimental work on quartz (Bishop, 1996; Stipp and Tullis, 2003; Stipp et al., 2006) demonstrates that recrystallized grain size decreases with increasing stress independently of water content and deformation temperature (figure 1). In experiments carried out at constant strain rate (which coincides with nearly constant stress under regime 2 and 3 conditions), the slope on a log-log plot of recrystallized grain size vs. stress is not dramatically affected by the transition from regime 2 to 3. The transition between regimes 1 and 2, however, is characterized by a break in slope. One of the outstanding questions of grain-size piezometry in quartz (not resolved in this study) is whether such a break also occurs under natural deformation conditions.

While no previous experimental studies have investigated the role of changing stress on recrystallized grain size in quartz, a number of previous studies have investigated the phenomenon in other materials or natural samples. Ross and Neilsen (1978) found that in experiments on enstatite, recrystallized grain size increased during stress relaxation—an experimental procedure in which the motor is stopped and elastic strains are converted to permanent strain as stress decays. Ross et al. (1980) deformed olivine under increasing and decreasing stress levels and found that recrystallized grain sizes adjust to increasing and decreasing stress levels in “minimal” (but unspecified) strains and times. Van der Wal et al. (1993) showed that the adjustment time for olivine is rapid (under ~3% strain). White et al. (1985) deformed impure magnesium to strains up to 1 and found that recrystallized grain size within shear zones in the samples remained equilibrated at peak stress levels during strain weakening. Recrystallized grains in zones bordering the shear zones equilibrated to the new stress conditions.

METHODS

Experimental Material and Methods

Experiments were conducted in two modified Griggs apparatuses (Tullis and Tullis, 1977) on beige-colored Black Hills Quartzite (6.3 mm diameter, 14 mm length). The quartzite is >99% pure quartz with a grain size of ~70 μm (Stipp and Kunze, 2008). The material lacks a lattice preferred orientation and deformation microstructures. Samples consisted of two short pieces of quartzite with 0.2 weight percent water added between the pieces. Platinum jackets were annealed for 15 minutes at 900°C and folded over annealed platinum disks on each end of the samples. The platinum-encased samples were inserted in a Ni sleeve and NaCl assembly identical to that described by Chernak et al. (2009). Samples were brought to pressure along a standard pressure-temperature path following Chernak et al. (2009) and underwent a "cold hit" at 300°C and ~13 kbar. Following the cold hit, samples were kept at 900° for ~12 hours prior to the initiation of uniaxial compression. Further information on the starting material and experimental methods can be found in the references given by Chernak et al. (2009). Differential stresses reported in table 1 and figure 1 are averages over the interval between 10% strain and the final strain. In two-phase experiments, only the second portion of the experiment is considered in the calculation of average stress.

Grain Size Analyses

Following a standard commercial polish, samples were polished for ~8 hours with 0.05 μm Al polishing suspension and left uncoated. Electron backscatter diffraction (EBSD) maps were made on a ZEISS 1550VP field emission scanning electron microscope equipped with an HKL EBSD system. Patterns were acquired at a working distance of 10 mm, an accelerating voltage of 20 kV, step size between 0.15 and 0.5 μm, 70° sample tilt, 7 nA beam current, and chamber pressure of 15 Pa. For samples with small step size, maps scanned from bottom to top rather than the conventional "top-down" approach yielded superior results.

EBSD patterns were saved and reanalyzed six times detecting both edges and centers of 5, 6 and 7 bands. The resulting maps were progressively overlain with higher quality maps on top. Noise reduction was done by first removing single points with orientations not shared by neighbors ("wild spikes"), then filling unindexed pixels with an average orientation of neighbors when six or more neighbors show similar orientation. Grains were identified automatically using the *CHANNEL 5* software using a misorientation angle of 10° to represent a high-angle grain boundary (White, 1977). Misorientations of 60±5 degrees about [001] were considered to be Dauphiné twins rather than grain boundaries. Before noise reduction, 68%–93% of points were indexed as quartz (table 1). Processing the raw data raised these percentages to 75%–99%. Potential grains comprising one, two, and in some cases three pixels were considered beyond the resolution of the technique and discarded. Additional error correction was done manually to remove misidentified grains of larger size. Each automatically identified grain was visually inspected (N = ~7500). Questionable "grains" were checked to see whether they coincide with grain or subgrain outlines in band contrast images. At smaller step sizes, the electron beam often overlapped two grains near grain boundaries, and resulting misindexed grains could be discarded at this stage. When grain identification remained questionable, the electron backscatter patterns of suspect grains were compared with patterns from neighboring points to clarify whether patterns were truly distinct from neighboring grains or resulted from misindexing. Following noise reduction, border grains and large unrecrystallized remnant grains were removed from grain size averages. No stereological correction was applied to calculated grain sizes. Figures 2 and 3 show histograms of the resulting data.

RESULTS

The mechanical data shown in figure 4 give a graphical summary of the experiments and an indication of the reproducibility of the experimental conditions. Experiments were carried out in regimes 1, 2 and within the regime 2–3 transition. The four experiments involving strain rates of 5×10^{-5} s^{-1} (experiments 1516, 1518, 1522, 1527) record very similar stress-strain curves, suggesting that experimental conditions were consistent among these experiments. Experiment 1524 was also carried out at 5×10^{-5} s^{-1}, however the loss of the thermocouple early in the experiment prevented accurate temperature monitoring. Segments of experiments carried out at 10^{-6} s^{-1} show less consistent stresses, perhaps largely as a results of the difficulty in accurately measuring low values of stress. In one case (experiment 1515), confining pressure was increased at a strain of ~7, causing an unexpected increase in differential stress.

Table 1 summarizes the experimental conditions and results for each experiment. In two of the samples, we analyzed grain size in two different areas of the sample. The difference between the measurements gives a sense of the internal variation present in the samples and perhaps a better sense of uncertainty than can be gained by analyzing grain size statistics from one area. As shown in figures 2 and 3, the grain size data in most cases approximates the lognormal distribution expected for recrystallized grains (Ranalli, 1984).

Under decreasing stress conditions near the regime 2–3 boundary, earlier regime 1 and regime 2 fabrics in thin section are completely overprinted with an equilibrium recrystallized grain size after 25% strain (compare figure 5a, 5b, 5c). Under increasing stress conditions, older, coarser recrystallized grains are deformed and overprinted by finer grains but remain sometimes quite recognizable (figure 6). In one sample deformed under regime 1 conditions and left for ~48 hours under decaying stress conditions, a partially annealed “foam” texture formed (figure 5d, figure 7).

Comparison with Previous Experimental Results

Previous experimental calibrations of the recrystallized grain size piezometer for quartz (Bishop, 1996; Stipp and Tullis, 2003; Stipp et al., 2006) are plotted as small black circles in stressgrain size space in figure 1. Our results, plotted as larger colored symbols, reproduce these results for most experiments, indicating little or no systematic error associated with differences between experimental procedures or grain size analysis techniques. Significant exceptions are two outliers plotted at small stress (experiments 1518, 1522). These two experiments are two-stage experiments in which grain size presumably had insufficient time to reach equilibrium. The other two-stage experiments are notable in that they fall along the trend of the steady-state data about as well as our steady-state experiments. This indicates that equilibrium with respect to recrystallized grain size was achieved in these experiments, a result supported by textural similarities between the samples (figure 5).

DISCUSSION

Rates of Microstructural Change and Comparison with Previous Results and Predictions

The rates of grain growth and grain size reduction we calculate (table 1) can be compared to a number of laboratory and theoretical predictions. The first comparison we make is with the theory of Hall and Parmentier (2003) who balance static grain growth, using the annealing experiments of Yund and Tullis (1982), with a rate of grain size reduction proportional to strain:

$$\dot{d} = K_g exp\left[\frac{-Q_g}{RT}\right] p^{-1} d^{1-p} - \frac{\dot{e}d}{\varepsilon_c} \ ,$$

where d = grain size, p = grain growth exponent, K_g = grain growth preexponential factor, Q_g = grain growth activation enthalpy, R = gas constant, T = temperature (K), $\dot{e}$ = strain rate, σ = differential stress, and ε_c = experimentally determined critical strain for microstructural evolution. The predictions of this theory for our experiments are shown in figure 8b, a plot of predicted grain size versus measured grain size, with the critical strain set to a value of 0.05 to best fit the results. For comparison, figures 8d and 8c show similar plots for the predictions of the piezometers of Twiss (1977) and Stipp and Tullis (2003), the best fit line through the small black circles on the plot.

A related formulation, the paleowattmeter (Austin and Evans, 2007, 2009), also balances static grain growth with grain size reduction, but provides a more sophisticated treatment of grain size reduction. Austin and Evans (2007, 2009) convert the rate of work done during deformation to a grain size reduction rate by assuming that a large percentage of work is used to create new grain boundaries during dynamic recrystallization:

$$\dot{d} = K_g exp\left[\frac{-Q_g}{RT}\right] p^{-1} d^{1-p} - \frac{\beta\lambda\sigma\dot{e}d^2}{c\gamma}$$

where, in addition to the terms defined above, c = a geometric constant, γ = grain boundary energy, β = fraction of the total mechanical work rate accommodated by dislocation creep, and λ = proportion of the energy associated with dislocation creep stored in the microstructure. The paleowattmeter does not include a tuning parameter and produces a better fit to the experimental results than the other approaches (figure 8), notably so for high stress experiments. Figure 9 shows the predictions of the paleowattmeter for the stress and strain rate history of our experiments and compares them with our results.

In all but three cases the paleowattmeter predicts grain size equilibration in times shorter than our experiments. For the three experiments where the wattmeter indicates equilibrium grain size was not yet reached (1518, 1522, 1524), grain size is within error of the prediction (note that experiment 1524 was carried out at an unknown, but probably cooler temperature than the assumed 900°C. A temperature of 830°C would match the experimental results exactly.

Grain Growth during Dynamic Recrystallization?

A key element of the theories of both Hall and Parmentier (2003) and Austin and Evans (2007, 2009) is the assumption that grain growth during dynamic recrystallization is driven by minimization of surface energy in an identical process to that occurring during static grain growth. This assumption, recently challenged by Platt and Behr (2011), is critical to the question of whether these relationships can be appropriately applied to deformation under geologic conditions. To first order, the success of the wattmeter in explaining the experimental data without a fitting parameter seems to support the assumption.s

The three experiments where stress was decreased significantly (1518, 1522, 1524) additionally offer some insight. These three experiments involve rather sharp decreases in stress and grain growth. The stress relaxation experiment (1522) shows clear petrographic criteria such as abundant 120° triple junctions or “foam texture” indicating grain growth driven by the reduction of surface energy, as well as indicators of growth of individual grains due to minimization of strain energy in old grains (figure 7). Thus sample 1522 demonstrates that both processes can be active simultaneously in the same sample. Strain rate was negligible by the end of the experiment, thus a geologic analogue of this experiment is postseismic stress relaxation similar to that modeled by Trepmann et al. (2007). These results do not demonstrate that simultaneous grain growth by the two processes occurs during plastic deformation. Experiment 1524 on the other hand involved a ~30 minute period of significantly decreased stress at a strain rate of $10^{-6}\,s^{-1}$. Microtextural analysis of this fabric also shows indications of grain growth due to grain boundary energy minimization (figure 10). Thus at least during a large stress reduction, “static” grain growth can be an important process. Unfortunately, the loss of the thermocouple in this experiment prevents us from reliably comparing grain growth rates for this experiment with predictions of purely static grain growth.

Sample 1516 experienced strain weakening under regime 1 conditions and a corresponding factor of two change in stress relative to peak conditions. In this sample, strain localized late in deformation. The resulting shear zone has a coarser grain size than other parts of the sample (e.g. table 1). Similar observations have been made in natural shear zones (Kohlstedt and Weathers, 1980). In figure 1 we plot the finer grain size matrix at the average stress of experiment 1516 and the coarser grain size in the shear zone at the final stress of the experiment. The resulting points fit well with the trend of the data for steady state experiments, but contrast with the predictions of the wattmeter. Both portions of the sample experienced a similar stress history, however more significant grain growth occurred in the higher strain rate portion of the sample. Austin and Evans (2009) observed similar behavior in calcite. The paleowattmeter and the relationship of Hall and Parmentier (2003) predict the opposite, i.e. higher strain rates under otherwise identical conditions should lead to smaller grain size. This observation suggests that deformation may act as a catalyst for grain growth.

Application of the Paleowattmeter at Geologic Conditions?

While the paleowattmeter provides a good fit to our experimental data, as discussed below, it predicts significantly lower stresses than traditional piezometers under geologic conditions. Before it can be applied at geologic conditions there are a number of issues that should be addressed: 1) The concern discussed by Platt and Behr (2011) that grain boundary energy has a minimal effect during dynamic recrystallization and therefore that the wattmeter and Hall and Parmentier formulations, which balance grain growth with grain size reduction, are fundamentally flawed. 2) An internal inconsistency in the wattmeter formulation for quartz (Austin and Evans, 2007) that causes it to predict significantly different stresses than the flow law it incorporates. This second point does not affect the laboratory results because strain rates in the lab can be directly observed. In nature they must often be estimated using a flow law. The inconsistency is well illustrated by comparing stress estimates based on the work of Dunlap et al. (1997) in the Ruby Gap Duplex, Australia. Hirth et al. (2001) predict a stress of 100 MPa associated with a recrystallized grain size of 20–40 μm in these rocks. The wattmeter however, incorporating the parameters of the Hirth et al. (2001) flow law, predicts stresses of 4–13 MPa at this grain size and deformation temperature of 250–350°C. This order of magnitude discrepancy in stress is not easily resolved by tweaking the flow law or the grain growth parameters of Tullis and Yund (1982).

Better experimental tests of the wattmeter could also be made by focusing on changes in grain size occurring shortly after stress changes. This would allow predicted grain size evolution rates to be compared directly to observed rates rather than the minimum rates reported here.

Implications for Paleopiezometry

One goal of this study is to aid in interpreting textural information about stress history. Typically for purposes of paleopiezometry it is assumed that a rock with a unimodal set of recrystallized grains experienced a certain (unquantified) amount of strain at a constant stress. A common example of a non-steady-state fabric is the case where rocks move from low to high stress, for example during exhumation up to the brittle-ductile transition where microstructures are frozen in (e.g. chapter 3). An early “phase” of deformation can often be deciphered in this case in the form of coarser, overprinted grains (e.g. chapter 1; Behr and Platt, 2011). Petrographers often interpret overprinted fabrics in terms of early and late deformation. This situation is analogous to the texture observed in sample 1509 (figure 6). Qualitatively at least, the grain size in the coarse recrystallized fraction of sample 1509 is similar in size of the recrystallized grains in sample 1505, which had an identical early stress history but did not have a high-stress overprint. Our data also indicate that the grain size of new grains that appear during a late high stress phases are not influenced by the presence of the older grains (e.g. in figure 1 all the fine grained samples fall along the piezometer of Stipp and Tullis (2003) regardless of early history). Thus two phases of deformation can be interpreted from this fabric and the grain size of each phase gives information about paleostress level. Future work in this direction should address potential changes in size of the early grains.

A second example of non-steady-state stress is the case where static grain growth or “annealing” may have occurred following deformation. This commonly cited concern motivated Hacker et al. (1992; 1990) to back-calculate initial possible grain sizes using experimental grain growth relationships. Our experiments from high to low stress offer some insight here, in that we observe either reequilibration at new stress levels or clear textural indications of annealing (e.g. figures 5d, 7, 10). We find it difficult to envision significant static grain growth that would not show such indications of annealing. Sample 1524 is of particular interest here since it experienced a short period of grain growth *while remaining at high (but decreasing) stress*. Even so, sample 1524 contains in places conspicuous textural evidence of annealing, i.e. grain growth due to the reduction of strain energy (figure 10). A sample undergoing a true stress-free annealing phase would surely have an even more conspicuous fabric. The textures shown by Hacker et al. (1992; 1990) and Behr and Platt (2011) in subsequent work on the same rocks do not have the textural characteristics of annealed materials. We concur with Behr and Platt (2011) that the grain size in these samples is representative of the stress state during the latest stages of deformation and was not influenced by significant grain growth. Back-calculating possible initial grain size is probably not necessary unless textures display indications of static grain growth.

A third non-steady-state situation involves very large changes in stress on timescales dictated by the earthquake cycle (Kuster and Stöckhert, 1998; Trepmann and Stöckhert, 2001; Trepmann and Stöckhert, 2003). Trepmann and Stöckhert (2003) documented four quartz fabrics in the Sesia zone associated with this types of stress change: 1) A-type are heterogeneous and barely recrystallized with textural similarities to regime 1 of Hirth and Tullis (1992), 2) Type B contain quartz ribbons, sometimes kinklike and surrounded by recrystallized grains, and conspicuous deformation lamellae, 3) C-type is characterized by heterogeneous aggregate of recrystallized grains with variable grain size, 4) D-type are completely recrystallized with a foam structure. Trepmann and Stöckhert (2003) suggested that postseismic strain following an early brittle or high-stress phase led to strong recrystallization (C- and D-type). They interpret that some samples avoided this stress-relaxation phase and remain contorted and little recrystallized (A- and B-type). Our experiments however show that high stress fabrics are overprinted equally fast by stress-relaxation (in which case an annealed texture develops) or continuing deformation at low stress (e.g. figure 5). This suggests an alternative possibility for the Sesia zone samples, that A and B-type fabrics formed in a later deformation event and that stress varied significantly in space, i.e. the earlier C- and D-type samples were not affected by the later high-stress event deforming the A- and B-type samples.

CONCLUSIONS

1) Recrystallized grain size in quartz adjusts rapidly to changing stress conditions. With both decreasing and increasing stress under quartzite dislocation creep regime 2 and within transitional regime 2–3 conditions, equilibrium recrystallized grain size is re-achieved in experiments with strains less than ~25%.
2) We find that the paleowattmeter does a better job of predicting the results of our experiments than more traditional piezometers. The wattmeter is not however ready to be applied under geologic conditions due in part to an internal inconsistency when integrated with flow laws at geologic conditions.
3) Non-steady-state deformation may be common in the crust. Examination of experimental samples with multiphase stress histories provides support for microstructural interpretations of the stress *history* of geologic samples. Tentatively, we observe three categories: 1) complete equilibratation at a late stress level with respect to recrystallized grain size, 2) under increasing stress, new grains form at a size consistent with paleopiezometric predictions while previous larger recrystallized grains remain. In this case, grain size of both older and younger recrystallized grains can be used to quantify

early stress conditions. 3) Transient fabrics developed under decreasing stress marked by the presence of annealed patches indicative of grain growth during grain boundary energy minimization. Thus, with the aid of microstructural analysis, grain-size stress relationships developed under steady state conditions can be applied to non-steady-state fabrics.

FIGURE LEGENDS AND TABLE TITLES

Figure 1. Recrystallized grain size versus stress. Experiments from this study are shown as colored symbols. Data from previous studies (Bishop, 1996; Stipp and Tullis, 2003; Stipp et al., 2006) are shown as small black symbols. Regime 1 samples are plotted using the stress at the end of the experiment. For the rest of the samples average stresses are used from either the entire experiment or, for two-phase experiments, the second half of the experiment.

Figure 2. Histograms of grain size (left column) and natural log of grain size (right column) from experiments that ended at high stress. Red lines are modeled distributions with the same mean and standard deviation as our data.

Figure 3. Histograms of grain size (left column) and log grain size (right column) from experiments that ended at low stress.

Figure 4. Differential stress vs. axial strain for the experiments. Labels on the right side of the plot show the quartz deformation regimes (Hirth and Tullis, 1992) and strain rates for the experiments.

Figure 5. Photomicrographs of four experimental samples. Samples 1510, 1518, and 1526 experienced different deformation regimes during an early phase of deformation but all ended with ~25% strain at low stress and a strain rate of 10^{-6} s^{-1}. Sample 1522 experienced high stress conditions similar to 1518, then the motor was stopped for ~24 hours. FOV in each image: ~175 μm.

Figure 6. A: Microphotograph of sample 1509 showing microstructure following an early deformation at low stress (intermediate size grains). B: Close-up of fine-recrystallized area showing some fine grains formed during the second, high-stress deformation phase.

Figure 7. Band contrast image of sample deformed at high stress, then undergoing stress relaxation (sample 1522). The prevalence of ~120° triple junctions and straight grain-boundary segments is indicative of grain growth due to the reduction of surface energy. Locally, large

differences in dislocation density between new grains (grains with uniform fill) and original coarse grains that experienced high stress (grains with uneven fill) drive grain boundary migration (arrows).

Figure 8. Measured grain size vs. grain size predicted by A) the Wattmeter (Austin and Evans, 2007), B) Hall and Parmentier (2003) fit to a critical strain of 0.05; C) Twiss (1977) using the average stress for the second half of the experiment (or entire experiment in one-stage experiments); D) Stipp and Tullis (2003) using the same stress values as in plot C. Data from Stipp and Tullis (2003) and Stipp et al. (2006) are shown as small black dots. Data from Bishop (1996) are shown as large black dots.

Figure 9. Predicted grain size evolution (Austin and Evans, 2007) vs. time for each experiment. Experimental results are shown as dots. For two-phase experiments, the starting point on the plot is the beginning of the second deformation phase assuming an initial grain size predicted by Stipp and Tullis (2003). The wiggles in the lines result from inprecision of strain estimates

Figure 10. Orientation contrast image of sample 1524, which underwent high stress, then a short period of deformation at a low strain rate. Arrows point to locations where places ~120° triple junctions and straight grain-boundary segments suggest grain growth due to the reduction of surface energy (“annealing”).

Table 1. Experimental data. Abbreviations: ε, strain; $\acute{\varepsilon}$, strain rate; g.s., grain size; sz, shear zone; subscripts “1” and “2” refer to parts one and two of the experiments and exclude the initial 10% ramp up. The columns labeled %quartz$_{\text{raw}}$ and %quartz$_{\text{final}}$ refer to the percent indexing of EBSD analyses.

REFERENCES

Austin, N. J., and Evans, B., 2007, Paleowattmeters: A scaling relation for dynamically recrystallized grain size: Geology, v. 35, no. 4, p. 343-346.

-, 2009, The kinetics of microstructural evolution during deformation of calcite: Journal of Geophysical Research, v. 114, no. B09402.

Behr, W. M., and Platt, J. P., 2011, A naturally constrained stress profile through the middle crust in an extensional terrane: Earth and Planetary Science Letters, v. 303, no. 3-4, p. 181-192.

Bishop, R. R., 1996, Grain boundary migration in experimentally deformed quartz aggregates: The relationship between dynamically recrystallized grain size and steady state flow stress [B. Sc.: Brown University, 36 p.

Chernak, L. J., Hirth, G., Sevlerstone, J., and Tullis, J., 2009, Effect of aqueous and carbonic fluids on the dislocation creep strength of quartz: Journal of Geophysical Research, v. 114, p. B04201.

Dunlap, W., Hirth, G., and Teyssier, C., 1997, Thermomechanical evolution of a ductile duplex: Tectonics, v. 16, no. 6, p. 983-1000.

Hacker, B. R., Yin, A., Christie, J. M., and Davis, G. A., 1992, Stress Magnitude, Strain Rate, and Rheology of Extended Middle Continental-Crust Inferred from Quartz Grain Sizes in the Whipple Mountains, California: Tectonics, v. 11, no. 1, p. 36-46.

Hacker, B. R., Yin, A., Christie, J. M., and Snoke, A. W., 1990, Differential Stress, Strain Rate, and Temperatures of Mylonitization in the Ruby Mountains, Nevada - Implications for the Rate and Duration of Uplift: Journal of Geophysical Research-Solid Earth and Planets, v. 95, no. B6, p. 8569-8580.

Hall, C. E., and Parmentier, E. M., 2003, Influence of grain size evolution on convective instability: Geochemistry Geophysics Geosystems, v. 4, no. 3.

Hirth, G., Teyssier, C., and Dunlap, W. J., 2001, An evaluation of quartzite flow laws based on comparisons between experimentally and naturally deformed rocks: International Journal of Earth Sciences (Geol Rundsch), v. 90, p. 77-87.

Hirth, G., and Tullis, J., 1992, Dislocation creep regimes in quartz aggregates: Journal of Structural Geology, v. 14, no. 2, p. 145-159.

Kohlstedt, D. L., and Weathers, M. S., 1980, Deformation-Induced Microstructures, Paleopiezometers, and Differential Stresses in Deeply Eroded Fault Zones: Journal of Geophysical Research, v. 85, no. Nb11, p. 6269-6285.

Kuster, M., and Stöckhert, B., 1998, High differential stress and sublithostatic pore fluid pressure in the ductile regime — microstructural evidence for short-term post-seismic creep in the Sesia Zone, Western Alps: Tectonophysics, v. 1998, no. 303, p. 263-277.

Lowry, A. R., and Pérez-Gussinyé, M., 2011, The role of crustal quartz in controlling Cordilleran deformation: Nature, v. 471, no. 7338, p. 353-357.

Nüchter, J. A., and Ellis, S., 2010, Complex states of stress during the normal faulting seismic cycle: Role of midcrustal postseismic creep: Journal of Geophysical Research, v. 115, p. B12411.

Platt, J. P., and Behr, W. M., 2011, Grainsize evolution in ductile shear zones: Implications for strain localization and the strength of the lithosphere: Journal of Structural Geology, v. 33, no. 4, p. 537-550.

Poirier, J. P., 1985, Creep of crystals: high-temperature deformation processes in metals, ceramics, and minerals, Cambridge University Press, Cambridge earth science series, 260 p.:

Prior, D. J., Knipe, R. J., and Handy, M. R., 1990, Estimates of the rates of microstructural changes in mylonites: Deformation mechanisms, rheology and tectonics, Geological Society Special Publications, 54, p. 309-319.

Ranalli, G., 1984, Grain size distribution and flow stress in tectonites: Journal of Structural Geology, v. 6, no. 4, p. 443-447.

Ross, J. V., Ave Lallemant, H. G., and Carter, N. L., 1980, Stress dependence of recrystallized-grain and subgrain size in olivine: Tectonophysics, v. 70, no. 1-2, p. 39-61.

Ross, J. V., and Nielsen, K. C., 1978, High-temperature flow of wet polycrystalline enstatite: Tectonophysics, v. 44, no. 1-4, p. 233-261.

Snoke, A. W., Tullis, J., and Todd, V. R., 1998, Fault-related rocks : a photographic atlas, Princeton, N.J., Princeton University Press, xv, 617 p. p.:

Stipp, M., and Kunze, K., 2008, Dynamic recrystallization near the brittle-plastic transition in naturally and experimentally deformed quartz aggregates: Tectonophysics, v. 448, no. 1-4, p. 77-97.

Stipp, M., and Tullis, J., 2003, The recrystallized grain size piezometer for quartz: Geophysical Research Letters, v. 30, no. 21.

Stipp, M., Tullis, J., and Behrens, H., 2006, Effect of water on the dislocation creep microstructure and flow stress of quartz and implications for the recrystallized grain size piezometer: Journal of Geophysical Research, v. 111, no. B4, p. 1-19.

Trepmann, C., and Stöckhert, B., 2001, Mechanical twinning of jadeite - an indication of synseismic loading beneath the brittle-plastic transition: International Journal of Earth Sciences (Geol Rundsch), v. 90, p. 4-13.

Trepmann, C., Stockhert, B., Dorner, D., Moghadam, R., Kuster, M., and Roller, K., 2007, Simulating coseismic deformation of quartz in the middle crust and fabric evolution during postseismic stress relaxation — An experimental study: Tectonophysics, v. 442, no. 1-4, p. 83-104.

Trepmann, C. A., and Stöckhert, B., 2003, Quartz microstructures developed during non-steady state plastic flow at rapidly decaying stress and strain rate: Journal of Structural Geology, v. 25, p. 2035-2051.

Tullis, J., and Yund, R. A., 1982, Grain growth kinetics of quartz an calcite aggregates: Journal of Geology, v. 90, no. 3, p. 301-318.

Tullis, T. E., and Tullis, J., 1977, Experimental rock deformation techniques: Mineral and rock deformation: laboratory studies.

Twiss, R. J., 1977, Theory and applicability of a recrystallized grain size paleopiezometer: Pure and Applied Geophysics, v. 115, p. 225-244.

Van der Wal, D., Chopra, P., Drury, M., and Fitz Gerald, J., 1993, Relationships between dynamically recrystallized grain size and deformation conditions in experimentally deformed olivine rocks: Geophysical Research Letters, v. 20, no. 14, p. 1479-1482.

White, S., 1977, Geological significance of recovery and recrystallization processes in quartz: Tectonophysics, v. 39, no. 1-3, p. 143-170.

White, S. H., Drury, M. R., Ion, S. E., and Humphreys, F. J., 1985, Large strain deformation studies using polycrystalline magnesium as a rock analogue. Part I: grain size paleopiezometry in mylonite zones: Physics of the Earth and Planetary Interiors, v. 40, no. 3, p. 201-207.

Yund, R. A., and Tullis, J., 1982, Grain growth kinetics of quartz and calcite aggregates: Journal of Geology, v. 90, p. 301-318.

Figure 1

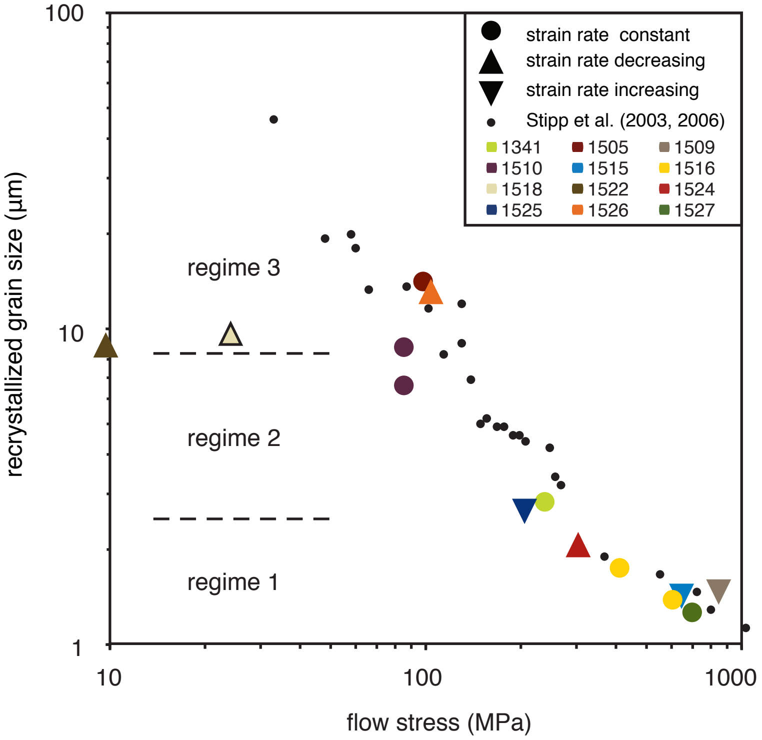
100
10
1
10
100
1000
recrystallized grain size (µm)
flow stress (MPa)
regime 3
regime 2
regime 1
● strain rate constant
▲ strain rate decreasing
▼ strain rate increasing
• Stipp et al. (2003, 2006)
1341
1505
1509
1510
1515
1516
1518
1522
1524
1525
1526
1527

Figure 2

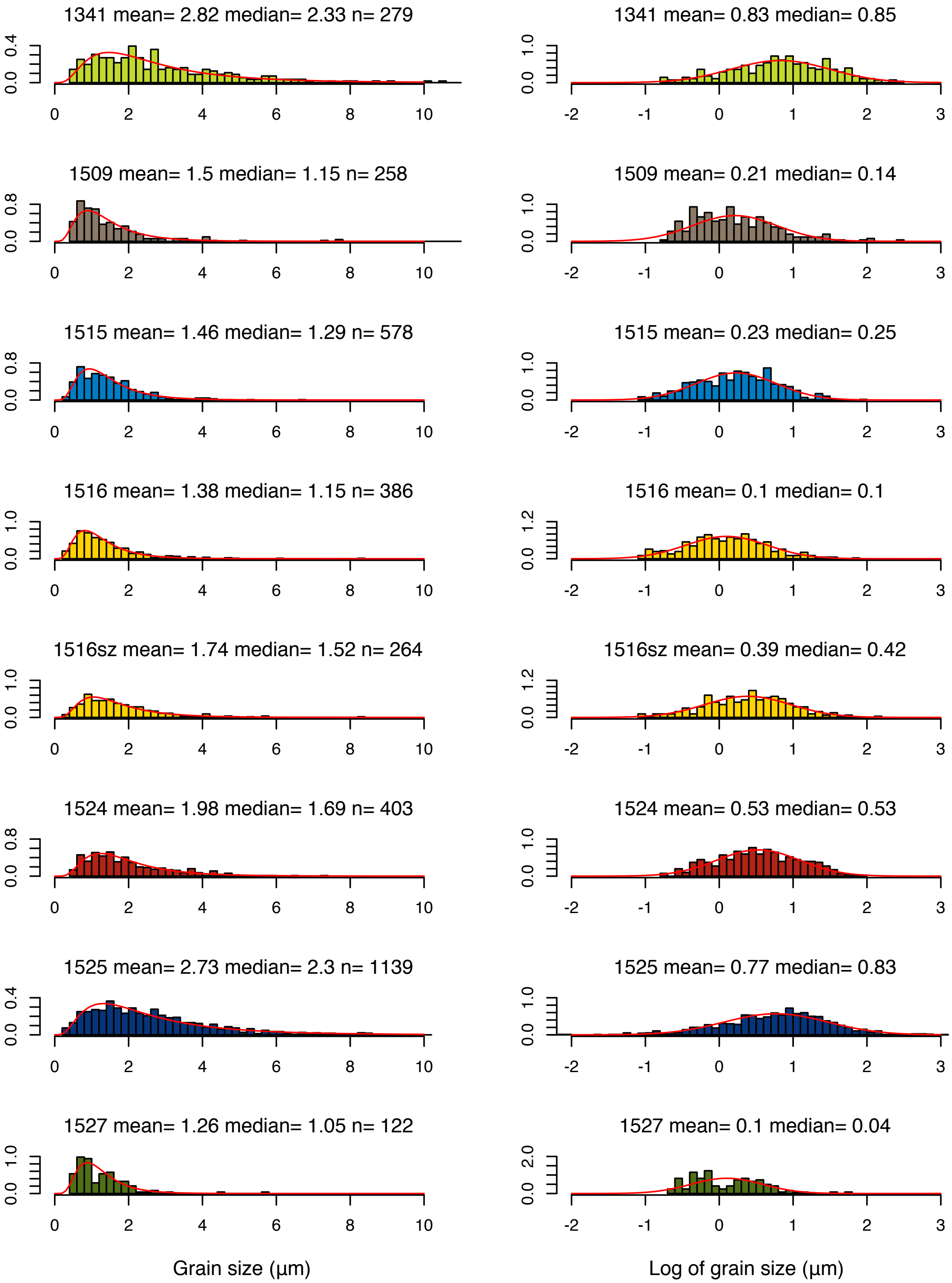
1341 mean= 2.82 median= 2.33 n= 279
1341 mean= 0.83 median= 0.85
1509 mean= 1.5 median= 1.15 n= 258
1509 mean= 0.21 median= 0.14
1515 mean= 1.46 median= 1.29 n= 578
1515 mean= 0.23 median= 0.25
1516 mean= 1.38 median= 1.15 n= 386
1516 mean= 0.1 median= 0.1
1516sz mean= 1.74 median= 1.52 n= 264
1516sz mean= 0.39 median= 0.42
1524 mean= 1.98 median= 1.69 n= 403
1524 mean= 0.53 median= 0.53
1525 mean= 2.73 median= 2.3 n= 1139
1525 mean= 0.77 median= 0.83
1527 mean= 1.26 median= 1.05 n= 122
1527 mean= 0.1 median= 0.04
0.0
0.4
0.8
1.0
1.2
2.0
0
2
4
6
8
10
-2
-1
0
1
2
3
Grain size (µm)
Log of grain size (µm)

Figure 3

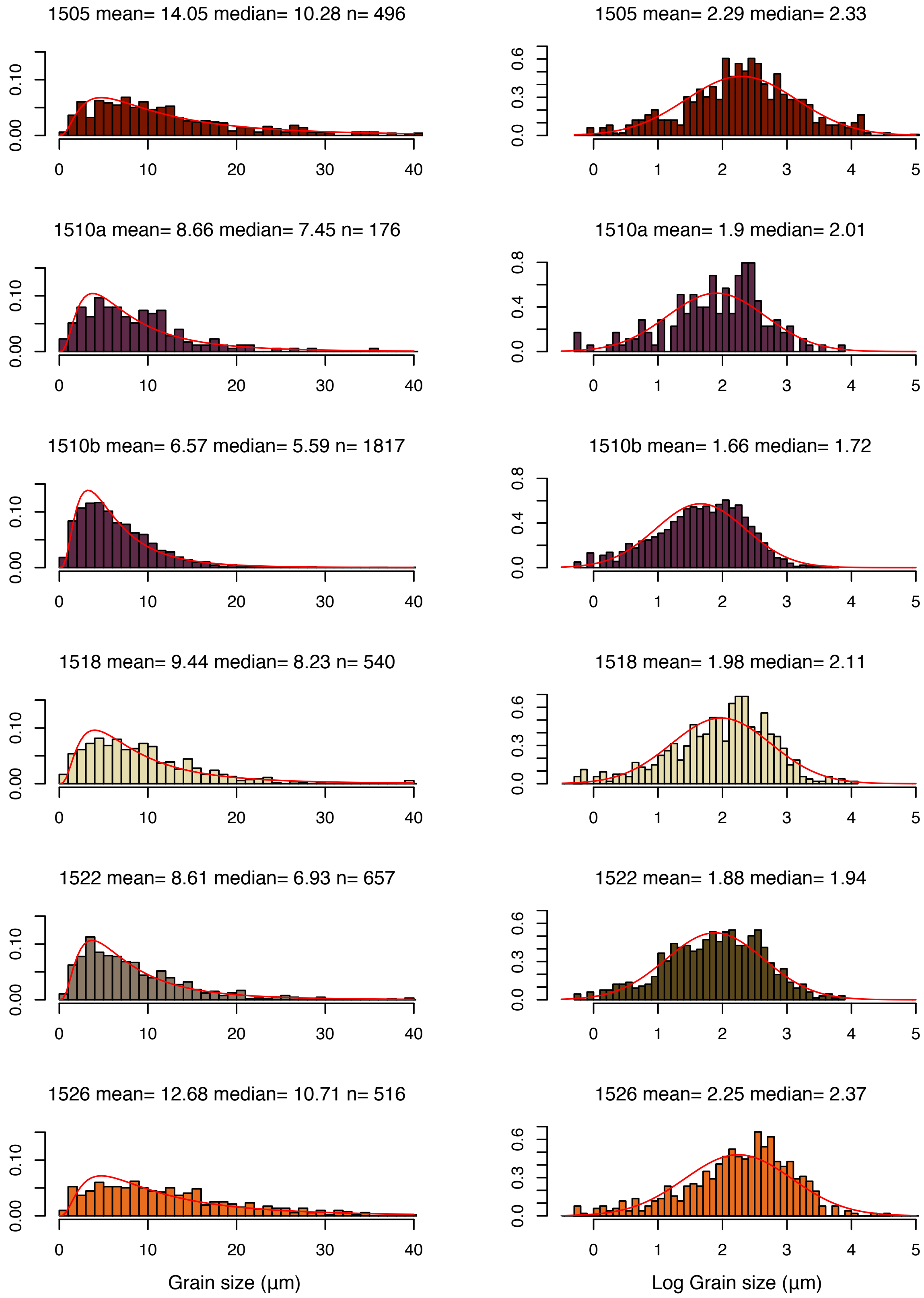
1505 mean= 14.05 median= 10.28 n= 496
1505 mean= 2.29 median= 2.33
1510a mean= 8.66 median= 7.45 n= 176
1510a mean= 1.9 median= 2.01
1510b mean= 6.57 median= 5.59 n= 1817
1510b mean= 1.66 median= 1.72
1518 mean= 9.44 median= 8.23 n= 540
1518 mean= 1.98 median= 2.11
1522 mean= 8.61 median= 6.93 n= 657
1522 mean= 1.88 median= 1.94
1526 mean= 12.68 median= 10.71 n= 516
1526 mean= 2.25 median= 2.37
0.00
0.10
0.0
0.3
0.6
0.4
0.8
0
10
20
30
40
0
1
2
3
4
5
Grain size (µm)
Log Grain size (µm)

Figure 4

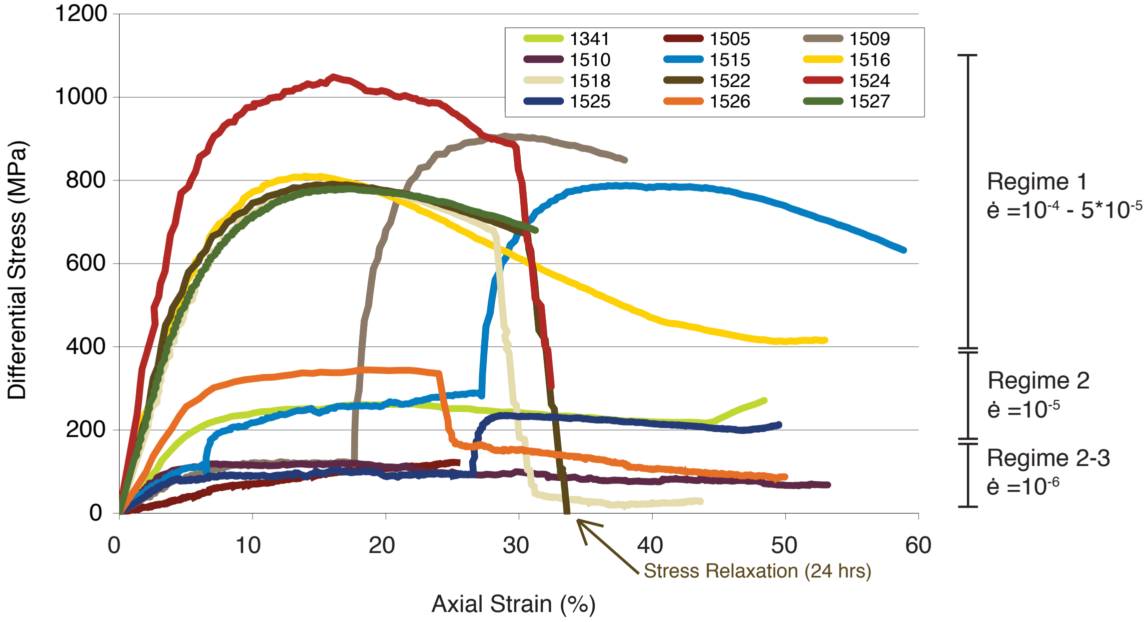

1200
1000
800
600
400
200
0
Differential Stress (MPa)
0
10
20
30
40
50
60
Axial Strain (%)
1341
1505
1509
1510
1515
1516
1518
1522
1524
1525
1526
1527
Regime 1
$\dot{e} = 10^{-4} - 5*10^{-5}$
Regime 2
$\dot{e} = 10^{-5}$
Regime 2-3
$\dot{e} = 10^{-6}$
Stress Relaxation (24 hrs)

Figure 5

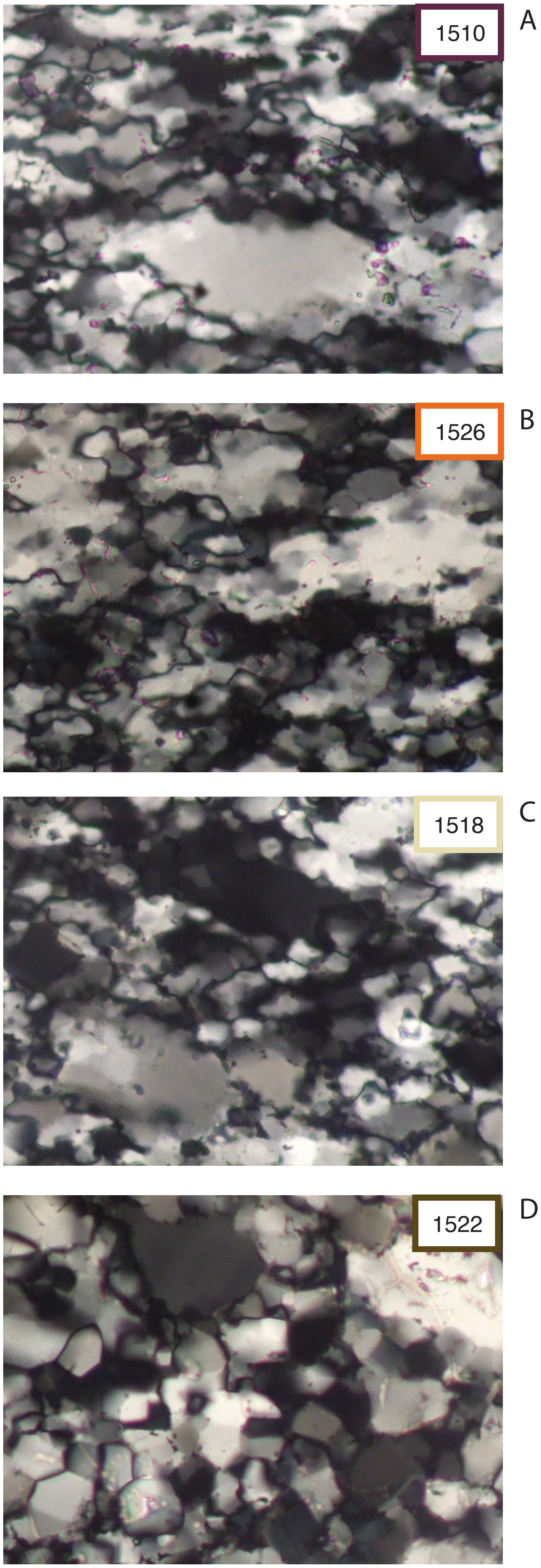

Figure 6

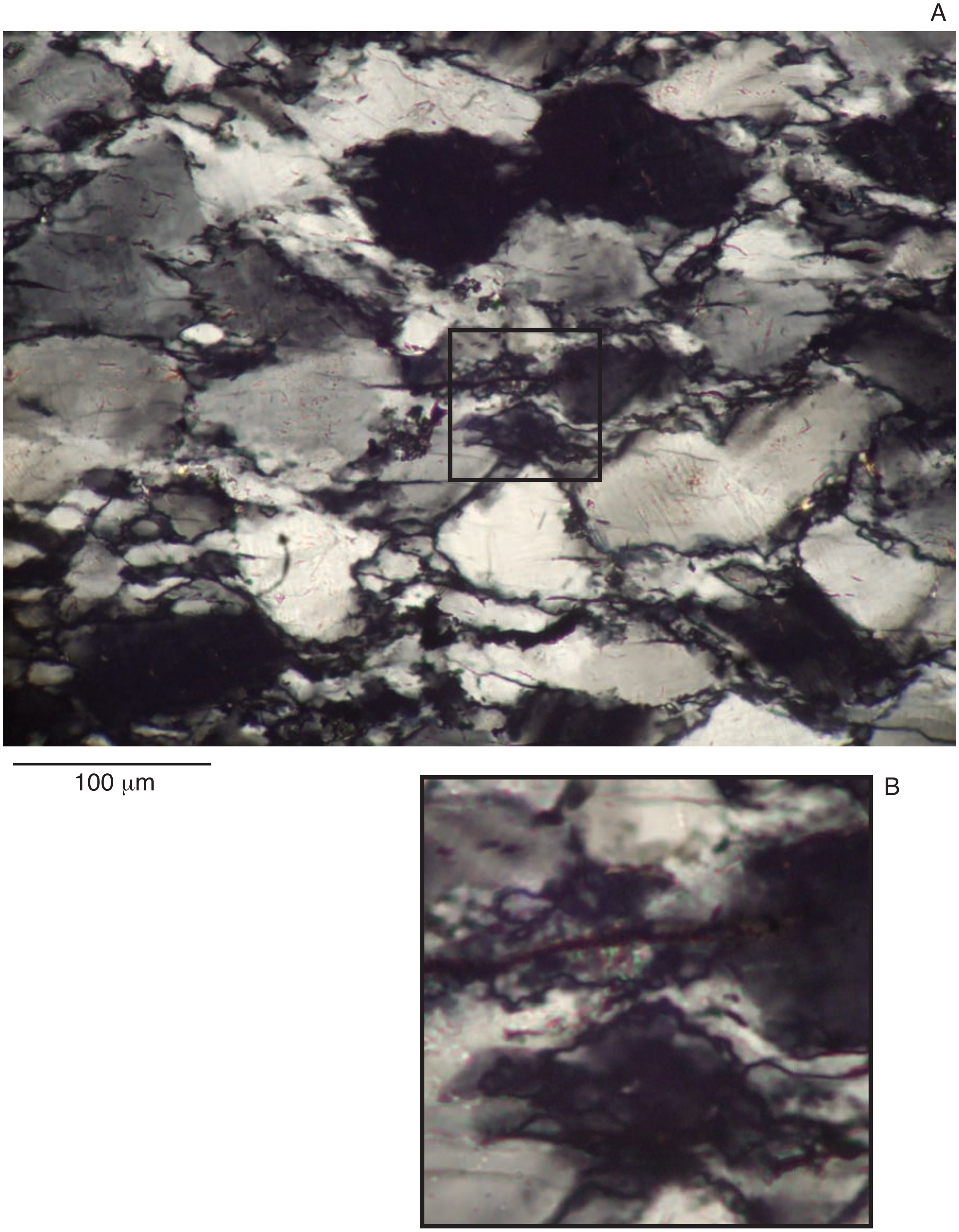

Figure 7

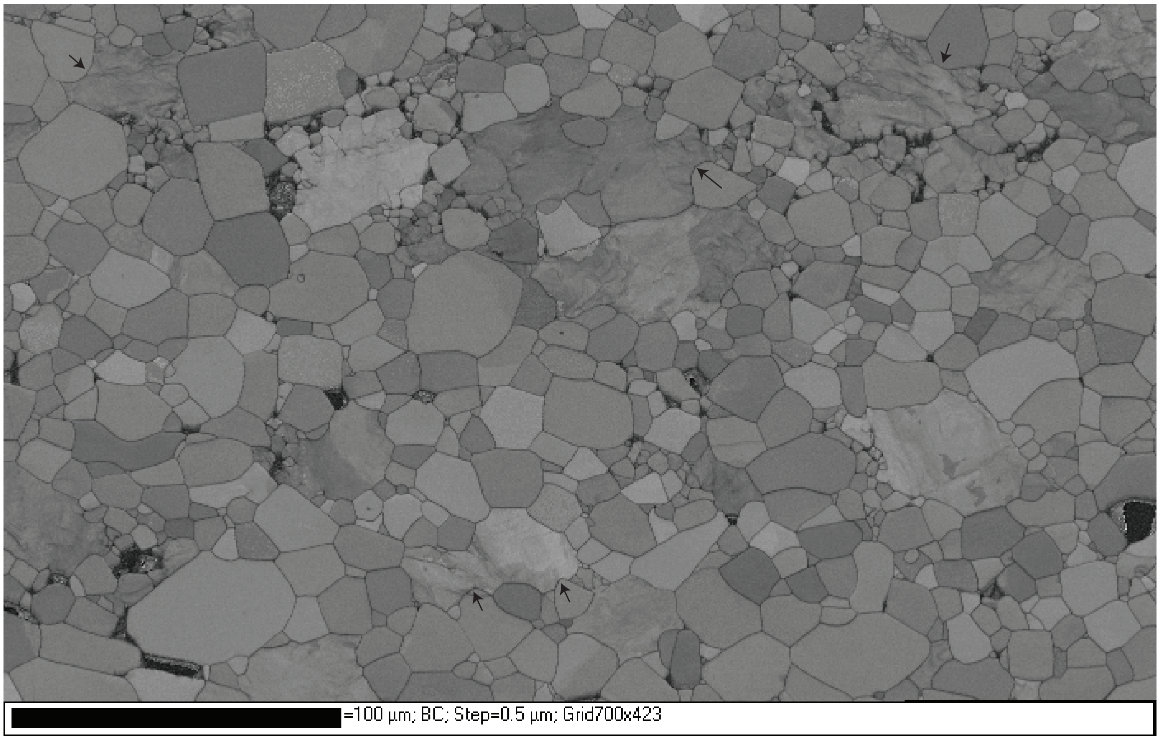

Figure 8

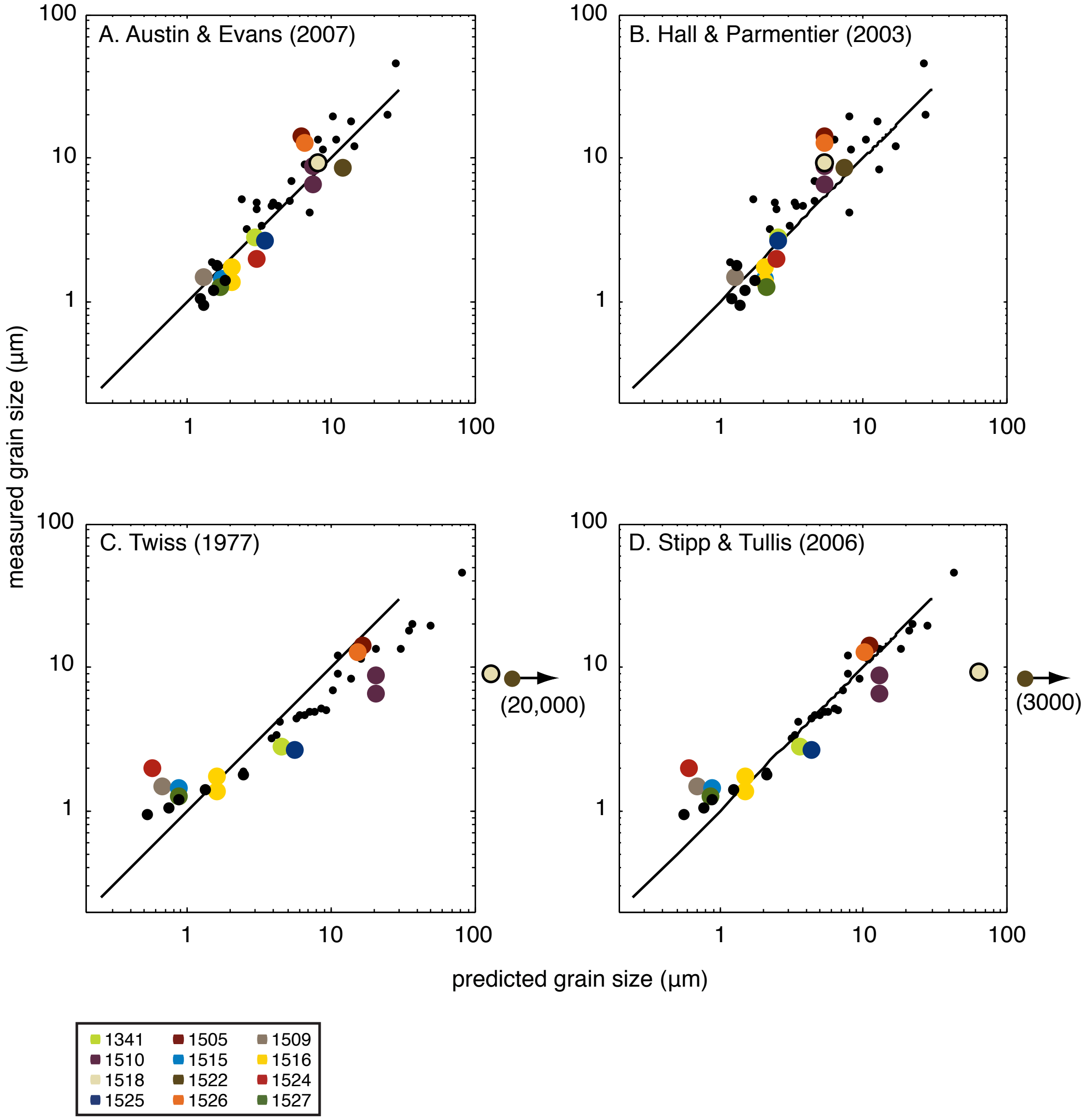

A. Austin & Evans (2007)
B. Hall & Parmentier (2003)
C. Twiss (1977)
D. Stipp & Tullis (2006)
measured grain size (µm)
predicted grain size (µm)
100
10
1
(20,000)
(3000)
1341
1505
1509
1510
1515
1516
1518
1522
1524
1525
1526
1527

Figure 9

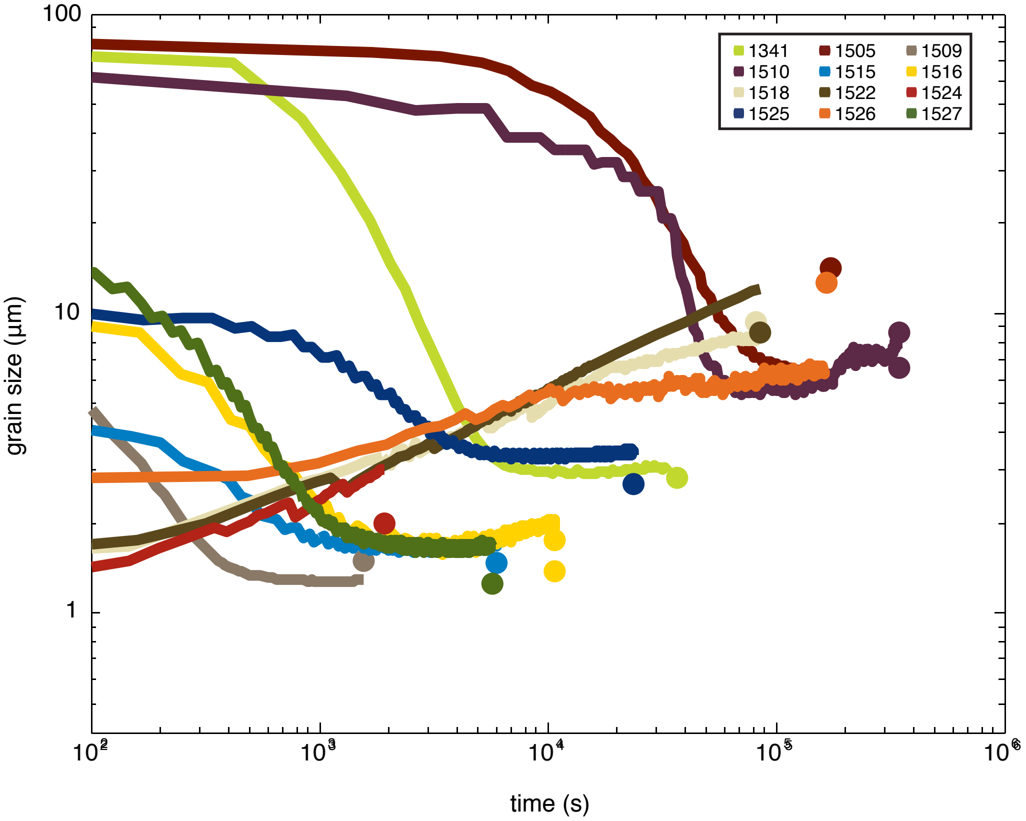
100
10
1
grain size (µm)
10^2
10^3
10^4
10^5
10^6
time (s)
1341
1505
1509
1510
1515
1516
1518
1522
1524
1525
1526
1527

Figure 10

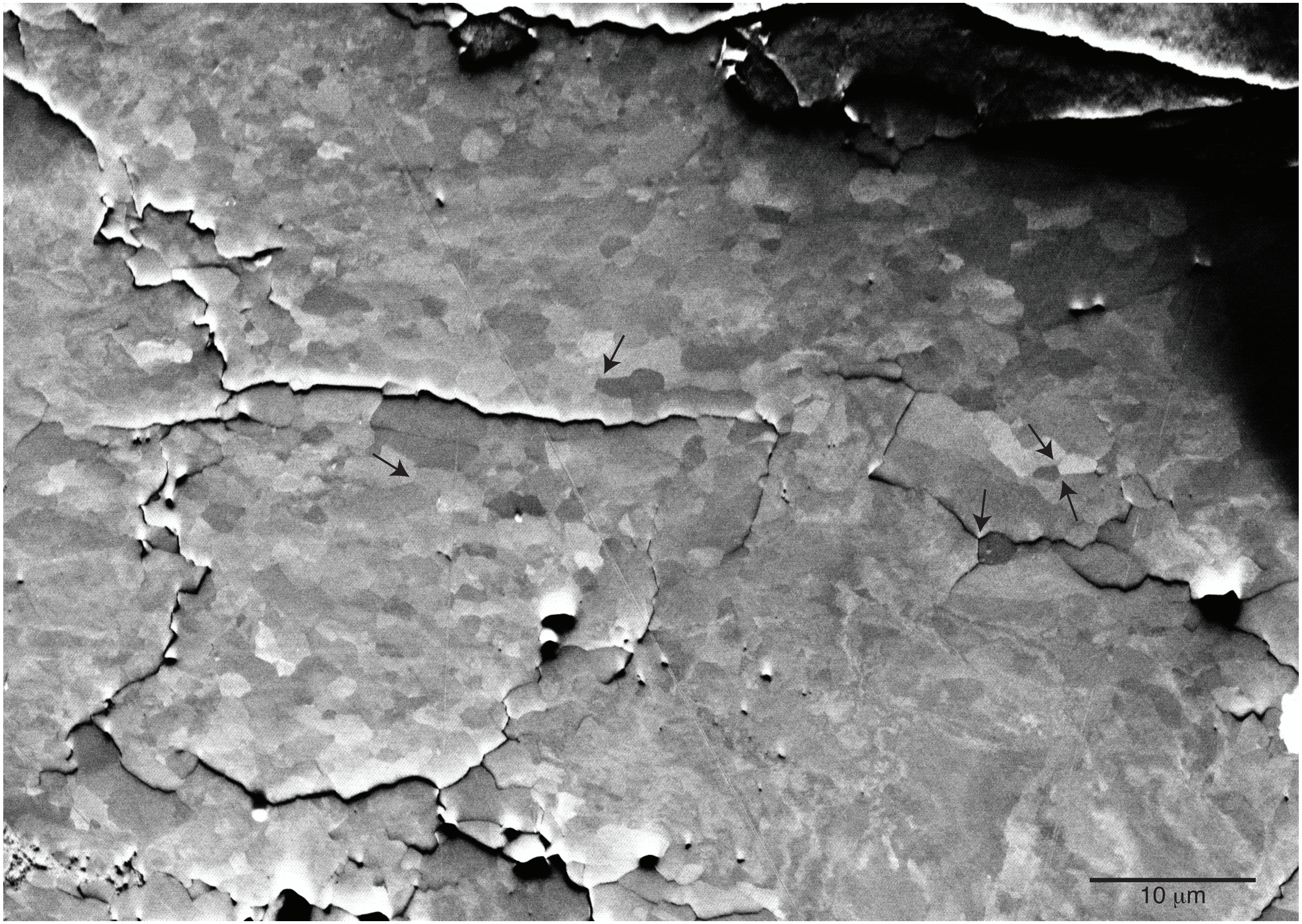

Table 1

experiment	$\dot{\varepsilon}_1$ (s^{-1})	$\dot{\varepsilon}_2$ (s^{-1})	ε_{total}	ε_2	final g.s. (µm)	stress (MPa)	%qtz$_{raw}$	%qtz$_{final}$	rate (μm s^{-1})
1341	1.48E-05	-	48.4	-	2.82	242	92.6	99.1	-1.80E-03
1505	1.45E-06	-	25.1	-	14.1	100	69.4	91.5	-3.18E-04
1509	1.44E-06	1.44E-04	37.9	20.3	1.50	886	69.0	75.4	-4.53E-03
1510a	1.45E-06	-	53.2	-	8.70	87	75.0	96.6	-1.74E-04
1510b	1.45E-06	-	53.2	-	6.57	87	91.2	98.4	-1.81E-04
1515	1.44E-06	2.89E-05	59.1	32.3	1.46	738	73.9	75.6	-3.09E-04
1516	2.88E-05	-	53.0	-	1.38	487	70.2	82.2	-6.24E-03
1516sz	>2.88E-05	-	>53.0	-	1.74	487	84.5	95.8	-6.21E-03
1518	2.88E-05	1.44E-06	43.6	15.5	9.40	25	92.4	98.5	1.03E-04
1522	2.91E-05	4.76E-07	33.6	4.0	8.60	10	84.1	97.6	9.08E-05
1524	2.92E-05	1.50E-06	32.4	2.8	2.00	600	90.9	96.3	7.24E-04
1525	1.43E-06	1.48E-05	49.5	23.0	2.70	210	69.1	96.0	-3.47E-04
1526	1.45E-05	1.45E-06	50.0	26.0	12.7	106	89.0	99.3	6.23E-05
1527	2.87E-05	-	31.2	-	1.26	748	68.0	78.2	-1.19E-02

CHAPTER 3

Constraints from Rocks in the Taiwan Orogen on Crustal Stress Levels and Rheology

Steven Kidder[1], Jean-Philippe Avouac[1], Yu-Chang Chan[2]

[1]*California Institute of Technology, MC 100-23, 1200 E. California Blvd, Pasadena, California, 91125, United States*

[2]*Institute of Earth Sciences, Academia Sinica, P.O. Box 1-55, Nankang, Taipei 115, Taiwan, ROC*

Submitted to *Journal of Geophysical Research*

ABSTRACT

Taiwan's Hsüehshan range experienced penetrative coaxial deformation within and near the brittle-ductile transition between ~6.5 and 3 Ma. This recent and short-lasting deformation in an active, well-studied orogen makes it an ideal natural laboratory for studying crustal rheology. Recrystallized grain size piezometry in quartz yields peak differential stresses at 250–300°C of ~200 MPa that taper off to ~80 MPa at ~350°C. Earlier deformation at temperatures ~400–500°C occurred at a stress of ~14 MPa. Stress results do not vary with lithology: recrystallized quartz veins in slates, siltstones and quartzites yield equivalent stresses as recrystallized grains in quartzites. Given tight geodetic and structural constraints on strain rate, we show that our stress estimates are consistent with the predictions of widely applied quartzite flow laws. We argue that our samples record stress levels at the brittle-ductile transition, indicating a coefficient of friction (μ) of 0.37 in the upper crust consistent with recent critical taper estimates in Taiwan. The integrated crustal strength of the Hsüehshan range based on our analysis amounts to 1.7×10^{12} N/m, consistent with potential energy constraints based on topography. Other strength profiles are considered, however high crustal stresses (>400 MPa) conflict with our analysis. The study supports the use of the recrystallized grain size piezometer as a quick and inexpensive method for

resolving stress histories in exhumed rocks. For consistency with the independent constraints presented here, we find it accurate to within +20%/-40%, significantly better than previously recognized.

1. INTRODUCTION

Despite its importance in geodynamics and earthquake physics, the magnitude and distribution of stress in the lithosphere is poorly known and controversial (e.g. *Bürgmann and Dresen*, 2008; *Burov and Watts*, 2006; *Jackson*, 2002). Quantifying differential stress (referred to below simply as “stress”), and developing and improving techniques for doing so (e.g. *Behr and Platt*, 2011), are thus important objectives in the Earth sciences. A promising tool for estimating paleostress in rocks is the recrystallized grain-size piezometer, which is based on the inverse correlation between the size of grains formed during dislocation creep and stress (e.g. *Etheridge and Wilkie*, 1981; *Mercier et al.*, 1977; *Poirier*, 1985; *Twiss*, 1977). Rapid and inexpensive measurements of grain size can be made in thin section, thus potential exists for routine use of the rock record to quantify stress histories. The usefulness of grain size piezometry, however, is limited by unknown inaccuracies introduced by extrapolation of laboratory-derived grain-size stress relationships to natural conditions (e.g. *Passchier and Trouw*, 2005).

In this study we apply recrystallized grain size piezometry in an active and well-studied setting, Taiwan’s Hsüehshan range (figure 1), where results can be compared with numerous independent constraints on stress levels. We first document deformation conditions at middle-crustal levels, then catalogue available constraints on stress magnitude. We demonstrate that the recrystallized grain size piezometer in quartz is accurate to within the uncertainties of more widely applied techniques, and indicates a fairly weak middle crust in Taiwan.

2. GEOLOGIC BACKGROUND AND DEFORMATION CONDITIONS

Taiwan is a result of the collision of the Luzon volcanic arc with the South China margin (figure 1a). The rocks comprising the Hsüehshan range are late Tertiary passive margin quartzites and mudstones. Prior to collision they experienced only minor extensional deformation (*Clark et al.*, 1993; *Tillman et al.*, 1992). Collision began at ~6.5 Ma at the latitude of the study area (*Lin et al.*, 2003), and ongoing exhumation in the Hsüehshan range exposes rocks deformed at depths up to ~20 km during early stages of collision (*M. Simoes et al.*, 2007). Due to the obliquity of the collision, the orogen propagates southward at a rate of ~30–90 km/m.y. (*M. Simoes and Avouac*, 2006, and references therein). While along-strike heterogeneities in the South China margin complicate the simple south-propagating model (e.g. *Byrne et al.*, 2011), modern-day southern Taiwan serves as a loose analogue for our study area during early collision.

A strip map and cross section of the Hsüehshan range are shown in figure 1b and 1c. The oldest unit in the stratigraphy is the Eocene-Oligocene Tachien Sandstone, a coarse-grained, massive quartzite with slate interbeds. The Tachien Sandstone compositionally 60-80% quartz (grains of quartz, quartzite, chert and quartz schist), and contains detrital feldspar and mica, and fragments of felsic volcanics and slate. The Tachien sandstone is overlain by the Oligocene Chiayang Formation, consisting of slate and rare fine-grained sandstones, and the Paileng Formation, an age-equivalent to the Chiayang Formation, consisting of fine- to coarse-grained quartzite with minor slaty interbeds (*Ho*, 1988). Ages of these units are uncertain due to lack of fossils. The structures shown in figure 1 formed during collision as the passive-margin sedimentary cover was transferred from the down-going Eurasian plate to the Taiwan orogenic wedge. The deepest exposures occur in the core of the Tachien anticline, where early collisional deformation occurred within the biotite stability field, above ~400°C. Deformation in most of the range—and significant retrograde deformation of the Tachien anticline (*Clark et al.*, 1993; *Chapter 1*)—occurred at 250–350°C (figure 1e). We refer to this lower temperature deformation below as “late” deformation.

Collisional deformation of the Hsüehshan range varies strongly from west to east. The Paileng Formation, particularly western portions, preserves sedimentary structures such as crossbedding and generally shows little evidence of deformation in thin section (figure 2a). Limited penetrative deformation was dominated by pressure solution (evidenced by occasional vertical cleavage striking NNE-SSW). Dynamic recrystallization of quartz in the Paileng formation is rare and occurs only occasionally along grain boundary (figure 2b). These relatively undeformed quartzites stand in sharp contrast to those in the Tachien anticline, which display a penetrative, collisional foliation (figures 1c, 3a), and axial strain of ~0.3 based on an R_f/φ analysis (*Chew*, 2003; *Lisle et al.*, 1983; *Ramsay*, 1967) of a representative sample (148d). This degree of strain is representative of quartzites in the inner 2–3 km of the anticline, with penetrative deformation decreasing moderately to the east and west. Based on the presence of strong undulose extinction, recrystallized grains and subgrains, and a weak lattice preferred orientation, much of this strain seems to have occurred by dislocation creep. A component of pressure solution creep cannot be excluded however, and in fact some of the finer-grained quartzites we sampled may have deformed exclusively by this mechanism. Strain is also high in slates in the eastern and central Hsüehshan range, where the strain analyses indicate > 30 km internal shortening (*Fisher et al.*, 2002).

Quartz veins are common in the central Hsüehshan range. A population of precollisional veins can be distinguished from collisional veins based on orientation (*Tillman et al.*, 1992). Collisional veins often occur in swarms in the cores of anticlines (e.g. figure 4). Both the extensional and collisional veins generally show evidence of some dynamic recrystallization, indicating deformation at temperatures above 250°C (the minimum temperature for dislocation creep in quartz, see e.g. references in *Trepmann and Stockhert*, 2009). Since collisional deformation occurred under generally retrograde conditions (*Clark et al.*, 1993; *Chapter 1*), such veins probably indicate alternating brittle and ductile behavior (brittle behavior during vein formation, ductile deformation responsible for recrystallization, then further brittle deformation during exhumation). Some collisional veins can be shown to have undergone at least two brittle-ductile episodes, being plastically deformed, crosscut by new veins and then plastically deformed again (*Chapter 1*).

The timing of deformation is constrained by collision at ~6.5 and cooling of the core of the Tachien anticline through zircon fission track closure temperatures of ~200–260°C at ~3 Ma (*Liu et al.*, 2001). Using 250°C as the cutoff temperature for dislocation creep in quartz, the fission track ages provide a minimum age for stresses based on recrystallized grain size. Dislocation microstructures, such as patches of recrystallized grains, are not generally overprinted by lower temperature features, suggesting that the 3 Ma cutoff age is a reasonable minimum estimate for the termination of shortening. Dividing the above strain estimate for the Tachien anticline by the 3.5 m.y. deformation interval yields a minimum estimate of strain rate of 2.9×10^{-15} s^{-1} for these rocks. We estimate a maximum strain rate of 7.0×10^{-14} s^{-1} by dividing the geodetic convergence rate by the width of the deformation zone. About 4.2 cm/yr convergence is accommodated west of the Eurasia-Philippine plate boundary (*Simoes and Avouac*, 2006). Structural analyses by ourselves and Tillman and Byrne (1995) indicate penetrative deformation occurred over an ~19 km wide zone (figure 1c). We cannot prove that penetrative deformation occurred simultaneously throughout this zone, however microstructures indicate fairly uniform coaxial deformation due to horizontal compression (*Fisher et al.*, 2002; *Tillman and Byrne*, 1995). To accomplish this diachronously would require a propagating wave of shortening across the zone that is not indicated by the spatial distribution of thermochronologic ages (*Liu et al.*, 2001; *Martine Simoes et al.*, 2012).

Deformation conditions were “wet” based on the presence of synkinematic biotite and chlorite (*Clark et al.*, 1993; *Chapter 1*; *Yen*, 1973) and abundant fluid inclusions in veins and quartzites. Fluid inclusions in veins from the eastern edge of the Hsüehshan range are ~85 wt% H_2O (*Chan et al.*, 2005).

3. METHODS

Approximately 75 thin sections were made from quartzite and quartz veins in slates, metasiltstones, and quartzites collected in the Hsüehshan range. Measurements of recrystallized grain size were made in all samples containing recrystallized quartz. Grain size estimates were not made in quartzite samples containing veins in order to minimize potential effects of stress concentration associated with veining. Both collisional and precollisional veins were recrystallized during collision (*Tillman et al.*, 1992) and were lumped together in our analysis.

Recrystallized grain size was measured under cross-polarized light using the linear intercept method (e.g. *Exner*, 1972) in thin (~30 μm) and ultrathin (~15 μm) sections. Linear intercepts were taken in the most densely recrystallized portions of samples. Following Hacker et al. (1992), geometric mean grain sizes and uncertainties are based on multiple linear intercepts (each containing 5–25 grains), and are not the same as those that would be estimated by measuring each grain diameter individually. Grain boundaries were defined as any visible sharp change in luminosity, thus optically visible subgrains were included in the analysis (e.g. figures 2b, 3b). Subgrains were included because 1) the size of subgrains and recrystallized grains in our samples is similar enough to be indistinguishable by eye (e.g. figures 2b, 3b), 2) the ambiguity of distinguishing grains from subgrains is removed, and 3) recrystallization was often of such limited extent that patches of fully recrystallized grains were often lacking. No stereological correction was made.

The characteristics of inherited recrystallization in undeformed quartzites from the western Hsüehshan range were noted and could generally be used in deformed samples to distinguish between likely inherited and collisional recrystallization. Such distinctions were generally straightforward—deformed quartzites are often typified by a fairly uniform recrystallized grain size and shape-preferred orientation consistent with horizontal east-west compression (e.g. figure 3a). Where ambiguous, recrystallization inherited from detrital sources was avoided by 1) restricting analyses to recrystallization concentrated along detrital grain boundaries or shared by 2–3 neighboring detrital grains, and/or 2) restricting analyses to recrystallized grains found in postdepositional quartz (e.g. quartz cement between detrital grains).

4. STRESS ESTIMATES

The recrystallized grain size from late deformation ranges from ~4 to 22 μm (table 1). These values are not likely influenced by post-deformational grain growth (e.g. *Hacker et al.*, 1992) since annealed textures (e.g. *Tullis and Yund*, 1982) are not prevalent (figures 2b, 3b), and the grain growth formulation of Wightman et al. (2006) predicts insufficient time for measurable growth since collision. Stresses corresponding to the measured grain size are ~210–57 MPa (*Stipp and Tullis*, 2003) and are plotted in figure 1d for veins and quartzites (colored and black symbols respectively). Some of the scatter in figure 1d is due to deformation over a range of stress levels during cooling, as evident in figure 5 where only data paired with well-constrained deformation temperatures are plotted. A grain size of ~130 μm (stress ~14 MPa) associated with the overprinted, early fabric (figure 3a) in the Tachien anticline was estimated in two representative samples.

5. DISCUSSION

5.1. Variability of Recrystallized Grain Size

Recrystallized grain size and deformation temperature are grossly correlated in the Hsüehshan range (compare figures 1d and 1e). Grain size and deformation temperature are greatest in the core of the Tachien anticline, and both decrease markedly to the west. The grain size data appear to cluster into three groups separated by the two main faults in the range, such that the deeper thrust sheets contain a progressively coarser recrystallized grain size. This trend demonstrates qualitatively that stress decreased with depth as expected in ductilely deforming rocks (e.g. *Bürgmann and Dresen*, 2008).

Due to the large sample size and the measurement of recrystallized grain size in a variety of rock types (quartzite; and veins in slate, siltstone, and quartzite), we can additionally address the effect on recrystallized grain size of stress concentrations due to viscosity contrast. It is unknown, for example, if veins in weak materials such as slate concentrate stress enough to significantly bias piezometric measurements in veins (e.g. *Kenis et al.*, 2005), or if grain-scale viscosity contrasts in polyphase rocks such as impure quartzite and granite cause significant variation in average stress in different minerals (e.g. *Bloomfield and Covey-Crump*, 1993). The data presented in figure 1d demonstrate that neighboring quartzites and veins have equivalent recrystallized grain sizes, and that the host lithology of veins does not significantly bias average recrystallized grain size. Thus, while some stress concentration probably occurs, on average it does not apparently lead to differences that would significantly alter interpretations of stress results.

5.2. Constraints on Middle Crustal Rheology

It is often assumed, particularly in numerical models (e.g. *Kaus et al.*, 2008; *Yamato et al.*, 2009), that middle crustal rheology can be approximated using a flow law for dislocation creep of the form

$$\dot{\varepsilon} = A\,\sigma^{n}\,e^{(-Q/RT)} \qquad (1)$$

where $\dot{\varepsilon}$ is strain rate, A is a material constant dependent on water fugacity, σ is differential stress (MPa) raised to an exponent n, Q is the creep activation energy (kJ mol^{-1}), R is the gas constant, and T is absolute temperature (e.g. *Poirier*, 1985). Despite the heterogeneity of deformation mechanisms and rock types in the crust, assumed values of the parameters A, n and Q are generally based on experimental deformation of pure quartzite (e.g. *Kohlstedt et al.*, 1995). This raises two important questions: Do quartzites in nature actually deform according to experimental predictions? If they do, can deformation of the crust—a heterogeneous suite of rocks containing little pure quartzite—be reasonably approximated using Equation 1? Our dataset addresses these questions in two ways.

We first calculate the viscosity of quartzite using our estimates of stress and strain rate, and compare it to the viscosity predicted using commonly applied quartzite flow laws. This is done for the two representative samples from the Tachien anticline core, since this is the only region where reasonably accurate strain measurements in quartzites were possible. Both samples contain a remnant early set of coarse recrystallized grains that are overprinted by finer recrystallized grains (figure 3). Deformation temperature is better constrained for the late, high stress deformation at ~330°C (figure 1e), and we calculate a viscosity for these conditions between 7.4×10^{20} and 3.6×10^{22} Pa s. During early deformation at ~400–500°C, we calculate a viscosity between 1.2×10^{20} and 5.8×10^{21} Pa s. These ranges assume the absolute error in stress estimated below of +20%/-40%. These viscosities are consistent with those predicted by the widely used quartzite flow laws of Hirth et al. (2001) and Paterson and Luan (1990). The consistency between our measurements and the experimental results can be seen graphically in figure 6, where these data are plotted as four large black dots. The shaded areas in figure 6 representing the two flow laws indicate the range of predicted stresses over the temperature range of 250–600°C given our strain rate constraints. At a minimum, this result demonstrates a consistency under natural conditions between the two independent approaches: recrystallized grain size piezometry and experimentally derived flow laws. It also strengthens the case that these flow laws accurately predict the rheology of real quartzite under geologic conditions (at least at temperatures of 300–500 °C), despite the impurity (20-40% non-quartz phases) of the Tachien sandstone.

Our data also allow a test of the applicability of such flow laws to a middle crust formed only partially of quartizite and deformed only partly by dislocation creep since: 1) roughly a third of the Hsüehshan range (the Chiayang formation) is composed of slate with a strong pressure solution cleavage, 2) slate interbeds and fine grained sandstones deformed by pressure solution are also common in the Paileng and Tachien sandstones, and 3) the dynamic recrystallization of collisional veins indicates brittle processes at elevated temperatures. Assuming a flow law of the form given in Equation 1, the ratio of the parameters Q and n associated with this multi-mechanism, multi-lithology deformation can be constrained using our stress-temperature data. We reformulate Equation 1 as

$$\ln(\sigma) = B + Q/(nRT) \tag{2}$$

where B incorporates A, n and $\acute{\varepsilon}$. The slope on an Arrhenius plot of ln σ vs. 1/T is Q/nR (figure 5). We assume here that bulk strain rates for the different exposed crustal levels were equal. Since the Hsüehshan range is a pop-up structure characterized by coaxial strain (*Clark et al.*, 1993), it seems likely that shortening rates would not be dramatically different between the different crustal levels. We find a slope equivalent to a value for Q/n of 41 ± 6 kJ/mol (~95% confidence) using the “model 2” linear regression of Ludwig (2001). This is consistent with Q/n values for many quartzite flow laws, which range from 34–84 kJ/mol (*Gleason and Tullis*, 1995). Estimates of activation energy for pressure solution creep (n=1) have a larger range, from 15–113 (e.g. *Kawabata et al.*, 2009), but intermediate values of Q/n would also be consistent with this result, at least down to temperatures of 250°C.

5.3. Strength of the Taiwan Orogenic Wedge

As a simplifying assumption, lithospheric strength can be considered a function of the two best-understood deformation mechanisms in rocks: Mohr-Coulomb friction and dislocation creep (e.g. *Scholz*, 2002). At cold temperatures where friction dominates, strength increases linearly with effective confining pressure. At sufficiently high temperatures, dislocation creep becomes more effective than friction and strength decreases. The crust is strongest where similar stresses are required to activate each process, the “brittle-ductile transition.” While deformation mechanisms such as pressure solution and semibrittle flow may in reality act to blunt peak stresses predicted by the two-mechanism approach (e.g. *Kohlstedt et al.*, 1995), dislocation creep and resulting dynamic recrystallization of quartz is expected and observed at the brittle-ductile transition (e.g. *Kuster and Stöckhert*, 1998). It is thus likely that the highest stresses in the crust are recorded in quartz dynamically recrystallized at the brittle-ductile transition.

There are several lines of evidence suggesting that our higher stress samples were deformed within the brittle-ductile transition zone: 1) The depth distribution of earthquakes in southern Taiwan (the present-day analogue to our study area) shows a clear peak at ~10 km (e.g. *Mouthereau and Petit*, 2003) using data from the Central Weather Bureau Seismic Network (*Shin*, 1992). Recrystallization of Hsüehshan range quartzites occurred roughly at this depth level and lower assuming a geothermal gradient of 25 °/km (figure 6). (Geotherm estimates for central Taiwan vary, however this estimate is consistent with the 25–30 °/km gradient in Raman spectroscopy of carbonaceous material (RSCM) temperature with stratigraphic depth in the study area (*Beyssac et al.*, 2007), the thermal history modeled by Simoes et al. (2007), and the average thermal gradient in exploration wells in Taiwan (*Zhou et al.*, 2003)). 2) Overlapping brittle and ductile deformation evident in veins from the central Hsüehshan range typifies behavior expected at the brittle-ductile transition. 3) The highest stress samples come from the western part of the Hsüehshan range, where penetrative deformation was minimal (e.g. figure 2a). Shortening here apparently was accomplished primarily via faulting, which in comparison with the penetratively deformed central Hsüehshan range suggests deformation conditions near the upper limit of the brittle-ductile transition. 4) Carena et al. (2002) estimated that Taiwan’s brittle-plastic transition (equivalent to or deeper than the brittle-ductile transition (*Kohlstedt et al.*, 1995)) occurs at a depth of 15–20 km (within the estimated depth range of our samples) based on the deviation at these depths from a linear relationship between topographic slope and detachment dip.

Assuming that our coolest and highest stress data reflect conditions at the brittle-ductile transition, we follow Behr and Platt (2011) in constructing a crustal strength envelope by fitting a line from the surface to a value typical of our highest stress samples, ~200 MPa (figure 6 "preferred brittle strength profile"). Assuming hydrostatic fluid pressure (see below), this implies a coefficient of friction in the upper crust, $\mu = \sim 0.37$.

Further insights into crustal strength in Taiwan can be gained by comparison with independent estimates of stress levels in Taiwan. Based on critical taper theory Suppe (2007) found that stress (σ_D) in Taiwan increases with depth in the brittle crust according to the relationship, $\sigma_D = Wrgz$, where $W = 0.6$. This constraint nearly coincides with the brittle portion of our preferred strength envelope (figure 6). Calcite twin orientations in southern Taiwan (*Lacombe*, 2001) provide an additional "order of magnitude" constraint on stress levels (figure 6). Finally maximum strength can be estimated based on Coulomb frictional-failure theory and the experimental results of Byerlee (1978) assuming hydrostatic fluid pressure

$$\tau = \mu \sigma_{eff} \qquad \sigma_n < 200 \text{ MPa} \qquad (3a)$$

$$\tau = 50 + \mu \sigma_{eff} \qquad 200 \text{ Mpa} < \sigma_n < 1700 \text{ MPa} \qquad (3b)$$

where τ is shear stress in MPa, m is the friction coefficient, and σ_{eff} is effective confining pressure (normal stress – pore fluid pressure) in MPa. Byerlee (1978) found values of $\mu = 0.85$ and 0.6 for equations 3a and 3b respectively (i.e. "Byerlee's law"). Stress levels in boreholes reaching depths of 3–8 km in Europe and Western North America are consistent with Byerlee's (1978) results, fitting equation 3a well with $\mu = 0.6–1$ (*Townend and Zoback*, 2000). The strength envelope labeled "Byerlee's law" in figure 6 is a maximum constraint since fluid pressure in shallow wells in Taiwan often exceeds hydrostatic (*J. Suppe and Wittke*, 1977; *Yue*, 2007). We suggest that the calcite twin study of Lacombe (2001) at least somewhat overestimates stress since 2 of the 3 data points indicate higher stresses than Byerlee's law. It is unclear why Suppe's (2007) and our stress estimates are lower than global borehole estimates. Perhaps there is a fundamental difference in crustal strength between the generally cratonic study areas probed by the boreholes and the Taiwan orogenic wedge.

These constraints on brittle strength can be combined with a curve fit through our stress-temperature data to constrain integrated crustal strength (figure 7). As a weak brittle endmember we use our preferred μ of 0.36 (figure 7a). As a strong endmember we construct a strength envelope assuming Byerlee's law (figure 7b). Integrating these strength envelopes to a depth of 30 km yields total crustal strengths of 1.7×10^{12} N/m and 3.5×10^{12} N/m respectively. These values can be compared with the horizontal stress required to support topography assuming isostatic balance and no contribution from vertical stresses (e.g. flexure). The Hsüehshan range rises to an altitude of ~2.5 km in the long-wavelength topography with a Moho depth of 35–45 km beneath the Hsüehshan range and 29–37 km in western Taiwan (*Kim et al.*, 2004; *McIntosh et al.*, 2005; *Shih et al.*, 1998; *Ustaszewski et al.*, in press). Following Molnar and Lyon-Caen (1988), we calculate a potential energy difference of 2.7×10^{12} N/m, equivalent to a strength of ~90 MPa averaged over a 30 km thickness (figures 6, 7). Since we ignore vertical stress contributions to topographic support, this calculation provides an upper limit on crustal strength in Taiwan. The "preferred" profile (figure 7a) is consistent with this constraint, while the higher strength end member (figure 7b) is stronger than possible given the potential energy constraint. Thus the high strength derived from Byerlee's law would only be consistent with the potential energy constraint if crustal strength estimate is truncated (e.g. *Kohlstedt et al.*, 1995) at a stress of ~240 MPa or smaller (figure 7c). Intermediate values for the coefficient of friction (μ = 0.36–0.65) would not require truncation. In any case, this analysis conflicts with high stresses (>400 MPa) as suggested by Moutherau and Petit (2003) and considered by Kaus et al. (2009).

While we find peak stresses at ~12 km similar to those estimated by Suppe (2007), the data on which his critical taper estimate is based were interpreted to indicate a brittle wedge to depths of 15–20 km (*Carena et al.*, 2002). The crustal strength profiles plotted in figures 6, 7a, 7b, and 7c suggest a much weaker crust at depths of 10–20 km. This discrepancy could be rectified by reducing our assumed geothermal gradient to 18 °/km (or smaller), a value within the range of plausible estimates in central Taiwan (e.g. *Gourley et al.*, 2007). This possibility is plotted in figure 7d. Given the potential energy constraint, the lower geotherm requires $\mu < 0.36$. The consistency of such a low geotherm with thermochronologic and metamorphic data can be tested in future studies. We note however that for consistency with the flow law of Hirth et al. (2001), this scenario requires a faster strain rate (1.5×10^{-13} s^{-1}) than permitted by our constraints.

5.4. Accuracy of the Recrystallized Grain Size Piezometer in Quartz

The overall consistency of our results with independent experimental and theoretical constraints on stress levels is striking (figure 6). Stresses are consistent with the predictions of the most widely applied quartzite flow laws. Our peak stress estimate is similar to that predicted by critical taper theory (*John Suppe*, 2007). Stress estimates fall below maximum constraints provided by Byerlee's law and Lacombe's (2001) calcite twinning study. Our data are generally consistent with Goetze's criterion ($\sigma_D < P_{eff}$ for plastic flow, (*Kohlstedt et al.*, 1995); figure 6, the single exception could be the result of a slight overestimate of the geotherm). Simple crustal strength profiles based on our data (figures 7a, 7c, and 7d) satisfy potential energy constraints based on topography. These independent constraints provide the strongest evidence to date that laboratory-based stress-grain size relationships are accurate under natural conditions. It does not appear that the geologic fluids, low temperature, or competing deformation processes in the Hsüehshan range affected the laboratory-based relationship.

To our knowledge, the only existing estimate of the accuracy of the recrystallized grain size is an "order of magnitude" (*Stockhert et al.*, 1999). The piezometer is clearly outperforming this evaluation in the Hsüehshan range. To maintain consistency with the various independent constraints provided here, we estimate the Stipp and Tullis (*Stipp and Tullis*, 2003) piezometer to be accurate to within +20%/-40%. An overestimate of 20% places our data at higher stress values than predicted by the quartzite flow laws, and would violate Goetze's criterion. An underestimate by 40% places peak stresses significantly (50 MPa) below the stress level estimated by Suppe

(2007), at 12 km depth, and would be even more discrepant with Byerlee's law and global borehole estimates.

This constraint on the accuracy of the Stipp and Tullis piezometer is at odds with a recent alternative recrystallized grain size–stress relationship, the "paleowattmeter" of Austin and Evans (2007; 2009). The paleowattmeter provides a remarkable fit to laboratory data, however it predicts a temperature dependence that results in very low stress estimates for geologic conditions (e.g. ~1 MPa for the late deformation in sample 148d). These low stresses are inconsistent with all published quartzite flow laws and are ruled out by the above analysis. This does not necessarily indicate a flaw with the paleowattmeter, which is heavily dependent on parameters whose values are not all well known. The temperature dependence stems from the difference in activation energy for grain growth and dislocation creep, and it may be that an improved understanding of grain growth in quartz would yield better results.

6. CONCLUSIONS

We estimate an integrated crustal strength in Taiwan of ~1.7×10^{12} N/m, with peak stress at the brittle-ductile transition ~200 MPa, and a coefficient of friction (μ) in the upper crust of 0.37. The consistency of these results with independent constraints indicates that the recrystallized grain size piezometer can be used to constrain stress histories in deformed rock with accuracy comparable to more widely used techniques. While we have merely demonstrated consistency for one mineral type in one locality, similar grain size-stress relationships occur in other minerals (e.g. olivine, feldspar, calcite, ice, salt), offering potential for making accurate, small-scale observation of stress histories in a variety of geologic materials. We encourage further tests of paleopiezometry in quartz and other minerals under natural conditions, and envision eventual routine calibration and testing of numerical models of lithospheric deformation based on analysis of the rock record.

FIGURE AND TABLE CAPTIONS

Figure 1. A: Map of Taiwan showing the Hsüehshan range (HR), Luzon volcanic arc (LV), study area, and plate convergence vector (*Sella et al.*, 2002). B: Map of the study area showing sample localities and major structures. C: Cross section showing major structures, foliation measurements, strain ellipses in slate (*Tillman and Byrne*, 1995), and our foliation measurements in quartzite. D: Grain size data and corresponding stress estimates plotted relative to position on cross section. Data points associated with good temperature constraints are enlarged. E: Summary of temperature constraints. Raman spectroscopy of carbonaceous material ("RSCM," *Beyssac et al.*, 2007) serves as a peak temperature constraint; titanium-in-quartz temperature estimates (*Chapter 1*) are deformation temperatures based on the Ti concentration of “late” recrystallized grains (note that the temperatures in chapter 1 are updated and slightly modified from those presented here). The grey-shaded field summarizes deformation-temperature constraints for late deformation (chapter 1).

Figure 2. Microphotographs of Paileng formation quartzite. A: quartz grains in sample 002. Diagenetic overgrowths (OG) are visible on a number of grains, often showing planar growth features. Undulose extinction is limited to the grain in the lower left and it’s overgrowth (labeled), possibly indicating minor post-depositional deformation. B: Typical dynamic recrystallization in western Hsüehshan range (vein sample 003). Recrystallization is limited to very small grains along grain boundaries in larger grains. Grain boundary bulging ("b") and subgrains (s) have similar grain size as fully recrystallized grain ("r"). Recrystallized grain size ~5 µm.

Figure 3. A: Cross-polarized microphotograph of quartzite sample 148d showing recrystallization due to “early” high temperature deformation. The image is oriented perpendicular to bedding (So) and vertical foliation (S1). A similar recrystallized grain and subgrain size (~130 µm) and shape preferred orientation is shared by ~12 detrital grains (outlined in white) demonstrating that the foliation and recrystallization post-dates collision. Inset in upper left shows location of (B). B: Close up of (a) showing late dynamically recrystallized grains (“r” grain size ~13), subgrains “s” and grain boundary bulging “b”.

Figure 4. Vein swarm in a quartzite from the core of a small anticline in the Tachien sandstone (sample 004 location). Multiple generations of veins crosscut one another. All the veins are dynamically recrystallized (see microphotograph in *Chapter 1*). Recrystallized grain size reflects stress conditions at the brittle-ductile transition. Titanium-in-quartz thermometry indicates vein emplacement at 260–300°C.

Figure 5. Arrhenius plot showing our temperature and stress data for samples with well-constrained temperature. Data with error bars are titanium-in-quartz measurements. The ranges indicated in blue are for samples with minimum and maximum temperature constraints (low temperature samples from the western Hsüehshan range, and two high temperature samples from the Tachien anticline). Error bars on the vertical axis are negligible on this plot. The slope of the line through the data equals Q/nR if strain rate was constant for the various samples (Equation 2).

Figure 6. Stres–depth diagram showing results for samples with good temperature constraints and independent constraints. Black dots are Titanium-in-quartz temperature estimates with 2s standard errors. Error bars without dots represent data with only minimum and maximum temperature constraints: high stress data use a minimum temperature estimate of 250°C required for dynamic recrystallization and a maximum of temperature of 290–300°C based on stratigraphic constraints and unpublished Raman spectroscopy of carbonaceous material (RSCM) data (Beyssac, personal communication). The two low-stress data use an RSCM peak temperature constraint and a minimum constraint of 400°C (*Chapter 1*). Also shown are predictions of widely used flow laws (*Greg Hirth et al.*, 2001; *Paterson and Luan*, 1990), plotted over the estimated strain rates from the Tachien anticline, critical taper results from Suppe (2007), and three stress constraints from calcite twinning (*Lacombe*, 2001). Larger black circles are Tachien anticline samples. Our preferred strength envelope is shown as a thick black line. Byerlee's law, coefficients of friction (μ), and Goetze's criterion are plotted assuming hydrostatic fluid pressure. Our data and the flow laws are plotted assuming a 25 °/km geotherm.

Figure 7. Alternative strength profile scenarios discussed in the text (thick dark lines), fields defined by our paleopiezometric data (dark grey), maximum integrated crustal strength based on potential energy (light grey), Byerlee's law (kinked black line), and various values of μ (thin lines). The curved portion of the strength profiles is a fit through the paleopiezometric data of the Hirth et al. (1995) flow law corresponding to a strain rate of 2×10^{-14} s^{-1}. A: "preferred" strength profile assuming that peak stresses in recrystallized quartz represent peak crustal stresses. B: Strength profile based on Byerlee's law and a quartzite flow law fit through our data. The integrated crustal strength for profile B exceeds the maximum potential energy constraint (area shown in light grey). C: Same profile as shown in profile B, but truncated at a stress of 240 MPa in order to satisfy the potential energy constraint. D: Strength profile constructed as profile A, but assuming a geothermal gradient of 18 °/km. Brittle portion corresponds to $\mu = 0.3$.

REFERENCES

Austin, N. J., and B. Evans (2007), Paleowattmeters: A scaling relation for dynamically recrystallized grain size, *Geology*, *35*(4), 343-346.

Austin, N. J., and B. Evans (2009), The kinetics of microstructural evolution during deformation of calcite, *Journal of Geophysical Research*, *114*(B09402), doi:10.1029/2008JB006138.

Behr, W. M., and J. P. Platt (2011), A naturally constrained stress profile through the middle crust in an extensional terrane, *Earth and Planetary Science Letters*, *303*(3-4), 181-192, doi:10.1016/J.Epsl.2010.11.044.

Beyssac, O., M. Simoes, J. P. Avouac, K. A. Farley, Y.-G. Chen, Y.-C. Chan, and B. Goffé (2007), Late Cenozoic metamorphic evolution and exhumation of Taiwan, *Tectonics*, *26*(6), 1-32.

Bloomfield, J. P., and S. J. Covey-Crump (1993), Correlating mechanical data with microstructural observations in deformation experiments on synthetic two-phase aggregates, *Journal of Structural Geology*, *15*(8), 1007-1019.

Bürgmann, R., and G. Dresen (2008), Rheology of the lower crust and upper mantle: Evidence from rock mechanics, geodesy, and field observations, *Annu. Rev. Earth Planet. Sci.*, *36*, 531-567, doi:10.1146/annurev.earth.36.031207.124326.

Burov, E. B., and A. B. Watts (2006), The long-term strength of continental lithosphere: "jelly sandwich" or "crème brûlée", *GSA Today*, *16*(1), 4-10.

Byerlee, J. (1978), Friction of Rocks, *Pure and Applied Geophysics*, *116*(4-5), 615-626.

Byrne, T., Y. C. Chan, R.-J. Rau, C. Y. Lu, Y.-H. Lee, and Y.-J. Wang (2011), The Arc-Continent Collision in Taiwan, in *Arc-Continent Collision*, edited by D. Brown and P. D. Ryan, pp. 213-245, Springer-Verlag, Berlin Heidelberg, doi:10.1007/978-3-540-88558-0_8.

Carena, S., J. Suppe, and H. Kao (2002), Active detachment of Taiwan illuminated by small earthquakes and its control of first-order topography, *Geology*, *30*(10), 935-938.

Chan, Y.-C., K. Okamoto, T.-F. Yui, Y. Iizuka, and H.-T. Chu (2005), Fossil fluid reservoir beneath a duplex fault structure within the Central Range of Taiwan: implications for fluid leakage and lubrication during earthquake rupturing process, *Terra Nova*, *17*(6), 493-499, doi:10.1111/j.1365-3121.2005.00636.x.

Chew, D. M. (2003), An Excel spreadsheet for finite strain analysis using the R-f/phi technique, *Comput Geosci-Uk*, *29*(6), 795-799, doi:10.1016/S0098-3004(03)00027-X.

Clark, M. B., D. M. Fisher, C.-Y. Lu, and C.-H. Chen (1993), Kinematic analyses of the Hsüehshan range, Taiwan: A large-scale pop-up structure, *Tectonics*, *12*(1), 205-217.

Etheridge, M. A., and J. C. Wilkie (1981), An assessment of dynamically recrystallized grain-size as a paleopiezometer in quartz-bearing mylonite zones, *Tectonophysics*, *78*(1-4), 475-508.

Exner, H. E. (1972), Analysis of grain- and particle-size distributions in metallic materials, *International Metallurgical Reviews*, *17*, 25-42.

Fisher, D. M., C.-Y. Lu, and H. T. Chu (2002), Taiwan Slate Belt: Insights into the ductile interior of an arc-continent collision, in *Geology and Geophysics of an Arc-Continent Collision, Taiwan*, edited by T. Byrne and C. S. Liu, pp. 93-106, Geological Society of America Special Paper 358, Boulder, Colorado.

Gleason, G. C., and J. Tullis (1995), A flow law for dislocation creep of quartz aggregates determined with the molten salt cell, *Tectonophysics*, *247*, 1-23.

Gourley, J. R., T. Byrne, Y.-C. Chan, F. Wu, and R.-J. Rau (2007), Fault geometries illuminated from seismicity in central Taiwan: Implications for crustal scale structural boundaries in the northern Central Range, *Tectonophysics*, *445*(3-4), 168-185, doi:10.1016/j.tecto.2007.08.013.

Hacker, B. R., A. Yin, J. M. Christie, and G. A. Davis (1992), Stress magnitude, strain rate, and rheology of extended middle continental-crust inferred from quartz grain sizes in the Whipple Mountains, California, *Tectonics*, *11*(1), 36-46.

Hirth, G., and D. L. Kohlstedt (1995), Experimental constraints on the dynamics of the partially molten upper mantle. Deformation in the diffusion creep regime, *Journal of Geophysical Research*, *100*, 15441-15449.

Hirth, G., C. Teyssier, and W. Dunlap (2001), An evaluation of quartzite flow laws based on comparisons between experimentally and naturally deformed rocks, *International Journal of Earth Sciences (Geol Rundsch)*, *90*, 77-87.

Ho, C. S. (1988), *An introduction to the geology of Taiwan: explanatory text of the geologic map of Taiwan*, 2nd ed., xiii, 192 p., 120 p. of plates pp., Central Geological Survey, Ministry of Economic Affairs, Taipei, Taiwan, Republic of China.

Jackson, J. (2002), Strength of the continental lithosphere: Time to abandon the jelly sandwich?, *GSA Today*, *12*(9), 4-10.

Kaus, B. J. P., Y. Liu, T. W. Becker, D. A. Yuen, and Y. Shi (2009), Lithospheric stress-states predicted from long-term tectonic models: Influence of rheology and possible application to Taiwan, *Journal of Asian Earth Sciences*, *36*(1), 119-134, doi:10.1016/j.jseaes.2009.04.004.

Kaus, B. J. P., C. Steedman, and T. W. Becker (2008), From passive continental margin to mountain belt: Insights from analytical and numerical models and application to Taiwan, *Physics of the Earth and Planetary Interiors*, *171*(1-4), 235-251, doi:10.1016/j.pepi.2008.06.015.

Kawabata, K., H. Tanaka, Y. Kitamura, and K.-F. Ma (2009), Apparent activation energy and rate-limiting process estimation from natural shale deformed by pressure solution in shallow subduction zone, *Earth and Planetary Science Letters*, *287*, 57-63.

Kenis, I., J. L. Urai, W. v. d. Zee, C. Hilgers, and M. Sintubin (2005), Rheology of fine-grained siliciclastic rocks in the middle crust—evidence from structural and numerical analysis, *Earth and Planetary Science Letters*, *233*, 351-360, doi:10.1016/j.epsl.2005.02.007.

Kim, K.-H., J.-M. Chiu, H. Kao, Q. Liu, and Y.-H. Yeh (2004), A preliminary study of crustal structures in Taiwan region using receiver function analysis, *Geophysical Journal International*, *159*, 146-164.

Kohlstedt, D. L., B. Evans, and S. J. Mackwell (1995), Strength of the lithosphere–constraints imposed by laboratory experiments, *J Geophys Res-Sol Ea*, *100*(B9), 17587-17602.

Kuster, M., and B. Stöckhert (1998), High differential stress and sublithostatic pore fluid pressure in the ductile regime — microstructural evidence for short-term post-seismic creep in the Sesia Zone, Western Alps, *Tectonophysics*, *1998*(303), 263-277.

Lacombe, O. (2001), Paleostress magnitudes associated with development of mountain belts: Insights from tectonic analyses of calcite twins in the Taiwan Foothills, *Tectonics*, *20*(6), 834-849.

Lin, A. T., A. B. Watts, and S. P. Hesselbo (2003), Cenozoic stratigraphy and subsidence history of the South China Sea margin in theTaiwan region, *Basin Research*, *15*, 453-478, doi:10.1046/j.1365-2117.2003.00215.x.

Lisle, R. J., H. E. Rondeel, D. Doorn, J. Brugge, and P. v. d. Gaag (1983), Estimation of viscosity contrast and finite strain from deformed elliptical inclusions, *Journal of Structural Geology*, *5*, 603-609.

Liu, T. K., S. Hsieh, Y. G. Chen, and W. S. Chen (2001), Thermo-kinematic evolution of the Taiwan oblique-collision mountain belt as revealed by zircon fission track dating, *Earth and Planetary Science Letters*, *186*(1), 45-56.

Ludwig, K. J. (2001), Users manual for Isoplot/Ex rev. 2.49., *Berkeley Geochronology Center Special Publication No. 1a*, 56.

McIntosh, K., Y. Nakamura, T.-K. Wang, R. C. Shih, A. Chen, and C. S. Liu (2005), Crustal-scale seismic profiles across Taiwan and the western Philippine Sea, *Tectonophysics*, *401*, 23-54.

Mercier, J.-C. C., D. A. Anderson, and N. L. Carter (1977), Stress in the lithosphere: Inferences from steady state flow of rocks, *Pure and Applied Geophysics PAGEOPH*, *115*(1-2), 199-226, doi:10.1007/bf01637104.

Molnar, P., and H. Lyon-Caen (1988), Some simple physical aspects of the support, structure, and evolution of mountain belts, *Geological Society of America Special Paper*, *218*, 179-207.

Mouthereau, F., and C. Petit (2003), Rheology and strength of the Eurasian continental lithosphere in the foreland of the Taiwan collision belt: Constraints from seismicity, flexure, and structural styles, *J Geophys Res-Sol Ea*, *108*(B11), doi:10.1029/2002JB002098.

Passchier, C. W., and R. A. J. Trouw (2005), *Microtectonics, 2nd edition*, Springer-Verlag, Berlin Heidelberg.

Paterson, M. S., and F. C. Luan (1990), Quartzite rheology under geological conditions, *Deformation mechanisms, rheology and tectonics*, 299-307.

Poirier, J. P. (1985), *Creep of crystals: high-temperature deformation processes in metals, ceramics, and minerals*, 260 pp., Cambridge University Press.

Ramsay, J. G. (1967), *Folding and Fracturing of Rocks*, 568 pp., McGraw-Hill, New York.

Scholz, C. H. (2002), *The Mechanics of Earthquakes and Faulting*, Cambridge Univ. Press, New York.

Sella, G. F., T. H. Dixon, and A. L. Mao (2002), REVEL: A model for Recent plate velocities from space geodesy, *J Geophys Res-Sol Ea*, *107*(B4), -, doi:10.1029/2000jb000033.

Shih, R. C., C. H. Lin, H. L. Lai, Y. H. Yeh, B. S. Hwang, and H. Y. Yen (1998), Preliminary crustal structures across central Taiwan from modeling of the onshore-offshore wideangle seismic data, *TAO*, *9*, 317-328.

Shin, T. C. (1992), Some implications of Taiwan tectonic features from the data collected by the Central Weather Bureau Seismic Network, *Meteorological Bulletin of the Central Weather Bureau*, *38*, 23-48 (in Chinese).

Simoes, M., and J. P. Avouac (2006), Investigating the kinematics of mountain building in Taiwan from the spatiotemporal evolution of the foreland basin and western foothills, *Journal of Geophysical Research*, *111*(B10), 1-25.

Simoes, M., J. P. Avouac, O. Beyssac, B. Goffé, K. A. Farley, and Y.-G. Chen (2007), Mountain building in Taiwan: A thermokinematic model, *Journal of Geophysical Research*, *112*(B11), 1-25.

Simoes, M., O. Beyssac, and Y.-G. Chen (2012), Late Cenozoic metamorphism and mountain building in Tawain: a review, *Journal of Asian Earth Sciences*, *In Press*.

Stipp, M., and J. Tullis (2003), The recrystallized grain size piezometer for quartz, *Geophysical Research Letters*, *30*(21), doi:10.1029/2003GL018444.

Stockhert, B., M. R. Brix, R. Kleinschrodt, A. J. Hurford, and R. Wirth (1999), Thermochronometry and microstructures of quartz - a comparison with experimental flow laws and predictions on the temperature of the brittle-plastic transition, *Journal of Structural Geology*, *21*(3), 351-369.

Suppe, J. (2007), Absolute fault and crustal strength from wedge tapers, *Geology*, *35*(12), 1127-1130.

Suppe, J., and J. H. Wittke (1977), Abnormal pore-fluid pressures in relation to stratigraphy and structure in the active fold-and-thrust belt of northwestern Taiwan, *Petroleum Geology of Taiwan*, *14*, 11-24.

Tillman, K. S., and T. B. Byrne (1995), Kinematic Analysis of the Taiwan Slate Belt, *Tectonics*, *14*(2), 322-341.

Tillman, K. S., T. B. Byrne, and C.-Y. Lu (1992), Pre-collision extensional structures from the central range, Taiwan: implications for the kinematic evolution of the South China Margin, *Acta Geologica Taiwanica*, *30*, 11-26.

Townend, J., and M. D. Zoback (2000), How faulting keeps the crust strong, *Geology*, *28*(5), 399-402.

Trepmann, C. A., and B. Stockhert (2009), Microfabric of folded quartz veins in metagreywackes: dislocation creep and subgrain rotation at high stress, *Journal of Metamorphic Geology*, *27*, 555-570.

Tullis, J., and R. A. Yund (1982), Grain growth kinetics of quartz an calcite aggregates, *Journal of Geology*, *90*(3), 301-318.

Twiss, R. J. (1977), Theory and applicability of a recrystallized grain size paleopiezometer, *Pure and Applied Geophysics*, *115*, 225-244.

Ustaszewski, K., Y.-M. Wu, J. Suppe, H.-H. Huang, C.-H. Huang, and S. Carena (in press), Crust-mantle boundaries in the Taiwan–Luzon arc-continent collision system determined from layered Vp models and local earthquake tomography, *Tectonophysics*.

Wightman, R., D. Prior, and T. Little (2006), Quartz veins deformed by diffusion creep-accommodated grain boundary sliding during a transient, high strain-rate event in the Southern Alps, New Zealand, *Journal of Structural Geology*, *28*(5), 902-918, doi:10.1016/j.jsg.2006.02.008.

Yamato, P., F. Mouthereau, and E. Burov (2009), Taiwan mountain building: insights from 2-D thermomechanical modelling of a rheologically stratified lithosphere, *Geophysical Journal International*, *176*(1), 307-326, doi:10.1111/j.1365-246X.2008.03977.x.

Yen, T. P. (1973), The Eocene sandstones in the Hsüehshan range terrain, Northern Taiwan, *Proceedings of the Geological Society of China*, *16*, 97-110.

Yue, L.-F. (2007), Active structural growth in central Taiwan in relationship to large earthquakes and pore-fluid pressures, Princeton University, Princeton, NJ.

Zhou, D., H.-S. Yu, H.-H. Xu, X.-B. Shi, and Y.-W. Chou (2003), Modeling of thermo-rheological structure of lithosphere under the foreland basin and mountain belt of Taiwan, *Tectonophysics*, *374*(3-4), 115-134, doi:10.1016/s0040-1951(03)00236-1.

Figure 1

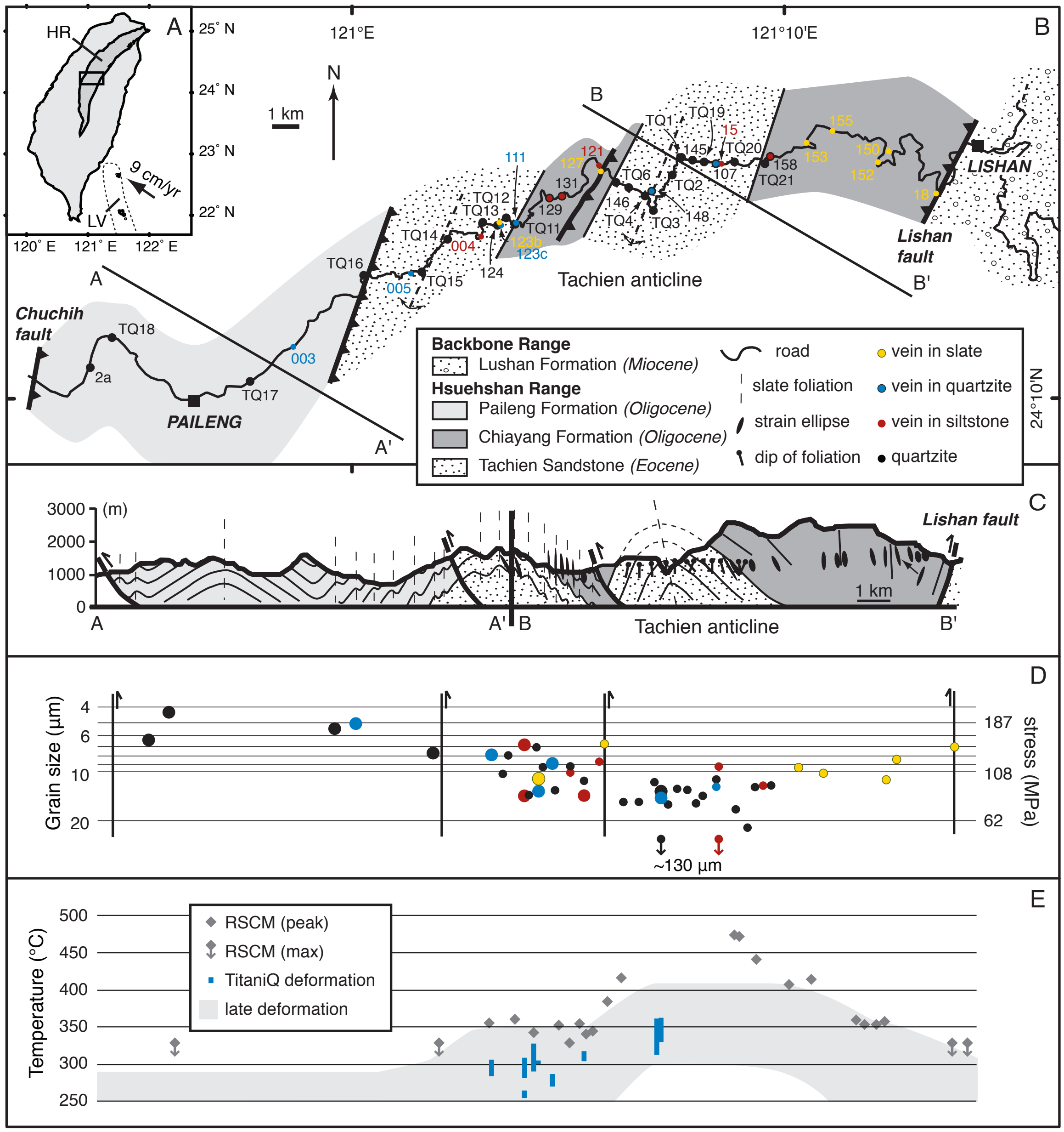
A
HR
LV
9 cm/yr
25° N
24° N
23° N
22° N
120° E
121° E
122° E
B
121°E
121°10'E
24°10'N
N
1 km
Chuchih fault
PAILENG
LISHAN
Lishan fault
Tachien anticline
TQ18
2a
TQ17
003
TQ16
005
TQ15
TQ14
004
TQ13
TQ12
124
111
TQ11
123b
123c
127
121
131
129
TQ6
146
TQ4
TQ3
148
TQ2
TQ1
TQ19
15
145
107
TQ20
158
TQ21
153
155
150
152
18
A
A'
B
B'
Backbone Range
Lushan Formation (Miocene)
Hsuehshan Range
Paileng Formation (Oligocene)
Chiayang Formation (Oligocene)
Tachien Sandstone (Eocene)
road
slate foliation
strain ellipse
dip of foliation
vein in slate
vein in quartzite
vein in siltstone
quartzite
C
3000
2000
1000
0
(m)
Lishan fault
1 km
A
A'
B
Tachien anticline
B'
D
Grain size (µm)
4
6
10
20
187
108
62
stress (MPa)
~130 µm
E
Temperature (°C)
500
450
400
350
300
250
RSCM (peak)
RSCM (max)
TitaniQ deformation
late deformation

Figure 2

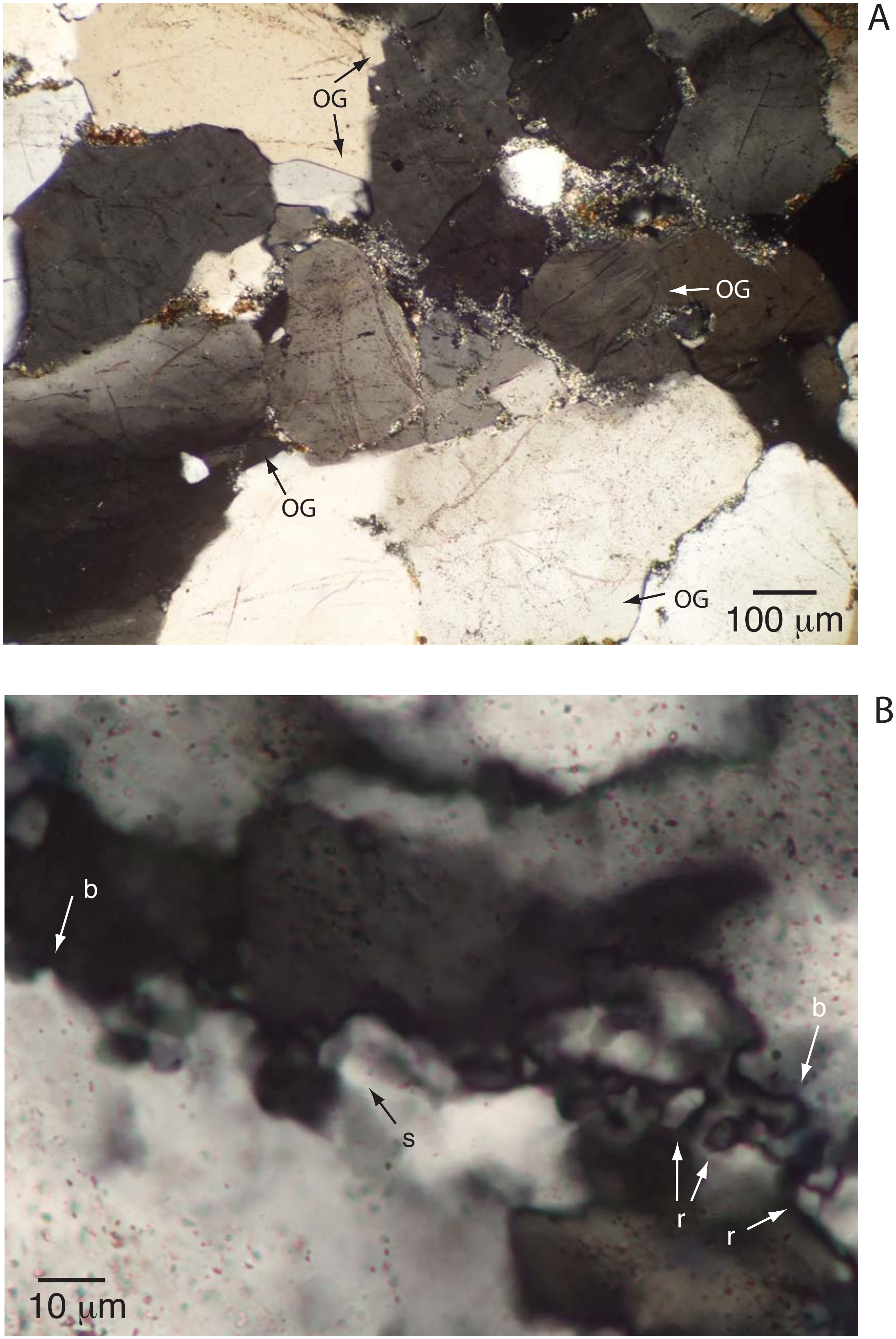

Figure 3

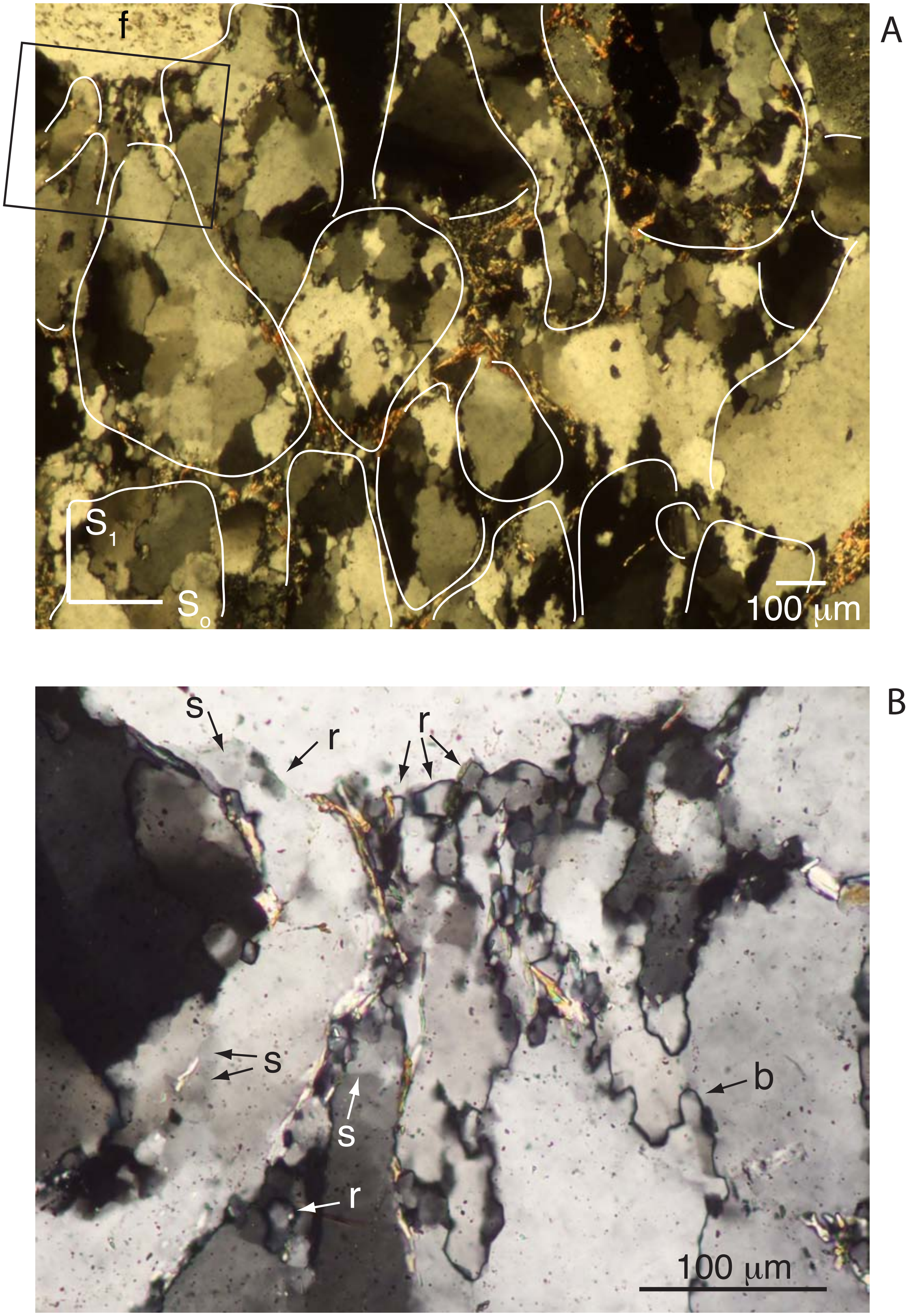

Figure 4

Figure 5

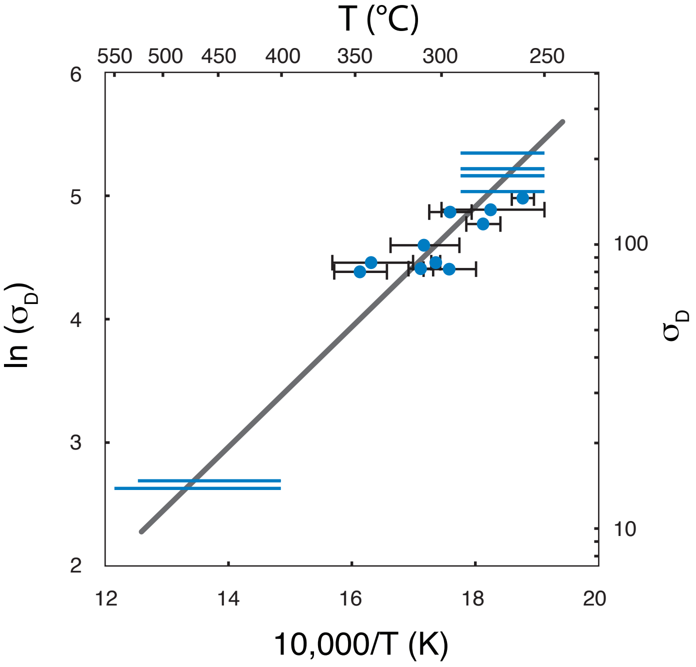
T (°C)
550
500
450
400
350
300
250
6
5
4
3
2
ln (σ_D)
100
10
σ_D
12
14
16
18
20
10,000/T (K)

Figure 6

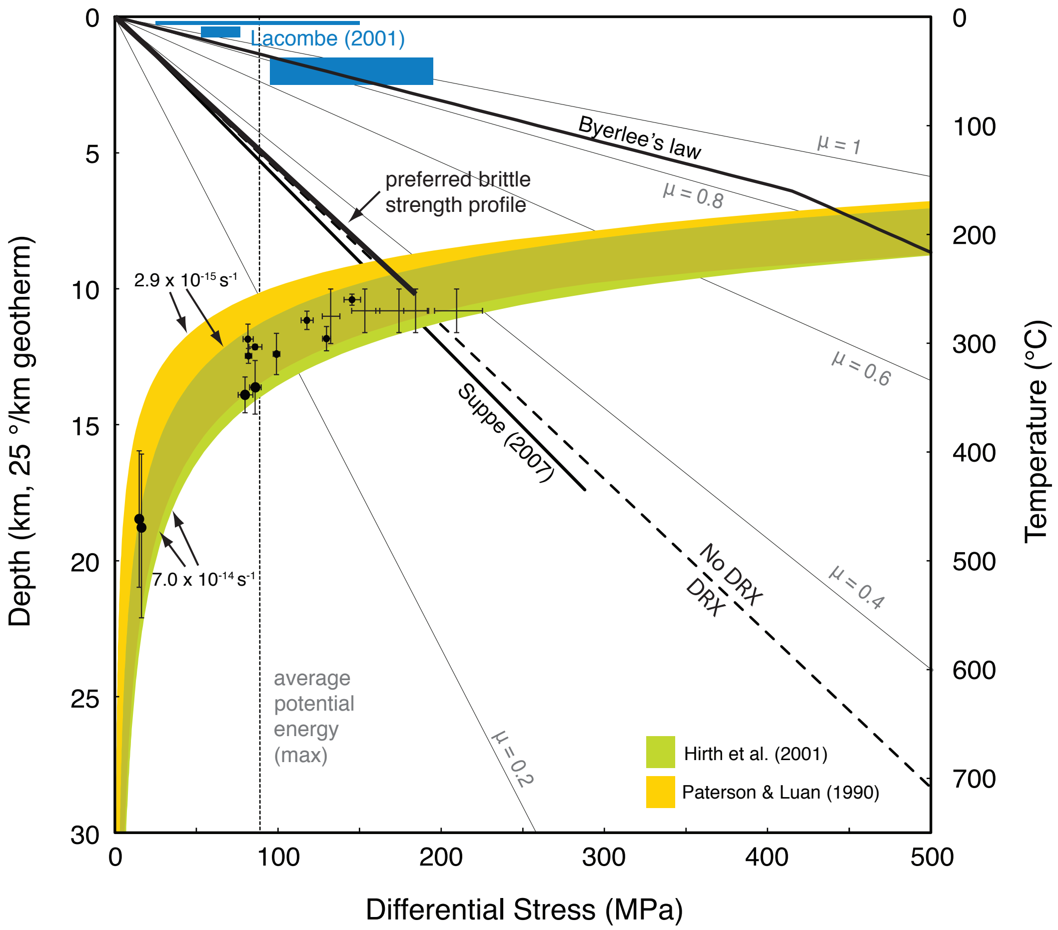
Lacombe (2001)
Byerlee's law
μ = 1
μ = 0.8
μ = 0.6
μ = 0.4
μ = 0.2
preferred brittle strength profile
2.9 x 10⁻¹⁵ s⁻¹
7.0 x 10⁻¹⁴ s⁻¹
Suppe (2007)
No DRX
DRX
average potential energy (max)
Hirth et al. (2001)
Paterson & Luan (1990)
Depth (km, 25 °/km geotherm)
0
5
10
15
20
25
30
Temperature (°C)
0
100
200
300
400
500
600
700
Differential Stress (MPa)
0
100
200
300
400
500

Figure 7

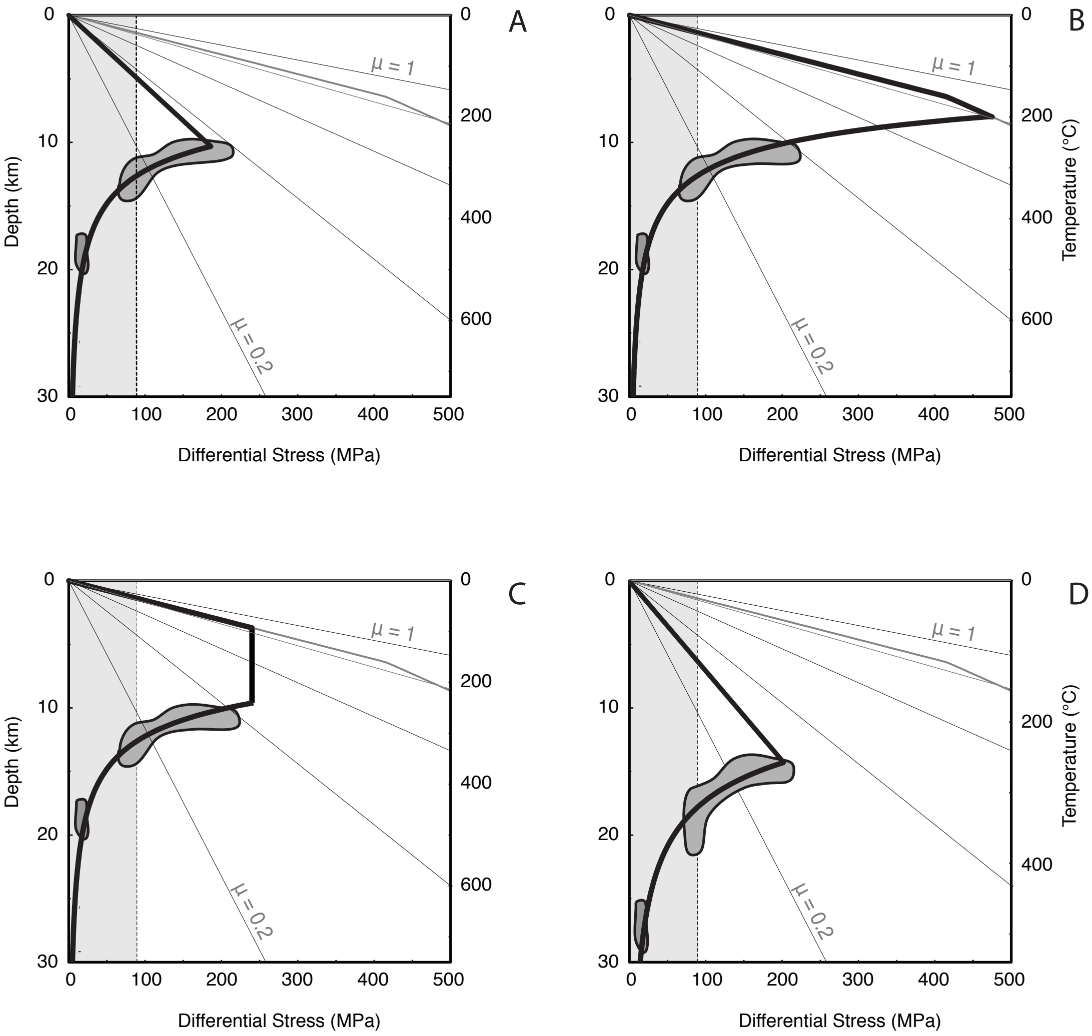
A
0
10
20
30
Depth (km)
0
200
400
600
μ = 1
μ = 0.2
0
100
200
300
400
500
Differential Stress (MPa)
B
0
10
20
30
0
200
400
600
Temperature (°C)
μ = 1
μ = 0.2
0
100
200
300
400
500
Differential Stress (MPa)
C
0
10
20
30
Depth (km)
0
200
400
600
μ = 1
μ = 0.2
0
100
200
300
400
500
Differential Stress (MPa)
D
0
10
20
30
0
200
400
Temperature (°C)
μ = 1
μ = 0.2
0
100
200
300
400
500
Differential Stress (MPa)

Table 1. Sample locations, stress measurements, and temperature constraints

sample	type[a]	easting[b]	northing[b]	g.s.[c]	1σ	N	stress[d]	+/- SE[e]	T (°C)[f]	SE[g]
002a	q	240222	2674693	6.4	2.3	104	153.5	4.4/4.2	<290	-
003	vq	247068	2675111	5.1	1.4	108	184.6	3.9/3.7	<290	-
4r2v2	vl	255063	2680085	6.8	1.5	102	145.7	2.6/2.5	259.8	2.5
4r345v2	vl	255063	2680085	14.1	3.4	101	81.9	1.6/1.5	295.95	6.9
005rp	vq	252309	2678535	7.9	1.0	115	130.0	1.3/1.2	295.5	5.6
15d	vl	264035	2682791	9.3	2.0	119	113.8	1.8/1.7	-	-
15dcrs	vl	264035	2682791	132.3	19.5	96	13.9	0.2/0.2	400-525	-
18c	vs	272472	2681848	7.0	3.1	117	142.1	4.8/4.4	-	-
107a	vq	263936	2682918	12.4	3.0	102	90.8	1.8/1.7	-	-
107b	q	263936	2682918	11.2	2.4	100	98.6	1.7/1.7	-	-
111br	vq	256048	2680584	8.9	1.8	102	118.0	1.9/1.8	278.7	4.2
121	vl	259460	2682666	8.7	1.9	108	120.3	2/1.9	-	-
123br	vs	255731	2680458	11.1	1.6	125	99.4	1/1	309.55	9.5
123cr	vq	255731	2680458	13.2	3.9	101	86.3	2/1.9	303.1	1.2
124f	q	255644	2680395	7.1	1.9	131	141.4	2.6/2.5	-	-
127b&c	vs	259507	2682469	6.8	2.3	140	146.9	3.4/3.2	-	-
129b	q	257529	2681538	9.3	2.7	104	114.3	2.6/2.5	-	-
129d	vl	257529	2681538	10.1	2.2	101	106.5	1.8/1.8	-	-
131b	q	258093	2681529	11.4	4.1	102	97.0	2.9/2.7	-	-
131gr	vl	258093	2681529	14.0	2.1	103	82.2	1/1	311.3	3.4
145	q	263352	2682879	15.7	4.2	109	75.2	1.6/1.5	-	-
146b	q	260673	2681855	15.4	4.4	107	76.5	1.7/1.6	-	-
148dr	q	261503	2681588	13.2	3.6	110	86.3	1.8/1.7	340.1	12.3
148dcrs	q	261503	2681588	128.2	27.2	109	14.2	0.2/0.2	400-550	-
148jr	vq	261503	2681588	14.5	5.5	115	80.1	2.3/2.2	347	8.2
150b	vs	270592	2683392	8.4	2.6	131	123.3	2.7/2.6	-	-
152b	vs	270167	2682977	11.2	1.7	109	98.2	1.1/1.1	-	-
153	vs	267395	2683616	9.4	2.2	100	112.7	2.2/2.1	-	-
155a&b	vs	268493	2684117	10.2	2.2	106	105.7	1.8/1.8	-	-
157b	q	265215	2682831	22.1	8.7	34	57.3	3.2/2.9	-	-
158b	q	265857	2683171	12.2	4.6	106	92.1	2.8/2.6	-	-
158b	vl	265857	2683171	12.2	2.7	104	91.8	1.6/1.6	-	-
TQ1	q	262746	2683033	13.0	3.5	106	87.6	1.9/1.8	-	-
TQ2	q	262327	2682370	12.8	2.8	111	88.6	1.5/1.4	-	-
TQ3	q	261709	2681214	15.9	6.5	105	74.3	2.4/2.3	-	-
TQ4	q	261397	2681612	11.6	3.9	103	95.6	2.6/2.4	-	-
TQ6	q	260122	2682121	15.4	2.2	102	76.5	0.9/0.9	-	-
TQ11	q	256407	2680543	13.0	4.4	110	87.2	2.3/2.2	-	-
TQ12	q	255907	2680623	9.4	5.5	103	113.2	5.5/4.9	-	-
TQ13	q	255085	2680460	14.0	2.2	113	82.6	1/1	-	-
TQ14	q	253739	2679923	7.9	2.5	104	129.1	3.2/3	-	-
TQ15	q	252606	2678618	10.3	4.0	103	104.9	3.3/3.1	-	-
TQ16	q	250654	2678560	7.7	2.0	106	132.6	2.8/2.6	<330	-
TQ17	q	246205	2674439	5.4	3.5	128	174.4	8.2/7.4	<290	-
TQ18	q	241051	2675978	4.3	1.9	100	209.8	7.6/7	<290	-
TQ19	q	263629	2682867	14.1	2.3	111	81.9	1/1	-	-
TQ20	q	264735	2682865	17.1	4.0	101	70.4	1.3/1.3	-	-
TQ21	q	265691	2682947	12.4	4.5	106	90.4	2.6/2.5	-	-

[a] abbreviations: q, quartzite; vq, vein in quartzite; vl, vein in metasiltstone; vs, vein in slate

[b] Taiwan grid, Hu-Tzu-Shan datum

[c] geometric mean grain size

[d] differential stress in MPa

[e] standard error of the mean

[f] temperatures reported with standard errors are TitaniQ temperatures from recrystallized collisional veins adjusted +20° based on the analysis of Kidder et al. [2012]. Other temperature constraints are discussed in the text.

[g] Reported errors exclude systematic error sources such as uncertainty in the geothermal gradient.

CHAPTER 4

A numerical model of flat subduction initiation and constraints on stress levels in the Pelona schist

Steven B. Kidder[1], Frédéric Herman[2], Jason Saleeby[1], Jean-Philippe Avouac[1], Mihai N. Ducea[3]

[1]*California Institute of Technology, Pasadena, California, United States*
[2]*ETH, Zurich, Switzerland*
[3]*University of Arizona, Tucson, Arizona, United States*

ABSTRACT

As a result of a steep inverted metamorphic field gradient, Southern California's Pelona schist has served as a classic locality where high stresses and significant shear heating have been postulated along a major geologic structure. Recent studies however have demonstrated that the Pelona schist was emplaced during the initiation of flat subduction, implying thermal and kinematic conditions not considered in earlier studies. We constructed a 2D finite element model of flat subduction initiation using geologic constraints from two localities of the Pelona schist. A model inversion, using the neighborhood algorithm of Sambridge (1999) was used to explore the influence of various parameters and to determine a range of stress values consistent with available metamorphic and thermochronologic constraints. The flat subduction initiation model reproduces available thermochronologic and metamorphic constraints without requiring high shear stresses. The inverted metamorphic field gradient and additional thermochronologic constraints can be reproduced with shear stresses less than 10 MPa, although stresses as high as 25 MPa cannot be ruled out.

INTRODUCTION

Low temperature-high pressure metamorphism is the defining feature of subducted sedimentary assemblages, and results from the flux of cold downgoing oceanic plates and their sedimentary cover beneath subduction zones. Anomalously high temperatures recorded along some subduction interfaces have been interpreted as the result of either high rates of shear heating (e.g. Graham and England, 1976), a transient thermal signature of subduction initiation (Peacock, 1987), or a combination of the two (Peacock, 1992). The Sierra Pelona exposure of southern California's Pelona schist has served as a key example of a high temperature anomaly along an exposed subduction interface. Graham and England (1976) and England and Molnar (1993), concluded that high temperatures along the interface were due to high levels of shear heating. Peacock (1992) showed that temperatures in subducting material are highest during subduction initiation, and suggested that high temperatures in the Pelona schist may be due to a combination of this and shear heating. Kidder and Ducea (2006) demonstrated that the rates of shear heating calculated by earlier workers are much higher than thought possible given the rheological properties of quartzofeldspathic rocks. Peak temperatures in the Pelona schist and analogous schist of Sierra de Salinas are 80 to 100% of upper plate temperatures (Jacobson, 1997; Kidder and Ducea, 2006). Without significant shear heating however, previously published one and two-dimensional models bring lower plate temperatures to a maximum of 60% of upper plate temperatures (Graham and England, 1976; Peacock, 1992).

Part of this discrepancy may be due to the fact that existing models of the schist (England and Molnar, 1993; Peacock, 1987, 1992) have modeled its emplacement as a steady state feature and/or as part of a normally-dipping subduction system. Kidder and Ducea (2006) proposed an alternative conceptual model based on the modern understanding of the emplacement of schist during initiation of flat subduction. This chapter presents the results of a simple 2D, kinematic-thermal model designed to investigate the thermal signature of this event. An inversion of the model allows us to explore the effects of 10 input parameters including shear stress. We find that metamorphic and thermochronologic data within and above the schist are well explained by the flat-subduction initiation model without major shear heating. The modeling additionally allows us to quantify accretion rates of the schist and address competing tectonic models for the origin of the schist.

GEOLOGIC BACKGROUND

San Gabriel Mountains

The San Gabriel Mountains comprise Proterozoic and Mesozoic crystalline rocks and two major structural windows exposing the underlying Pelona schist: the Sierra Pelona and East Fork (of San Gabriel River) exposures (figure 1). The bulk of the upper plate comprises Proterozoic amphibolite facies banded gneiss intruded by Mesozoic arc-related plutons. Late Cretaceous calc-alkaline granodiorites and tonalites, including the Josephine Mountain Intrusion with an age of 72-86 Ma (Barth et al., 1995), make up ~30% of the upper plate.

The two schist bodies lie within 100 km of one other with no major structures separating them, and have similar detrital zircon and Ar ages (Grove et al., 2003). Significant variations exist however in metamorphic and thermochronologic characteristics between the two exposures. The East Fork schist was metamorphosed to greenschist facies, a maximum of 480° (Jacobson, 1997), while the Sierra Pelona reached 620-650°C near the Vincent thrust (Graham and Powell, 1984) with greenschist facies metamorphism at lower levels. The Sierra Pelona contains an inverted metamorphic field gradient in its upper portions (figure 2), however the structure separating it from upper plate rocks has been reactivated as a low temperature normal fault. The structural thickness of exposed schist in the Sierra Pelona is ~1 km (Ehlig, 1981) and ~4 km in the East Fork. The Vincent "thrust," which separates the schist and upper plate in the East Fork locality preserves an earlier tectonic contact (Jacobson, 1997), however Behr et al. (2008) found that sufficient deformation occurred along it to impart a pervasive sense of shear in the schist and overlying rocks antithetic to the probable subduction direction. The antithetic sense of shear is common to other schist localities (e.g. Chapman, 2012) and reflects deformation conditions during exhumation.

Late Cretaceous- Early Tertiary tectonic history

The Pelona schist is one of a number of Franciscan-affinity accretionary assemblages known elsewhere as the Orocopia schist, Rand schist and Schist of Sierra de Salinas (Figure 1). This collection of schists, referred to as the “POR schist,” was emplaced beneath the southern Californian continental arc between 60 and 90 Ma (Grove et al., 2003). Emplacement of the schist began in the north and propagated ~ 500 km southward coinciding with the termination of arc magmatism. The emplacement of the POR schist well inboard of the trench coincided with the loss of the lower arc crust and lithospheric mantle. These events resulted from the same late Cretaceous slab-flattening episode associated with the Laramide Orogeny in more inland portions of North America (Saleeby, 2003). Saleeby (2003) suggested that slab flattening was due to the arrival of a conjugate of the Hess and Schatsky rise at the trench. The Hess and Schatsky rises are large oceanic plateaus formed on a ridge axis or triple junction at 148-132 Ma and 98-110 Ma respectively (Nakanishi et al., 1999; Pringle and Dalrymple, 1993). Figure 3a illustrates one scenario for the two-dimensional tectonic history of schist emplacement.

MODEL DESCRIPTION AND TECHNIQUE

Our numerical modeling uses a two dimensional modification of the finite element program Pecube (Braun, 2003) with no topography. Pecube solves the transient heat transfer equation taking into account heat production and heat transport by conduction and advection along faults. A grid spacing of 250 m in x and z directions is used in all models. The model geometry consists of a single thrust fault with ramp-flat geometry (figure 4). The fault breaks the surface near the left edge of the model, dips to the right at angle α, flattens at depth d and continues horizontally off the edge of the model (figure 4). Temperature conditions at the surface and base of the model are held constant. Temperatures at the right and left edge of the model are free to fluctuate. Particle tracers are introduced in the model in order to record the thermal and transport history of material points of interest in the upper plate and schist. An example of the thermal evolution of a single model is shown in figure 3f.

In order to better constrain stress levels, accretion rates, and emplacement histories of the schist, we ran a model inversion using the neighborhood algorithm of Sambridge (1999). Model parameters are allowed to vary within prescribed ranges, and results are tabulated and ranked according to a user-defined misfit function. Calculations on up to 200 processors were carried out on Caltech's Pangu cluster. In running the neighborhood algorithm, the user designates a proportion of exploratory models that probe the model space at random, while the remaining models use information from previous-run models to converge on combinations of parameters likely to best reduce misfit. Our primary interest was in establishing ranges of input parameters that are consistent with good models, therefore we emphasized the exploratory nature of the neighborhood algorithm rather than optimizing the parameters of the single best model. Typically, 50% of our models were exploratory. The parameters we allowed to vary are described below:

Oceanic geothermal gradient

Oceanic geothermal gradients were estimated following Turcotte and Schubert (2002) for oceanic crust of age 30-50 m.y. This age range corresponds with the age difference between the formation of the Hess and Shatsky rises, and their arrival at the California margin.

Continental geothermal gradient

Just prior to the emplacement of the schist, the western margin of North America was an active continental arc. Thermal gradients in continental arcs vary in time and are poorly constrained. Kelemen et al. (2003) summarize the results of numerous large scale models predicting temperatures at depths of 30 km between 400 and 1300 °C. In a pluton-scale model, Barton and Hanson (1989) modeled the expected metamorphic gradient in the Sierra Nevada batholith resulting from the repeated intrusion of granitic rocks. They suggest a maximum temperature of ~750°C at 30 km. A final temperature constraint of 800-950°C at 30 km is based on pressure-temperature estimates from lower crust xenoliths found in the Sierra Nevada. The San Gabriel Mountains contain a smaller volume of Mesozoic intrusions than the Sierra Nevada, suggesting lower temperatures in the San Gabriel Mountains than recorded in the xenoliths. We allowed initial temperature at 30 km to range between 450 and 700 °C. The shape of the geotherm above and below 30 km in our model follows Turcotte and Schubert's (2002) oceanic crust geotherm calculations.

Convergence rate

We allowed convergence rates to vary between 80 and 130 km/m.y. in accordance with estimated Late Cretaceous convergence rates (see references in Saleeby, 2003).

Radiogenic Heating

Brady et al. (2006) measured the concentration of heat producing elements in a variety of exposures from various depths in the Southern Californian arc. We use their best-fit heat production profile and allow it to vary 50% more and less than the estimated values.

Accretion rate and accretion zone width

The accretion rate is the rate at which material is transferred from the lower plate to the upper plate in the accretion zone (figure 4). We allowed accretion rate to reach as high as 10 km/m.y. A width of the zone of accretion of ~75 km is suggested by a lower-crustal seismic anisotropy attributed to the schist (Porter et al., 2011). We allowed accretion zone width to vary between 0 and 150 km.

Trench-arc distance

The trench-arc distance in the model is the width at the surface of the model of the stationary portion separating the downgoing plate from the accretion zone (figure 4). A distance of 200-300 km is typical of modern trench-arc distances as well as the present-day distance between the Franciscan complex and Sierra Nevada batholith in the Great Valley (figure 1). During the flat subduction initiation we model here, the trench-arc distance must have shortened somewhat in order to subduct the Franciscan-equivalent sediments that became the schist. We allowed trench-arc distance to vary between 150 and 250 kilometers.

Decollement depth

The depth at which the subducting plate flattens in the model was allowed to vary between 20 and 40 km, consistent with available barometric estimates for the peak conditions the schist reached during metamorphism.

Shear Heating

Shear heating is introduced into the model through the relationship $Q = \tau V$, where Q = rate of shear heating, τ = shear stress, and V = slip rate. A uniform stress field is assumed throughout the model. Peacock (2003) estimated that shear stress on subducting plate interfaces averages ~10 MPa based on heat flow measurements in forearcs. Graham and England (1976) and England and Molnar (1993) estimated higher shear stresses for the emplacement of the Pelona schist of up to 100 MPa. We allowed shear stress to vary between 0 and 100 MPa.

Models constraints

Thermochronologic and metamorphic data for the Pelona schist and overlying "upper plate" rocks are shown in figure 2 and include Ar/Ar and K/Ar cooling ages for hornblende, muscovite, potassium feldspar and biotite (Grove and Lovera, 1996; Jacobson, 1990; Miller and Morton, 1980). In order to test the degree to which model runs reproduce the constraints, the thermochronologic and metamorphic data were simplified to six constraints shown as open symbols in figure 2: 1) cooling age of a point ~10 km above the Vincent thrust through the low temperature end (~150°C) of multiple diffusion domain modeling age for potassium feldspar; 2) timing of cooling through ~300 °C at 1 km, and 3) 7 km above the Vincent thrust; 4) the timing of cooling through the Ar/Ar closure temperature for hornblende of ~500°C; 5) the peak recorded temperature in the schist at a structural depth of 200 m; and 6) the peak recorded temperature in the schist at a structural depth of 650 m. Following a model run, results were compared to the available constraints and the model was assigned a misfit value based on the agreement between the model and the six constraints. Low values correspond to a model run well-matching input constraints. The various constraints are weighted relative to one another based on geologic intuition, thus the numerical value of the misfit is necessarily qualitative.

Sierra Pelona Model

Temperatures at the Vincent "thrust" in the Sierra Pelona are estimated at 635° ± 15 and decrease at 240 ± 40°/km to 480° at a depth of 600-700 m below the thrust (Graham and Powell, 1984).

Detrital zircons ages and Ar/Ar cooling ages indicate a gap in time of 10 m.y. between crystallization of the youngest zircon at 68 Ma and schist cooling through muscovite closure temperature at 58 Ma.

East Fork Model

The schist exposure in the East Fork of the San Gabriel River is entirely within the greenschist facies and contains no detectable inverted geothermal gradient. Peak temperature apparently reached only 460°. There is a 6.4 m.y. gap between a youngest detrital zircon age of 69 Ma and upper plate cooling through muscovite closure temperature at 62.6 Ma. Difference in Ar/Ar age between various mineral pairs ~10 and ~3.5 km above the decollement indicate upper plate cooling rates of ~15°/m.y. (Jacobson, 1990; Mahaffie and Dokka, 1986; Miller and Morton, 1977). The gradient of upper plate cooling ages is ~1 m.y./km. There is a gap of ~10 m.y. between youngest detrital zircon ages and mica cooling ages in the schist, placing a minimum cooling rate at high temperatures in the schist of ~28.5°/m.y. We ignore three argon ages in hornblende in the schist as they do not show good plateaus or are older than deposition.

Combination Model

Models were run using a combination of constraints from the Sierra Pelona and East Fork localities. The assumption is that both bodies were emplaced under the same conditions, as suggested by their close proximity, compositional similarities, structural position, and detrital zircon characteristics. The main differences between the two localities are the high density of thermochronologic data available for the East Fork exposure, the high metamorphic grade and inverted metamorphic field gradient in the uppermost 700 m of the Sierra Pelona exposure, and the late deformation overprinting the contact in the Sierra Pelona. For the combination model, we combine the thermochronologic constraints for the East Fork exposure with the metamorphic constraints from the Sierra Pelona. We assume that the upper portion of the East Fork section was cut out of the section after emplacement.

Combination Model, no zircon

Further combination models were run using the available constraints from both the Sierra Pelona and East Fork localities, but excluding the detrital zircon constraints.

RESULTS

Results for the four model families are shown in figures 5, 6, 7, and 8. Individual models in these figures are represented by circles filled with a color corresponding to the misfit of the model. Models colored in blue fit independent constraints well. Models in yellow and red have high misfits and therefore combinations of input parameters that do not reproduce available constraints well.

Many of the parameters in the models, including radiogenic heating, trench-arc distance, ocean crust age and width of accretion zone are essentially unconstrained by our modeling. We find models with good fits that span the entire range of input values for these constraints (figures 5, 6, 7, and 8). The misfit is sensitive to shear stress and accretion rate (e.g. figures 5 and 6). No models with shear stress above ~50 MPa provide a good fit to the data. Accretion rates above 2 km/m.y. are not permitted by the results of the inversions.

The best-fitting model has a shear stress of 11.7 MPa, a trench-arc distance of 167 km, a decollement depth of 31.7 km, a convergence rate of 120 km/m.y., a temperature at the base of the model of 1300, an accretion rate of 0.8 km/m.y., an accretion zone width of 121.8 km, an oceanic age of 35 m.y., a continental arc “age” of 24.4, and heat production 13% higher than estimated by Brady et al. (2006). Thermochronologic and metamorphic constraints from this model are shown in figure 2.

DISCUSSION

Constraints on stress state

The model demonstrates that high stresses are not required to explain the inverted metamorphic gradient in the Pelona schist as previously concluded (England and Molnar, 1993; Graham and

England, 1976). In fact, the inverted metamorphic gradient in the Sierra Pelona appears to limit allowable shear stress to smaller values than in the East Fork where no inverted gradient is preserved (figures 5 and 6).

Zircon constraints

The short time interval between reported ages of youngest zircons in the schist and Ar/Ar cooling ages in the upper plate (Grove et al., 2003) provides a strong constraint on the models. As a result of this constraint, no reasonable solution was found in the inversion combining constraints for the two Pelona schist exposures (figure 7). With the detrital zircon constraint removed, models were easily found that satisfied the remaining thermochronologic and metamorphic constraints (figure 8). Chapman (2012) found that zircons in the Rand schist of the San Emigdio Mountains have clear metamorphic overgrowths associated with metamorphism of the schist. These zircons give young, metamorphic ages rather than crystallization ages. Grove et al. (2003) filtered their zircon data using trace element ratios to detect metamorphic effects, but do not report results of cathodoluminescence images of their zircons. Such images however provided crucial data in Chapman's (2012) analyses. We conclude that the youngest zircon ages provided by Grove et al. (2003) are likely to be affected by metamorphism, and that the inversion excluding the zircon constraints provides the more reliable result.

Accretion rates and origin of the schist

A universal characteristic of satisfactory models is an accretion rate of ~0.5 - 1 km/m.y., implying that the thickest exposures of schist were built over 4-8 m.y. as material was scraped off 300-600 km of subducting ocean crust. While we have assumed above that the Pelona schist originated as Franciscan-affinity sediments near the trench, two alternative models have been put forth for the tectonic origin of the schist (Haxel et al., 2002): 1) the schist was deposited in transpressive basins, a modern example being the Salton trough, and 2) the schist represents the underthrust equivalent of the Great Valley sequence. In both of these alternative models, basin widths are ~100 km or smaller. However, at the accretion rates constrained by the model inversion, ~4 m.y. are required to accrete the observed thickness of schist. At modeled convergence rates of 100 km/m.y., this would involve at least 400 km of shortening. This line of reasoning may present a problem for the small basin origin hypotheses. We did not explicitly explore the possibility however that while upper levels of the schist accreted via a mechanism such as that proposed here, the lower portion may have accreted *en masse*. This idea is consistent with the observation of Chapman et al (2010), that be the proportion of coaxial to noncoaxial strain increases with depth, while overall strain decreases. This possibility, and other insights into schist origin, could be explored by a detailed study of detrital zircon characteristics at different levels in the schist.

Model limitations

While the simplicity of the model allows for a powerful exploration of the specified parameter space, it also limits its capabilities. We note, for example, that only simple shear is permitted in the model. Another limitation is the model's inability to permit return flow. The sense of shear generally recorded in the schists is opposite of that implied by our model (e.g. Chapman et al., 2010), indicating that the schist first traveled further inboard than its present location, then via return flow or extrusion was brought back its present position. Our model instead assumes the shortest path for the schist between the trench and current location.

The nature of the neighborhood algorithm, and inverse methods in general, results in an additional limitation: the difficulty in proving a negative. By choosing a high proportion of exploratory models in each run, our hope was to detect good combinations of parameters that fall outside of the misfit "valley" associated with the best models. We cannot, however, prove that some unexplored corner of the model does not have a low misfit. The method is, however, a vast improvement over the general modeling practice of manually determining only a handful of "good" models.

CONCLUSIONS

1) A model of flat subduction initiation can reproduce available thermochronologic and metamorphic constraints for both the East Fork and Sierra Pelona localities of the Pelona schist.
2) No acceptable models were found when combining constraints from both localities, unless detrital zircon constraints are relaxed. Youngest zircon ages in the Pelona schist are probably affected by metamorphic overgrowths.
3) High shear stresses are not required to explain the sharp inverted gradient in the Sierra Pelona exposure of the Pelona schist. The gradient can be reproduce with shear stresses less than 10 MPa, although stresses as high as 25 MPa can not be ruled out.
4) Accretion rates of the schist were ~0.5-1 km/m.y., implying that the thickest exposures of schist were built over 4-8 m.y. as material was scraped off 300-600 km of subducting ocean crust. Alternative conceptual models positing a schist origin in a narrow marginal basin are unlikely.

FIGURE CAPTIONS

Figure 1. Map of Southern California and parts of Arizona, Sonora, and Baja California showing Pelona and related schists in blue. Mesozoic plutonic rocks in dark grey.

Figure 2. Thermochronologic and metamorphic constraints. Filled symbols are data from the literature, open symbols are model results. A: Thermochronologic data from near the East Fork exposure of the Pelona schist. Ages are plotted versus estimated structural depth relative to the Vincent thrust. Mineral abbreviations: hbl, hornblende; ms, muscovite; kfs, potassium feldspar; bt, biotite. Data are separated by the grey field into temperature domains. The grey field indicates ages of cooling through ~300°C. B: Metamorphic constraints on schist temperature in the Sierra Pelona. The model results shown are for the best fitting model combining constraints for both the schist and upper plate.

Figure 3. Cartoon representation of schist emplacement. A: Normal subduction, with approaching overthickened oceanic crust. B: Early arc detritus (future schist) deposited in trench, and subducted during slab flattening. C: Accretion and extension begin, upper plate cools through 500 °C, uppermost schist metamorphosed at peak conditions. D: Lower portions of schist are accreted, exhumation imparts a sense of shear antithetic to subduction. E: Schist is juxtaposed against current upper plate exposures. F: Thermal evolution from a model showing upper plate and schist tracers. The time sequence roughly corresponds to the evolution depicted in A-E.

Figure 4. Model kinematics showing velocity vectors for a typical model.

Figure 5. Results from 39,500 model runs based on constraints available in the Sierra Pelona exposure of the Pelona Schist.

Figure 6. Results from 18,700 model runs based on constraints available in the Sierra Pelona exposure of the Pelona Schist.

Figure 7. Results from 170,000 model runs based on constraints available in the East Fork exposure of the Pelona Schist. No satisfactory models were identified.

Figure 8. Results from 2,200 model runs using combined constraints, with the exception of youngest detrital zircon ages, for the Sierra Pelona and East Fork exposures of the Pelona schist.

BIBLIOGRAPHY

Barth, A. P., Wooden, J. L., Tosdal, R. M., and Morrison, J., 1995, Crustal contamination in the petrogenesis of a calc-alkalic rock series: Josephine Mountain intrusion, California: Geological Society of America Bulletin, v. 107, no. 2, p. 201.

Behr, W. M., Alpert, L. A., Economos, R., Johanesen, K., Platt, J. P., and Zhang, T., Microstructural analysis of deformation and metamorphism along the Vincent thrust in the Eastern San Gabriel Mountains, California, *in* Proceedings Cordilleran Section and Rocky Mountain Section Joint Meeting, Los Vegas, 2008, Volume Abstracts with Programs, Vol. 40, No. 1, Geological Societry of America, p. 47.

Brady, R. J., Ducea, M. N., Kidder, S. B., and Saleeby, J. B., 2006, The distribution of radiogenic heat production as a function of depth in the Sierra Nevada Batholith, California: Lithos, v. 86, no. 3-4, p. 229-244.

Braun, J., 2003, Pecube: a new finite-element code to solve the 3D heat transport equation including the effects of a time-varying, finite amplitude surface topography: Computers & Geosciences, v. 29, no. 6, p. 787-794.

Chapman, A. D., 2012, Late Crtaceous gravitational collapse of the southern Sierra Nevada batholith and adjacent areas above underplated schists, southern California [PhD: California Institute of Technology, 425 p.

Chapman, A. D., Kidder, S., Saleeby, J. B., and Ducea, M. N., 2010, Role of extrusion of the Rand and Sierra de Salinas schists in Late Cretaceous extension and rotation of the southern Sierra Nevada and vicinity: Tectonics, v. 29, no. 5.

Ehlig, P. L., 1981, Origin and tectonic history of the basement terrane of the San Gabriel Mountains, Central Transverse Ranges, *in* Ernst, W. G., ed., The geotectonic development of California (Rubey Volume 1): Englewood Cliffs, New Jersey, Prentice-Hall, p. 253-283.

England, P. C., and Molnar, P., 1993, The interpretation of inverted metamorphic isograds using simple physical calculations: Tectonics, v. 12, no. 1, p. 145-157.

Graham, C. M., and England, P. C., 1976, Thermal regimes and regional metamorphism in the vicinity of overthrustfaults: An exampleof shear heating and inverted metamorphic zonation from southern California: Earth and Planetary Science Letters, v. 31, p. 142-152.

Graham, C. M., and Powell, R., 1984, A garnet-hornblende geothermometer: calibration, testing, and application to the Pelona Schist, Southern California: Journal of Metamorphic Geology, v. 2, p. 13-31.

Grove, M., Jacobson, C. E., Barth, A. P., and Vucic, A., 2003, Temporal and spatial trends of Late Cretaceous-early Tertiary underplating of Pelona and related schist beneath southern California and southwestern Arizona: Geologic Society of America, Special Paper, v. 374.

Grove, M., and Lovera, O. M., 1996, Slip-history of the Vincent thrust: Role of denudation during shallow subduction, *in* Bebout, G. E., ed., Subduction top to bottom, Volume American Geophysical Union Geophysical Monograph 96, p. 163-170.

Hanson, R. B., and Barton, M. D., 1989, Thermal Development of Low-Pressure Metamorphic Belts - Results from Two-Dimensional Numerical-Models: Journal of Geophysical Research-Solid Earth and Planets, v. 94, no. B8, p. 10363-10377.

Haxel, G. B., Jacobson, C. E., Richard, S. M., Tosdal, R. M., and Grubensky, M. J., 2002, The Orocopia schist of southwest Arizona: Early Tertiary oceanic rocks trapped or transported far inland, *in* Barth, A. P., ed., Contributions to Crustal Evolution of the Southwestern United States, Volume Geological Society of America Special Paper 365: Boulder, Colorado, p. 99-128.

Jacobson, C., 1990, The (super 40) Ar/ (super 39) Ar geochronology of the Pelona Schist and related rocks, Southern California: Journal of Geophysical Research, v. 95, no. 1, p. 509-528.

-, 1997, Metamorphic convergence of the upper and lower plates of the Vincent thrust, San Gabriel Mountains, southern California, USA: Journal of Metamorphic Geology, v. 15, p. 155-165.

Kelemen, P. B., Rilling, J. L., Parmentier, E. M., Mehl, L., and Hacker, B. R., 2003, Thermal structure due to solid-state flow in the mantle wedge beneath arcs, *in* Eiler, J., ed., Inside the Subduction Factory, Volume Geophysical Monograph Series, vol 138, American Geophysical Union, p. 311.

Kidder, S. B., and Ducea, M. N., 2006, High temperatures and inverted metamorphism in the schist of Sierra de Salinas, California: Earth and Planetary Science Letters, v. 241, p. 422-437.

Mahaffie, M. J., and Dokka, R. K., 1986, Thermochronologic evidence for the age and cooling history of the upper plate of the Vincent thrust, Californi: Geological Society of America Abstracts with Programs, v. 18, no. 153.

Miller, F. K., and Morton, D. M., 1977, Comparison of granitic intrusions in the Pelona and Orocopia Schists, southern California: J. Res. U.S. Geol. Surv., v. 5, p. 643-649.

-, 1980, Potassium-argon geochronology of the eastern Transverse Ranges and southern Mojave Desert, southern California: U.S. Geological Survey Professional Paper, v. 1152, p. 30.

Nakanishi, M., Sager, W. W., and Klaus, A., 1999, Magnetic lineations within Shatsky Rise, northwest Pacific Ocean: Implications for hot spot-triple junction interaction and oceanic plateau formation: Journal of Geophysical Research, v. 104, no. B4, p. 7539-7556.

Peacock, S. M., 1987, Creation and preservation of subduction-related inverted metamorphic gradients: Journal of Geophysical Research, v. 92, no. B12, p. 12763-12781.

-, 1992, Blueschist-facies metamorphism, shear heating, and P-T-t Paths in Subduction Shear Zones: Journal of Geophysical Research, v. 97, no. B12, p. 17693-17707.

-, 2003, Thermal structure and metamorphic evolution of subducting slabs, Inside the Subduction Factory,, Volume Geophysical Monograph 138, p. 7-22.

Porter, R., Zandt, G., and McQuarrie, N., 2011, Pervasive lower-crustal seismic anisotropy in Southern California: Evidence for underplated schists and active tectonics: Lithosphere, v. 3, no. 3, p. 201-220.

Pringle, M. S., and Dalrymple, G. B., 1993, Geochronological constraints on a possible hot spot origin for Hess Rise and the Wentworth seamount chain, The Mesozoic Pacific: Geology, tectonics and volcanism, Volume Geophysics Monograph v. 77: Washington D.C., American Geophysical Union p. 263-277.

Saleeby, J. B., 2003, segmentation of the Laramide Slab—evidence from the southern Sierra Nevada region: GSA Bulletin, v. 115, no. 6, p. 655-668.

Sambridge, M., 1999, Geophysical inversion with a neighbourhood algorithm - I. Searching a parameter space: Geophysical Journal International, v. 138, no. 2, p. 479-494.

Simoes, M., Avouac, J. P., Beyssac, O., Goffé, B., Farley, K. A., and Chen, Y.-G., 2007, Mountain building in Taiwan: A thermokinematic model: Journal of Geophysical Research, v. 112, no. B11, p. 1-25.

Turcotte, D. L., and Schubert, G., 2002, Geodynamics, Cambridge, Cambridge University Press.

Figure 1

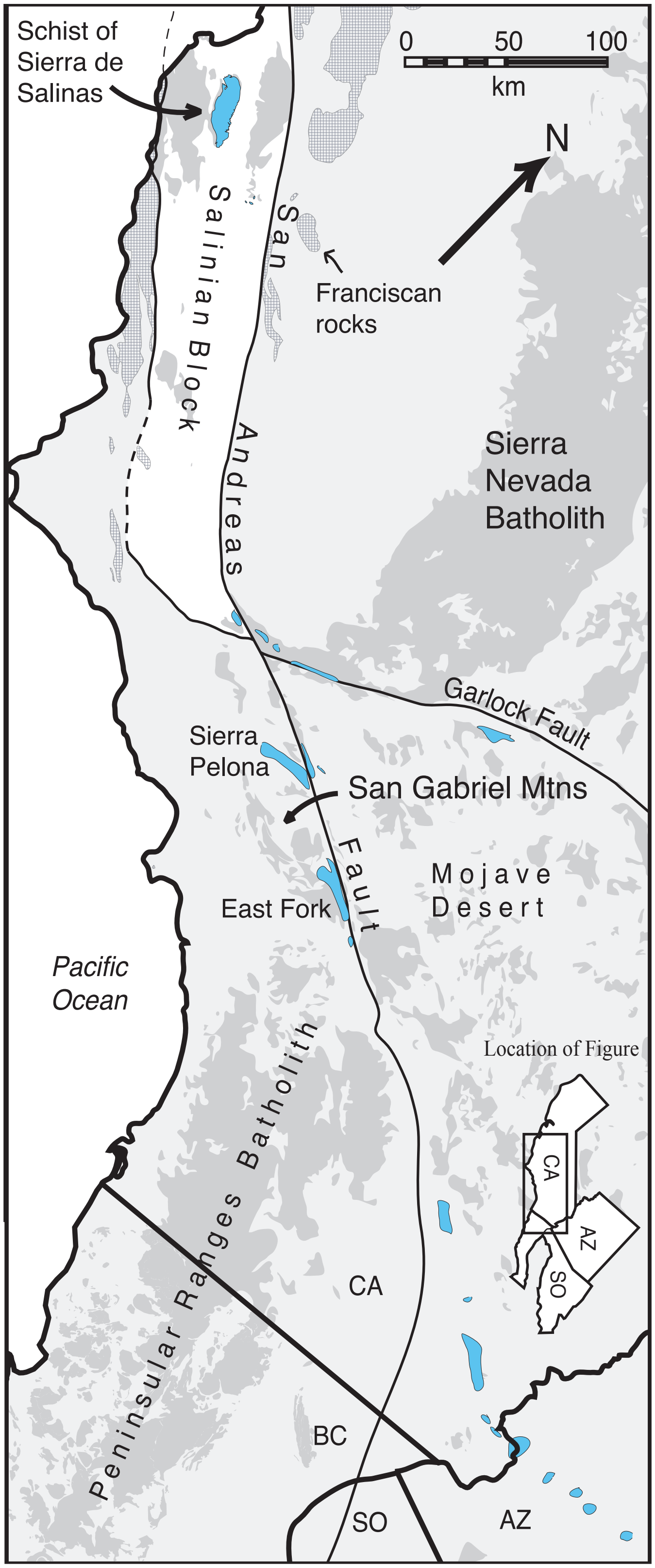
Schist of
Sierra de
Salinas
0
50
100
km
N
Salinian Block
San
Andreas
Fault
Franciscan
rocks
Sierra
Nevada
Batholith
Garlock Fault
Sierra
Pelona
San Gabriel Mtns
East Fork
Mojave
Desert
Pacific
Ocean
Peninsular Ranges Batholith
Location of Figure
CA
AZ
SO
CA
BC
SO
AZ

Figure 2

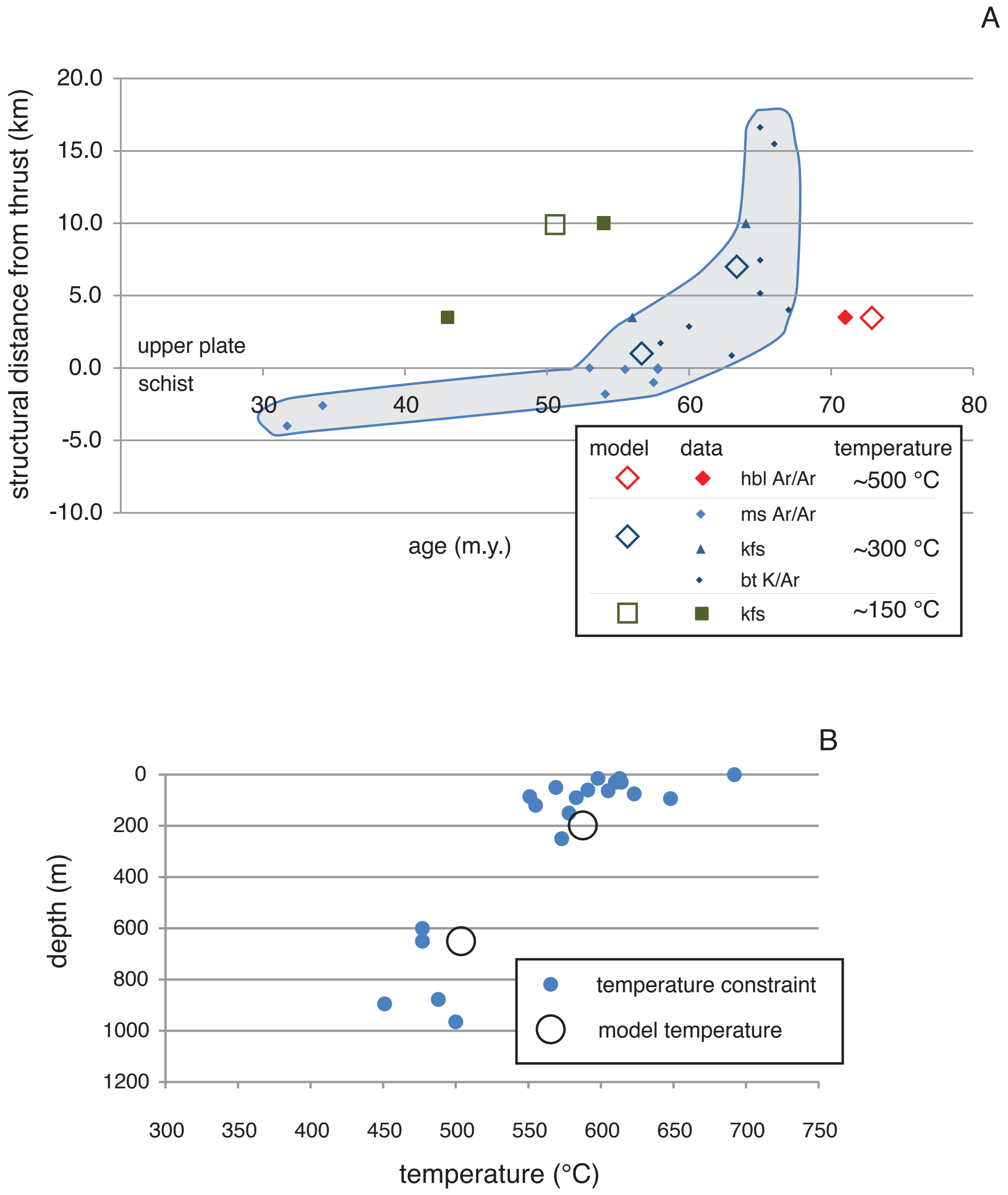
A
structural distance from thrust (km)
20.0
15.0
10.0
5.0
0.0
-5.0
-10.0
upper plate
schist
30
40
50
60
70
80
age (m.y.)
model
data
temperature
hbl Ar/Ar
~500 °C
ms Ar/Ar
kfs
~300 °C
bt K/Ar
kfs
~150 °C
B
depth (m)
0
200
400
600
800
1000
1200
300
350
400
450
500
550
600
650
700
750
temperature (°C)
temperature constraint
model temperature

Figure 3

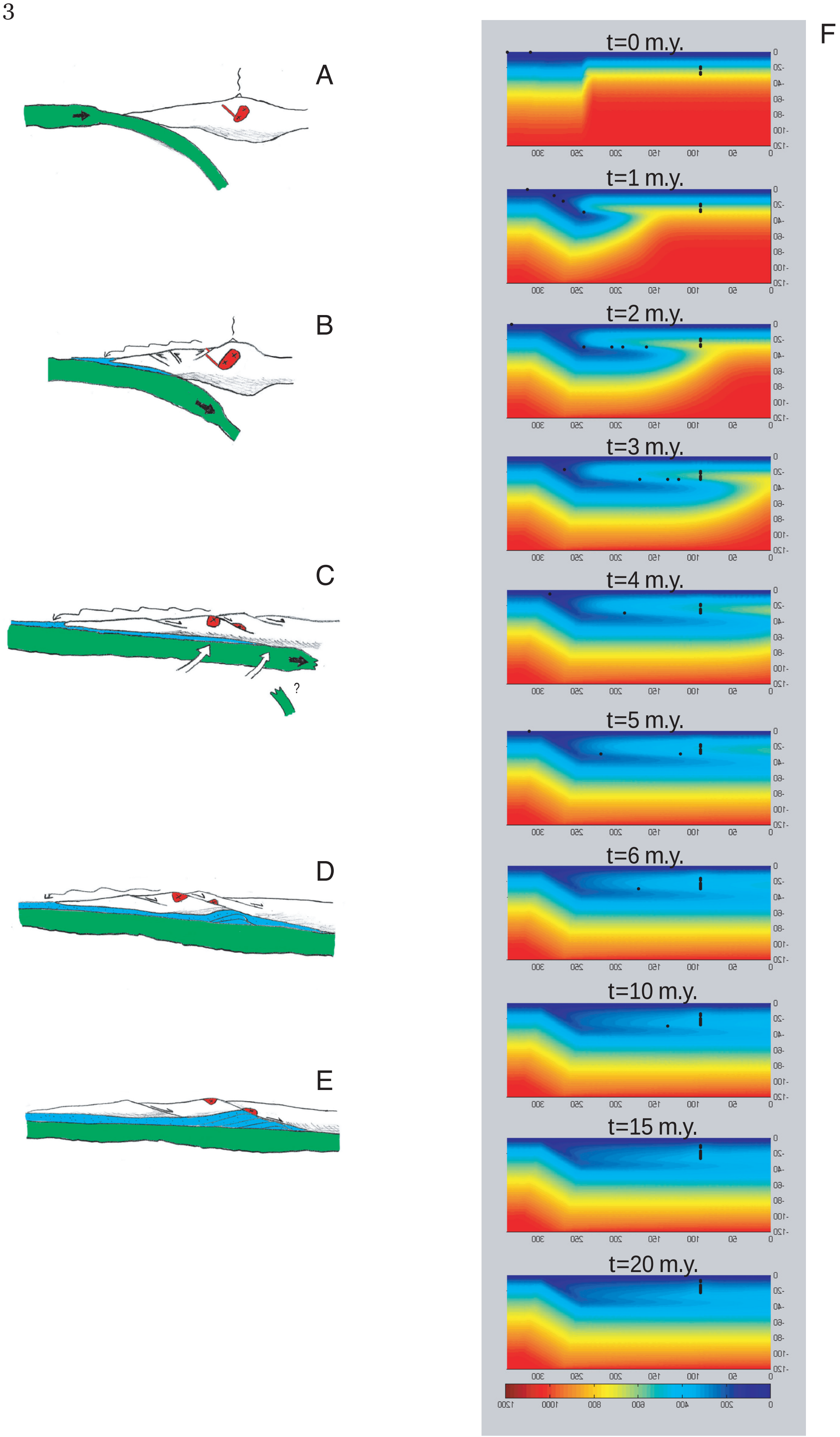
A
B
C
?
D
E
F
t=0 m.y.
t=1 m.y.
t=2 m.y.
t=3 m.y.
t=4 m.y.
t=5 m.y.
t=6 m.y.
t=10 m.y.
t=15 m.y.
t=20 m.y.
300
250
200
150
100
50
0
-20
-40
-60
-80
-100
-120
1200
1000
800
600
400
200

Figure 4

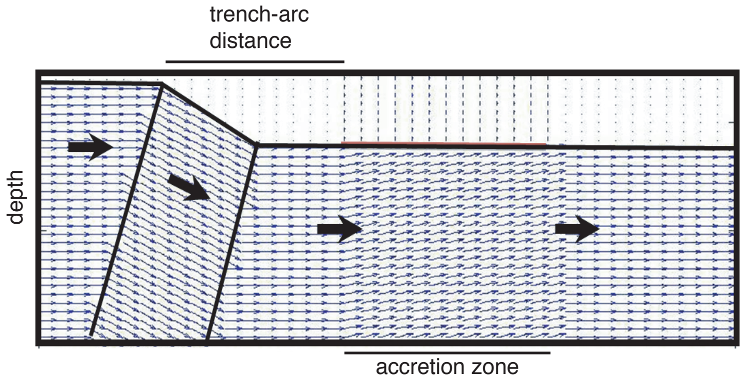

Figure 5

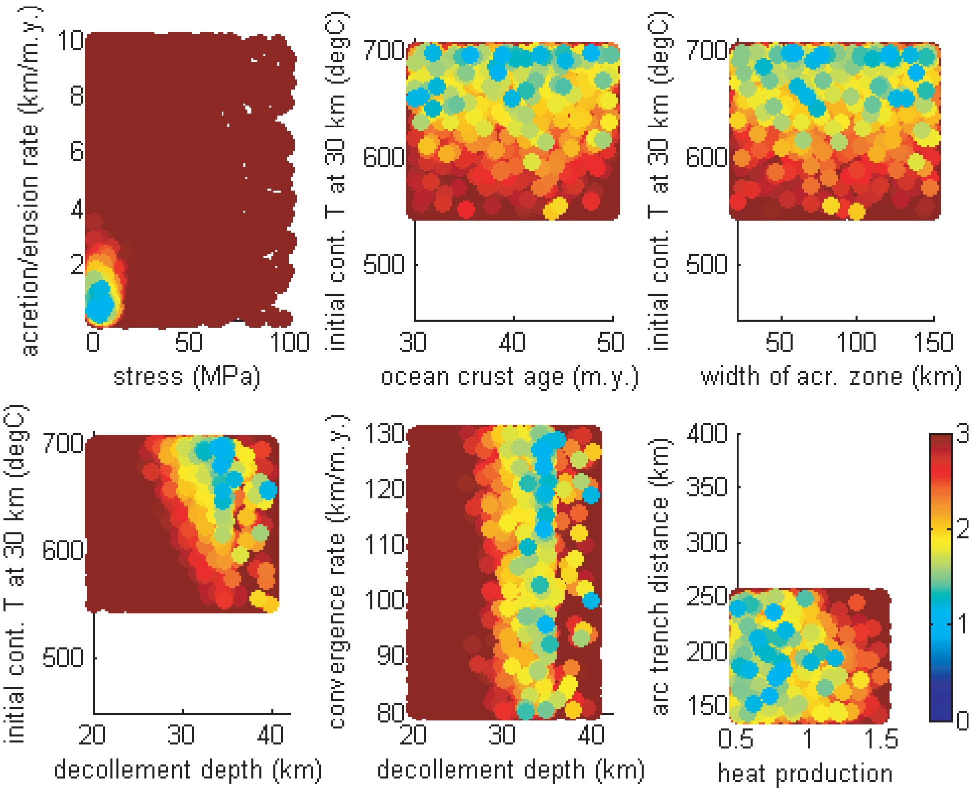
acretion/erosion rate (km/m.y.)
10
8
6
4
2
0
50
100
stress (MPa)
initial cont. T at 30 km (degC)
700
600
500
30
40
50
ocean crust age (m.y.)
initial cont. T at 30 km (degC)
700
600
500
50
100
150
width of acr. zone (km)
initial cont. T at 30 km (degC)
700
600
500
20
30
40
decollement depth (km)
convergence rate (km/m.y.)
130
120
110
100
90
80
20
30
40
decollement depth (km)
arc trench distance (km)
400
350
300
250
200
150
0.5
1
1.5
heat production
3
2
1
0

Figure 6

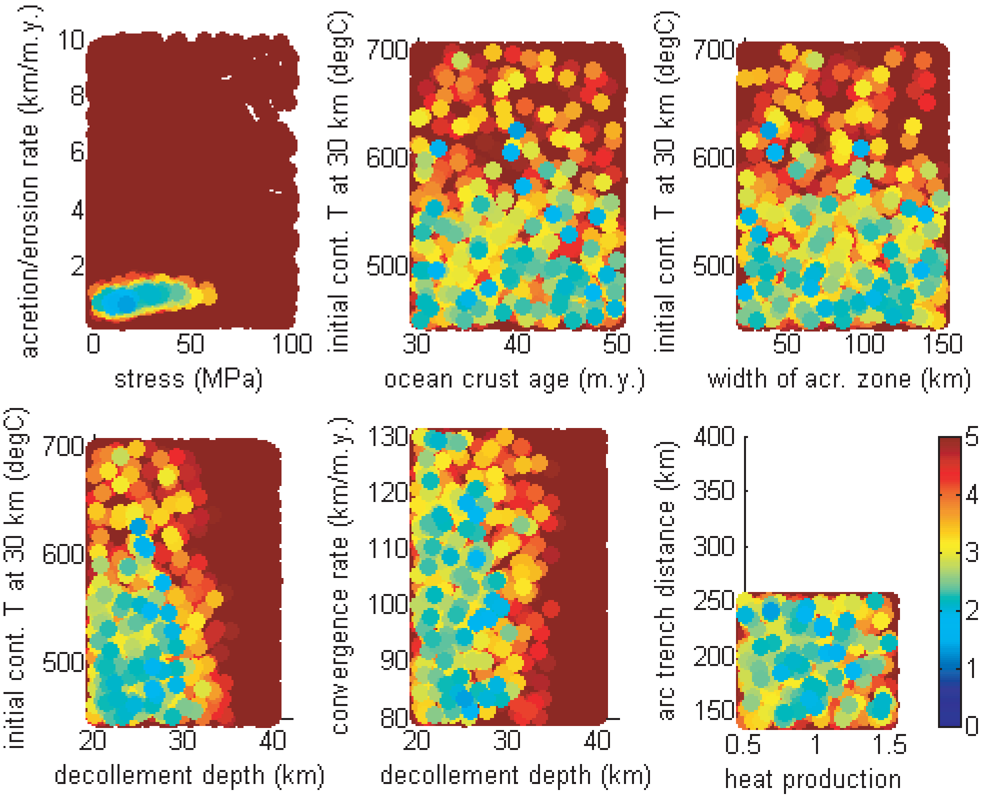
acretion/erosion rate (km/m.y.)
10
8
6
4
2
0
50
100
stress (MPa)
initial cont. T at 30 km (degC)
700
600
500
30
40
50
ocean crust age (m.y.)
initial cont. T at 30 km (degC)
700
600
500
50
100
150
width of acr. zone (km)
initial cont. T at 30 km (degC)
700
600
500
20
30
40
decollement depth (km)
convergence rate (km/m.y.)
130
120
110
100
90
80
20
30
40
decollement depth (km)
arc trench distance (km)
400
350
300
250
200
150
0.5
1
1.5
heat production
5
4
3
2
1
0

Figure 7

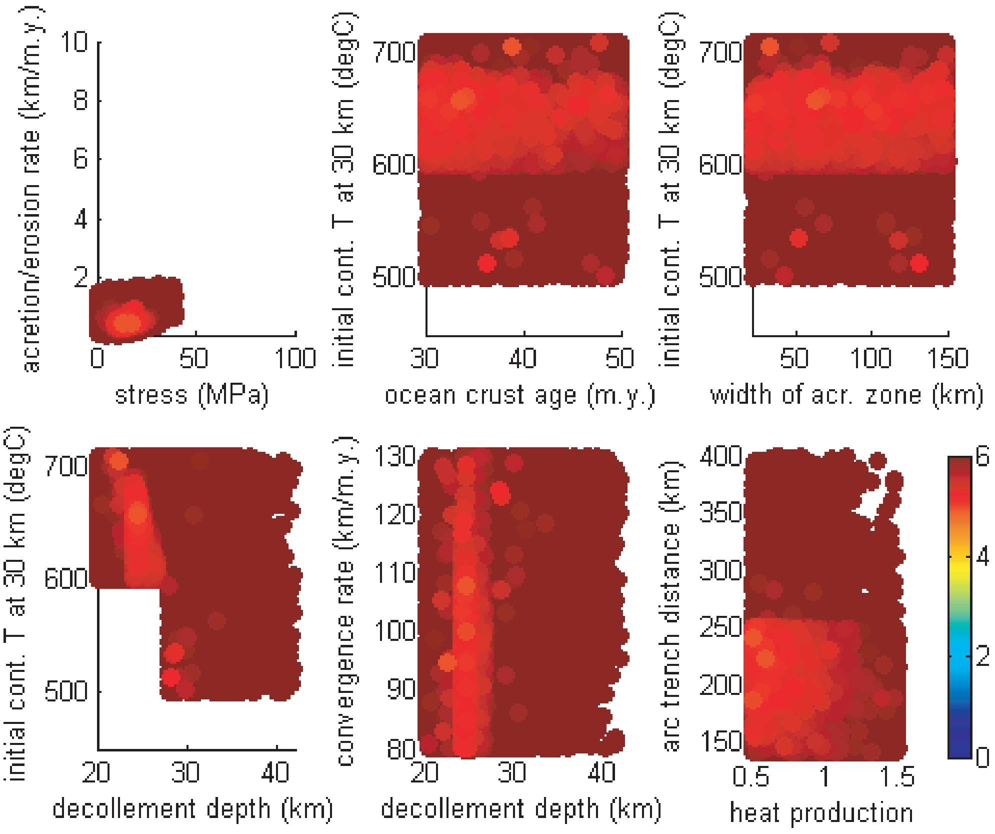
acretion/erosion rate (km/m.y.)
10
8
6
4
2
0
50
100
stress (MPa)
initial cont. T at 30 km (degC)
700
600
500
30
40
50
ocean crust age (m.y.)
initial cont. T at 30 km (degC)
700
600
500
50
100
150
width of acr. zone (km)
initial cont. T at 30 km (degC)
700
600
500
20
30
40
decollement depth (km)
convergence rate (km/m.y.)
130
120
110
100
90
80
20
30
40
decollement depth (km)
arc trench distance (km)
400
350
300
250
200
150
0.5
1
1.5
heat production
6
4
2
0

Figure 8

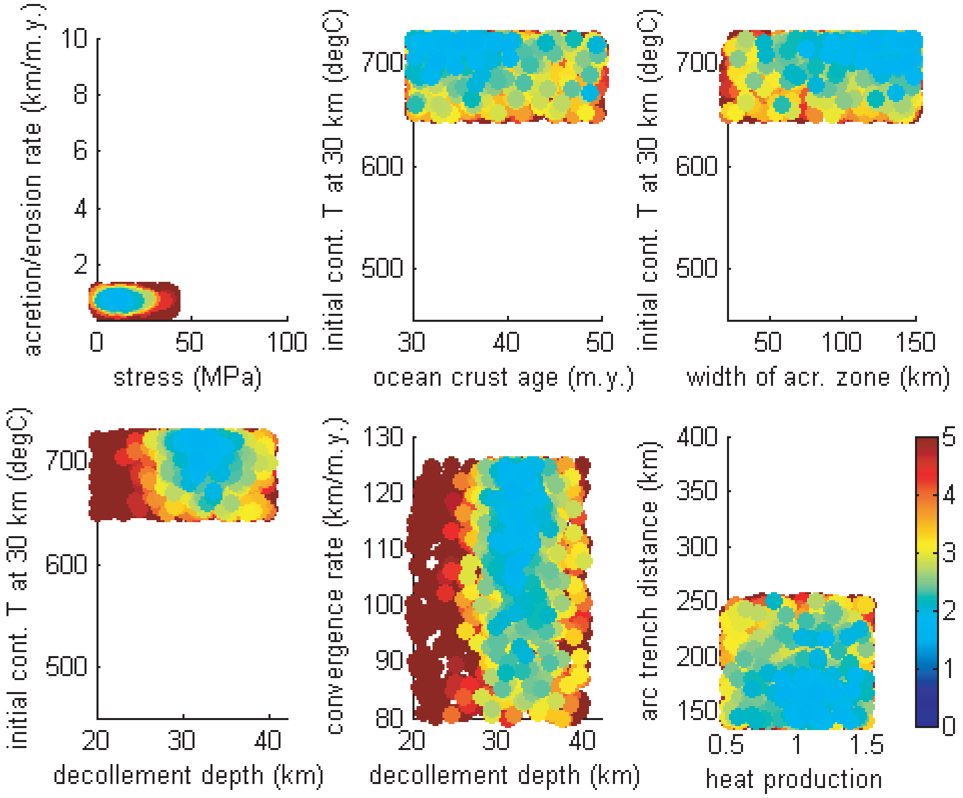
acretion/erosion rate (km/m.y.)
10
8
6
4
2
0
50
100
stress (MPa)
initial cont. T at 30 km (degC)
700
600
500
30
40
50
ocean crust age (m.y.)
initial cont. T at 30 km (degC)
700
600
500
50
100
150
width of acr. zone (km)
initial cont. T at 30 km (degC)
700
600
500
20
30
40
decollement depth (km)
convergence rate (km/m.y.)
130
120
110
100
90
80
20
30
40
decollement depth (km)
arc trench distance (km)
400
350
300
250
200
150
0.5
1
1.5
heat production
5
4
3
2
1
0

THESIS CONCLUSIONS

1) The concentration of titanium in quartz equilibrates at low temperatures (~350°C) in dynamically recrystallizing quartzites. Titanium concentrations in low temperature primary vein material and in recrystallized zones are consistent with the predictions of the most recent experimental calibration of the Titanium-in-quartz thermobarometer, "TitaniQ." Titanium-in-quartz thermobarometry thus holds significant promise as a means of estimating deformation temperature in rutile-present greenschist facies rocks.

2) Microfabrics resulting from non steady state deformation may be prevalent in naturally deformed rocks. In experimentally deformed quartzites, recrystallized fabrics respond quickly to changing stress conditions. Recrystallized grain size either completely equilibrates to new conditions, or under increasing stress, new grains form at a size consistent with paleopiezometric predictions while previous larger recrystallized grains remain. Grain size of the early grains in this case can be used to quantify early stress conditions. Transient fabrics developed under decreasing stress can be identified by the presence of annealed patches indicative of grain growth due to grain boundary energy minimization. Thus, with the aid of microstructural analysis, grain-size stress relationships developed under steady-state conditions can be applied to non steady state fabrics.

3) The paleowattmeter describes grain size evolution during experimental quartz deformation experiments well, but in its present form it cannot reliably be applied to natural conditions.

4) The recrystallized grain size piezometer in quartz produces stress estimates at the brittle-ductile transition in Taiwan's Hsüehshan range consistent with multiple independent constraints including widely applied quartzite flow laws, critical taper, potential energy estimates resulting from elevation differences, Byerlee's rule and Goetze's criteria. The piezometer is accurate to within a factor of two of experimental predictions.

5) The activation energy of naturally deformed quartzite is >133 kJ/mol, consistent with experimental determinations.

6) Peak differential stress in the Hsüehshan range was ~210 MPa. Our results indicate hydrostatic fluid pressure and a low friction coefficient within the Taiwan wedge of ~0.38. Integrated crustal strength in Taiwan is 1.5-2.1*10^{12} N/m.

7) Strain-weakening, rather than extreme fluid pressure, is likely responsible for low stresses at deep levels on major faults in Taiwan.

8) Inverted metamorphism and thermochronologic data in and near the Pelona schist of the San Gabriel mountains is well explained by a model of flat-subduction initiation and tectonic superposition due to accretion. Accretion rates for the schist were ~1 km/m.y. High shear stresses are not required on the Vincent thrust and are constrained to be lower than 50 MPa.

APPENDIX 1. Analyses of NIST glasses and other standards. For session 1, measured 28Si have been scaled to 30Si using a mole fraction ratio of 28Si/30Si of 29.8 (De Laeter et al., 2003). BDL = below detection limit

Sample	Session	^{47}Ti/^{30}Si	σ_{mean}	^{49}Ti/^{30}Si	σ_{mean}	Ti (ppm)	1σ
NIST610	1	8.72E-03	1.32E-05	6.34E-03	9.61E-06	434	15
	1	7.82E-03	4.85E-05	5.68E-03	3.53E-05	434	15
	2	9.02E-03	8.12E-05	6.72E-03	4.11E-05	434	15
	2	9.11E-03	4.32E-05	6.69E-03	3.37E-05	434	15
	3	9.12E-03	3.60E-05	6.79E-03	2.92E-05	434	15
	3	9.12E-03	3.80E-05	6.67E-03	5.13E-05	434	15
NIST612	1	7.37E-04	1.62E-06	5.43E-04	1.96E-06	44	5
	1	7.21E-04	8.18E-06	5.49E-04	8.59E-06	44	5
	1	7.11E-04	8.58E-06	5.37E-04	8.26E-06	44	5
	2	7.40E-04	8.10E-06	5.57E-04	5.73E-06	44	5
	2	7.62E-04	6.03E-06	5.74E-04	6.81E-06	44	5
	2	7.50E-04	6.76E-06	5.53E-04	8.39E-06	44	5
	2	7.34E-04	1.06E-05	5.54E-04	8.89E-06	44	5
	2	7.16E-04	1.17E-05	5.08E-04	8.35E-06	44	5
	2	7.94E-04	1.11E-05	5.89E-04	1.27E-05	44	5
	2	7.06E-04	9.71E-06	5.07E-04	9.46E-06	44	5
	3	7.67E-04	1.18E-05	5.59E-04	9.87E-06	44	5
	3	7.44E-04	1.07E-05	5.63E-04	6.90E-06	44	5
QTip17_light	3	5.14E-04	5.43E-06	3.82E-04	4.39E-06	53	2.9
	3	5.30E-04	6.36E-06	3.98E-04	3.92E-06	53	2.9
QTip17_dark	3	4.18E-04	3.57E-06	3.08E-04	4.97E-06	40	2.4
	3	4.25E-04	5.87E-06	3.20E-04	4.27E-06	40	2.4
Herkimer	1	BDL	-	2.11E-07	2.91E-07	<0.006	-
	1	BDL	-	1.05E-07	1.46E-07	<0.006	-
	2	4.30E-08	2.44E-08	3.10E-08	2.35E-08	<0.006	-
	3	2.43E-08	1.71E-08	3.56E-08	2.03E-08	<0.006	-

APPENDIX 2. SIMS data table for samples. Abbreviations: q (quartzite), v (vein), r (recrystallized), g.s. (grain size in µm), g.b. (grain boundary). Ratios involving ^{28}Si (data points where Fe and ^{48}Ti were measured) have been scaled to ^{30}Si using a mole fraction ratio of ^{28}Si/^{30}Si of 29.8 (De Laeter et al., 2003). Details regarding the calculations of uncertainties are given in the methods section. Uncertainties in pressure are based on uncertainties in temperature assuming a 25 °/km geotherm.

Sample	ID	Type	Session	Area ID	Vein #	g.s.	g.b.?	^{27}Al/^{30}Si	1σ	^{44}Ca/^{30}Si	1σ	^{56}Fe/^{30}Si	1σ	^{47}Ti/^{30}Si	1σ	^{48}Ti/^{30}Si	1σ	^{49}Ti/^{30}Si	1σ	^{47}Ti (ppm)	1σ	^{49}Ti (ppm)	1σ	T (°C)	1σ	P (kbar)	1σ
004	0	v	3	3	1	-	n	5.32E-02	1.72E-03	4.22E-05	4.71E-06	-	-	5.48E-06	6.60E-07	-	-	3.95E-06	4.08E-07	0.58	0.07	0.57	0.06	284.5	3.3	3.1	0.05
004	1	v	3	3	1	-	n	4.27E-03	2.49E-04	2.19E-05	3.27E-06	-	-	3.44E-06	3.42E-07	-	-	2.15E-06	3.01E-07	0.36	0.04	0.31	0.05	260.8	3.2	2.9	0.05
004	2	v	3	3	1	-	n	1.49E-02	3.06E-03	3.00E-05	3.63E-06	-	-	4.52E-06	4.68E-07	-	-	2.79E-06	4.17E-07	0.48	0.05	0.41	0.06	272.4	3.5	3.0	0.05
004	3	vr	3	3	1	-	n	6.87E-03	8.41E-05	1.15E-04	6.86E-06	-	-	7.26E-06	6.06E-07	-	-	6.33E-06	4.76E-07	0.77	0.07	0.92	0.08	302.7	2.5	3.3	0.04
004	4	v	3	3	2	-	n	1.23E-02	9.46E-04	2.24E-05	4.47E-06	-	-	5.03E-06	4.84E-07	-	-	3.81E-06	4.20E-07	0.53	0.05	0.56	0.06	281.7	3.0	3.1	0.04
004	5	v	3	3	2	-	n	6.57E-03	8.98E-04	3.13E-05	3.35E-06	-	-	2.62E-06	3.30E-07	-	-	2.13E-06	2.95E-07	0.28	0.04	0.31	0.04	254.8	3.5	2.8	0.05
004	6	v	3	3	2	-	n	2.97E-02	1.75E-03	3.60E-05	3.66E-06	-	-	5.15E-06	6.07E-07	-	-	3.68E-06	4.72E-07	0.55	0.07	0.54	0.07	281.4	3.5	3.1	0.05
004	7	v	3	3	2	-	n	3.07E-02	2.26E-03	3.54E-05	3.89E-06	-	-	6.94E-06	6.24E-07	-	-	5.64E-06	5.37E-07	0.73	0.07	0.82	0.08	298.7	2.9	3.3	0.04
004	8	vr	3	4	1	-	n	4.12E-03	5.00E-05	3.69E-05	4.51E-06	-	-	2.21E-06	3.09E-07	-	-	1.82E-06	2.62E-07	0.23	0.03	0.26	0.04	248.1	3.6	2.7	0.05
004	9	vr	3	4	1	-	n	8.97E-02	9.85E-03	6.31E-05	1.02E-05	-	-	1.73E-05	2.55E-06	-	-	1.18E-05	1.44E-06	1.84	0.28	1.72	0.22	342.0	4.7	3.8	0.07
004	10	v	3	4	1	-	n	2.05E-02	1.78E-03	3.35E-05	4.16E-06	-	-	9.33E-06	8.49E-07	-	-	6.53E-06	5.83E-07	0.99	0.10	0.95	0.09	309.6	2.9	3.4	0.04
004	11	vr	3	4	1	-	n	3.17E-02	2.47E-03	9.67E-05	1.20E-05	-	-	5.21E-05	2.43E-05	-	-	3.41E-05	1.58E-05	5.52	2.58	4.97	2.31	409.8	18.9	4.5	0.28
004	12	v	3	4	1	-	n	4.42E-02	2.87E-03	3.78E-05	4.58E-06	-	-	7.45E-06	7.33E-07	-	-	5.66E-06	4.79E-07	0.79	0.08	0.82	0.07	300.5	2.9	3.3	0.04
004	13	v	3	4	1	-	n	1.08E-02	8.72E-04	3.40E-05	3.55E-06	-	-	3.11E-06	3.17E-07	-	-	2.31E-06	3.18E-07	0.33	0.04	0.34	0.05	260.1	3.2	2.9	0.05
004	14	v	3	5	2	-	n	1.57E-02	1.88E-03	3.24E-05	3.65E-06	-	-	3.88E-06	5.18E-07	-	-	3.17E-06	3.50E-07	0.41	0.06	0.46	0.05	271.8	3.4	3.0	0.05
004	15	v	3	5	2	-	n	3.13E-02	8.05E-04	4.22E-05	4.32E-06	-	-	2.18E-06	3.38E-07	-	-	1.57E-06	2.82E-07	0.23	0.04	0.23	0.04	244.8	4.1	2.7	0.06
004	16	v	3	5	2	-	n	6.12E-03	1.89E-04	3.07E-05	3.99E-06	-	-	2.84E-06	3.73E-07	-	-	1.22E-06	2.03E-07	0.30	0.04	0.18	0.03	246.4	3.7	2.7	0.05
004	17	v	3	5	1	-	n	4.33E-02	4.90E-03	3.62E-05	4.28E-06	-	-	5.63E-06	5.55E-07	-	-	4.02E-06	4.48E-07	0.60	0.06	0.59	0.07	285.6	3.1	3.1	0.05
004	18	v	3	5	1	-	n	1.54E-02	2.52E-03	3.90E-05	4.74E-06	-	-	1.92E-06	3.18E-07	-	-	1.82E-06	3.62E-07	0.20	0.03	0.26	0.05	245.5	4.7	2.7	0.07
004	19	v	3	5	1	-	n	6.66E-03	9.08E-05	3.22E-05	3.95E-06	-	-	4.05E-06	3.95E-07	-	-	2.54E-06	3.18E-07	0.43	0.04	0.37	0.05	267.8	3.0	2.9	0.04
004	20	vr	3	5	2	-	n	4.98E-02	1.79E-03	7.39E-05	8.62E-06	-	-	1.99E-05	9.96E-07	-	-	1.44E-05	7.60E-07	2.11	0.13	2.10	0.13	351.7	2.1	3.9	0.03
004	22	v	3	5	2	-	n	1.33E-02	6.64E-04	2.76E-04	8.62E-05	-	-	4.63E-06	8.86E-07	-	-	3.33E-06	9.37E-07	0.49	0.10	0.49	0.14	276.8	6.6	3.0	0.10
004	23	v	3	5	2	-	n	1.68E-02	2.82E-04	2.85E-04	6.74E-05	-	-	5.45E-06	8.77E-07	-	-	2.44E-06	3.76E-07	0.58	0.09	0.35	0.06	274.7	4.5	3.0	0.07
004	24	v	3	5	2	-	n	1.40E-02	1.28E-03	4.44E-05	4.54E-06	-	-	3.63E-06	4.60E-07	-	-	2.54E-06	4.16E-07	0.38	0.05	0.37	0.06	265.4	3.9	2.9	0.06
004	25	v	3	2	2	-	n	1.24E-02	1.79E-03	3.70E-05	5.14E-06	-	-	2.19E-06	3.96E-07	-	-	1.19E-06	2.28E-07	0.23	0.04	0.17	0.03	239.8	4.5	2.6	0.07
004	26	v	3	2	2	-	n	5.84E-03	5.18E-05	3.68E-05	5.87E-06	-	-	2.11E-06	3.12E-07	-	-	1.77E-06	3.15E-07	0.22	0.03	0.26	0.05	246.6	4.1	2.7	0.06
004	27	v	3	2	2	-	n	6.08E-03	1.36E-04	3.98E-05	4.66E-06	-	-	2.05E-06	4.03E-07	-	-	1.08E-06	2.10E-07	0.22	0.04	0.16	0.03	236.8	4.7	2.6	0.07
004	28	v	3	2	1	-	n	3.87E-02	9.01E-03	3.70E-05	5.25E-06	-	-	5.01E-06	6.27E-07	-	-	3.85E-06	4.79E-07	0.53	0.07	0.56	0.07	281.9	3.6	3.1	0.05
004	29	v	3	2	1	-	n	3.32E-03	4.93E-05	3.60E-05	3.47E-06	-	-	3.76E-06	4.07E-07	-	-	1.67E-06	3.50E-07	0.40	0.04	0.24	0.05	258.4	3.9	2.8	0.06
004	30	v	3	2	1	-	n	5.73E-03	6.72E-05	3.82E-05	5.68E-06	-	-	1.99E-06	4.56E-07	-	-	1.68E-06	2.75E-07	0.21	0.05	0.24	0.04	244.4	4.8	2.7	0.07
004	31	v	3	2	1	-	n	4.01E-03	7.07E-05	8.26E-05	5.56E-06	-	-	5.49E-06	4.54E-07	-	-	3.87E-06	4.39E-07	0.58	0.05	0.56	0.07	284.1	2.9	3.1	0.04
004	32	v	3	2	1	-	n	7.43E-03	1.13E-04	1.35E-04	8.45E-06	-	-	4.92E-06	5.10E-07	-	-	4.35E-06	5.12E-07	0.52	0.06	0.63	0.08	284.4	3.3	3.1	0.05
004	33	v	3	2	1	-	n	8.37E-03	2.78E-04	6.96E-05	7.44E-06	-	-	2.60E-06	5.11E-07	-	-	2.00E-06	3.31E-07	0.28	0.05	0.29	0.05	253.3	4.6	2.8	0.07
004	34	v	3	2	1	-	n	4.89E-03	2.29E-04	3.36E-05	4.24E-06	-	-	2.63E-06	2.93E-07	-	-	1.64E-06	3.22E-07	0.28	0.03	0.24	0.05	249.6	3.9	2.7	0.06
004	35	v	3	2	2	-	n	6.10E-03	8.72E-05	3.76E-05	5.03E-06	-	-	1.33E-06	2.60E-07	-	-	1.47E-06	3.54E-07	0.14	0.03	0.21	0.05	234.6	5.5	2.6	0.08
004	36	v	3	2	2	-	n	4.35E-03	5.60E-05	3.04E-05	5.88E-06	-	-	1.19E-06	3.45E-07	-	-	1.41E-06	3.92E-07	0.13	0.04	0.21	0.06	232.0	6.8	2.5	0.10
004	37	v	3	4	2	-	n	6.33E-03	9.59E-05	4.19E-05	5.56E-06	-	-	3.41E-06	2.88E-07	-	-	3.04E-06	4.27E-07	0.36	0.03	0.44	0.06	268.2	3.3	2.9	0.05
004	38	v	3	4	2	-	n	1.23E-02	7.62E-04	3.63E-05	3.75E-06	-	-	3.22E-06	4.62E-07	-	-	3.56E-06	4.60E-07	0.34	0.05	0.52	0.07	271.1	3.7	3.0	0.06
004	39	v	3	4	1	-	n	3.69E-02	1.73E-03	3.57E-05	4.42E-06	-	-	4.80E-06	4.62E-07	-	-	2.93E-06	3.30E-07	0.51	0.05	0.43	0.05	274.9	2.9	3.0	0.04
004	40	v	3	4	1	-	n	2.83E-03	5.69E-05	3.51E-05	4.53E-06	-	-	1.78E-06	2.88E-07	-	-	9.80E-07	3.03E-07	0.19	0.03	0.14	0.04	232.0	5.4	2.5	0.08
004	41	v	3	3	1	-	n	1.17E-01	4.16E-03	5.50E-05	4.94E-06	-	-	4.36E-05	1.74E-06	-	-	3.18E-05	1.69E-06	4.62	0.24	4.63	0.29	401.2	2.3	4.4	0.03
004	43	v	3	3	1	-	n	1.04E-02	4.86E-04	2.42E-05	4.33E-06	-	-	4.53E-06	4.70E-07	-	-	3.62E-06	4.84E-07	0.48	0.05	0.53	0.07	278.2	3.4	3.1	0.05
004	44	v	3	3	1	-	n	5.76E-02	2.95E-03	2.76E-05	3.52E-06	-	-	1.13E-05	7.31E-07	-	-	7.32E-06	5.86E-07	1.20	0.09	1.07	0.09	317.5	2.5	3.5	0.04
004	45	v	3	3	1	-	n	1.67E-02	3.97E-04	3.18E-05	4.93E-06	-	-	9.10E-06	8.98E-07	-	-	6.11E-06	4.46E-07	0.96	0.10	0.89	0.07	307.3	2.8	3.4	0.04
004	46	vr	3	3	1	-	n	1.36E-02	5.12E-04	3.94E-05	5.01E-06	-	-	4.91E-06	5.63E-07	-	-	4.16E-06	5.37E-07	0.52	0.06	0.61	0.08	283.3	3.6	3.1	0.05
004	47	vr	3	3	1	-	n	8.72E-03	9.94E-04	5.18E-05	7.45E-06	-	-	8.95E-06	1.40E-06	-	-	6.13E-06	8.89E-07	0.95	0.15	0.89	0.13	307.0	4.6	3.4	0.07
004	48	v	3	3	1	-	n	8.57E-03	9.04E-05	3.95E-05	4.63E-06	-	-	4.77E-06	5.54E-07	-	-	3.42E-06	4.32E-07	0.51	0.06	0.50	0.06	278.0	3.4	3.1	0.05
004	49	v	3	3	1	-	n	1.66E-02	3.39E-03	2.75E-05	2.81E-06	-	-	4.60E-06	5.32E-07	-	-	2.94E-06	4.21E-07	0.49	0.06	0.43	0.06	273.9	3.6	3.0	0.05
004	50	v	3	4	1	-	n	1.33E-02	2.52E-03	4.17E-05	4.49E-06	-	-	2.82E-06	4.06E-07	-	-	3.07E-06	4.51E-07	0.30	0.04	0.45	0.07	264.9	4.0	2.9	0.06
004	51	v	3	4	1	-	n	3.87E-03	3.38E-05	2.84E-05	4.03E-06	-	-	2.60E-06	5.01E-07	-	-	2.11E-06	3.38E-07	0.28	0.05	0.31	0.05	254.5	4.5	2.8	0.07
004	52	v	3	4	2	-	n	7.38E-02	5.44E-03	3.90E-05	5.81E-06	-	-	7.62E-06	7.78E-07	-	-	6.24E-06	6.14E-07	0.81	0.09	0.91	0.09	303.5	3.1	3.3	0.05
004	53	v	3	4	2	-	n	2.61E-02	1.27E-03	3.92E-05	5.90E-06	-	-	3.83E-06	3.83E-07	-	-	3.32E-06	4.89E-07	0.41	0.04	0.48	0.07	272.6	3.6	3.0	0.05
004	54	v	3	4	2	-	n	1.51E-02	7.67E-04	5.44E-05	6.02E-06	-	-	4.61E-06	3.82E-07	-	-	3.37E-06	4.54E-07	0.49	0.04	0.49	0.07	276.9	3.2	3.0	0.05
004	55	v	3	4	2	-	n	4.78E-02	6.10E-03	1.42E-04	2.40E-05	-	-	5.97E-06	8.40E-07	-	-	3.54E-06	6.30E-07	0.63	0.09	0.52	0.09	284.2	4.5	3.1	0.07
004	56	vr	3	3	1	-	n	3.51E-03	5.65E-05	3.87E-05	4.75E-06	-	-	2.28E-06	3.64E-07	-	-	1.82E-06	3.71E-07	0.24	0.04	0.27	0.05	248.7	4.6	2.7	0.07
004	57	vr	3	3	1	-	n	2.37E-02	2.61E-04	6.11E-05	7.31E-06	-	-	9.28E-06	1.51E-06	-	-	6.44E-06	6.15E-07	0.98	0.16	0.94	0.09	309.1	4.2	3.4	0.06

Sample	ID	Type	Session	Area ID	Vein #	g.s.	g.b.?	^{27}Al/^{30}Si	1σ	^{44}Ca/^{30}Si	1σ	^{56}Fe/^{30}Si	1σ	^{47}Ti/^{30}Si	1σ	^{48}Ti/^{30}Si	1σ	^{49}Ti/^{30}Si	1σ	^{47}Ti (ppm)	1σ	^{49}Ti (ppm)	1σ	T (°C)	1σ	P (kbar)	1σ
004	58	v	3	5	2	-	n	4.16E-02	6.44E-04	3.70E-05	5.12E-06	-	-	3.42E-06	5.29E-07	-	-	1.94E-06	3.28E-07	0.36	0.06	0.28	0.05	258.7	4.2	2.8	0.06
004	61	v	3	5	1	-	n	6.40E-02	7.30E-03	7.54E-05	9.20E-06	-	-	1.21E-05	1.92E-06	-	-	8.69E-06	1.67E-06	1.28	0.21	1.27	0.25	323.8	5.7	3.6	0.08
004	62	v	3	5	1	-	n	1.11E-02	6.03E-04	4.63E-05	6.98E-06	-	-	5.38E-06	8.42E-07	-	-	4.26E-06	7.12E-07	0.57	0.09	0.62	0.11	285.9	4.6	3.1	0.07
004	63	v	3	5	2	-	n	1.26E-02	5.42E-04	4.94E-05	5.92E-06	-	-	5.71E-06	7.17E-07	-	-	4.68E-06	5.05E-07	0.60	0.08	0.68	0.08	289.5	3.4	3.2	0.05
004	64	v	3	5	2	-	n	4.53E-03	6.26E-05	3.37E-05	4.92E-06	-	-	2.39E-06	3.52E-07	-	-	2.07E-06	3.55E-07	0.25	0.04	0.30	0.05	252.4	4.1	2.8	0.06
004	65	v	3	5	2	-	n	5.76E-03	1.98E-04	3.77E-05	5.27E-06	-	-	2.90E-06	5.02E-07	-	-	2.58E-06	3.84E-07	0.31	0.05	0.38	0.06	261.1	4.2	2.9	0.06
005	1-1	v	1	-	-	-	n	1.61E-01	1.72E-02	-	-	2.35E-04	3.35E-05	1.11E-05	1.16E-06	5.31E-05	5.59E-06	6.64E-06	7.79E-07	1.17	0.13	0.97	0.12	314.6	3.5	3.5	0.05
005	1-2	v	1	-	-	-	n	2.67E-02	2.15E-03	-	-	1.31E-03	2.73E-04	6.09E-06	5.93E-07	4.76E-05	4.73E-06	3.87E-06	5.26E-07	0.64	0.07	0.56	0.08	286.6	3.4	3.1	0.05
005	3	vr	1	-	-	-	n	4.80E-02	6.39E-04	-	-	4.18E-05	4.17E-06	4.60E-06	3.60E-07	2.04E-05	1.95E-06	2.85E-06	3.70E-07	0.49	0.04	0.41	0.06	273.3	2.9	3.0	0.04
005	4-1	v	1	-	-	-	n	3.21E-02	7.43E-04	-	-	1.50E-05	2.51E-06	2.84E-06	2.62E-07	1.96E-05	1.95E-06	2.55E-06	3.19E-07	0.30	0.03	0.37	0.05	260.5	3.0	2.9	0.04
005	0	v	3	-	-	-	n	3.71E-02	9.58E-03	6.34E-05	3.72E-06	-	-	4.21E-06	7.57E-07	-	-	3.58E-06	6.90E-07	0.45	0.08	0.52	0.10	276.3	5.2	3.0	0.08
005	1	vr	3	-	-	-	n	7.62E-03	6.20E-04	4.09E-05	4.00E-06	-	-	3.28E-06	2.94E-07	-	-	2.30E-06	1.64E-07	0.35	0.03	0.33	0.03	261.0	2.3	2.9	0.03
005	2	vr	3	-	-	-	n	6.27E-02	3.32E-02	9.88E-05	1.10E-05	-	-	7.57E-06	3.07E-06	-	-	5.09E-06	1.88E-06	0.80	0.33	0.74	0.27	298.3	11.4	3.3	0.17
005	3	vr	3	-	-	-	n	2.14E-02	1.61E-03	3.69E-05	1.90E-06	-	-	3.81E-06	2.96E-07	-	-	2.65E-06	2.17E-07	0.40	0.03	0.39	0.03	267.4	2.3	2.9	0.03
005	4	v	3	-	-	-	n	2.00E-02	9.47E-04	3.13E-05	1.77E-06	-	-	2.65E-06	2.39E-07	-	-	1.89E-06	1.56E-07	0.28	0.03	0.28	0.02	252.5	2.3	2.8	0.03
005	5	v	3	-	-	-	n	6.72E-02	1.41E-02	8.16E-05	5.79E-06	-	-	9.79E-05	2.89E-05	-	-	7.10E-05	2.08E-05	10.36	3.08	10.34	3.05	460.7	13.6	5.1	0.20
005	6	vr	3	-	-	-	n	2.42E-02	7.84E-04	1.52E-04	1.01E-05	-	-	3.97E-06	2.75E-07	-	-	2.93E-06	3.68E-07	0.42	0.03	0.43	0.06	270.4	2.8	3.0	0.04
005	7	vr	3	-	-	-	n	2.24E-02	6.05E-03	1.06E-04	1.02E-05	-	-	5.45E-06	7.26E-07	-	-	3.76E-06	4.07E-07	0.58	0.08	0.55	0.06	283.3	3.5	3.1	0.05
111b	15	vr	1	1	-	-	n	2.04E-02	2.52E-04	-	-	1.93E-05	1.97E-06	3.42E-06	3.22E-07	4.65E-05	3.67E-06	2.72E-06	3.14E-07	0.36	0.04	0.40	0.05	265.6	2.9	2.9	0.04
111b	16	v	1	1	-	-	n	1.87E-02	9.60E-04	-	-	1.95E-04	1.63E-05	3.69E-06	3.39E-07	4.20E-05	3.12E-06	2.72E-06	3.08E-07	0.39	0.04	0.40	0.05	267.2	2.8	2.9	0.04
111b	17	vr	1	1	-	-	n	9.83E-03	1.91E-04	-	-	1.23E-05	1.75E-06	2.09E-06	3.10E-07	4.05E-05	2.24E-06	2.07E-06	3.44E-07	0.22	0.03	0.30	0.05	249.9	4.1	2.7	0.06
111b	20	vr	1	1	-	-	n	6.44E-03	3.15E-04	-	-	1.76E-05	1.55E-06	2.70E-06	2.73E-07	1.76E-05	1.76E-06	2.05E-06	2.86E-07	0.29	0.03	0.30	0.04	254.6	3.2	2.8	0.05
111b	21	v	1	1	-	-	n	8.23E-03	1.68E-04	-	-	1.65E-05	1.37E-06	3.78E-06	2.50E-07	2.69E-05	1.75E-06	3.06E-06	2.46E-07	0.40	0.03	0.44	0.04	270.4	2.2	3.0	0.03
111b	22	v	1	1	-	-	n	2.13E-02	6.08E-04	-	-	4.82E-05	6.70E-06	3.54E-06	2.50E-07	2.83E-05	1.89E-06	2.41E-06	2.46E-07	0.37	0.03	0.35	0.04	263.7	2.4	2.9	0.04
111b	23	v	1	1	-	-	n	7.43E-03	8.64E-05	-	-	7.78E-05	8.68E-06	2.70E-06	1.93E-07	1.89E-05	1.46E-06	1.91E-06	2.04E-07	0.29	0.02	0.28	0.03	253.1	2.4	2.8	0.04
111b	24	v	1	1	-	-	n	4.88E-03	7.58E-05	-	-	1.28E-05	2.26E-06	1.53E-06	1.59E-07	1.26E-05	1.24E-06	1.18E-06	1.73E-07	0.16	0.02	0.17	0.03	232.3	3.1	2.5	0.05
111b	25	v	1	1	-	-	n	8.99E-03	2.89E-04	-	-	6.63E-05	1.05E-05	2.95E-06	2.13E-07	2.43E-05	2.67E-06	2.07E-06	2.16E-07	0.31	0.02	0.30	0.03	256.6	2.4	2.8	0.04
111b	26	v	1	1	-	-	n	7.09E-03	3.24E-04	-	-	2.59E-05	4.82E-06	3.61E-06	2.36E-07	2.55E-05	1.70E-06	3.17E-06	2.51E-07	0.38	0.03	0.46	0.04	270.3	2.2	3.0	0.03
111b	27	vr	1	1	-	-	n	4.44E-03	5.56E-05	-	-	6.12E-06	1.21E-06	1.84E-06	2.64E-07	1.42E-05	1.44E-06	1.51E-06	2.44E-07	0.19	0.03	0.22	0.04	240.7	3.8	2.6	0.06
111b	28	v	1	1	-	-	n	5.33E-03	4.42E-05	-	-	9.78E-06	1.15E-06	2.67E-06	2.05E-07	2.11E-05	1.60E-06	1.88E-06	1.93E-07	0.28	0.02	0.27	0.03	252.5	2.4	2.8	0.04
111b	29	vr	1	1	-	-	n	6.07E-03	1.01E-04	-	-	8.27E-06	9.44E-07	2.68E-06	2.85E-07	1.56E-05	1.65E-06	1.53E-06	2.26E-07	0.28	0.03	0.22	0.03	248.6	3.2	2.7	0.05
111b	30	vr	1	1	-	-	n	1.30E-02	1.46E-03	-	-	7.46E-05	1.89E-05	2.65E-06	2.15E-07	1.80E-05	1.59E-06	2.23E-06	2.31E-07	0.28	0.02	0.32	0.04	256.0	2.5	2.8	0.04
111b	31	v	1	1	-	-	n	7.00E-03	7.01E-05	-	-	1.32E-05	1.58E-06	1.79E-06	1.84E-07	1.35E-05	1.54E-06	1.22E-06	1.85E-07	0.19	0.02	0.18	0.03	236.0	3.1	2.6	0.05
111b	32	v	1	2	-	-	n	7.71E-02	9.35E-03	-	-	5.94E-05	9.95E-06	1.15E-05	1.10E-06	8.77E-05	8.65E-06	8.90E-06	8.58E-07	1.21	0.12	1.30	0.13	323.0	3.2	3.5	0.05
111b	33	v	1	2	-	-	n	3.05E-02	1.85E-03	-	-	9.27E-06	1.17E-06	1.10E-05	5.01E-07	7.29E-05	3.42E-06	7.42E-06	4.81E-07	1.16	0.07	1.08	0.08	317.1	2.0	3.5	0.03
111b	34	v	1	2	-	-	n	6.97E-02	5.18E-03	-	-	2.22E-04	6.23E-05	9.34E-06	7.03E-07	6.10E-05	4.69E-06	7.00E-06	5.51E-07	0.99	0.08	1.02	0.09	311.4	2.5	3.4	0.04
111b	35	v	1	2	-	-	n	1.87E-02	4.51E-03	-	-	5.21E-06	1.18E-06	5.51E-06	5.57E-07	3.48E-05	3.21E-06	4.00E-06	4.86E-07	0.58	0.06	0.58	0.07	284.9	3.3	3.1	0.05
111b	36	v	1	2	-	-	n	1.39E-01	1.29E-02	-	-	1.63E-05	1.61E-06	1.43E-05	2.08E-06	1.16E-04	1.49E-05	9.02E-06	1.33E-06	1.51	0.23	1.31	0.20	329.3	4.8	3.6	0.07
123b	0	v	1	1	-	-	n	4.52E-03	6.10E-05	-	-	1.55E-06	1.16E-06	5.28E-06	5.16E-07	3.06E-05	4.58E-06	4.10E-06	5.32E-07	0.56	0.06	0.60	0.08	284.5	3.4	3.1	0.05
123b	1	v	1	1	-	-	n	2.09E-03	6.42E-05	-	-	1.95E-06	1.51E-06	2.86E-06	3.90E-07	8.12E-06	2.33E-06	2.20E-06	3.41E-07	0.30	0.04	0.32	0.05	257.3	3.8	2.8	0.06
123b	2	v	1	1	-	-	n	3.25E-03	5.13E-05	-	-	1.53E-06	7.50E-07	4.45E-06	3.44E-07	3.00E-05	3.40E-06	3.10E-06	3.45E-07	0.47	0.04	0.45	0.05	274.3	2.7	3.0	0.04
123b	3	v	1	1	-	-	n	3.62E-03	1.63E-04	-	-	2.45E-06	1.11E-06	3.03E-06	3.81E-07	2.42E-05	4.12E-06	2.86E-06	2.86E-07	0.32	0.04	0.42	0.04	264.5	3.0	2.9	0.04
123b	4	vr	1	1	-	-	n	9.07E-02	2.09E-02	-	-	2.40E-05	6.43E-06	1.04E-05	1.91E-06	6.13E-05	1.16E-05	8.04E-06	1.38E-06	1.10	0.20	1.17	0.20	317.7	5.6	3.5	0.08
123b	5	vr	1	1	-	-	n	8.23E-03	1.70E-04	-	-	4.28E-05	7.79E-06	2.83E-06	3.02E-07	2.13E-05	2.85E-06	2.22E-06	2.82E-07	0.30	0.03	0.32	0.04	257.3	3.1	2.8	0.05
123b	6	vr	1	1	-	-	n	4.95E-02	9.95E-03	-	-	8.52E-04	2.20E-04	2.07E-06	2.85E-07	1.08E-05	2.27E-06	1.76E-06	3.41E-07	0.22	0.03	0.26	0.05	246.2	4.3	2.7	0.06
123b	7	vr	1	1	-	-	n	1.00E-02	2.89E-04	-	-	7.74E-06	1.71E-06	3.29E-06	3.14E-07	2.29E-05	2.46E-06	2.46E-06	2.68E-07	0.35	0.04	0.36	0.04	262.5	2.8	2.9	0.04
123b	8	vr	1	1	-	-	n	3.83E-02	1.46E-03	-	-	4.92E-05	7.33E-06	6.63E-06	3.42E-07	6.86E-05	5.48E-06	5.27E-06	4.03E-07	0.70	0.04	0.77	0.06	295.9	2.1	3.2	0.03
123b	9	vr	1	1	-	-	n	9.04E-03	2.87E-04	-	-	1.06E-05	1.92E-06	4.14E-06	2.94E-07	3.27E-05	4.24E-06	2.97E-06	2.94E-07	0.44	0.03	0.43	0.05	271.7	2.5	3.0	0.04
123b	10	vr	1	1	-	-	n	1.56E-02	2.28E-03	-	-	2.11E-05	3.88E-06	5.69E-06	5.36E-07	4.48E-05	6.84E-06	3.57E-06	3.19E-07	0.60	0.06	0.52	0.05	283.2	2.7	3.1	0.04
123b	11	vr	1	1	-	-	n	9.12E-03	1.07E-04	-	-	4.10E-06	1.27E-06	2.62E-06	2.01E-07	1.66E-05	2.29E-06	1.91E-06	2.53E-07	0.28	0.02	0.28	0.04	252.5	2.8	2.8	0.04
123b	12	v	1	1	-	-	n	1.43E-02	8.56E-04	-	-	1.20E-04	9.79E-06	4.45E-06	4.33E-07	3.00E-05	3.69E-06	3.33E-06	3.53E-07	0.47	0.05	0.49	0.05	275.9	2.9	3.0	0.04
123b	13	v	1	1	-	-	n	1.41E-02	4.81E-04	-	-	6.14E-05	7.70E-06	2.63E-06	2.81E-07	1.61E-05	2.19E-06	1.98E-06	2.61E-07	0.28	0.03	0.29	0.04	253.3	3.1	2.8	0.05
123b	14	v	1	1	-	-	n	5.00E-03	9.56E-05	-	-	1.18E-05	2.56E-06	2.02E-06	2.55E-07	1.00E-05	2.17E-06	1.16E-06	2.10E-07	0.21	0.03	0.17	0.03	237.5	3.7	2.6	0.05
123b	15	vr	1	1	-	-	n	1.10E-02	1.02E-03	-	-	4.10E-06	1.38E-06	5.28E-06	3.16E-07	3.24E-05	3.29E-06	3.17E-06	3.56E-07	0.56	0.04	0.46	0.05	278.9	2.5	3.1	0.04
123b	16	vr	1	1	-	-	n	4.29E-03	1.91E-04	-	-	7.92E-06	1.56E-06	3.90E-06	3.29E-07	2.84E-05	3.61E-06	3.37E-06	3.26E-07	0.41	0.04	0.49	0.05	273.4	2.6	3.0	0.04
123b	17	vr	1	1	-	-	n	5.15E-03	2.81E-04	-	-	6.70E-06	1.28E-06	3.83E-06	2.90E-07	2.32E-05	2.95E-06	2.94E-06	2.96E-07	0.41	0.03	0.43	0.05	269.7	2.5	3.0	0.04

Sample	ID	Type	Session	Area ID	Vein #	g.s.	g.b.?	^{27}Al/^{30}Si	1σ	^{44}Ca/^{30}Si	1σ	^{56}Fe/^{30}Si	1σ	^{47}Ti/^{30}Si	1σ	^{48}Ti/^{30}Si	1σ	^{49}Ti/^{30}Si	1σ	^{47}Ti (ppm)	1σ	^{49}Ti (ppm)	1σ	T (°C)	1σ	P (kbar)	1σ
123b	18	v	1	1	-	-	n	1.09E-02	6.09E-04	-	-	6.20E-05	7.70E-06	2.45E-06	2.80E-07	1.03E-05	1.59E-06	1.68E-06	2.62E-07	0.26	0.03	0.25	0.04	248.6	3.4	2.7	0.05
123b	19	v	1	1	-	-	n	6.75E-03	4.14E-04	-	-	5.49E-05	7.65E-06	2.57E-06	2.78E-07	1.04E-05	2.45E-06	1.69E-06	2.20E-07	0.27	0.03	0.25	0.03	249.7	3.0	2.7	0.04
123b	20	vr	1	1	-	-	n	5.11E-03	6.05E-05	-	-	1.12E-05	1.70E-06	3.49E-06	2.55E-07	2.39E-05	3.12E-06	2.93E-06	4.34E-07	0.37	0.03	0.43	0.06	267.7	3.3	2.9	0.05
123b	21	vr	1	1	-	-	n	2.26E-02	3.13E-03	-	-	2.28E-05	3.34E-06	6.59E-06	6.20E-07	3.43E-05	3.96E-06	4.56E-06	4.81E-07	0.70	0.07	0.66	0.07	292.2	3.0	3.2	0.04
123b	22	vr	1	1	-	-	n	2.80E-03	1.81E-04	-	-	7.81E-06	2.16E-06	2.26E-06	1.81E-07	2.05E-05	2.80E-06	1.35E-06	2.49E-07	0.24	0.02	0.20	0.04	242.6	3.3	2.7	0.05
123b	24	v	1	1	-	-	n	9.07E-03	3.83E-04	-	-	2.13E-05	7.81E-06	4.27E-06	7.81E-07	3.43E-05	9.69E-06	9.30E-07	4.61E-07	0.45	0.08	0.14	0.07	254.8	6.5	2.8	0.10
123b	25	v	1	2	-	-	n	8.13E-03	4.04E-04	-	-	3.02E-05	7.59E-06	9.35E-06	9.92E-07	4.42E-05	7.54E-06	4.62E-06	8.20E-07	0.99	0.11	0.67	0.12	301.9	4.1	3.3	0.06
123b	26	v	1	2	-	-	n	4.74E-03	3.30E-04	-	-	2.04E-05	4.39E-06	3.76E-06	5.35E-07	2.74E-05	4.87E-06	2.85E-06	5.04E-07	0.40	0.06	0.41	0.07	268.6	4.4	2.9	0.06
123b	27	v	1	2	-	-	n	3.84E-03	1.73E-04	-	-	1.48E-05	3.20E-06	4.13E-06	4.12E-07	2.90E-05	4.14E-06	2.64E-06	3.31E-07	0.44	0.05	0.38	0.05	269.1	3.1	3.0	0.05
123b	28	v	1	2	-	-	n	1.46E-02	7.52E-04	-	-	1.22E-04	2.08E-05	5.68E-06	5.20E-07	3.09E-05	4.48E-06	3.68E-06	4.90E-07	0.60	0.06	0.54	0.07	283.8	3.2	3.1	0.05
123b	29	v	1	2	-	-	n	4.82E-02	3.81E-03	-	-	3.32E-04	2.81E-05	7.87E-06	5.93E-07	6.16E-05	4.97E-06	6.77E-06	6.11E-07	0.83	0.07	0.99	0.09	306.4	2.7	3.4	0.04
123b	30	v	1	2	-	-	n	3.85E-01	1.99E-02	-	-	2.82E-03	8.03E-05	3.53E-05	1.93E-06	1.63E-04	1.16E-05	2.88E-05	1.53E-06	3.74	0.24	4.20	0.26	391.0	2.4	4.3	0.04
123b	31	v	1	2	-	-	n	2.05E-02	2.73E-03	-	-	1.51E-05	2.62E-06	7.69E-06	1.22E-06	4.55E-05	6.28E-06	5.47E-06	6.88E-07	0.81	0.13	0.80	0.10	300.4	4.3	3.3	0.06
123b	32	v	1	2	-	-	n	1.06E-02	2.52E-04	-	-	2.59E-05	3.43E-06	4.31E-06	2.79E-07	3.43E-05	3.89E-06	3.28E-06	3.71E-07	0.46	0.03	0.48	0.06	274.8	2.7	3.0	0.04
123b	33	v	1	2	-	-	n	7.84E-02	3.20E-03	-	-	4.42E-04	4.25E-05	1.34E-05	6.74E-07	6.87E-05	5.39E-06	1.12E-05	7.37E-07	1.42	0.09	1.62	0.12	333.3	2.2	3.7	0.03
123c	Tnd	v	1	-	-	-	n	5.55E-03	3.88E-04	-	-	1.72E-05	3.27E-06	2.70E-06	3.17E-07	1.73E-05	2.90E-06	1.64E-06	2.17E-07	0.29	0.03	0.24	0.03	250.2	3.2	2.7	0.05
123c	0	v	1	-	-	-	n	5.38E-02	4.15E-03	-	-	3.43E-04	2.72E-05	9.56E-06	6.21E-07	5.48E-05	3.37E-06	8.07E-06	6.67E-07	1.01	0.07	1.18	0.10	315.8	2.5	3.5	0.04
123c	1	v	1	-	-	-	n	1.25E-01	1.32E-02	-	-	2.60E-04	3.58E-05	1.45E-05	1.15E-06	6.59E-05	5.04E-06	1.06E-05	1.01E-06	1.53	0.13	1.54	0.16	334.0	3.1	3.7	0.05
123c	2	vr	1	-	-	-	n	1.56E-02	3.33E-04	-	-	1.89E-04	4.91E-05	4.82E-06	3.85E-07	3.38E-05	4.23E-06	3.39E-06	4.58E-07	0.51	0.04	0.49	0.07	278.1	3.1	3.1	0.05
123c	3	vr	1	-	-	-	n	1.85E-02	1.53E-04	-	-	3.00E-05	3.56E-06	4.97E-06	3.04E-07	4.41E-05	3.81E-06	3.65E-06	3.86E-07	0.53	0.04	0.53	0.06	280.4	2.5	3.1	0.04
123c	4	v	1	-	-	-	n	1.18E-02	3.13E-04	-	-	6.27E-05	1.48E-05	4.59E-06	3.36E-07	5.10E-05	4.70E-06	3.43E-06	6.00E-07	0.49	0.04	0.50	0.09	277.3	3.8	3.0	0.06
123c	5	v	1	-	-	-	n	8.89E-03	5.00E-04	-	-	3.05E-05	4.62E-06	4.24E-06	3.12E-07	2.44E-05	2.68E-06	2.66E-06	2.76E-07	0.45	0.04	0.39	0.04	269.9	2.5	3.0	0.04
123c	6	v	1	-	-	-	n	6.42E-03	9.07E-04	-	-	8.78E-06	1.81E-06	3.14E-06	2.52E-07	1.93E-05	2.91E-06	2.88E-06	3.81E-07	0.33	0.03	0.42	0.06	265.3	3.1	2.9	0.05
123c	7	v	1	-	-	-	n	1.93E-02	1.98E-03	-	-	1.06E-04	1.56E-05	4.41E-06	2.66E-07	3.34E-05	3.99E-06	3.52E-06	3.63E-07	0.47	0.03	0.51	0.06	276.9	2.5	3.0	0.04
131g	1	vr	1	-	-	-	n	3.33E-02	6.59E-04	-	-	2.48E-04	3.02E-05	5.80E-06	3.37E-07	2.54E-05	2.06E-06	4.15E-06	3.78E-07	0.61	0.04	0.60	0.06	286.9	2.3	3.1	0.03
131g	2	v	1	-	-	-	n	8.96E-03	8.43E-04	-	-	8.45E-05	1.51E-05	4.86E-06	3.10E-07	3.60E-05	2.29E-06	3.69E-06	3.85E-07	0.51	0.04	0.54	0.06	280.2	2.6	3.1	0.04
131g	3	vr	1	-	-	-	n	5.94E-03	1.80E-04	-	-	1.83E-05	1.86E-06	6.08E-06	3.62E-07	3.70E-05	2.21E-06	4.48E-06	3.67E-07	0.64	0.04	0.65	0.06	289.9	2.2	3.2	0.03
131g	4	v	1	-	-	-	n	5.68E-03	7.09E-05	-	-	7.35E-06	1.34E-06	6.65E-06	3.75E-07	3.82E-05	2.60E-06	4.03E-06	3.31E-07	0.70	0.05	0.59	0.05	289.7	2.2	3.2	0.03
131g	5	vr	1	-	-	-	n	5.92E-03	5.72E-05	-	-	1.32E-05	1.74E-06	6.49E-06	4.33E-07	3.71E-05	2.73E-06	4.10E-06	3.52E-07	0.69	0.05	0.60	0.05	289.4	2.3	3.2	0.03
131g	6	v	1	-	-	-	n	7.27E-03	4.07E-05	-	-	5.36E-06	9.17E-07	8.52E-06	4.24E-07	5.04E-05	2.71E-06	6.34E-06	3.86E-07	0.90	0.05	0.92	0.06	306.6	1.9	3.4	0.03
131g	Jn0	v	3	-	-	-	n	3.61E-03	3.39E-05	2.50E-05	2.55E-06	-	-	4.97E-06	2.35E-07	-	-	3.46E-06	3.27E-07	0.53	0.03	0.50	0.05	279.2	2.2	3.1	0.03
131g	Jn1	v	3	-	-	-	n	1.04E-02	1.35E-03	3.13E-05	3.01E-06	-	-	6.49E-06	2.54E-07	-	-	4.85E-06	3.08E-07	0.69	0.04	0.71	0.05	293.3	1.8	3.2	0.03
131g	Jn2	v	3	-	-	-	n	3.18E-03	2.78E-05	2.85E-05	1.82E-06	-	-	3.40E-06	1.87E-07	-	-	2.73E-06	2.57E-07	0.36	0.02	0.40	0.04	265.6	2.2	2.9	0.03
131g	Jn3	v	3	-	-	-	n	4.58E-03	4.64E-05	2.50E-05	1.75E-06	-	-	5.80E-06	3.58E-07	-	-	4.19E-06	1.83E-07	0.61	0.04	0.61	0.03	287.2	1.8	3.2	0.03
131g	Jn4	vr	3	-	-	-	n	3.93E-02	1.55E-03	1.02E-04	8.80E-06	-	-	5.86E-06	8.09E-07	-	-	4.16E-06	8.10E-07	0.62	0.09	0.61	0.12	287.3	4.8	3.2	0.07
131g	Jn5	vr	3	-	-	-	n	1.77E-02	9.52E-04	7.15E-05	3.97E-06	-	-	6.82E-06	3.65E-07	-	-	4.59E-06	3.21E-07	0.72	0.05	0.67	0.05	293.2	2.0	3.2	0.03
131g	Jn6	vr	3	-	-	-	n	7.28E-02	5.50E-03	1.57E-04	1.52E-05	-	-	6.40E-06	4.52E-07	-	-	4.99E-06	2.42E-07	0.68	0.05	0.73	0.04	293.7	2.0	3.2	0.03
131g	Jn7	vr	3	-	-	-	n	1.91E-02	1.38E-03	3.82E-05	2.58E-06	-	-	6.44E-06	3.60E-07	-	-	4.40E-06	1.58E-07	0.68	0.04	0.64	0.03	290.9	1.6	3.2	0.02
131g	Jn8	vr	3	-	-	-	n	1.70E-02	5.76E-04	7.04E-05	4.65E-06	-	-	9.09E-06	5.08E-07	-	-	6.83E-06	4.00E-07	0.96	0.06	1.00	0.07	310.1	2.0	3.4	0.03
131g	Jn9	vr	3	-	-	-	n	4.09E-03	2.41E-05	3.33E-05	2.19E-06	-	-	7.06E-06	3.80E-07	-	-	5.32E-06	2.82E-07	0.75	0.05	0.77	0.05	297.6	1.8	3.3	0.03
131g	Jn10	v	3	-	-	-	n	3.42E-03	8.53E-05	2.73E-05	1.99E-06	-	-	4.75E-06	3.33E-07	-	-	3.52E-06	2.09E-07	0.50	0.04	0.51	0.03	278.6	2.0	3.1	0.03
148j	LPQ3	v	2	-	-	500	n	8.73E-03	5.64E-04	1.92E-04	5.93E-05	-	-	5.06E-06	6.60E-07	-	-	3.25E-06	4.18E-07	0.54	0.07	0.47	0.06	278.3	3.7	3.1	0.05
148j	LPQ4	vr	2	-	-	45	n	4.50E-02	1.48E-03	3.59E-04	6.09E-05	-	-	1.08E-05	6.47E-07	-	-	8.37E-06	8.34E-07	1.14	0.08	1.22	0.13	319.7	2.8	3.5	0.04
148j	LPQ5	v	2	-	-	120	n	5.53E-03	4.31E-04	1.89E-04	5.26E-05	-	-	6.72E-06	6.47E-07	-	-	4.51E-06	6.22E-07	0.71	0.07	0.66	0.09	292.4	3.5	3.2	0.05
148j	LPQ7	vr	2	-	-	13	n	9.03E-02	3.70E-03	2.52E-04	6.71E-05	-	-	1.64E-05	1.09E-06	-	-	1.08E-05	8.47E-07	1.74	0.13	1.57	0.13	338.0	2.6	3.7	0.04
148j	NPT33	v	2	-	-	100	n	1.56E-02	1.99E-03	2.70E-04	7.68E-05	-	-	1.95E-05	2.17E-06	-	-	1.52E-05	1.87E-06	2.06	0.24	2.21	0.28	352.6	4.2	3.9	0.06
148j	NPT34	v	2	-	-	150	n	3.92E-02	2.16E-03	2.12E-04	1.33E-05	-	-	7.05E-06	5.17E-07	-	-	4.45E-06	2.89E-07	0.75	0.06	0.65	0.05	293.4	2.2	3.2	0.03
148j	NPT35	vr	2	-	-	18	n	1.31E-01	6.87E-03	3.95E-04	8.71E-05	-	-	2.10E-05	1.33E-06	-	-	1.61E-05	1.02E-06	2.23	0.16	2.34	0.17	356.5	2.5	3.9	0.04
148j	NPT36	v	2	-	-	125	n	3.61E-02	1.16E-03	2.48E-04	6.53E-05	-	-	1.16E-05	1.10E-06	-	-	7.84E-06	7.04E-07	1.23	0.12	1.14	0.11	319.9	3.1	3.5	0.05
148j	NPT37	v	2	-	-	38	y	1.15E-02	1.04E-03	2.84E-04	7.13E-05	-	-	7.98E-06	8.13E-07	-	-	5.97E-06	5.97E-07	0.84	0.09	0.87	0.09	303.4	3.1	3.3	0.05
148j	NPT38	v	2	-	-	125	y	7.10E-02	3.02E-03	3.42E-04	6.69E-05	-	-	1.78E-05	8.13E-07	-	-	1.39E-05	1.12E-06	1.88	0.11	2.02	0.18	347.4	2.5	3.8	0.04
148j	NPT39	v	2	-	-	63	n	3.20E-01	4.44E-02	5.28E-04	9.71E-05	-	-	4.69E-04	8.69E-05	-	-	3.42E-04	6.28E-05	49.61	9.35	49.76	9.28	612.8	12.1	6.7	0.18
148j	NPT40	vr	2	-	-	23	y	3.64E-02	1.48E-03	4.35E-04	8.06E-05	-	-	8.34E-06	8.68E-07	-	-	6.41E-06	8.06E-07	0.88	0.10	0.93	0.12	306.3	3.6	3.4	0.05
148j	NPT41	v	2	-	-	185	n	6.16E-03	5.67E-04	2.40E-04	7.02E-05	-	-	4.85E-06	4.84E-07	-	-	2.89E-06	4.67E-07	0.51	0.05	0.42	0.07	274.9	3.6	3.0	0.05
148j	NPT42	v	2	-	-	185	n	7.08E-03	5.98E-04	2.30E-04	6.45E-05	-	-	3.34E-06	4.73E-07	-	-	3.19E-06	6.06E-07	0.35	0.05	0.46	0.09	268.9	4.7	3.0	0.07
148j	NPT43	v	2	-	-	115	n	5.14E-02	2.69E-03	3.66E-04	1.01E-04	-	-	1.55E-05	9.31E-07	-	-	1.06E-05	8.15E-07	1.64	0.11	1.54	0.13	335.8	2.5	3.7	0.04

Sample	ID	Type	Session	Area ID	Vein #	g.s.	g.b.?	^{27}Al/^{30}Si	1σ	^{44}Ca/^{30}Si	1σ	^{56}Fe/^{30}Si	1σ	^{47}Ti/^{30}Si	1σ	^{48}Ti/^{30}Si	1σ	^{49}Ti/^{30}Si	1σ	^{47}Ti (ppm)	1σ	^{49}Ti (ppm)	1σ	T (°C)	1σ	P (kbar)	1σ
148j	NPT44	v	2	-	-	115	n	1.11E-02	1.45E-03	2.72E-04	8.62E-05	-	-	2.17E-05	2.59E-06	-	-	1.69E-05	1.81E-06	2.30	0.28	2.46	0.28	358.9	4.1	3.9	0.06
148j	NPT45	v	2	-	-	150	n	1.72E-01	2.63E-03	2.54E-04	6.98E-05	-	-	2.74E-05	1.36E-06	-	-	2.08E-05	1.25E-06	2.90	0.17	3.02	0.21	372.3	2.4	4.1	0.03
148j	NPT46	v	2	-	-	135	n	7.10E-03	6.03E-04	3.01E-04	8.31E-05	-	-	1.99E-06	3.15E-07	-	-	1.90E-06	3.92E-07	0.21	0.03	0.28	0.06	247.2	4.8	2.7	0.07
148j	NPT47	v	2	-	-	125	n	6.88E-03	5.55E-04	2.80E-04	8.13E-05	-	-	3.90E-06	4.56E-07	-	-	3.16E-06	4.75E-07	0.41	0.05	0.46	0.07	271.8	3.8	3.0	0.06
148j	NPT48	v	2	-	-	115	n	8.36E-03	7.59E-04	3.13E-04	8.12E-05	-	-	6.17E-05	1.05E-05	-	-	4.62E-05	7.63E-06	6.54	1.13	6.72	1.13	426.6	7.2	4.7	0.11
148j	NPT49	v	2	-	-	150	n	7.77E-03	6.56E-04	3.17E-04	8.79E-05	-	-	4.25E-06	6.09E-07	-	-	3.23E-06	4.80E-07	0.45	0.07	0.47	0.07	274.2	4.0	3.0	0.06
148j	NPT50	v	2	-	-	120	n	1.84E-01	2.87E-03	3.71E-04	9.40E-05	-	-	1.41E-05	8.60E-07	-	-	1.12E-05	1.19E-06	1.49	0.10	1.63	0.18	334.8	3.1	3.7	0.05
148j	NPT71	vr	2	-	-	15	y	5.99E-02	4.98E-03	3.41E-04	9.24E-05	-	-	1.21E-05	1.15E-06	-	-	8.22E-06	8.85E-07	1.28	0.13	1.20	0.13	322.2	3.4	3.5	0.05
148j	NPT72	vr	2	-	-	400	y	7.35E-02	8.99E-03	3.94E-04	9.09E-05	-	-	1.45E-05	1.35E-06	-	-	1.25E-05	1.26E-06	1.53	0.15	1.81	0.19	338.6	3.4	3.7	0.05
148j	NPT73	v	2	-	-	15	y	2.16E-02	1.46E-03	3.70E-04	9.91E-05	-	-	8.16E-06	1.01E-06	-	-	7.09E-06	8.73E-07	0.86	0.11	1.03	0.13	308.5	3.9	3.4	0.06
148j	NPT74	v	2	-	-	170	n	6.82E-03	5.26E-04	3.07E-04	8.10E-05	-	-	4.70E-06	5.49E-07	-	-	3.39E-06	5.48E-07	0.50	0.06	0.49	0.08	277.5	3.9	3.0	0.06
148j	NPT75	v	2	-	-	500	n	1.34E-02	1.56E-03	2.86E-04	8.83E-05	-	-	3.75E-06	5.97E-07	-	-	3.24E-06	5.83E-07	0.40	0.06	0.47	0.09	271.6	4.7	3.0	0.07
148j	NPT76	v	2	-	-	190	n	6.05E-03	5.29E-04	2.65E-04	7.46E-05	-	-	5.03E-06	6.88E-07	-	-	4.29E-06	5.83E-07	0.53	0.07	0.62	0.09	284.6	3.9	3.1	0.06
148j	NPT77	v	2	-	-	85	n	3.05E-02	8.51E-04	3.28E-04	7.73E-05	-	-	5.98E-04	9.22E-05	-	-	4.62E-04	7.02E-05	63.34	9.98	67.24	10.46	646.0	10.8	7.1	0.16
148j	NPT78	v	2	-	-	400	y	4.57E-02	4.10E-03	4.21E-04	1.04E-04	-	-	1.17E-05	1.04E-06	-	-	8.82E-06	7.26E-07	1.24	0.12	1.28	0.11	323.3	2.9	3.5	0.04
148j	NPT79	vr	2	-	-	500	n	4.55E-02	3.73E-03	4.02E-04	9.31E-05	-	-	1.62E-05	2.03E-06	-	-	1.05E-05	1.04E-06	1.71	0.22	1.53	0.16	336.9	3.9	3.7	0.06
148j	NPT80	vr	2	-	-	500	y	2.22E-02	2.92E-03	5.25E-04	9.39E-05	-	-	7.15E-06	1.24E-06	-	-	4.43E-06	1.29E-06	0.76	0.13	0.64	0.19	293.6	6.7	3.2	0.10
148j	NPT81	vr	2	-	-	500	y	8.53E-03	6.28E-04	3.09E-04	9.23E-05	-	-	4.36E-06	5.79E-07	-	-	4.28E-06	5.30E-07	0.46	0.06	0.62	0.08	281.6	3.7	3.1	0.05
148j	NPT82	v	2	-	-	250	n	7.69E-03	5.75E-04	2.71E-04	8.31E-05	-	-	6.65E-06	7.48E-07	-	-	5.21E-06	7.48E-07	0.70	0.08	0.76	0.11	295.7	3.9	3.2	0.06
148j	NPT83	v	2	-	-	300	n	9.97E-03	6.21E-04	2.64E-04	6.78E-05	-	-	6.23E-06	6.85E-07	-	-	4.23E-06	5.27E-07	0.66	0.08	0.62	0.08	289.1	3.4	3.2	0.05
148j	NPT84	v	2	-	-	100	n	7.99E-03	5.30E-04	2.66E-04	7.73E-05	-	-	4.23E-06	6.54E-07	-	-	3.19E-06	4.77E-07	0.45	0.07	0.46	0.07	273.7	4.2	3.0	0.06
148j	NPT85	v	2	-	-	500	n	1.04E-02	6.56E-04	3.15E-04	9.33E-05	-	-	6.09E-06	7.58E-07	-	-	5.18E-06	6.27E-07	0.64	0.08	0.75	0.09	293.5	3.7	3.2	0.05
148d	FJX0	qr	2	-	-	10	y	2.44E-02	4.02E-03	1.94E-04	3.54E-05	-	-	1.57E-05	2.39E-06	-	-	1.05E-05	1.61E-06	1.67	0.26	1.53	0.24	336.2	5.1	3.7	0.08
148d	FJX1	qr	2	-	-	25	n	3.22E-02	2.94E-03	2.22E-04	1.56E-05	-	-	1.74E-05	7.95E-07	-	-	1.38E-05	8.66E-07	1.84	0.10	2.02	0.14	346.7	2.2	3.8	0.03
148d	FJX2	qr	2	-	-	25	y	1.70E-02	8.70E-04	1.87E-04	2.48E-05	-	-	1.15E-05	1.31E-06	-	-	7.91E-06	7.93E-07	1.22	0.14	1.15	0.12	320.0	3.5	3.5	0.05
148d	FJX3	q	2	-	-	175	n	5.26E-02	6.87E-04	1.32E-04	2.00E-05	-	-	9.61E-05	6.14E-06	-	-	7.31E-05	4.73E-06	10.17	0.73	10.64	0.77	461.1	3.3	5.1	0.05
148d	FJX4	q	2	-	-	500	n	1.38E-02	1.80E-03	1.15E-04	2.20E-05	-	-	1.02E-04	1.62E-05	-	-	7.40E-05	1.20E-05	10.76	1.75	10.77	1.78	463.9	7.6	5.1	0.45
148d	FJX5	q	2	-	-	200	n	9.47E-03	5.84E-04	1.09E-04	2.18E-05	-	-	6.36E-05	2.71E-06	-	-	4.84E-05	2.51E-06	6.73	0.36	7.04	0.43	429.3	2.5	4.7	0.14
148d	FJX6	q	2	-	-	200	n	5.27E-03	6.35E-05	4.01E-05	4.66E-06	-	-	5.35E-05	2.16E-06	-	-	3.96E-05	1.63E-06	5.67	0.29	5.77	0.30	415.9	2.1	4.6	0.13
148d	FJX7	qr	2	-	-	250	n	1.14E-02	4.00E-04	1.48E-04	2.92E-05	-	-	1.09E-05	8.45E-07	-	-	7.21E-06	8.21E-07	1.15	0.10	1.05	0.12	316.1	3.1	3.5	0.18
148d	FJX8	q	2	-	-	250	n	8.99E-03	9.78E-05	4.89E-05	7.24E-06	-	-	8.48E-06	7.92E-07	-	-	7.69E-06	8.30E-07	0.90	0.09	1.12	0.13	311.6	3.3	3.4	0.19
148d	FJX9	q	2	-	-	250	y	1.51E-02	2.63E-04	1.33E-04	2.70E-05	-	-	4.82E-05	3.31E-06	-	-	3.40E-05	2.26E-06	5.10	0.39	4.95	0.37	406.9	3.0	4.5	0.18
148d	FJX10	q	2	-	-	250	y	3.99E-01	2.10E-02	2.29E-04	3.07E-05	-	-	1.38E-04	4.08E-06	-	-	9.83E-05	3.21E-06	14.59	0.64	14.32	0.66	488.5	2.2	5.4	0.13
148d	FJX11	qr	2	-	-	250	y	4.54E-02	1.00E-02	2.26E-04	3.22E-05	-	-	3.04E-05	1.98E-06	-	-	2.45E-05	1.37E-06	3.22	0.23	3.57	0.23	380.8	2.6	4.2	0.15
148d	FJX12	q	2	-	-	125	n	1.64E-02	2.61E-03	1.74E-04	4.06E-05	-	-	8.95E-06	8.37E-07	-	-	7.09E-06	9.09E-07	0.95	0.09	1.03	0.14	310.7	3.6	3.4	0.21
148d	FJX13	q	2	-	-	75	y	1.17E-02	8.91E-04	2.03E-04	5.10E-05	-	-	6.29E-05	8.02E-06	-	-	4.64E-05	6.07E-06	6.66	0.88	6.75	0.91	427.4	5.7	4.7	0.33
148d	FJX14	q	2	-	-	125	n	7.23E-03	4.94E-04	2.39E-04	7.46E-05	-	-	7.61E-06	6.70E-07	-	-	5.98E-06	6.16E-07	0.81	0.08	0.87	0.09	302.3	3.0	3.3	0.18
148d	FJX15	q	2	-	-	35	y	1.41E-02	8.96E-04	2.44E-04	6.28E-05	-	-	1.69E-05	1.53E-06	-	-	1.20E-05	1.20E-06	1.78	0.17	1.74	0.18	341.6	3.4	3.7	0.20
148d	FJX16	q	2	-	-	125	n	3.33E-02	1.70E-03	1.51E-04	3.47E-05	-	-	1.67E-04	7.60E-06	-	-	1.18E-04	5.62E-06	17.68	0.99	17.15	0.99	505.0	2.9	5.5	0.17
148d	FJX17	q	2	-	-	125	n	7.61E-03	5.83E-04	1.92E-04	5.57E-05	-	-	1.01E-04	6.73E-06	-	-	7.40E-05	5.96E-06	10.68	0.79	10.77	0.94	463.5	3.8	5.1	0.22
148d	FJX18	qr	2	-	-	15	y	9.33E-03	8.89E-04	2.18E-04	6.30E-05	-	-	8.02E-06	7.83E-07	-	-	6.49E-06	6.93E-07	0.85	0.09	0.94	0.11	305.7	3.2	3.4	0.19
148d	FJX19	q	2	-	-	250	n	6.84E-02	1.41E-03	1.99E-04	5.15E-05	-	-	6.21E-06	7.72E-07	-	-	4.95E-06	6.79E-07	0.66	0.08	0.72	0.10	292.8	3.9	3.2	0.23
148d	FJX20	q	2	-	-	250	n	5.35E-01	8.30E-03	1.34E-04	3.98E-05	-	-	4.15E-05	1.43E-06	-	-	2.90E-05	1.23E-06	4.40	0.21	4.23	0.23	396.5	2.0	4.4	0.12
148d	FJX21	q	2	-	-	250	n	6.93E-02	3.61E-03	1.33E-04	4.35E-05	-	-	7.08E-06	8.52E-07	-	-	4.95E-06	7.16E-07	0.75	0.09	0.72	0.11	295.9	4.0	3.2	0.23
148d	FJX22	q	2	-	-	140	n	7.71E-03	6.47E-04	2.64E-04	8.05E-05	-	-	2.13E-05	1.36E-06	-	-	1.62E-05	8.84E-07	2.26	0.16	2.36	0.15	357.2	2.4	3.9	0.14
148d	FJX23	q	2	-	-	140	n	8.70E-03	5.26E-04	2.67E-04	7.15E-05	-	-	1.87E-05	1.40E-06	-	-	1.28E-05	1.39E-06	1.98	0.16	1.87	0.21	346.5	3.3	3.8	0.20
148d	FJX24	q	2	-	-	500	y	2.71E-02	1.07E-03	2.49E-04	7.58E-05	-	-	4.93E-04	1.78E-05	-	-	3.57E-04	1.47E-05	52.20	2.54	51.97	2.73	618.4	3.3	6.8	0.19
148d	FJX25	q	2	-	-	500	n	5.86E-02	6.64E-03	2.37E-04	6.18E-05	-	-	1.32E-03	5.95E-05	-	-	9.28E-04	4.56E-05	140.17	7.79	135.06	7.98	750.6	4.8	8.2	0.28
148d	FJX26	q	2	-	-	500	n	9.11E-03	7.01E-04	1.12E-04	1.44E-05	-	-	1.22E-03	5.56E-05	-	-	8.97E-04	4.01E-05	128.95	7.24	130.64	7.23	741.6	4.6	8.1	0.27
148d	FJX27	q	2	-	-	500	n	7.97E-02	1.61E-03	2.08E-04	5.16E-05	-	-	1.14E-03	4.05E-05	-	-	8.33E-04	2.73E-05	120.77	5.83	121.28	5.61	730.9	3.8	8.0	0.22
148d	FJX28	q	2	-	-	500	n	2.67E-02	7.73E-04	2.22E-04	6.86E-05	-	-	6.36E-04	2.02E-05	-	-	4.66E-04	1.45E-05	67.39	3.07	67.79	3.07	650.4	3.2	7.1	0.19
148d	FJX29	q	2	-	-	500	n	1.19E-02	5.78E-04	2.66E-04	6.88E-05	-	-	8.89E-04	4.11E-05	-	-	6.67E-04	2.96E-05	94.16	5.33	97.09	5.36	696.7	4.2	7.6	0.25
148d	FJX30	q	2	-	-	500	n	8.07E-02	2.93E-03	2.62E-04	7.31E-05	-	-	1.84E-03	5.66E-05	-	-	1.35E-03	4.15E-05	194.95	8.75	196.82	8.83	809.0	4.1	8.9	0.24
148d	FJX31	q	2	-	-	500	n	1.12E-02	6.79E-04	2.85E-04	7.75E-05	-	-	1.17E-05	9.17E-07	-	-	9.01E-06	7.56E-07	1.23	0.11	1.31	0.12	323.7	2.8	3.6	0.16
148d	FJX32	q	2	-	-	500	n	1.47E-01	3.25E-02	3.34E-04	9.35E-05	-	-	5.58E-05	3.69E-06	-	-	4.15E-05	2.35E-06	5.91	0.44	6.04	0.39	419.1	2.9	4.6	0.17
148d	FJX33	q	2	-	-	500	n	1.99E-02	1.92E-04	5.65E-05	5.99E-06	-	-	4.73E-05	2.11E-06	-	-	3.39E-05	1.36E-06	5.01	0.28	4.94	0.26	406.2	2.1	4.5	0.13

Sample	ID	Type	Session	Area ID	Vein #	g.s.	g.b.?	^{27}Al/^{30}Si	1σ	^{44}Ca/^{30}Si	1σ	^{56}Fe/^{30}Si	1σ	^{47}Ti/^{30}Si	1σ	^{48}Ti/^{30}Si	1σ	^{49}Ti/^{30}Si	1σ	^{47}Ti (ppm)	1σ	^{49}Ti (ppm)	1σ	T (°C)	1σ	P (kbar)	1σ
148d	FJX34	q	2	-	-	500	n	6.63E-03	5.04E-04	2.25E-04	7.02E-05	-	-	1.81E-04	1.99E-05	-	-	1.30E-04	1.48E-05	19.22	2.19	18.96	2.25	513.4	6.1	5.6	0.36
148d	FJX35	q	2	-	-	500	n	1.18E-02	5.43E-04	2.55E-04	7.23E-05	-	-	2.64E-05	1.50E-06	-	-	1.93E-05	1.23E-06	2.80	0.18	2.82	0.20	369.0	2.5	4.0	0.15
148d	FJX36	qr	2	-	-	15	y	7.16E-02	7.77E-03	2.73E-04	7.10E-05	-	-	8.76E-05	5.30E-06	-	-	6.37E-05	4.57E-06	9.28	0.64	9.27	0.73	452.0	3.3	5.0	0.20
148d	FJX37	qr	2	-	-	40	y	2.63E-02	3.27E-03	2.99E-04	7.95E-05	-	-	1.49E-05	1.13E-06	-	-	1.02E-05	7.70E-07	1.58	0.13	1.49	0.12	333.9	2.7	3.7	0.16
148d	FJX38	q	2	-	-	40	n	8.26E-03	1.48E-04	4.86E-05	6.70E-06	-	-	1.22E-05	8.94E-07	-	-	8.23E-06	8.23E-07	1.30	0.10	1.20	0.13	322.7	2.9	3.5	0.17
148d	FJX39	q	2	-	-	50	y	1.28E-02	7.44E-04	3.45E-04	9.95E-05	-	-	1.38E-05	8.78E-07	-	-	1.02E-05	1.07E-06	1.47	0.10	1.49	0.16	331.7	3.0	3.6	0.18
148d	FJX40	q	2	-	-	500	n	2.01E-02	2.38E-04	3.24E-04	9.42E-05	-	-	1.79E-04	1.97E-05	-	-	1.35E-04	1.49E-05	18.97	2.17	19.67	2.27	514.5	6.0	5.6	0.35
148d	FJX41	q	2	-	-	500	n	3.38E-02	5.47E-03	4.00E-04	1.02E-04	-	-	1.61E-04	1.06E-05	-	-	1.14E-04	6.82E-06	17.06	1.25	16.64	1.13	502.0	3.6	5.5	0.21
148d	FJX42	q	2	-	-	500	n	1.09E-02	8.75E-04	3.50E-04	9.83E-05	-	-	2.00E-04	1.98E-05	-	-	1.45E-04	1.42E-05	21.12	2.20	21.09	2.18	522.8	5.5	5.7	0.33
148d	FJX43	q	2	-	-	200	n	9.52E-03	7.40E-04	3.05E-04	8.32E-05	-	-	3.81E-04	2.12E-05	-	-	2.80E-04	1.41E-05	40.29	2.60	40.76	2.45	589.6	3.8	6.5	0.23
148d	FJX44	q	2	-	-	200	n	1.22E-02	1.78E-03	3.77E-04	1.14E-04	-	-	1.66E-04	3.51E-05	-	-	1.08E-04	2.36E-05	17.52	3.76	15.76	3.47	500.9	11.0	5.5	0.65
148d	FJX45	q	2	-	-	85	n	6.69E-03	6.36E-04	3.35E-04	9.99E-05	-	-	9.27E-06	9.60E-07	-	-	7.32E-06	8.50E-07	0.98	0.11	1.07	0.13	312.4	3.5	3.4	0.21
148d	FJX46	q	2	-	-	125	n	7.95E-03	6.82E-04	3.30E-04	9.72E-05	-	-	9.74E-06	6.51E-07	-	-	8.76E-06	7.67E-07	1.03	0.08	1.28	0.12	318.5	2.7	3.5	0.16
148d	FJX47	q	2	-	-	95	y	9.72E-03	1.15E-03	3.73E-04	9.49E-05	-	-	6.43E-06	6.88E-07	-	-	5.64E-06	6.23E-07	0.68	0.08	0.82	0.09	296.9	3.3	3.3	0.20
148d	FJX48	q	2	-	-	500	n	2.64E-02	1.21E-03	3.83E-04	9.22E-05	-	-	3.77E-04	3.01E-05	-	-	2.65E-04	2.26E-05	39.90	3.45	38.57	3.52	586.0	5.4	6.4	0.32
148d	FJX49	q	2	-	-	500	n	2.62E-01	3.23E-03	4.18E-04	1.06E-04	-	-	1.25E-03	5.46E-05	-	-	9.06E-04	4.29E-05	131.88	7.21	131.86	7.59	744.0	4.6	8.2	0.27
148d	FJX51	q	2	-	-	500	n	1.07E-01	9.90E-04	3.84E-04	1.08E-04	-	-	1.84E-03	2.89E-05	-	-	1.31E-03	2.68E-05	194.48	7.05	190.33	7.34	805.9	3.4	8.8	0.20
148d	FJX52	q	2	-	-	175	n	7.88E-03	7.66E-04	3.63E-04	9.52E-05	-	-	6.58E-06	7.53E-07	-	-	5.17E-06	6.89E-07	0.70	0.08	0.75	0.10	295.2	3.7	3.2	0.22
148d	FJX53	q	2	-	-	125	n	1.81E-02	1.64E-03	4.09E-04	1.13E-04	-	-	9.13E-05	8.00E-06	-	-	6.94E-05	6.71E-06	9.67	0.90	10.11	1.03	457.0	4.5	5.0	0.26
148d	FJX54	q	2	-	-	100	y	5.31E-02	8.55E-03	5.62E-04	1.15E-04	-	-	1.74E-05	2.40E-06	-	-	1.41E-05	1.83E-06	1.84	0.26	2.05	0.27	347.1	4.7	3.8	0.27
148d	FJX56	q	2	-	-	300	y	1.34E-02	8.95E-04	3.76E-04	9.33E-05	-	-	3.42E-05	1.88E-06	-	-	2.54E-05	1.15E-06	3.62	0.23	3.69	0.21	385.7	2.3	4.2	0.13
148d	FJX57	q	2	-	-	300	y	8.21E-03	1.47E-04	5.63E-05	6.92E-06	-	-	3.18E-05	2.99E-06	-	-	2.30E-05	2.08E-06	3.36	0.34	3.35	0.32	380.1	3.7	4.2	0.22
148d	FJX58	q	2	-	-	300	y	1.17E-02	9.99E-04	4.11E-04	9.44E-05	-	-	1.04E-04	8.68E-06	-	-	7.51E-05	7.17E-06	11.03	0.99	10.93	1.10	465.5	4.4	5.1	0.26
148d	FJX59	q	2	-	-	300	y	5.20E-03	1.59E-04	5.71E-05	9.20E-06	-	-	7.80E-05	6.23E-06	-	-	5.60E-05	4.98E-06	8.26	0.71	8.15	0.77	442.5	4.0	4.9	0.23
148d	FJX60	q	2	-	-	500	n	1.35E-02	1.04E-03	3.99E-04	9.64E-05	-	-	4.20E-04	9.03E-05	-	-	3.03E-04	6.25E-05	44.51	9.67	44.14	9.22	599.6	13.4	6.6	0.79
148d	FJX61	q	2	-	-	500	n	1.04E-02	9.02E-04	5.11E-04	1.18E-04	-	-	7.86E-05	7.17E-06	-	-	5.75E-05	4.89E-06	8.32	0.81	8.37	0.76	443.8	4.2	4.9	0.24
148d	FJX62	q	2	-	-	500	n	7.21E-03	3.00E-04	7.91E-05	5.85E-06	-	-	4.76E-05	3.42E-06	-	-	3.79E-05	2.60E-06	5.04	0.40	5.52	0.42	410.3	3.1	4.5	0.18
148d	FJX63	q	2	-	-	500	n	2.27E-02	2.68E-03	3.57E-04	7.99E-05	-	-	1.76E-04	8.39E-06	-	-	1.33E-04	6.96E-06	18.63	1.08	19.34	1.19	512.9	3.1	5.6	0.18
148d	FJX64	q	2	-	-	500	n	1.21E-01	2.08E-03	4.83E-04	1.14E-04	-	-	1.48E-03	5.90E-05	-	-	1.09E-03	4.07E-05	156.99	8.08	158.13	7.87	772.2	4.4	8.5	0.26
148d	FJX65	q	2	-	-	500	n	8.93E-02	4.24E-03	4.80E-04	1.12E-04	-	-	7.76E-04	4.20E-05	-	-	5.73E-04	3.57E-05	82.17	5.19	83.37	5.86	676.9	4.9	7.4	0.29
148d	FJX70	q	2	-	-	500	n	6.53E-03	4.72E-04	1.69E-04	3.87E-05	-	-	1.77E-06	2.59E-07	-	-	1.59E-06	3.69E-07	0.19	0.03	0.23	0.05	241.2	4.9	2.6	0.29
148d	FJX72	q	2	-	-	500	n	7.80E-03	4.81E-04	1.92E-04	3.37E-05	-	-	1.32E-06	2.23E-07	-	-	1.19E-06	2.78E-07	0.14	0.02	0.17	0.04	229.7	5.0	2.5	0.29
148d	FJX79	qr	2	-	-	15	y	6.89E-03	4.77E-04	1.92E-04	5.18E-05	-	-	1.05E-05	7.29E-07	-	-	6.95E-06	6.06E-07	1.11	0.09	1.01	0.09	314.2	2.6	3.4	0.15
148d	FJX80	qr	2	-	-	20	y	1.60E-02	6.95E-04	2.27E-04	2.20E-05	-	-	7.16E-05	2.29E-06	-	-	5.28E-05	2.39E-06	7.59	0.35	7.69	0.43	437.1	2.2	4.8	0.13
148d	FJX81	qr	2	-	-	20	y	1.27E-02	9.70E-04	2.48E-04	6.94E-05	-	-	2.03E-05	1.16E-06	-	-	1.44E-05	8.84E-07	2.15	0.14	2.10	0.15	352.3	2.3	3.9	0.14
148d	FJX82	q	2	-	-	150	n	3.81E-02	2.71E-04	2.22E-04	4.97E-05	-	-	1.78E-04	1.45E-05	-	-	1.19E-04	8.05E-06	18.80	1.66	17.37	1.30	508.4	4.3	5.6	0.25
148d	FJX83	q	2	-	-	150	n	7.38E-03	5.26E-04	2.82E-04	7.15E-05	-	-	4.68E-05	2.83E-06	-	-	3.31E-05	1.69E-06	4.95	0.34	4.82	0.29	404.9	2.6	4.4	0.15
148d	FJX84	q	2	-	-	75	y	7.16E-02	1.87E-03	2.89E-04	5.07E-05	-	-	2.67E-04	7.65E-06	-	-	2.00E-04	6.11E-06	28.27	1.23	29.13	1.30	552.9	2.5	6.1	0.15
148d	FJX85	q	2	-	-	100	n	1.06E-02	4.44E-04	2.29E-04	5.81E-05	-	-	3.22E-05	7.80E-06	-	-	2.01E-05	4.19E-06	3.40	0.83	2.93	0.62	376.4	8.6	4.1	0.50
148d	g1	q	2	-	-	300	n	5.97E-03	1.18E-03	1.21E-04	1.24E-05	-	-	1.24E-06	3.28E-07	-	-	9.81E-07	2.62E-07	0.13	0.04	0.14	0.04	224.9	6.1	2.5	0.36
148d	g1_0	q	2	-	-	300	n	2.18E-02	1.52E-03	9.26E-05	1.00E-05	-	-	3.22E-06	4.58E-07	-	-	3.00E-06	5.06E-07	0.34	0.05	0.44	0.08	266.7	4.3	2.9	0.25
148d	g1_1	q	2	-	-	300	n	6.39E-03	2.81E-04	9.64E-05	9.18E-06	-	-	2.01E-06	3.69E-07	-	-	1.87E-06	2.86E-07	0.21	0.04	0.27	0.04	246.9	4.2	2.7	0.24
148d	g1_2	q	2	-	-	300	n	7.50E-03	3.49E-04	8.69E-05	1.02E-05	-	-	1.35E-06	2.67E-07	-	-	1.16E-06	2.61E-07	0.14	0.03	0.17	0.04	229.7	5.0	2.5	0.29
148d	g1_3	q	2	-	-	300	n	4.60E-01	6.80E-03	4.31E-04	2.00E-05	-	-	5.32E-05	2.10E-06	-	-	3.82E-05	1.71E-06	5.63	0.29	5.56	0.31	414.4	2.2	4.5	0.13
148d	g1_4	q	2	-	-	80	n	4.85E-03	2.60E-04	9.35E-05	9.56E-06	-	-	2.59E-06	4.08E-07	-	-	2.15E-06	2.64E-07	0.27	0.04	0.31	0.04	254.8	3.6	2.8	0.21
148d	g1_5	q	2	-	-	80	y	3.24E-03	1.95E-04	8.97E-05	1.20E-05	-	-	4.89E-06	6.23E-07	-	-	3.39E-06	3.95E-07	0.52	0.07	0.49	0.06	278.4	3.5	3.1	0.20
148d	g1_6	q	2	-	-	80	n	2.94E-03	1.73E-04	8.84E-05	8.14E-06	-	-	5.06E-06	4.73E-07	-	-	3.80E-06	4.19E-07	0.54	0.05	0.55	0.06	281.8	3.0	3.1	0.17
148d	g1_7	q	2	-	-	300	n	4.89E-03	3.03E-04	9.53E-05	1.18E-05	-	-	1.32E-06	2.48E-07	-	-	5.09E-07	1.56E-07	0.14	0.03	0.07	0.02	215.9	5.1	2.4	0.30
148d	Tnt8	qr	2	-	-	100	y	2.84E-02	4.61E-04	1.56E-04	2.12E-05	-	-	8.66E-06	4.46E-07	-	-	7.04E-06	7.68E-07	0.92	0.06	1.02	0.12	309.7	2.9	3.4	0.17
148d	Tnt9	q	2	-	-	300	n	1.17E-01	3.83E-03	7.66E-05	1.33E-05	-	-	1.87E-06	3.07E-07	-	-	1.82E-06	4.08E-07	0.20	0.03	0.26	0.06	245.0	5.1	2.7	0.30
148d	Tnt10	q	2	-	-	300	n	4.21E-03	3.08E-04	9.85E-05	1.14E-05	-	-	1.32E-06	2.60E-07	-	-	1.42E-06	2.61E-07	0.14	0.03	0.21	0.04	233.8	4.5	2.6	0.27
148d	Tnt11	q	2	-	-	300	n	5.75E-03	4.70E-04	9.25E-05	1.27E-05	-	-	2.69E-06	4.03E-07	-	-	2.07E-06	3.10E-07	0.29	0.04	0.30	0.05	254.7	3.9	2.8	0.23
148d	Tnt12	q	2	-	-	50	n	1.03E-02	3.38E-04	1.85E-04	1.32E-05	-	-	1.11E-05	7.87E-07	-	-	7.23E-06	4.50E-07	1.17	0.09	1.05	0.07	316.6	2.3	3.5	0.14
148d	Tnt13	q	2	-	-	50	n	5.08E-03	3.92E-04	1.08E-04	1.38E-05	-	-	6.30E-06	5.83E-07	-	-	4.23E-06	5.11E-07	0.67	0.07	0.62	0.08	289.4	3.2	3.2	0.19
148d	Tnt14	q	2	-	-	40	n	2.54E-02	3.92E-04	1.03E-04	9.96E-06	-	-	8.55E-06	6.06E-07	-	-	6.90E-06	5.09E-07	0.91	0.07	1.01	0.08	308.9	2.4	3.4	0.14
148d	Tnt15	qr	2	-	-	25	y	1.58E-02	9.33E-04	1.21E-04	1.41E-05	-	-	1.18E-05	8.31E-07	-	-	9.14E-06	6.55E-07	1.25	0.10	1.33	0.10	324.4	2.5	3.6	0.15

Sample	ID	Type	Session	Area ID	Vein #	g.s.	g.b.?	^{27}Al/^{30}Si	1σ	^{44}Ca/^{30}Si	1σ	^{56}Fe/^{30}Si	1σ	^{47}Ti/^{30}Si	1σ	^{48}Ti/^{30}Si	1σ	^{49}Ti/^{30}Si	1σ	^{47}Ti (ppm)	1σ	^{49}Ti (ppm)	1σ	T (°C)	1σ	P (kbar)	1σ
148d	Tnt16	q	2	-	-	60	y	5.76E-03	3.03E-04	8.68E-05	1.24E-05	-	-	6.02E-06	6.30E-07	-	-	5.21E-06	4.68E-07	0.64	0.07	0.76	0.07	293.4	2.9	3.2	0.17
148d	Tnt17	q	2	-	-	60	n	6.34E-03	3.66E-04	1.06E-04	9.64E-06	-	-	3.71E-06	4.89E-07	-	-	3.31E-06	4.85E-07	0.39	0.05	0.48	0.07	271.9	3.9	3.0	0.23
148d	Tnt18	q	2	-	-	50	y	1.59E-02	2.40E-04	1.06E-04	1.75E-05	-	-	7.82E-06	5.74E-07	-	-	7.11E-06	6.84E-07	0.83	0.07	1.04	0.11	307.6	2.8	3.4	0.17
148d	Tnt19	q	2	-	-	75	n	5.01E-03	2.99E-04	9.43E-05	1.04E-05	-	-	2.49E-05	1.36E-06	-	-	1.73E-05	8.21E-07	2.64	0.17	2.51	0.15	363.7	2.2	4.0	0.13
148d	Tnt20	q	2	-	-	35	y	2.87E-02	2.48E-04	5.80E-05	5.93E-06	-	-	1.11E-05	7.81E-07	-	-	8.35E-06	7.24E-07	1.17	0.09	1.22	0.11	320.4	2.7	3.5	0.16
148d	Tnt21	q	2	-	-	75	n	5.30E-03	3.02E-04	1.01E-04	1.28E-05	-	-	2.45E-05	1.09E-06	-	-	1.67E-05	1.03E-06	2.60	0.14	2.43	0.17	362.2	2.2	4.0	0.13
148d	Tnt22	q	2	-	-	100	n	1.77E-02	3.51E-04	9.07E-05	1.20E-05	-	-	5.65E-05	2.60E-06	-	-	3.61E-05	1.53E-06	5.98	0.34	5.26	0.28	414.7	2.3	4.6	0.13
148d	Tnt23	q	2	-	-	100	n	1.62E-02	2.89E-03	9.26E-05	1.41E-05	-	-	7.31E-06	8.47E-07	-	-	4.74E-06	7.16E-07	0.77	0.09	0.69	0.11	295.7	4.0	3.2	0.23
148d	Tnt24	q	2	-	-	60	n	5.97E-03	2.79E-04	1.09E-04	1.30E-05	-	-	4.87E-06	4.91E-07	-	-	3.28E-06	4.71E-07	0.52	0.05	0.48	0.07	277.6	3.5	3.0	0.20
148d	Tnt25	q	2	-	-	60	n	4.60E-03	3.03E-04	8.86E-05	1.20E-05	-	-	3.84E-06	4.71E-07	-	-	2.17E-06	3.52E-07	0.41	0.05	0.32	0.05	263.6	3.7	2.9	0.22
148d	Tnt26	q	2	-	-	300	n	7.03E-03	3.81E-04	1.20E-04	1.40E-05	-	-	1.78E-06	2.63E-07	-	-	1.68E-06	3.85E-07	0.19	0.03	0.24	0.06	242.4	5.0	2.7	0.29
148d	Tnt27	q	2	-	-	90	n	1.61E-02	3.06E-03	1.05E-04	1.29E-05	-	-	8.18E-06	1.11E-06	-	-	6.26E-06	6.72E-07	0.87	0.12	0.91	0.10	305.2	3.8	3.4	0.22
148d	Tnt28	q	2	-	-	250	n	1.52E-02	2.96E-03	1.10E-04	1.44E-05	-	-	4.90E-04	3.41E-05	-	-	3.64E-04	2.41E-05	51.88	3.99	52.93	3.92	619.1	4.9	6.8	0.29
148d	Tnt29	q	2	-	-	250	n	6.37E-03	3.63E-04	1.17E-04	1.58E-05	-	-	6.19E-04	4.17E-05	-	-	4.58E-04	3.14E-05	65.49	4.91	66.74	5.07	647.6	5.2	7.1	0.31
148d	Tnt30	q	2	-	-	125	n	5.40E-03	3.33E-04	9.67E-05	1.31E-05	-	-	5.77E-04	4.60E-05	-	-	4.32E-04	3.68E-05	61.10	5.27	62.96	5.74	639.6	6.1	7.0	0.36
148d	Tnt31	q	2	-	-	125	n	2.46E-02	3.11E-03	1.11E-04	1.41E-05	-	-	4.68E-04	1.17E-05	-	-	3.55E-04	1.13E-05	49.52	2.04	51.73	2.36	615.0	2.8	6.8	0.17
148d	Tnt32	q	2	-	-	350	n	7.27E-03	3.79E-04	9.76E-05	1.22E-05	-	-	4.94E-04	3.26E-05	-	-	3.62E-04	2.20E-05	52.34	3.85	52.65	3.64	619.3	4.7	6.8	0.28
148d	Tnt33	q	2	-	-	350	n	5.22E-03	1.47E-04	5.13E-05	4.69E-06	-	-	4.41E-04	3.17E-05	-	-	3.41E-04	2.54E-05	46.68	3.69	49.62	4.03	609.1	5.2	6.7	0.30
148d	Tnt34	q	2	-	-	175	n	4.58E-03	2.84E-04	8.54E-05	1.10E-05	-	-	1.95E-05	1.77E-06	-	-	1.67E-05	1.31E-06	2.06	0.20	2.43	0.21	355.6	3.1	3.9	0.18
148d	Tnt35	q	2	-	-	175	n	1.65E-02	2.89E-03	1.15E-04	2.23E-05	-	-	2.22E-05	1.15E-06	-	-	1.63E-05	1.01E-06	2.35	0.14	2.37	0.17	358.5	2.3	3.9	0.14
148d	Tnt36	q	2	-	-	175	n	4.96E-03	3.31E-04	9.64E-05	1.01E-05	-	-	1.28E-05	8.42E-07	-	-	9.91E-06	7.43E-07	1.35	0.10	1.44	0.12	328.7	2.5	3.6	0.15
148d	Tnt37	q	2	-	-	30	n	4.37E-03	1.94E-04	6.75E-05	1.08E-05	-	-	3.33E-06	4.14E-07	-	-	1.84E-06	3.04E-07	0.35	0.05	0.27	0.05	257.1	3.7	2.8	0.22
148d	Tnt38	q	2	-	-	300	y	6.54E-03	3.44E-04	1.05E-04	1.33E-05	-	-	3.18E-06	4.54E-07	-	-	1.85E-06	3.09E-07	0.34	0.05	0.27	0.05	256.1	4.0	2.8	0.23
148d	Tnt39	q	2	-	-	20	y	1.99E-02	3.37E-03	1.77E-04	2.29E-05	-	-	8.10E-06	7.51E-07	-	-	6.22E-06	6.87E-07	0.86	0.08	0.91	0.10	304.8	3.2	3.3	0.19
148d	Tnt40	q	2	-	-	350	n	1.14E-02	9.37E-04	1.19E-04	1.38E-05	-	-	1.87E-06	2.82E-07	-	-	1.26E-06	3.52E-07	0.20	0.03	0.18	0.05	237.5	5.3	2.6	0.31
148d	Tnt83	q	2	-	-	85	n	1.20E-02	5.35E-04	1.40E-04	2.05E-05	-	-	5.53E-06	5.27E-07	-	-	5.32E-06	5.66E-07	0.59	0.06	0.77	0.09	292.2	3.1	3.2	0.18
148d	Tnt84	q	2	-	-	85	n	1.09E-02	2.86E-04	1.32E-04	2.03E-05	-	-	7.02E-06	5.18E-07	-	-	5.43E-06	3.55E-07	0.74	0.06	0.79	0.06	298.0	2.2	3.3	0.13
148d	Tnt85	q	2	-	-	75	y	7.89E-03	3.54E-04	8.92E-05	1.42E-05	-	-	7.04E-06	5.84E-07	-	-	5.15E-06	6.19E-07	0.75	0.07	0.75	0.09	296.7	3.1	3.3	0.19
148d	Tnt86	q	2	-	-	90	n	3.96E-03	7.16E-05	4.59E-05	5.87E-06	-	-	4.88E-06	6.41E-07	-	-	3.64E-06	4.41E-07	0.52	0.07	0.53	0.07	280.0	3.6	3.1	0.21
148d	Tnt87	q	2	-	-	90	n	5.67E-03	5.52E-04	9.31E-05	1.59E-05	-	-	6.87E-06	7.40E-07	-	-	4.87E-06	6.25E-07	0.73	0.08	0.71	0.09	294.8	3.5	3.2	0.21
148d	Tnt88	q	2	-	-	350	n	4.61E-02	3.77E-03	1.33E-04	2.60E-05	-	-	4.92E-06	7.97E-07	-	-	3.74E-06	5.74E-07	0.52	0.09	0.54	0.09	280.8	4.4	3.1	0.26
148d	Tnt89	q	2	-	-	350	n	5.18E-03	3.15E-04	1.23E-04	2.16E-05	-	-	2.22E-06	3.61E-07	-	-	1.14E-06	2.10E-07	0.24	0.04	0.17	0.03	239.3	4.2	2.6	0.25
148d	In1_1	qr	2	-	-	10	n	5.08E-02	3.50E-03	6.36E-05	4.31E-06	-	-	2.84E-05	2.01E-06	-	-	2.07E-05	1.26E-06	3.00	0.23	3.01	0.21	373.2	2.7	4.1	0.16
148d	In1_2	qr	2	-	-	8	n	7.45E-02	1.34E-03	6.77E-05	3.95E-06	-	-	1.06E-05	6.73E-07	-	-	7.72E-06	5.03E-07	1.12	0.08	1.12	0.08	317.1	2.2	3.5	0.13
148d	In1_5	qr	2	-	-	300	n	2.57E-02	1.89E-03	3.88E-04	1.44E-04	-	-	1.99E-05	1.19E-06	-	-	1.31E-05	9.66E-07	2.11	0.14	1.91	0.15	349.0	2.5	3.8	0.15
148d	In1_6	qr	2	-	-	5	y	2.02E-02	1.21E-03	1.66E-04	1.67E-05	-	-	1.38E-05	9.80E-07	-	-	1.05E-05	7.17E-07	1.46	0.11	1.53	0.12	332.4	2.5	3.6	0.15
148d	In1_7	q	2	-	-	90	n	2.57E-01	1.41E-02	1.72E-04	1.12E-05	-	-	1.02E-04	2.81E-06	-	-	7.69E-05	3.11E-06	10.77	0.46	11.20	0.58	465.5	2.2	5.1	0.13
148d	In1_8	q	2	-	-	90	n	7.10E-02	3.18E-02	3.19E-04	5.94E-05	-	-	1.27E-04	2.33E-05	-	-	1.04E-04	2.51E-05	13.47	2.51	15.08	3.69	487.4	10.9	5.4	0.64
148d	In1_9	q	2	-	-	90	n	1.12E-02	2.97E-03	7.98E-05	1.03E-05	-	-	5.84E-05	5.60E-06	-	-	4.44E-05	4.32E-06	6.18	0.63	6.47	0.66	423.1	4.3	4.6	0.25
148d	In1_10	q	2	-	-	90	y	9.82E-02	3.28E-03	1.09E-04	1.37E-05	-	-	6.77E-05	4.94E-06	-	-	5.15E-05	3.54E-06	7.16	0.57	7.50	0.57	434.0	3.4	4.8	0.20
148d	In1_11	qr	2	-	-	20	y	1.59E-01	7.73E-03	8.69E-05	7.29E-06	-	-	1.06E-04	3.34E-06	-	-	8.29E-05	2.60E-06	11.23	0.51	12.07	0.55	470.3	2.1	5.2	0.13
148d	In1_12	qr	2	-	-	10	y	8.73E-02	1.97E-03	1.24E-04	9.97E-06	-	-	1.37E-05	7.55E-07	-	-	1.06E-05	5.98E-07	1.45	0.09	1.55	0.10	332.6	2.1	3.7	0.12
148d	In1_13	q	2	-	-	300	n	4.85E-03	2.29E-04	6.42E-05	5.79E-06	-	-	1.13E-05	6.00E-07	-	-	8.00E-06	5.28E-07	1.20	0.07	1.16	0.09	319.8	2.1	3.5	0.13
148d	In1_14	q	2	-	-	300	n	7.13E-03	2.73E-04	7.40E-05	1.01E-05	-	-	4.48E-04	4.76E-05	-	-	3.40E-04	3.73E-05	47.44	5.27	49.50	5.66	609.9	7.3	6.7	0.43
148d	In1_15	q	2	-	-	300	n	5.23E-02	3.86E-03	1.15E-04	8.84E-06	-	-	3.92E-04	2.15E-05	-	-	2.85E-04	1.59E-05	41.46	2.65	41.50	2.68	592.2	4.0	6.5	0.23
148d	In1_16	q	2	-	-	300	n	1.88E-01	1.21E-02	1.14E-04	8.52E-06	-	-	6.13E-04	2.88E-05	-	-	4.62E-04	2.06E-05	64.87	3.71	67.22	3.72	647.4	3.9	7.1	0.23
148d	In1_17	q	2	-	-	300	n	5.01E-02	5.25E-03	1.87E-04	1.02E-05	-	-	2.51E-04	1.40E-05	-	-	1.84E-04	1.19E-05	26.55	1.72	26.77	1.94	545.5	3.9	6.0	0.23
148d	In1_18	qr	2	-	-	300	n	9.85E-03	1.90E-04	1.56E-04	7.24E-06	-	-	3.98E-05	3.76E-06	-	-	2.72E-05	2.86E-06	4.22	0.42	3.97	0.44	393.0	4.1	4.3	0.24
148d	In1_19	q	2	-	-	300	n	5.31E-02	4.70E-03	1.76E-04	9.48E-06	-	-	1.48E-04	1.81E-05	-	-	1.08E-04	1.47E-05	15.67	1.98	15.76	2.21	495.8	6.7	5.4	0.39
148d	In1_20	q	2	-	-	300	n	1.01E-01	1.37E-02	8.37E-05	8.42E-06	-	-	7.73E-04	4.88E-05	-	-	5.77E-04	3.65E-05	81.80	5.82	83.95	5.98	677.1	5.2	7.4	0.31
148d	In1_21	q	2	-	-	300	n	1.49E-02	1.35E-03	1.35E-04	1.07E-05	-	-	1.96E-05	1.16E-06	-	-	1.41E-05	6.32E-07	2.07	0.14	2.05	0.11	350.5	2.1	3.8	0.13
148d	In1_22	q	2	-	-	35	y	6.42E-03	1.88E-04	1.10E-04	9.01E-06	-	-	1.30E-05	6.04E-07	-	-	1.02E-05	5.73E-07	1.38	0.08	1.49	0.10	330.2	2.0	3.6	0.12
148d	In1_23	q	2	-	-	300	n	6.59E-03	2.97E-04	8.45E-05	8.35E-06	-	-	2.98E-05	3.00E-06	-	-	2.22E-05	2.41E-06	3.16	0.33	3.24	0.37	377.1	4.1	4.1	0.24
148d	In1_24	q	2	-	-	300	n	1.48E-01	9.19E-03	2.44E-04	1.87E-05	-	-	3.56E-04	2.48E-05	-	-	2.61E-04	1.50E-05	37.72	2.90	38.01	2.51	582.1	4.4	6.4	0.26
148d	In1_25	q	2	-	-	300	n	1.53E-02	2.67E-03	7.10E-05	9.48E-06	-	-	4.23E-04	4.55E-05	-	-	3.07E-04	3.21E-05	44.74	5.04	44.68	4.90	600.6	7.0	6.6	0.41
148d	In1_26	qr	2	-	-	20	n	1.08E-02	2.33E-04	1.36E-04	1.05E-05	-	-	1.09E-05	5.65E-07	-	-	8.59E-06	5.51E-07	1.16	0.07	1.25	0.09	320.8	2.1	3.5	0.12

Sample	ID	Type	Session	Area ID	Vein #	g.s.	g.b.?	^{27}Al/^{30}Si	1σ	^{44}Ca/^{30}Si	1σ	^{56}Fe/^{30}Si	1σ	^{47}Ti/^{30}Si	1σ	^{48}Ti/^{30}Si	1σ	^{49}Ti/^{30}Si	1σ	^{47}Ti (ppm)	1σ	^{49}Ti (ppm)	1σ	T (°C)	1σ	P (kbar)	1σ
148d	ln1_28	qr	2	-	-	15	n	6.72E-02	2.08E-02	1.41E-04	1.70E-05	-	-	9.71E-06	2.56E-06	-	-	7.34E-06	1.84E-06	1.03	0.27	1.07	0.27	313.6	7.9	3.4	0.47
148d	ln1_29	qr	2	-	-	10	n	1.01E-02	1.16E-03	1.36E-04	1.44E-05	-	-	2.83E-05	5.05E-06	-	-	2.06E-05	3.75E-06	2.99	0.54	2.99	0.55	372.9	6.7	4.1	0.39
148d	ln1_30	qr	2	-	-	99	y	1.39E-01	2.40E-02	1.23E-04	1.60E-05	-	-	3.33E-04	1.26E-05	-	-	2.38E-04	9.53E-06	35.26	1.77	34.69	1.79	573.5	3.0	6.3	0.18
148d	ln1_31	q	2	-	-	400	n	6.17E-03	2.52E-04	8.34E-05	1.13E-05	-	-	1.02E-03	9.15E-05	-	-	7.60E-04	6.72E-05	108.24	10.31	110.73	10.43	716.1	7.5	7.9	0.44
148d	ln1_32	q	2	-	-	400	n	8.03E-03	4.18E-04	7.33E-05	8.87E-06	-	-	3.51E-04	3.24E-05	-	-	2.69E-04	2.59E-05	37.15	3.64	39.21	3.99	583.0	6.1	6.4	0.36
148d	ln1_33	q	2	-	-	400	n	9.33E-03	1.21E-04	1.50E-04	8.33E-06	-	-	1.23E-04	1.73E-05	-	-	9.39E-05	1.28E-05	13.06	1.88	13.67	1.92	481.8	6.9	5.3	0.41
148d	ln1_34	q	2	-	-	400	n	1.33E-02	6.16E-04	4.13E-04	4.64E-05	-	-	4.00E-04	2.55E-05	-	-	2.87E-04	1.85E-05	42.30	3.03	41.84	3.02	593.7	4.5	6.5	0.26
148d	ln1_35	q	2	-	-	400	n	1.41E-02	2.24E-03	1.91E-04	2.87E-05	-	-	2.84E-04	1.91E-05	-	-	2.14E-04	1.44E-05	30.10	2.25	31.11	2.33	559.5	4.3	6.1	0.26
148d	ln1_36	q	2	-	-	400	n	3.82E-02	3.18E-03	2.59E-04	1.66E-05	-	-	2.97E-04	3.23E-05	-	-	2.19E-04	2.25E-05	31.40	3.57	31.94	3.44	563.0	6.5	6.2	0.38
148d	ln1_37	q	2	-	-	400	n	4.52E-03	2.01E-04	7.57E-05	6.67E-06	-	-	8.79E-04	3.15E-05	-	-	6.41E-04	2.40E-05	93.08	4.52	93.31	4.64	693.1	3.7	7.6	0.22
148d	ln1_38	q	2	-	-	400	n	4.59E-03	2.01E-04	8.13E-05	6.89E-06	-	-	1.90E-04	9.61E-06	-	-	1.37E-04	7.31E-06	20.09	1.21	19.94	1.25	517.8	3.2	5.7	0.19
148d	ln1_39	q	2	-	-	400	n	6.91E-03	7.10E-04	7.20E-05	9.06E-06	-	-	4.76E-04	3.45E-05	-	-	3.57E-04	2.75E-05	50.44	4.01	51.91	4.35	616.3	5.3	6.8	0.31
148d	ln1_40	q	2	-	-	400	n	4.29E-03	2.27E-04	1.09E-04	1.27E-05	-	-	3.59E-04	4.39E-05	-	-	2.58E-04	3.31E-05	37.98	4.81	37.61	4.97	581.9	7.9	6.4	0.46
148d	ln1_41	q	2	-	-	400	n	1.13E-01	2.19E-02	1.63E-04	3.05E-05	-	-	3.65E-04	1.45E-05	-	-	2.72E-04	1.17E-05	38.66	1.99	39.55	2.14	585.6	3.2	6.4	0.19
148d	ln1_42	q	2	-	-	400	n	4.46E-03	2.20E-04	7.79E-05	9.75E-06	-	-	1.65E-04	2.64E-05	-	-	1.23E-04	1.92E-05	17.42	2.85	17.95	2.86	506.4	8.3	5.6	0.49
148d	ln1_43	q	2	-	-	400	n	5.52E-03	2.13E-04	7.67E-05	9.95E-06	-	-	9.25E-05	3.83E-06	-	-	6.96E-05	3.57E-06	9.79	0.52	10.13	0.62	457.6	2.6	5.0	0.15
148d	ln1_44	q	2	-	-	500	n	1.24E-02	1.78E-04	1.05E-04	9.28E-06	-	-	1.18E-03	6.37E-05	-	-	8.54E-04	4.52E-05	124.48	7.87	124.36	7.73	735.1	5.1	8.1	0.30
148d	ln1_45	q	2	-	-	500	n	7.67E-03	1.83E-04	8.82E-05	1.05E-05	-	-	5.95E-04	3.88E-05	-	-	4.33E-04	2.93E-05	63.01	4.59	63.03	4.74	641.5	5.1	7.0	0.30
148d	ln1_46	q	2	-	-	500	n	1.61E-02	1.29E-03	2.27E-04	1.58E-05	-	-	1.87E-05	8.09E-07	-	-	1.36E-05	8.83E-07	1.98	0.11	1.98	0.14	348.2	2.2	3.8	0.13
148d	ln1_47	q	2	-	-	500	n	1.90E-02	1.48E-03	9.69E-05	1.22E-05	-	-	1.00E-04	6.17E-06	-	-	7.02E-05	4.65E-06	10.63	0.74	10.22	0.76	461.2	3.3	5.1	0.19
148d	ln1_48	q	2	-	-	500	n	6.36E-03	3.57E-04	7.65E-05	1.05E-05	-	-	7.73E-04	3.63E-05	-	-	5.77E-04	2.66E-05	81.84	4.68	84.00	4.75	677.1	4.2	7.4	0.25
148d	ln1_49	q	2	-	-	500	n	5.59E-03	2.46E-04	9.10E-05	1.34E-05	-	-	9.29E-04	3.66E-05	-	-	6.85E-04	2.56E-05	98.39	5.03	99.75	4.95	701.7	3.9	7.7	0.23
148d	l21_1	q	2	-	-	500	n	4.42E-03	1.68E-04	7.66E-05	9.14E-06	-	-	2.85E-04	1.79E-05	-	-	2.01E-04	1.25E-05	30.21	2.14	29.29	2.05	556.6	4.1	6.1	0.24
148d	l21_2	q	2	-	-	500	n	6.58E-03	3.12E-04	8.61E-05	9.17E-06	-	-	2.41E-04	2.76E-05	-	-	1.82E-04	2.25E-05	25.53	3.04	26.52	3.39	543.1	6.9	6.0	0.41
148d	l21_3	q	2	-	-	500	n	4.79E-03	2.14E-04	1.01E-04	1.43E-05	-	-	2.35E-04	1.14E-05	-	-	1.76E-04	8.47E-06	24.89	1.46	25.61	1.49	540.1	3.2	5.9	0.19
148d	l21_4	q	2	-	-	500	n	4.29E-03	2.21E-04	7.74E-05	1.05E-05	-	-	2.40E-04	1.67E-05	-	-	1.80E-04	1.26E-05	25.39	1.95	26.24	2.03	542.3	4.3	6.0	0.25
148d	l21_5	q	2	-	-	500	n	3.53E-02	7.15E-03	1.05E-04	1.26E-05	-	-	1.83E-04	2.65E-05	-	-	1.44E-04	2.06E-05	19.42	2.88	20.95	3.08	518.6	7.8	5.7	0.46
148d	l21_6	q	2	-	-	500	n	4.41E-03	2.45E-04	8.12E-05	7.33E-06	-	-	1.63E-04	1.91E-05	-	-	1.23E-04	1.53E-05	17.26	2.10	17.94	2.31	506.0	6.4	5.6	0.38
148d	l21_7	q	2	-	-	500	n	4.14E-03	2.20E-04	8.49E-05	1.39E-05	-	-	2.30E-04	1.82E-05	-	-	1.71E-04	1.40E-05	24.31	2.08	24.89	2.19	537.5	4.8	5.9	0.28
148d	l21_8	q	2	-	-	500	n	4.09E-03	2.22E-04	9.32E-05	1.31E-05	-	-	1.81E-04	1.54E-05	-	-	1.34E-04	1.16E-05	19.14	1.75	19.55	1.80	514.6	4.8	5.6	0.28
148d	l21_9	q	2	-	-	99	n	1.27E-02	1.32E-03	2.23E-04	2.44E-05	-	-	1.04E-04	1.03E-05	-	-	7.25E-05	7.00E-06	11.02	1.15	10.56	1.08	464.0	4.8	5.1	0.28
148d	l21_10	qr	2	-	-	19	n	9.96E-03	6.39E-04	1.55E-04	1.27E-05	-	-	3.38E-05	1.76E-06	-	-	2.50E-05	1.19E-06	3.58	0.22	3.64	0.21	384.8	2.3	4.2	0.13
148d	l21_11	qr	2	-	-	8	n	5.48E-02	3.83E-03	1.99E-04	1.23E-05	-	-	2.97E-05	2.14E-06	-	-	2.11E-05	1.67E-06	3.14	0.25	3.08	0.26	375.3	3.0	4.1	0.18
148d	l21_12	qr	2	-	-	30	y	8.28E-01	1.59E-02	5.00E-04	5.86E-05	-	-	2.40E-04	6.07E-06	-	-	1.75E-04	5.03E-06	25.39	1.05	25.44	1.11	540.7	2.4	5.9	0.14
148d	l21_13	q	2	-	-	60	n	3.04E-01	1.25E-02	1.94E-04	1.12E-05	-	-	6.46E-05	2.06E-06	-	-	4.71E-05	1.80E-06	6.84	0.31	6.86	0.35	428.9	2.0	4.7	0.12
148d	l21_14	q	2	-	-	60	n	3.43E-02	1.06E-03	1.16E-04	1.19E-05	-	-	3.01E-05	1.28E-06	-	-	2.12E-05	1.06E-06	3.19	0.17	3.09	0.18	375.9	2.1	4.1	0.12
148d	l21_15	q	2	-	-	95	n	5.03E-03	2.40E-04	9.86E-05	1.06E-05	-	-	4.40E-05	1.24E-05	-	-	3.13E-05	1.02E-05	4.66	1.32	4.56	1.49	400.9	12.1	4.4	0.71
148d	l21_16	q	2	-	-	20	y	1.03E+00	7.42E-02	2.74E-04	2.36E-05	-	-	1.76E-04	1.61E-05	-	-	1.34E-04	1.34E-05	18.68	1.81	19.58	2.06	513.6	5.3	5.6	0.31
148d	l21_17	q	2	-	-	500	n	5.61E-03	2.20E-04	9.50E-05	1.38E-05	-	-	2.58E-04	1.92E-05	-	-	1.94E-04	1.58E-05	27.36	2.22	28.23	2.48	549.7	4.8	6.0	0.28
148d	l21_18	q	2	-	-	500	n	6.85E-03	7.71E-04	1.11E-04	1.20E-05	-	-	2.70E-04	2.20E-05	-	-	1.95E-04	1.46E-05	28.59	2.51	28.45	2.32	552.3	4.8	6.1	0.28
148d	l21_19	q	2	-	-	500	n	6.93E-03	1.30E-04	1.04E-04	1.12E-05	-	-	2.48E-04	1.40E-05	-	-	1.84E-04	9.17E-06	26.24	1.71	26.80	1.60	544.9	3.5	6.0	0.21
148d	l21_20	q	2	-	-	500	n	5.88E-03	2.64E-04	9.67E-05	1.26E-05	-	-	2.39E-04	1.74E-05	-	-	1.68E-04	1.05E-05	25.25	2.02	24.50	1.73	538.6	4.2	5.9	0.25
148d	LPQ1	qr	2	-	-	30	n	7.21E-03	1.91E-04	5.60E-05	5.18E-06	-	-	1.26E-04	2.49E-05	-	-	9.75E-05	1.87E-05	13.38	2.67	14.20	2.77	484.5	9.6	5.3	0.57
148d	LPQb2	q	2	-	-	95	n	4.13E-03	1.18E-04	8.65E-05	8.15E-06	-	-	2.26E-05	2.54E-06	-	-	1.75E-05	1.35E-06	2.40	0.28	2.55	0.21	361.2	3.6	4.0	0.21
148d	LPQb3	q	2	-	-	70	n	4.85E-03	9.81E-05	6.90E-05	7.18E-06	-	-	1.56E-05	9.21E-07	-	-	1.16E-05	7.62E-07	1.65	0.11	1.68	0.12	338.4	2.3	3.7	0.14
148d	LPQb4	qr	2	-	-	25	n	7.21E-03	4.57E-04	9.42E-05	9.68E-06	-	-	1.09E-05	8.23E-07	-	-	7.08E-06	7.46E-07	1.16	0.10	1.03	0.11	315.8	3.0	3.5	0.17
148d	LPQb5	q	2	-	-	65	n	4.83E-03	1.97E-04	8.83E-05	1.26E-05	-	-	9.25E-06	6.88E-07	-	-	6.59E-06	5.06E-07	0.98	0.08	0.96	0.08	309.6	2.5	3.4	0.15
148d	LPQg5	q	2	-	-	400	n	4.01E-03	2.04E-04	7.24E-05	8.52E-06	-	-	6.39E-06	6.52E-07	-	-	4.48E-06	3.78E-07	0.68	0.07	0.65	0.06	291.0	2.8	3.2	0.17
148d	LPQg4	q	2	-	-	160	n	3.66E-03	2.53E-04	7.92E-05	9.45E-06	-	-	1.13E-04	2.36E-05	-	-	8.49E-05	1.76E-05	11.92	2.53	12.36	2.60	473.7	10.0	5.2	0.59
148d	LPQg6	q	2	-	-	110	n	4.67E-02	1.25E-02	7.63E-05	1.08E-05	-	-	3.57E-05	2.99E-06	-	-	2.50E-05	2.26E-06	3.78	0.34	3.65	0.35	386.6	3.5	4.2	0.21
148d	LPQg9	q	2	-	-	110	n	3.75E-03	2.16E-04	7.94E-05	8.15E-06	-	-	1.89E-05	3.64E-06	-	-	1.36E-05	2.63E-06	2.00	0.39	1.99	0.39	348.6	6.7	3.8	0.39
148d	LPQg10	q	2	-	-	190	n	4.04E-03	2.32E-04	8.16E-05	1.25E-05	-	-	3.07E-05	4.38E-06	-	-	2.34E-05	3.78E-06	3.25	0.48	3.41	0.56	379.6	5.8	4.2	0.34
148d	LPQg2	q	2	-	-	-	n	3.72E-03	2.82E-04	1.33E-04	1.58E-05	-	-	3.18E-04	2.16E-05	-	-	2.50E-04	1.49E-05	33.63	2.54	36.40	2.47	573.6	4.3	6.3	0.25
148d	LPQg3L	q	2	-	-	-	n	5.50E-03	3.52E-04	1.17E-04	2.38E-05	-	-	2.07E-05	1.14E-06	-	-	1.46E-05	6.35E-07	2.19	0.14	2.13	0.12	353.2	2.1	3.9	0.12
148d	LPQg3R	q	2	-	-	-	n	2.84E-02	3.34E-04	1.21E-04	2.02E-05	-	-	8.37E-04	1.52E-05	-	-	6.17E-04	1.03E-05	88.67	3.31	89.81	3.30	687.1	2.8	7.5	0.16
148d	LPQg2L	q	2	-	-	-	n	5.29E-03	3.73E-04	1.45E-04	2.59E-05	-	-	4.40E-05	2.55E-06	-	-	3.24E-05	1.22E-06	4.66	0.31	4.71	0.23	402.1	2.3	4.4	0.14

Sample	ID	Type	Session	Area ID	Vein #	g.s.	g.b.?	^{27}Al/^{30}Si	1σ	^{44}Ca/^{30}Si	1σ	^{56}Fe/^{30}Si	1σ	^{47}Ti/^{30}Si	1σ	^{48}Ti/^{30}Si	1σ	^{49}Ti/^{30}Si	1σ	^{47}Ti (ppm)	1σ	^{49}Ti (ppm)	1σ	T (°C)	1σ	P (kbar)	1σ
148d	LPQg8	q	2	-	-	500	n	1.18E-02	2.06E-04	8.13E-05	8.27E-06	-	-	8.21E-06	4.95E-07	-	-	6.14E-06	3.70E-07	0.87	0.06	0.89	0.06	304.8	2.0	3.3	0.12
148d	Tnt41	q	2	-	-	500	n	4.96E-03	3.54E-04	1.06E-04	1.68E-05	-	-	7.36E-06	6.53E-07	-	-	4.87E-06	5.30E-07	0.78	0.07	0.71	0.08	296.5	3.0	3.3	0.18
148d	Tnt42	q	2	-	-	500	n	6.44E-03	1.31E-03	1.19E-04	1.50E-05	-	-	7.46E-06	7.33E-07	-	-	6.66E-06	7.56E-07	0.79	0.08	0.97	0.11	304.8	3.4	3.3	0.20
148d	Tnt43	q	2	-	-	500	n	6.67E-03	4.15E-04	1.10E-04	1.26E-05	-	-	7.96E-06	4.91E-07	-	-	6.44E-06	7.77E-07	0.84	0.06	0.94	0.12	305.3	3.1	3.4	0.18
148d	Tnt44	q	2	-	-	500	n	4.86E-03	2.88E-04	1.01E-04	1.50E-05	-	-	7.21E-06	7.54E-07	-	-	6.48E-06	5.54E-07	0.76	0.08	0.94	0.09	303.3	2.9	3.3	0.17
148d	Tnt45	q	2	-	-	500	n	4.42E-03	2.75E-04	9.83E-05	1.51E-05	-	-	7.13E-06	8.02E-07	-	-	6.07E-06	7.15E-07	0.76	0.09	0.88	0.11	301.2	3.5	3.3	0.21
148d	Tnt46	q	2	-	-	500	n	4.05E-03	3.20E-04	8.72E-05	1.41E-05	-	-	6.87E-06	6.40E-07	-	-	5.86E-06	5.98E-07	0.73	0.07	0.85	0.09	299.4	3.0	3.3	0.18
148d	Tnt47	q	2	-	-	99	y	9.29E-02	4.33E-03	1.90E-04	1.88E-05	-	-	1.11E-05	9.48E-07	-	-	7.78E-06	6.54E-07	1.18	0.11	1.13	0.10	318.6	2.8	3.5	0.17
148d	Tnt48	q	2	-	-	99	y	1.31E-02	1.13E-03	1.04E-04	1.51E-05	-	-	5.20E-06	5.33E-07	-	-	4.02E-06	4.57E-07	0.55	0.06	0.59	0.07	283.7	3.2	3.1	0.19
148d	Tnt49	q	2	-	-	99	y	7.36E-03	2.86E-04	6.06E-05	1.39E-05	-	-	5.22E-06	5.09E-07	-	-	3.05E-06	4.15E-07	0.55	0.06	0.44	0.06	277.8	3.3	3.0	0.19
148d	Tnt50	q	2	-	-	99	n	4.03E-03	7.57E-05	3.82E-05	5.24E-06	-	-	2.77E-06	5.03E-07	-	-	2.43E-06	2.92E-07	0.29	0.05	0.35	0.04	258.9	3.9	2.8	0.23
148d	Tnt51	qr	2	-	-	200	y	1.46E-02	1.78E-03	1.59E-04	1.60E-05	-	-	1.08E-05	8.98E-07	-	-	7.61E-06	7.19E-07	1.14	0.10	1.11	0.11	317.3	2.9	3.5	0.17
148d	Tnt52	qr	2	-	-	200	y	4.96E-03	9.42E-05	8.21E-05	6.00E-06	-	-	6.49E-06	4.96E-07	-	-	3.61E-06	3.56E-07	0.69	0.06	0.53	0.05	286.7	2.6	3.1	0.15
148d	Tnt53	qr	2	-	-	200	n	4.38E-03	2.27E-04	1.74E-04	1.63E-05	-	-	6.04E-06	6.03E-07	-	-	3.81E-06	4.35E-07	0.64	0.07	0.56	0.07	286.1	3.1	3.1	0.18
148d	Tnt54	qr	2	-	-	200	y	3.20E-02	1.40E-03	1.46E-04	2.06E-05	-	-	1.17E-05	8.19E-07	-	-	7.80E-06	1.00E-06	1.24	0.10	1.14	0.15	320.1	3.3	3.5	0.20
148d	Tnt55	q	2	-	-	150	n	4.93E-03	4.07E-04	1.15E-04	1.37E-05	-	-	3.11E-04	1.64E-05	-	-	2.18E-04	9.07E-06	32.94	2.04	31.76	1.68	565.3	3.4	6.2	0.20
148d	Tnt56	q	2	-	-	500	n	2.05E-02	1.22E-04	1.36E-04	1.47E-05	-	-	9.30E-06	9.57E-07	-	-	7.27E-06	6.58E-07	0.98	0.11	1.06	0.10	312.3	3.1	3.4	0.18
148d	Tnt57	q	2	-	-	500	n	1.82E-01	6.88E-03	2.11E-04	2.12E-05	-	-	1.07E-04	2.24E-05	-	-	9.11E-05	1.94E-05	11.28	2.40	13.26	2.86	474.6	10.3	5.2	0.60
148d	Tnt58	q	2	-	-	500	n	3.44E+00	3.40E-01	8.03E-04	8.03E-05	-	-	1.23E-03	1.31E-04	-	-	8.97E-04	9.38E-05	130.22	14.53	130.66	14.31	742.3	9.1	8.1	0.54
148d	Tnt59	q	2	-	-	500	n	4.98E-03	2.78E-04	1.08E-04	1.73E-05	-	-	8.12E-06	6.15E-07	-	-	6.30E-06	6.78E-07	0.86	0.07	0.92	0.10	305.2	3.0	3.4	0.17
148d	Tnt60	q	2	-	-	500	n	7.55E-03	1.35E-03	1.14E-04	1.70E-05	-	-	7.85E-06	7.77E-07	-	-	5.09E-06	5.00E-07	0.83	0.09	0.74	0.08	299.2	3.0	3.3	0.18
148d	Tnt61	q	2	-	-	500	n	4.85E-03	2.46E-04	1.03E-04	9.21E-06	-	-	5.64E-06	4.09E-07	-	-	4.34E-06	5.64E-07	0.60	0.05	0.63	0.08	287.4	3.1	3.2	0.19
148d	Tnt62	q	2	-	-	500	n	3.77E-02	4.98E-03	1.72E-04	2.69E-05	-	-	8.27E-06	9.54E-07	-	-	5.66E-06	6.24E-07	0.88	0.10	0.82	0.09	303.0	3.5	3.3	0.21
148d	Tnt63	q	2	-	-	500	n	7.81E-03	7.37E-04	9.70E-05	1.26E-05	-	-	5.69E-06	5.25E-07	-	-	3.75E-06	4.90E-07	0.60	0.06	0.55	0.07	284.2	3.2	3.1	0.19
148d	Tnt64	q	2	-	-	500	n	3.09E-03	5.38E-05	3.52E-05	4.14E-06	-	-	5.43E-06	5.24E-07	-	-	3.58E-06	5.18E-07	0.57	0.06	0.52	0.08	282.0	3.5	3.1	0.20
148d	Tnt65	q	2	-	-	15	y	4.47E-02	3.85E-03	1.40E-04	2.05E-05	-	-	2.64E-05	2.06E-06	-	-	1.87E-05	1.62E-06	2.80	0.24	2.72	0.25	367.9	3.2	4.0	0.19
148d	Tnt66	q	2	-	-	20	y	2.20E-02	1.78E-03	1.43E-04	2.83E-05	-	-	1.30E-05	7.67E-07	-	-	1.11E-05	8.53E-07	1.37	0.09	1.62	0.13	332.4	2.5	3.6	0.15
148d	Tnt67	q	2	-	-	200	n	4.33E-02	5.31E-03	2.03E-04	3.33E-05	-	-	1.50E-05	1.01E-06	-	-	1.26E-05	1.16E-06	1.59	0.12	1.84	0.18	340.0	3.0	3.7	0.17
148d	Tnt68	q	2	-	-	350	n	1.83E-02	2.48E-04	1.56E-04	1.92E-05	-	-	7.64E-05	2.59E-06	-	-	5.75E-05	2.32E-06	8.09	0.38	8.37	0.43	442.7	2.2	4.9	0.13
148d	Tnt69	q	2	-	-	100	n	6.00E-03	3.56E-04	1.18E-04	1.97E-05	-	-	9.72E-06	9.03E-07	-	-	7.69E-06	6.03E-07	1.03	0.10	1.12	0.10	314.8	2.8	3.5	0.17
148d	Tnt70	qr	2	-	-	50	n	2.35E-01	5.12E-02	2.65E-04	2.51E-05	-	-	2.90E-05	5.20E-06	-	-	2.25E-05	3.67E-06	3.07	0.56	3.27	0.54	376.5	6.4	4.1	0.38
148d	Tnt71	q	2	-	-	75	y	8.34E-03	3.02E-04	2.23E-04	2.13E-05	-	-	3.50E-06	5.39E-07	-	-	3.12E-06	4.77E-07	0.37	0.06	0.45	0.07	269.3	4.2	3.0	0.25
148d	Tnt72	q	2	-	-	50	n	2.01E-02	5.18E-04	1.37E-04	2.80E-05	-	-	3.84E-05	1.27E-06	-	-	3.04E-05	1.50E-06	4.06	0.19	4.43	0.26	395.5	2.1	4.3	0.12
148d	Tnt73	q	2	-	-	75	y	6.75E-03	5.25E-04	1.42E-04	2.38E-05	-	-	8.63E-06	7.55E-07	-	-	6.48E-06	6.70E-07	0.91	0.09	0.94	0.10	307.4	3.0	3.4	0.18
148d	Tnt74	q	2	-	-	500	n	7.13E-03	3.64E-04	1.33E-04	2.12E-05	-	-	2.90E-04	1.57E-05	-	-	2.08E-04	1.17E-05	30.65	1.94	30.23	1.97	558.9	3.7	6.1	0.22
148d	Tnt75	q	2	-	-	125	n	8.32E-03	2.24E-04	1.30E-04	1.85E-05	-	-	6.14E-06	5.46E-07	-	-	4.56E-06	5.06E-07	0.65	0.06	0.66	0.08	290.6	3.0	3.2	0.18
148d	Tnt76	q	2	-	-	125	n	6.75E-03	3.49E-04	9.25E-05	1.44E-05	-	-	2.41E-06	3.31E-07	-	-	1.93E-06	3.49E-07	0.26	0.04	0.28	0.05	251.1	4.1	2.8	0.24
148d	Tnt77	q	2	-	-	125	n	1.94E-02	9.65E-04	1.73E-04	2.93E-05	-	-	9.71E-06	5.83E-07	-	-	9.18E-06	6.01E-07	1.03	0.07	1.34	0.10	319.9	2.2	3.5	0.13
148d	Tnt78	q	2	-	-	500	n	9.04E-03	2.94E-04	9.72E-05	1.35E-05	-	-	5.00E-06	4.99E-07	-	-	3.49E-06	4.78E-07	0.53	0.06	0.51	0.07	279.5	3.4	3.1	0.20
148d	Tnt79	q	2	-	-	500	n	1.00E-02	5.94E-04	1.38E-04	2.15E-05	-	-	1.49E-04	1.08E-05	-	-	1.09E-04	8.30E-06	15.81	1.26	15.94	1.32	496.7	4.1	5.5	0.24
148d	Tnt80	q	2	-	-	99	y	1.22E-02	3.83E-04	1.48E-04	2.29E-05	-	-	2.45E-05	3.26E-06	-	-	1.74E-05	1.97E-06	2.60	0.36	2.53	0.30	363.4	4.6	4.0	0.27
148d	Tnt81	q	2	-	-	500	n	4.95E-03	2.94E-04	9.81E-05	1.80E-05	-	-	7.16E-04	8.52E-05	-	-	5.44E-04	6.21E-05	75.84	9.36	79.22	9.41	668.2	8.7	7.3	0.51
148d	Tnt82	q	2	-	-	165	n	1.20E-01	3.40E-02	1.11E-04	1.54E-05	-	-	9.38E-05	2.44E-05	-	-	6.30E-05	1.72E-05	9.93	2.60	9.17	2.53	454.3	12.2	5.0	0.72
148d	g7_0	q	3	-	-	38	n	6.91E-03	5.93E-04	3.61E-05	2.40E-06	-	-	3.67E-04	5.54E-05	-	-	2.79E-04	4.25E-05	38.82	6.00	40.63	6.33	587.4	9.5	6.4	0.56
148d	g7_1	q	3	-	-	38	n	2.97E-03	4.14E-05	3.96E-05	3.25E-06	-	-	4.60E-04	4.15E-05	-	-	3.43E-04	3.33E-05	48.66	4.67	50.01	5.11	612.0	6.4	6.7	0.38
148d	g7_2	qr	3	-	-	99	n	9.45E-03	5.77E-04	1.94E-04	1.50E-05	-	-	6.69E-05	1.30E-05	-	-	4.60E-05	8.78E-06	7.09	1.40	6.69	1.30	429.4	8.3	4.7	0.49
148d	g7_3	q	3	-	-	358	n	8.86E-02	1.49E-02	3.59E-05	3.39E-06	-	-	9.63E-04	8.95E-05	-	-	6.97E-04	6.31E-05	102.00	10.05	101.45	9.76	705.5	7.5	7.7	0.44
148d	g7_4	q	3	-	-	358	n	4.54E-03	1.76E-04	2.92E-05	2.34E-06	-	-	2.88E-04	5.41E-05	-	-	2.03E-04	4.34E-05	30.47	5.81	29.62	6.40	557.6	11.7	6.1	0.69
148d	g7_5	q	3	-	-	358	n	4.87E-03	4.27E-05	3.33E-05	2.97E-06	-	-	1.93E-04	1.85E-05	-	-	1.37E-04	1.72E-05	20.45	2.07	20.01	2.59	518.8	6.1	5.7	0.36
148d	g7_6	q	3	-	-	358	n	5.42E-02	1.81E-02	5.46E-05	1.13E-05	-	-	3.22E-04	3.96E-05	-	-	2.17E-04	2.66E-05	34.10	4.34	31.62	4.01	566.9	7.5	6.2	0.44
148d	g7_7	q	3	-	-	358	n	4.17E-03	6.44E-05	3.73E-05	3.57E-06	-	-	2.24E-04	4.59E-05	-	-	1.62E-04	3.21E-05	23.74	4.92	23.53	4.74	533.6	11.2	5.9	0.66
148d	g7_8	q	3	-	-	358	n	8.75E-02	2.21E-02	3.44E-05	2.71E-06	-	-	4.06E-04	6.51E-05	-	-	2.78E-04	4.36E-05	43.03	7.03	40.41	6.49	592.8	10.1	6.5	0.59
148d	g7_9	q	3	-	-	358	n	7.09E-03	7.40E-04	3.07E-05	3.59E-06	-	-	2.81E-04	2.05E-05	-	-	2.12E-04	1.70E-05	29.79	2.38	30.94	2.68	558.7	4.8	6.1	0.28
148d	g7_10	q	3	-	-	358	n	2.38E-02	1.83E-03	4.07E-05	3.28E-06	-	-	3.80E-04	5.88E-05	-	-	2.78E-04	4.82E-05	40.24	6.37	40.54	7.15	589.2	10.3	6.5	0.61
148d	g7_11	q	3	-	-	358	n	3.96E-02	1.19E-02	3.88E-05	3.43E-06	-	-	1.74E-04	2.31E-05	-	-	1.30E-04	1.66E-05	18.43	2.52	18.97	2.49	511.5	7.0	5.6	0.41
148d	g7_12	q	3	-	-	358	n	1.45E-02	2.12E-03	3.27E-05	2.67E-06	-	-	4.57E-04	7.44E-05	-	-	3.19E-04	5.68E-05	48.40	8.04	46.51	8.41	607.5	11.1	6.7	0.65

Sample	ID	Type	Session	Area ID	Vein #	g.s.	g.b.?	^{27}Al/^{30}Si	1σ	^{44}Ca/^{30}Si	1σ	^{56}Fe/^{30}Si	1σ	^{47}Ti/^{30}Si	1σ	^{48}Ti/^{30}Si	1σ	^{49}Ti/^{30}Si	1σ	^{47}Ti (ppm)	1σ	^{49}Ti (ppm)	1σ	T (°C)	1σ	P (kbar)	1σ
148d	g7_13	q	3	-	-	358	n	6.96E-03	6.18E-05	3.63E-05	3.34E-06	-	-	1.58E-04	1.86E-05	-	-	1.14E-04	1.17E-05	16.72	2.05	16.55	1.78	500.9	5.9	5.5	0.34
148d	g7_14	q	3	-	-	358	n	2.77E-03	6.12E-05	3.79E-05	2.82E-06	-	-	2.54E-04	1.35E-05	-	-	1.95E-04	1.24E-05	26.93	1.68	28.40	2.03	549.2	3.8	6.0	0.22
148d	g7_15	q	3	-	-	128	y	1.39E-02	4.86E-04	5.47E-04	3.91E-05	-	-	5.54E-05	2.07E-06	-	-	3.65E-05	1.24E-06	5.86	0.29	5.32	0.25	414.3	2.0	4.5	0.12
148d	g7_16	q	3	-	-	128	n	4.85E-03	7.22E-05	3.36E-05	3.50E-06	-	-	1.68E-05	6.26E-07	-	-	1.21E-05	5.84E-07	1.77	0.09	1.76	0.10	341.7	1.8	3.8	0.11
148d	g7_17	q	3	-	-	128	n	3.44E-03	5.86E-05	3.38E-05	3.17E-06	-	-	8.37E-05	3.79E-06	-	-	5.97E-05	3.23E-06	8.86	0.49	8.69	0.55	447.7	2.7	4.9	0.16
148d	g7_18	q	3	-	-	128	y	3.36E-03	3.17E-05	2.68E-05	3.47E-06	-	-	1.02E-04	1.58E-05	-	-	7.55E-05	1.16E-05	10.80	1.71	11.00	1.72	464.9	7.3	5.1	0.43
148d	g7_19	q	3	-	-	448	n	2.23E-02	7.16E-04	1.76E-04	1.21E-05	-	-	2.85E-05	2.95E-06	-	-	1.91E-05	9.87E-07	3.01	0.33	2.78	0.17	370.8	3.3	4.1	0.19
148d	g7_20	q	3	-	-	448	n	3.52E-03	5.61E-05	2.87E-05	3.87E-06	-	-	2.63E-04	5.51E-05	-	-	1.97E-04	3.97E-05	27.82	5.91	28.64	5.86	551.2	11.9	6.1	0.70
148d	g7_21	q	3	-	-	99	y	4.37E-03	1.81E-04	3.20E-05	3.24E-06	-	-	7.52E-05	1.55E-05	-	-	4.92E-05	9.26E-06	7.96	1.66	7.17	1.37	436.3	8.7	4.8	0.51
148d	g7_22	q	3	-	-	99	y	9.93E-03	1.53E-04	2.14E-04	1.34E-05	-	-	4.04E-04	1.17E-04	-	-	2.95E-04	8.57E-05	42.74	12.46	42.98	12.56	595.8	18.2	6.5	1.07
148d	g7_23	q	3	-	-	448	n	4.15E-03	5.09E-05	3.14E-05	1.68E-06	-	-	1.05E-04	3.03E-05	-	-	8.22E-05	2.29E-05	11.08	3.23	11.97	3.35	469.4	13.5	5.2	0.79
148d	g7_24	q	3	-	-	448	n	3.17E-03	4.90E-05	3.28E-05	2.83E-06	-	-	7.25E-05	2.32E-05	-	-	5.98E-05	1.76E-05	7.67	2.47	8.71	2.58	442.3	13.6	4.9	0.80
148d	g7_25	q	3	-	-	448	n	3.94E-03	4.57E-05	2.88E-05	2.84E-06	-	-	1.47E-04	2.60E-05	-	-	1.11E-04	1.79E-05	15.55	2.80	16.10	2.66	496.5	8.7	5.4	0.51
148d	g7_26	q	3	-	-	448	n	4.23E-03	7.96E-05	5.68E-05	1.14E-05	-	-	3.54E-05	1.21E-06	-	-	2.72E-05	1.05E-06	3.75	0.18	3.96	0.20	389.1	1.9	4.3	0.11
148d	g7_27	q	3	-	-	448	n	5.12E-03	7.27E-05	4.12E-05	4.14E-06	-	-	3.75E-05	2.24E-06	-	-	2.71E-05	1.73E-06	3.97	0.27	3.95	0.28	390.8	2.7	4.3	0.16
148d	g7_28	q	3	-	-	448	n	4.08E-03	4.73E-04	3.47E-05	2.89E-06	-	-	7.98E-05	9.99E-06	-	-	5.83E-05	7.46E-06	8.45	1.09	8.49	1.12	444.9	5.8	4.9	0.34
148d	g7_29	q	3	-	-	448	n	3.89E-03	1.23E-04	3.63E-05	3.19E-06	-	-	1.25E-04	6.13E-06	-	-	9.51E-05	4.88E-06	13.26	0.78	13.85	0.84	483.0	2.9	5.3	0.17
148d	g7_30	q	3	-	-	448	n	2.98E-03	5.65E-05	3.34E-05	3.06E-06	-	-	8.92E-05	2.05E-05	-	-	6.55E-05	1.44E-05	9.44	2.19	9.54	2.12	453.8	10.3	5.0	0.61
148d	g7_31	q	3	-	-	448	n	3.23E-03	3.65E-05	3.26E-05	2.12E-06	-	-	1.90E-04	4.26E-05	-	-	1.47E-04	3.19E-05	20.11	4.55	21.43	4.70	521.2	11.9	5.7	0.70
148d	g7_32	q	3	-	-	448	n	4.52E-03	5.35E-04	3.72E-05	3.62E-06	-	-	7.90E-05	2.27E-05	-	-	5.68E-05	1.73E-05	8.37	2.41	8.27	2.54	443.5	13.2	4.9	0.77
148d	g7_33	q	3	-	-	448	n	4.43E-03	1.15E-04	3.35E-05	2.95E-06	-	-	1.82E-04	5.89E-05	-	-	1.30E-04	3.07E-05	19.26	6.26	18.98	4.51	513.5	14.9	5.6	0.88
148d	g7_34	q	3	-	-	448	n	3.20E-03	5.60E-05	3.45E-05	2.75E-06	-	-	8.47E-04	2.64E-04	-	-	6.41E-04	1.96E-04	89.71	28.12	93.27	28.63	690.6	23.3	7.6	1.37
148d	g7_35	q	3	-	-	448	n	2.27E-01	4.71E-02	3.10E-05	2.41E-06	-	-	5.73E-04	9.63E-05	-	-	4.14E-04	7.20E-05	60.68	10.39	60.25	10.67	636.4	11.8	7.0	0.69
148d	g7_36	q	3	-	-	448	n	2.79E-03	6.78E-05	3.34E-05	3.16E-06	-	-	1.47E-04	3.19E-05	-	-	1.11E-04	2.30E-05	15.60	3.41	16.09	3.39	496.6	10.8	5.5	0.63
148d	g7_37	q	3	-	-	448	n	5.36E-03	7.45E-04	3.55E-05	4.00E-06	-	-	4.07E-05	4.17E-06	-	-	3.44E-05	4.15E-06	4.31	0.46	5.01	0.63	401.7	4.7	4.4	0.28
148d	g7_38	q	3	-	-	448	n	3.11E-03	7.12E-05	3.34E-05	3.19E-06	-	-	9.22E-05	1.35E-05	-	-	6.74E-05	9.89E-06	9.76	1.47	9.81	1.47	456.2	6.9	5.0	0.40
148d	g7_39	q	3	-	-	448	n	3.23E-03	6.31E-05	2.95E-05	2.88E-06	-	-	5.28E-05	3.83E-06	-	-	3.95E-05	3.18E-06	5.60	0.44	5.76	0.50	415.4	3.4	4.6	0.20
148d	g7_41	q	3	-	-	448	n	3.52E-03	4.12E-05	4.32E-05	4.57E-06	-	-	3.73E-05	2.98E-06	-	-	2.56E-05	2.38E-06	3.95	0.34	3.73	0.37	388.9	3.5	4.3	0.21
148d	g7_42	q	3	-	-	448	n	3.87E-03	6.56E-05	3.09E-05	3.64E-06	-	-	1.84E-04	1.05E-05	-	-	1.40E-04	8.79E-06	19.49	1.29	20.42	1.44	517.5	3.6	5.7	0.21
148d	g7_43	q	3	-	-	448	n	4.23E-03	2.02E-04	3.57E-05	3.13E-06	-	-	1.17E-04	2.74E-05	-	-	9.21E-05	2.90E-05	12.39	2.93	13.42	4.25	478.8	13.6	5.3	0.80
148d	g7_44	q	3	-	-	448	n	3.99E-03	5.96E-05	3.55E-05	3.63E-06	-	-	1.73E-04	2.64E-05	-	-	1.21E-04	1.75E-05	18.27	2.86	17.55	2.61	507.5	7.9	5.6	0.46
148d	g7_45	q	3	-	-	448	n	5.43E-03	1.06E-04	3.23E-05	2.91E-06	-	-	1.44E-04	3.72E-05	-	-	9.75E-05	2.51E-05	15.21	3.98	14.19	3.68	490.0	12.9	5.4	0.76
148d	g7_46	q	3	-	-	448	n	6.92E-03	6.15E-04	3.81E-05	2.88E-06	-	-	7.24E-05	1.20E-05	-	-	5.54E-05	8.98E-06	7.67	1.30	8.07	1.33	439.3	7.3	4.8	0.43
148d	g7_47	q	3	-	-	448	n	4.16E-03	6.48E-05	3.87E-05	3.22E-06	-	-	8.84E-05	1.27E-05	-	-	6.12E-05	9.25E-06	9.36	1.37	8.91	1.38	450.8	6.8	4.9	0.40
148d	g7_48	q	3	-	-	448	n	1.27E-02	9.12E-04	5.70E-05	4.63E-06	-	-	5.93E-05	1.29E-05	-	-	4.35E-05	1.01E-05	6.28	1.38	6.33	1.48	422.9	9.5	4.6	0.56
148d	g7L2_0	q	3	-	-	205	n	3.95E-03	1.59E-04	4.32E-05	2.57E-06	-	-	1.93E-05	8.30E-07	-	-	1.38E-05	5.41E-07	2.04	0.11	2.02	0.10	349.6	1.8	3.8	0.11
148d	g7L2_1	q	3	-	-	205	n	4.25E-03	1.52E-04	3.60E-05	3.55E-06	-	-	5.49E-05	7.80E-06	-	-	4.27E-05	6.31E-06	5.82	0.85	6.21	0.94	419.5	6.2	4.6	0.36
148d	g7L2_2	q	3	-	-	205	n	8.52E-03	6.13E-05	3.28E-05	3.18E-06	-	-	4.24E-05	5.36E-06	-	-	2.88E-05	2.07E-06	4.49	0.59	4.19	0.33	397.0	4.3	4.4	0.25
148d	g7L2_3	q	3	-	-	205	n	3.28E-03	6.28E-05	3.92E-05	3.69E-06	-	-	9.14E-05	8.00E-06	-	-	6.89E-05	6.26E-06	9.68	0.90	10.04	0.97	456.8	4.3	5.0	0.26
148d	g7L2_4	q	3	-	-	205	n	3.61E-03	5.99E-05	3.46E-05	3.45E-06	-	-	3.39E-04	3.50E-05	-	-	2.54E-04	2.38E-05	35.90	3.89	36.92	3.67	577.9	6.3	6.3	0.37
148d	g7L2_5	q	3	-	-	205	n	1.81E-01	1.29E-03	4.28E-05	3.34E-06	-	-	4.84E-04	2.08E-05	-	-	3.60E-04	1.66E-05	51.29	2.77	52.44	2.96	617.9	3.6	6.8	0.21
148d	g7L2_6	q	3	-	-	205	n	4.13E-03	6.61E-05	2.90E-05	3.34E-06	-	-	3.00E-05	1.31E-06	-	-	2.29E-05	1.39E-06	3.18	0.17	3.33	0.23	378.1	2.3	4.2	0.14
148d	g7L2_7	q	3	-	-	205	n	3.76E-03	5.07E-05	3.82E-05	3.01E-06	-	-	3.57E-05	5.80E-06	-	-	2.84E-05	5.50E-06	3.78	0.63	4.14	0.81	390.8	7.1	4.3	0.41
148d	g7L2_8	q	3	-	-	205	n	9.87E-03	7.96E-04	6.19E-05	3.87E-06	-	-	2.72E-05	1.11E-06	-	-	2.03E-05	7.27E-07	2.88	0.15	2.96	0.14	371.3	1.8	4.1	0.11
148d	g7L2_9	q	3	-	-	115	n	2.62E-03	6.02E-05	3.50E-05	3.17E-06	-	-	4.15E-05	7.48E-06	-	-	3.22E-05	5.96E-06	4.40	0.80	4.69	0.88	400.0	7.3	4.4	0.43
148d	g7L2_10	q	3	-	-	115	n	2.11E-02	1.67E-02	3.84E-05	2.40E-06	-	-	4.05E-05	1.79E-05	-	-	3.64E-05	1.65E-05	4.29	1.90	5.30	2.41	403.7	18.0	4.4	1.06
148d	g7L2_11	q	3	-	-	115	n	1.15E+00	2.29E-01	4.17E-05	4.76E-06	-	-	7.93E-04	1.59E-04	-	-	5.66E-04	1.18E-04	83.98	17.10	82.48	17.35	677.6	15.2	7.4	0.89
148d	g7L2_12	q	3	-	-	115	n	3.54E-03	5.66E-05	3.10E-05	3.39E-06	-	-	1.66E-05	3.18E-06	-	-	1.28E-05	2.44E-06	1.76	0.34	1.86	0.36	343.1	6.5	3.8	0.38
148d	g7L2_13	q	3	-	-	101	n	4.19E-01	2.71E-02	7.67E-05	1.03E-05	-	-	3.25E-04	3.98E-05	-	-	2.40E-04	2.92E-05	34.38	4.36	34.87	4.40	572.5	7.5	6.3	0.44
148j	LPQ1	q	2	-	-	170	n	6.20E-03	4.74E-04	2.14E-04	6.64E-05	-	-	5.29E-06	5.42E-07	-	-	3.17E-06	4.04E-07	0.56	0.06	0.46	0.06	278.8	3.2	3.1	0.19
148j	LPQ2	q	2	-	-	130	n	1.09E-02	8.23E-04	2.21E-04	6.80E-05	-	-	2.73E-04	1.14E-05	-	-	2.14E-04	1.16E-05	28.95	1.53	31.19	1.97	557.7	3.4	6.1	0.20
148j	LPQ6	q	2	-	-	175	n	7.77E-03	5.10E-04	1.81E-04	6.73E-05	-	-	3.01E-04	1.67E-05	-	-	2.20E-04	1.27E-05	31.92	2.05	32.06	2.13	564.1	3.8	6.2	0.22
148j	NPT4	q	2	-	-	38	y	1.14E-02	6.52E-04	1.69E-04	3.33E-05	-	-	7.17E-06	6.24E-07	-	-	5.46E-06	5.40E-07	0.76	0.07	0.80	0.08	298.6	2.9	3.3	0.17
148j	NPT5	q	2	-	-	30	y	7.55E-03	4.63E-04	1.95E-04	4.99E-05	-	-	6.95E-06	6.05E-07	-	-	4.57E-06	5.56E-07	0.74	0.07	0.67	0.08	293.6	3.1	3.2	0.18
148j	NPT7	q	2	-	-	100	n	1.63E-02	8.15E-04	2.04E-04	5.29E-05	-	-	1.94E-04	2.86E-05	-	-	1.32E-04	1.60E-05	20.56	3.10	19.21	2.41	517.2	7.4	5.7	0.43
148j	NPT8	q	2	-	-	100	n	3.00E-01	1.26E-02	1.67E-04	4.16E-05	-	-	3.88E-04	1.31E-05	-	-	2.85E-04	9.03E-06	41.05	1.93	41.46	1.89	591.6	2.9	6.5	0.17

Sample	ID	Type	Session	Area ID	Vein #	g.s.	g.b.?	^{27}Al/^{30}Si	1σ	^{44}Ca/^{30}Si	1σ	^{56}Fe/^{30}Si	1σ	^{47}Ti/^{30}Si	1σ	^{48}Ti/^{30}Si	1σ	^{49}Ti/^{30}Si	1σ	^{47}Ti (ppm)	1σ	^{49}Ti (ppm)	1σ	T (°C)	1σ	P (kbar)	1σ
148j	NPT9	q	2	-	-	125	n	1.15E-02	4.63E-04	2.07E-04	5.92E-05	-	-	3.18E-04	2.62E-05	-	-	2.30E-04	1.97E-05	33.72	2.98	33.54	3.07	569.3	5.3	6.2	0.31
148j	NPT10	q	2	-	-	112	n	1.02E-02	9.09E-04	1.87E-04	4.65E-05	-	-	1.48E-05	6.95E-07	-	-	1.22E-05	9.70E-07	1.57	0.09	1.77	0.15	338.5	2.5	3.7	0.15
148j	NPT11	qr	2	-	-	33	n	2.99E-02	6.00E-03	2.62E-04	7.08E-05	-	-	1.49E-05	1.41E-06	-	-	9.20E-06	1.03E-06	1.58	0.16	1.34	0.16	331.1	3.5	3.6	0.20
148j	NPT12	q	2	-	-	63	n	1.99E-02	1.80E-03	2.00E-04	5.24E-05	-	-	1.15E-04	8.36E-06	-	-	8.56E-05	5.73E-06	12.12	0.97	12.47	0.93	474.8	3.7	5.2	0.22
148j	NPT13	q	2	-	-	100	n	1.56E-02	6.41E-04	2.71E-04	5.71E-05	-	-	1.10E-05	6.19E-07	-	-	8.51E-06	7.14E-07	1.17	0.08	1.24	0.11	320.8	2.5	3.5	0.15
148j	NPT14	q	2	-	-	175	n	2.54E-02	4.04E-03	2.26E-04	6.36E-05	-	-	1.81E-05	1.53E-06	-	-	1.53E-05	1.18E-06	1.91	0.17	2.23	0.19	350.8	3.0	3.9	0.18
148j	NPT15	q	2	-	-	175	n	4.31E-02	5.23E-03	2.83E-04	5.88E-05	-	-	2.31E-05	1.38E-06	-	-	1.89E-05	1.08E-06	2.44	0.17	2.76	0.18	364.3	2.4	4.0	0.14
148j	NPT16	qr	2	-	-	50	n	3.63E-02	2.19E-03	2.01E-04	5.76E-05	-	-	1.22E-05	8.55E-07	-	-	8.31E-06	6.76E-07	1.30	0.10	1.21	0.11	322.9	2.6	3.5	0.15
148j	NPT17	qr	2	-	-	125	n	1.40E-02	9.42E-04	2.56E-04	6.61E-05	-	-	1.18E-05	9.13E-07	-	-	9.17E-06	1.04E-06	1.25	0.10	1.34	0.16	324.6	3.3	3.6	0.19
148j	NPT18	q	2	-	-	150	n	8.05E-02	3.25E-03	3.06E-04	5.93E-05	-	-	2.10E-05	1.81E-06	-	-	1.49E-05	1.39E-06	2.22	0.20	2.17	0.21	354.1	3.3	3.9	0.19
148j	NPT19	q	2	-	-	100	y	3.11E-01	2.31E-02	5.15E-04	9.03E-05	-	-	1.66E-04	1.42E-05	-	-	1.20E-04	9.54E-06	17.57	1.61	17.51	1.50	505.6	4.6	5.5	0.27
148j	NPT20	q	2	-	-	170	n	9.29E-03	6.49E-04	2.33E-04	7.08E-05	-	-	7.36E-06	5.47E-07	-	-	7.15E-06	6.35E-07	0.78	0.06	1.04	0.10	306.4	2.7	3.4	0.16
148j	NPT21	q	2	-	-	170	n	6.42E-03	4.25E-04	2.48E-04	7.71E-05	-	-	4.97E-06	5.99E-07	-	-	3.46E-06	7.39E-07	0.53	0.07	0.50	0.11	279.2	4.8	3.1	0.28
148j	NPT22	qr	2	-	-	30	y	8.58E-02	1.01E-02	3.09E-04	7.94E-05	-	-	1.70E-05	1.68E-06	-	-	1.28E-05	1.32E-06	1.80	0.19	1.87	0.20	343.8	3.6	3.8	0.21
148j	NPT23	qr	2	-	-	30	n	1.55E-02	1.17E-03	2.92E-04	8.34E-05	-	-	1.01E-05	1.17E-06	-	-	8.30E-06	8.62E-07	1.07	0.13	1.21	0.13	318.0	3.5	3.5	0.21
148j	NPT24	q	2	-	-	33	n	3.32E-02	1.97E-03	2.75E-04	7.27E-05	-	-	3.03E-05	1.32E-06	-	-	2.06E-05	1.43E-06	3.20	0.17	3.01	0.23	375.2	2.4	4.1	0.14
148j	NPT25	q	2	-	-	30	n	1.03E-02	6.15E-04	2.61E-04	7.10E-05	-	-	1.00E-05	8.44E-07	-	-	6.05E-06	7.68E-07	1.06	0.10	0.88	0.12	309.7	3.3	3.4	0.19
148j	NPT26	qr	2	-	-	20	y	2.28E-02	2.67E-03	2.95E-04	7.85E-05	-	-	9.10E-06	1.04E-06	-	-	8.47E-06	8.80E-07	0.96	0.11	1.23	0.13	316.0	3.5	3.5	0.21
148j	NPT27	qr	2	-	-	100	y	1.00E-01	9.11E-03	3.85E-04	8.39E-05	-	-	2.30E-05	2.32E-06	-	-	1.65E-05	1.85E-06	2.44	0.26	2.40	0.28	360.0	3.9	4.0	0.23
148j	NPT28	q	2	-	-	125	n	3.57E-02	1.25E-03	2.92E-04	9.02E-05	-	-	2.71E-05	1.36E-06	-	-	2.28E-05	1.40E-06	2.87	0.17	3.32	0.23	375.0	2.4	4.1	0.14
148j	NPT29	q	2	-	-	60	n	1.65E-02	2.15E-03	3.16E-04	8.10E-05	-	-	1.35E-05	1.94E-06	-	-	9.17E-06	1.25E-06	1.43	0.21	1.34	0.19	328.1	4.6	3.6	0.27
148j	NPT30	qr	2	-	-	500	n	1.69E-02	1.17E-03	3.17E-04	8.23E-05	-	-	9.49E-05	1.19E-05	-	-	7.21E-05	1.03E-05	10.05	1.30	10.50	1.54	460.1	6.4	5.0	0.38
148j	NPT31	qr	2	-	-	125	y	2.85E-02	6.95E-03	2.82E-04	7.47E-05	-	-	4.55E-05	5.46E-06	-	-	3.37E-05	4.65E-06	4.82	0.60	4.91	0.70	404.6	5.3	4.4	0.31
148j	NPT32	q	2	-	-	300	n	4.86E-02	4.46E-03	2.73E-04	7.24E-05	-	-	1.05E-04	5.50E-06	-	-	7.78E-05	5.82E-06	11.14	0.69	11.33	0.93	467.3	3.4	5.1	0.20
148j	NPT51	qr	2	-	-	18	y	1.36E-01	7.26E-03	7.74E-04	1.17E-04	-	-	1.13E-04	1.03E-05	-	-	8.12E-05	6.48E-06	11.94	1.16	11.82	1.02	471.9	4.4	5.2	0.26
148j	NPT52	q	2	-	-	65	n	1.15E-02	8.69E-04	3.89E-04	1.02E-04	-	-	1.12E-04	8.88E-06	-	-	8.47E-05	7.80E-06	11.89	1.02	12.34	1.21	473.5	4.4	5.2	0.26
148j	NPT53	q	2	-	-	65	n	2.55E-02	1.21E-03	3.81E-04	9.31E-05	-	-	4.23E-04	1.24E-05	-	-	3.13E-04	8.58E-06	44.82	1.97	45.56	1.94	601.8	2.7	6.6	0.16
148j	NPT54	q	2	-	-	125	n	1.48E-01	2.24E-02	4.34E-04	1.02E-04	-	-	1.82E-04	2.06E-05	-	-	1.30E-04	1.48E-05	19.27	2.27	18.89	2.25	513.3	6.2	5.6	0.36
148j	NPT55	q	2	-	-	500	n	5.04E-02	1.85E-03	3.56E-04	8.54E-05	-	-	1.71E-04	1.41E-05	-	-	1.25E-04	1.09E-05	18.11	1.61	18.23	1.70	508.9	4.7	5.6	0.28
148j	NPT56	qr	2	-	-	250	y	1.38E-02	1.03E-03	5.64E-04	1.07E-04	-	-	1.56E-05	1.21E-06	-	-	1.17E-05	1.17E-06	1.65	0.14	1.70	0.18	338.7	3.2	3.7	0.19
148j	NPT57	qr	2	-	-	30	y	4.65E-02	3.44E-03	6.89E-04	9.53E-05	-	-	8.07E-05	7.40E-06	-	-	5.46E-05	5.32E-06	8.55	0.83	7.94	0.82	442.9	4.4	4.9	0.26
148j	NPT59	q	2	-	-	500	y	8.23E-02	3.81E-03	5.47E-04	9.31E-05	-	-	2.76E-05	1.76E-06	-	-	2.27E-05	1.58E-06	2.92	0.21	3.31	0.25	375.4	2.8	4.1	0.16
148j	NPT60	q	2	-	-	350	n	1.06E-02	7.11E-04	3.61E-04	8.93E-05	-	-	4.43E-04	1.67E-05	-	-	3.28E-04	1.47E-05	46.95	2.34	47.83	2.65	607.3	3.4	6.7	0.20
148j	NPT61	q	2	-	-	500	y	2.29E-02	1.54E-03	4.90E-04	1.02E-04	-	-	1.88E-04	1.38E-05	-	-	1.31E-04	9.34E-06	19.92	1.60	19.01	1.50	515.2	4.2	5.7	0.25
148j	NPT62	q	2	-	-	500	n	1.50E-02	1.42E-03	3.81E-04	9.29E-05	-	-	1.19E-04	3.64E-06	-	-	8.57E-05	3.00E-06	12.57	0.56	12.47	0.60	476.3	2.2	5.2	0.13
148j	NPT63	q	2	-	-	500	n	3.68E-02	2.95E-03	4.24E-04	1.15E-04	-	-	3.09E-04	4.18E-05	-	-	2.26E-04	2.96E-05	32.73	4.55	32.90	4.45	566.8	8.1	6.2	0.47
148j	NPT65	qr	2	-	-	25	y	8.08E-02	2.47E-02	5.94E-04	1.13E-04	-	-	1.45E-04	1.29E-05	-	-	1.12E-04	1.07E-05	15.31	1.45	16.32	1.65	496.4	4.9	5.4	0.29
148j	NPT70	q	2	-	-	500	n	7.55E-02	1.10E-03	2.70E-04	6.69E-05	-	-	3.18E-04	1.93E-05	-	-	2.40E-04	1.16E-05	33.63	2.32	34.96	2.04	571.4	3.8	6.3	0.22
148d	GBM1	q	4	-	-	123	n	3.58E-03	9.87E-05	3.70E-05	3.55E-06	-	-	9.23E-05	2.48E-05	-	-	6.96E-05	1.61E-05	9.77	2.64	10.13	2.37	457.5	11.5	5.0	0.68
148d	GBM2	q	4	-	-	123	n	1.38E-02	2.14E-04	3.11E-05	3.43E-06	-	-	1.22E-04	1.83E-05	-	-	9.48E-05	1.67E-05	12.93	1.98	13.81	2.48	481.8	8.2	5.3	0.48
148d	GBM3	q	4	-	-	123	n	2.00E-02	1.35E-03	2.21E-05	2.98E-06	-	-	5.17E-04	9.84E-05	-	-	3.66E-04	6.78E-05	54.74	10.57	53.27	10.03	622.7	12.6	6.8	0.74
148d	GBM4	q	4	-	-	123	n	3.49E-03	4.06E-05	2.91E-05	2.08E-06	-	-	1.73E-05	6.59E-07	-	-	1.28E-05	5.62E-07	1.84	0.09	1.86	0.10	344.2	1.8	3.8	0.10
148d	GBM5	q	4	-	-	90	n	9.97E-02	1.01E-02	2.90E-05	3.33E-06	-	-	2.17E-04	1.79E-05	-	-	1.64E-04	1.42E-05	22.97	2.04	23.94	2.21	532.8	5.0	5.8	0.29
148d	GBM6	q	4	-	-	90	n	2.96E-02	1.35E-03	3.30E-05	3.98E-06	-	-	1.43E-04	8.44E-06	-	-	1.07E-04	5.45E-06	15.16	1.02	15.56	0.94	493.8	3.2	5.4	0.19
148d	GBM7	q	4	-	-	500	n	3.14E-01	3.41E-02	3.34E-05	2.42E-06	-	-	1.23E-04	1.08E-05	-	-	9.06E-05	8.15E-06	13.00	1.22	13.20	1.26	480.1	4.6	5.3	0.27
148d	GBM8	q	4	-	-	90	n	4.04E-03	7.69E-05	3.09E-05	3.17E-06	-	-	4.00E-04	4.75E-05	-	-	2.82E-04	2.74E-05	42.36	5.22	41.13	4.21	592.9	7.1	6.5	0.42
148d	GBM9	q	4	-	-	500	n	1.81E-02	6.57E-03	4.32E-05	3.73E-06	-	-	9.83E-04	4.58E-05	-	-	7.28E-04	4.03E-05	104.07	5.93	105.94	6.81	710.0	4.7	7.8	0.28
148d	GBM10	q	4	-	-	500	n	9.89E-03	9.50E-04	4.60E-05	4.33E-06	-	-	1.14E-03	3.81E-05	-	-	8.66E-04	2.74E-05	120.97	5.65	126.08	5.74	734.0	3.7	8.1	0.22
148d	GBM11	q	4	-	-	500	n	1.15E-02	6.48E-04	3.97E-05	2.79E-06	-	-	8.98E-04	6.42E-05	-	-	6.57E-04	4.42E-05	95.04	7.47	95.67	7.16	696.3	5.8	7.6	0.34
148d	GBN1	q	4	-	-	500	n	3.82E-03	3.57E-05	3.98E-05	3.23E-06	-	-	1.91E-04	2.26E-05	-	-	1.45E-04	1.40E-05	20.27	2.48	21.13	2.16	520.9	6.0	5.7	0.35
148d	GBN2	q	4	-	-	500	n	8.42E-02	1.79E-02	6.17E-05	1.14E-05	-	-	2.81E-04	2.94E-05	-	-	2.03E-04	1.98E-05	29.79	3.26	29.54	3.04	556.3	6.1	6.1	0.36
148d	GBN3	q	4	-	-	205	n	7.03E-03	2.07E-04	1.73E-04	5.75E-05	-	-	4.23E-04	1.04E-04	-	-	3.01E-04	8.00E-05	44.79	11.16	43.78	11.74	599.5	16.3	6.6	0.96
148d	GBN4	q	4	-	-	205	n	1.48E-02	4.65E-03	4.41E-04	1.83E-04	-	-	7.31E-04	2.23E-04	-	-	5.18E-04	1.60E-04	77.39	23.69	75.49	23.36	666.3	22.1	7.3	1.30
148d	GBN5	q	4	-	-	205	n	4.31E-03	4.14E-04	3.28E-05	2.79E-06	-	-	1.97E-04	2.27E-05	-	-	1.35E-04	1.41E-05	20.87	2.50	19.68	2.15	519.0	6.1	5.7	0.36
148d	GBN6	q	4	-	-	205	n	4.06E-03	5.62E-05	2.70E-05	2.04E-06	-	-	2.09E-04	1.57E-05	-	-	1.58E-04	1.44E-05	22.09	1.81	23.04	2.23	529.1	4.9	5.8	0.29
148d	GBN7	q	4	-	-	267	n	2.47E-03	3.70E-05	2.98E-05	3.70E-06	-	-	1.95E-04	2.67E-05	-	-	1.46E-04	1.72E-05	20.68	2.91	21.19	2.60	522.0	7.0	5.7	0.41

Sample	ID	Type	Session	Area ID	Vein #	g.s.	g.b.?	$^{27}\text{Al}/^{30}\text{Si}$	1σ	$^{44}\text{Ca}/^{30}\text{Si}$	1σ	$^{56}\text{Fe}/^{30}\text{Si}$	1σ	$^{47}\text{Ti}/^{30}\text{Si}$	1σ	$^{48}\text{Ti}/^{30}\text{Si}$	1σ	$^{49}\text{Ti}/^{30}\text{Si}$	1σ	^{47}Ti (ppm)	1σ	^{49}Ti (ppm)	1σ	T (°C)	1σ	P (kbar)	1σ
148d	GBN8	q	4	-	-	267	n	2.41E-02	5.98E-03	3.08E-05	2.31E-06	-	-	3.56E-04	2.27E-05	-	-	2.60E-04	1.45E-05	37.70	2.71	37.79	2.45	581.8	4.2	6.4	0.24
148d	GBN9	q	4	-	-	66	n	5.82E-01	5.00E-02	9.32E-05	5.31E-06	-	-	2.22E-03	1.72E-04	-	-	1.64E-03	1.22E-04	235.49	19.75	239.42	19.47	843.7	8.0	9.3	0.47
148d	GBN10	q	4	-	-	66	n	3.58E-03	3.03E-05	2.35E-05	1.93E-06	-	-	8.82E-06	5.23E-07	-	-	5.98E-06	2.60E-07	0.93	0.06	0.87	0.05	306.0	1.9	3.4	0.11
148d	GBN11	q	4	-	-	267	n	4.91E-03	2.92E-04	4.96E-05	4.17E-06	-	-	2.39E-04	1.31E-05	-	-	1.74E-04	1.06E-05	25.32	1.61	25.29	1.74	540.3	3.7	5.9	0.22
148d	GBN12	q	4	-	-	267	n	5.37E-03	1.72E-04	2.84E-05	2.51E-06	-	-	3.51E-04	1.73E-05	-	-	2.55E-04	1.40E-05	37.14	2.19	37.19	2.37	580.1	3.7	6.4	0.22
148d	GBN13	q	4	-	-	103	n	4.06E-03	1.05E-04	2.92E-05	2.46E-06	-	-	1.16E-05	4.31E-07	-	-	9.39E-06	4.17E-07	1.23	0.06	1.37	0.08	324.9	1.7	3.6	0.10
148d	GBN14	q	4	-	-	103	n	5.04E-02	8.59E-03	3.32E-05	3.37E-06	-	-	8.77E-05	1.36E-05	-	-	6.77E-05	1.08E-05	9.29	1.47	9.86	1.61	454.5	7.3	5.0	0.43
148d	GBN15	q	4	-	-	103	n	2.95E-03	3.08E-05	3.11E-05	2.85E-06	-	-	1.57E-04	3.78E-05	-	-	1.22E-04	2.53E-05	16.66	4.04	17.69	3.73	503.7	11.6	5.5	0.68
148d	GBN16	q	4	-	-	82	n	5.81E-03	8.95E-05	4.02E-05	3.36E-06	-	-	1.10E-03	2.13E-04	-	-	7.67E-04	1.51E-04	115.97	22.82	111.67	22.31	721.8	15.8	7.9	0.93
148d	GBN17	q	4	-	-	82	n	3.86E-03	5.26E-05	3.26E-05	2.52E-06	-	-	4.09E-05	1.62E-05	-	-	3.14E-05	1.20E-05	4.33	1.72	4.58	1.75	398.6	15.3	4.4	0.90
148d	GBN18	q	4	-	-	82	n	8.14E-02	1.65E-02	3.29E-05	2.96E-06	-	-	8.41E-04	7.92E-05	-	-	5.97E-04	5.36E-05	89.08	8.88	86.88	8.30	685.2	7.3	7.5	0.43
148d	GBN19	q	4	-	-	500	n	3.73E-03	6.37E-05	3.59E-05	2.41E-06	-	-	9.36E-04	4.82E-05	-	-	7.35E-04	4.00E-05	99.12	6.05	106.95	6.79	707.3	4.8	7.8	0.28
148d	GBN20	q	4	-	-	500	n	2.63E-03	3.14E-05	2.98E-05	2.13E-06	-	-	7.64E-04	9.36E-05	-	-	5.42E-04	6.96E-05	80.85	10.25	78.92	10.46	672.1	9.4	7.4	0.55
148d	GBN21	q	4	-	-	500	n	3.15E-02	1.07E-02	2.94E-05	3.37E-06	-	-	3.47E-04	2.55E-05	-	-	2.55E-04	1.81E-05	36.70	2.96	37.09	2.91	579.3	4.8	6.4	0.28
148d	GBN22	q	4	-	-	500	n	1.94E-01	4.06E-02	1.33E-04	2.44E-05	-	-	1.04E-03	2.58E-04	-	-	7.52E-04	1.89E-04	110.11	27.56	109.48	27.81	716.5	19.8	7.9	1.17
148d	GBN23	q	4	-	-	500	n	2.96E-01	2.53E-02	5.28E-05	3.58E-06	-	-	6.42E-05	2.03E-06	-	-	4.65E-05	1.61E-06	6.80	0.31	6.77	0.32	428.2	2.0	4.7	0.12
148d	GBN24	q	4	-	-	500	n	3.74E-03	6.95E-05	3.67E-05	3.85E-06	-	-	2.86E-04	2.39E-05	-	-	2.13E-04	1.45E-05	30.24	2.72	30.96	2.35	559.5	4.8	6.1	0.28
148d	GBN25	q	4	-	-	500	n	5.27E-02	3.51E-03	1.09E-04	8.17E-06	-	-	3.64E-04	2.28E-05	-	-	2.77E-04	1.56E-05	38.51	2.72	40.33	2.63	586.5	4.2	6.4	0.24
148d	GBN26	q	4	-	-	86	n	8.48E-03	1.55E-03	2.16E-04	5.37E-05	-	-	1.25E-04	2.60E-05	-	-	9.10E-05	1.80E-05	13.21	2.79	13.24	2.65	480.9	10.0	5.3	0.59
148d	GBN27	q	4	-	-	86	n	3.18E-03	7.37E-05	3.52E-05	2.36E-06	-	-	3.56E-05	9.29E-06	-	-	2.72E-05	7.11E-06	3.77	0.99	3.96	1.04	389.2	10.1	4.3	0.59
148d	GBN28	q	4	-	-	150	y	3.09E-03	7.93E-05	3.28E-05	3.46E-06	-	-	6.08E-04	1.50E-05	-	-	4.44E-04	1.30E-05	64.39	2.64	64.68	2.84	644.5	2.9	7.1	0.17
148d	GBN29	q	4	-	-	150	y	5.08E-03	7.02E-05	5.39E-05	3.65E-06	-	-	1.53E-04	5.73E-05	-	-	1.25E-04	4.82E-05	16.24	6.09	18.17	7.04	503.9	19.6	5.5	1.15
148d	GBN30	q	4	-	-	500	n	1.58E-02	4.26E-03	2.81E-05	2.27E-06	-	-	2.89E-04	2.48E-05	-	-	2.19E-04	2.13E-05	30.55	2.81	31.84	3.27	561.5	5.7	6.2	0.33
148d	GBN31	q	4	-	-	500	n	1.20E-02	1.57E-03	3.76E-05	4.48E-06	-	-	2.72E-04	2.16E-05	-	-	1.94E-04	1.37E-05	28.80	2.47	28.31	2.20	552.4	4.7	6.1	0.27
148d	GBN32	q	4	-	-	189	n	7.61E-03	5.79E-04	3.02E-05	2.28E-06	-	-	4.02E-04	3.04E-05	-	-	2.83E-04	1.88E-05	42.51	3.51	41.14	3.05	593.1	4.9	6.5	0.29
148d	GBN33	q	4	-	-	189	n	5.79E-02	1.82E-02	5.75E-05	7.44E-06	-	-	4.20E-04	3.99E-05	-	-	3.17E-04	2.46E-05	44.51	4.47	46.14	3.89	602.2	5.8	6.6	0.34
148d	GBN34	q	4	-	-	189	n	2.40E-03	2.71E-05	2.45E-05	2.05E-06	-	-	5.99E-05	4.49E-06	-	-	4.09E-05	1.98E-06	6.34	0.52	5.96	0.35	421.1	3.0	4.6	0.18
148d	GBN35	q	4	-	-	500	n	6.44E-03	5.44E-04	2.69E-05	2.46E-06	-	-	1.82E-04	1.95E-05	-	-	1.30E-04	1.44E-05	19.29	2.16	18.99	2.18	513.6	5.9	5.6	0.35
148d	GBN36	q	4	-	-	111	n	2.75E+00	1.40E-01	5.87E-05	4.02E-06	-	-	1.09E-03	5.53E-05	-	-	7.89E-04	4.04E-05	115.58	6.97	114.86	6.98	723.6	4.8	7.9	0.28
148d	GBN37	q	4	-	-	111	n	2.56E-03	3.33E-05	2.71E-05	3.17E-06	-	-	9.92E-05	4.52E-06	-	-	7.30E-05	3.79E-06	10.50	0.59	10.64	0.65	462.4	2.7	5.1	0.16
148d	GBN38	q	4	-	-	111	n	8.65E-01	6.04E-02	3.34E-05	2.68E-06	-	-	1.70E-04	1.48E-05	-	-	1.21E-04	1.01E-05	17.97	1.67	17.67	1.58	507.1	4.7	5.6	0.28
148d	GBN39	q	4	-	-	111	n	6.76E-03	2.34E-04	3.90E-05	2.86E-06	-	-	9.15E-06	5.87E-07	-	-	6.31E-06	4.15E-07	0.97	0.07	0.92	0.07	308.2	2.2	3.4	0.13
148d	GBN40	q	4	-	-	500	n	4.02E-03	4.18E-05	2.91E-05	2.51E-06	-	-	8.15E-05	8.45E-06	-	-	6.50E-05	8.30E-06	8.63	0.94	9.46	1.25	450.0	5.5	4.9	0.32
148d	GBN41	q	4	-	-	500	n	3.78E-03	3.71E-05	2.83E-05	2.92E-06	-	-	3.01E-04	2.63E-05	-	-	2.25E-04	2.03E-05	31.89	2.97	32.70	3.15	565.1	5.6	6.2	0.33
148d	GBN42	q	4	-	-	500	n	4.05E-03	4.38E-05	3.07E-05	2.53E-06	-	-	6.81E-05	2.44E-06	-	-	4.89E-05	1.50E-06	7.21	0.35	7.12	0.32	432.3	2.0	4.7	0.12
148d	GBN43	q	4	-	-	111	n	8.65E-03	1.42E-04	2.86E-05	2.43E-06	-	-	5.56E-06	3.05E-07	-	-	4.07E-06	2.21E-07	0.59	0.04	0.59	0.04	285.6	1.8	3.1	0.10
148d	GBN44	q	4	-	-	111	n	5.94E-01	5.49E-02	3.59E-05	2.85E-06	-	-	1.10E-04	1.30E-05	-	-	7.53E-05	9.86E-06	11.67	1.43	10.96	1.48	467.9	6.0	5.1	0.36
148d	GBN45	q	4	-	-	246	n	1.08E-01	2.29E-02	3.67E-05	3.10E-06	-	-	3.75E-04	2.97E-05	-	-	2.73E-04	1.93E-05	39.73	3.40	39.79	3.09	587.5	5.0	6.4	0.30
148d	GBN46	q	4	-	-	246	n	3.61E-02	6.73E-03	3.57E-05	2.69E-06	-	-	1.02E-04	6.44E-06	-	-	7.51E-05	5.09E-06	10.84	0.77	10.93	0.82	464.8	3.4	5.1	0.20
148d	GBN47	q	4	-	-	246	n	1.21E-02	1.84E-03	3.36E-05	3.03E-06	-	-	2.83E-04	2.55E-05	-	-	2.07E-04	1.78E-05	29.98	2.88	30.16	2.77	557.7	5.4	6.1	0.32
148d	GBN48	q	4	-	-	246	n	6.36E-03	3.79E-04	7.35E-05	5.21E-06	-	-	1.52E-04	2.39E-05	-	-	1.16E-04	1.83E-05	16.13	2.59	16.83	2.72	500.0	8.2	5.5	0.48
148d	GBN49	q	4	-	-	267	n	3.13E-01	4.09E-02	6.30E-05	1.75E-05	-	-	8.89E-04	1.00E-04	-	-	6.42E-04	7.42E-05	94.14	11.07	93.46	11.23	694.0	9.0	7.6	0.53
148d	GBN50	q	4	-	-	49	n	1.17E-02	2.56E-03	2.92E-05	2.81E-06	-	-	1.92E-04	2.71E-05	-	-	1.51E-04	2.29E-05	20.31	2.94	22.01	3.42	523.0	8.1	5.7	0.47
148d	GBN51	q	4	-	-	267	n	6.28E-03	2.46E-04	2.98E-05	3.14E-06	-	-	3.35E-04	2.32E-05	-	-	2.53E-04	2.13E-05	35.52	2.72	36.88	3.33	577.2	5.0	6.3	0.30
148d	GBN52	q	4	-	-	41	n	1.13E-01	4.17E-03	9.96E-05	4.79E-06	-	-	6.39E-05	3.20E-06	-	-	4.78E-05	2.36E-06	6.76	0.40	6.96	0.41	429.1	2.5	4.7	0.15
148d	GBN53	q	4	-	-	267	n	7.12E-03	5.26E-04	3.01E-05	2.88E-06	-	-	2.26E-04	1.41E-05	-	-	1.68E-04	1.28E-05	23.94	1.68	24.51	2.03	536.0	4.2	5.9	0.25
148d	GBN54	q	4	-	-	267	n	6.36E-03	1.41E-03	3.09E-05	2.35E-06	-	-	2.59E-04	1.25E-05	-	-	1.93E-04	8.44E-06	27.45	1.59	28.13	1.54	549.6	3.2	6.0	0.19
148d	GBN55	q	4	-	-	246	n	8.78E-03	2.19E-04	3.30E-05	1.75E-06	-	-	2.05E-04	1.36E-05	-	-	1.54E-04	1.11E-05	21.71	1.60	22.43	1.77	527.0	4.1	5.8	0.24
148d	GBN56	q	4	-	-	-	n	2.77E-01	2.32E-02	1.52E-04	7.54E-06	-	-	1.31E-04	9.21E-06	-	-	9.97E-05	6.69E-06	13.92	1.08	14.52	1.08	487.1	3.7	5.3	0.22
148d	GBN57	q	4	-	-	103	n	1.09E-02	2.07E-04	4.61E-05	4.73E-06	-	-	1.16E-05	4.16E-07	-	-	7.42E-06	4.08E-07	1.23	0.06	1.08	0.07	318.5	1.7	3.5	0.10
148d	GBN58	q	4	-	-	103	n	2.20E-03	2.92E-05	2.54E-05	2.47E-06	-	-	3.63E-06	2.61E-07	-	-	2.34E-06	2.58E-07	0.38	0.03	0.34	0.04	263.7	2.5	2.9	0.15
148d	GBN59	q	4	-	-	246	n	8.69E-02	1.29E-02	4.15E-05	5.23E-06	-	-	4.10E-04	2.75E-05	-	-	2.97E-04	2.14E-05	43.38	3.24	43.30	3.42	597.1	4.8	6.6	0.28
148d	GBN60	q	4	-	-	246	n	5.01E-03	4.45E-04	3.84E-05	2.50E-06	-	-	3.97E-04	1.78E-05	-	-	2.92E-04	1.59E-05	42.06	2.33	42.52	2.70	594.3	3.7	6.5	0.22

APPENDIX 3

Some General Notes on Geologic Strain Rates

Strain rate is a second order tensor, however in geologic applications 3D strains are often unknown or of little importance given much larger uncertainties associated with estimating the length of time over which geologic events occur. As a result geologic strain rates are often simplified to a single value indicating the change in length of a line (typically the maximum or minimum strain axis). If a line extends by a 10th its length (an elongation, "e" of 0.1) in 1 second, strain rate is 10^{-1} s^{-1}. For materials deforming at geologic timescales, it is easier to visualize strain rate in units of $m.y.^{-1}$. A strain of e = 1 in 1 m.y. would be 1 $m.y.^{-1}$, or ~10^{-13} s^{-1}. Thus one can take a typical slow strain rate of 10^{-15} s^{-1} and visualize it as 0.01 $m.y.^{-1}$, i.e. a strain of 1 in 100 m.y. While units of $m.y.^{-1}$ are easier to envision, we use the standard units of s^{-1} throughout this thesis.

Observed "geologic" strain rates are mostly faster than 10^{-15} s^{-1} since tectonic events generally do not last longer than ~10 m.y. and strains much smaller than 0.1 are generally not measurable (Pfiffner and Ramsay, 1982). Slower strain rates of course occur, but result in "undeformed" rocks. With the exception of seismic events, strain rates in shear zones or other sites where strain is localized in time or space are likely to be on the order of 10^{-12} - 10^{-10} s^{-1} (Albertz et al., 2005; Herwegh et al., 2005; Kenkmann and Dresen, 2002; Van der Pluijm and Marshak, 2003). Published strain rate estimates typically span a range on the order of 2-3 orders of magnitude. Rock squeezing experiments occur at strain rates between 10^{-4} to 10^{-8} s^{-1}. Thus a typical experiment at 10^{-6} s^{-1} occurs at rates 100 million times faster than a typical geologic strain rate of 10^{-14} s^{-1}.

Albertz, M., Paterson, S. R., and Okaya, D., 2005, Fast strain rates during pluton emplacement: Magmatically folded leucocratic dikes in aureoles of the Mount Stuart Batholith, Washington, and the Tuolumne Intrusive Suite, California: Geological Society of America Bulletin, v. 117, no. 3-4, p. 450-465.

Herwegh, M., Bresser, J. H. P. d., and Heege, J. H. t., 2005, Combining natural microstructures with composite flow laws: an improved approach for the extrapolation of lab data to nature: Journal of Structural Geology, v. 27, p. 503-521.

Kenkmann, T., and Dresen, G., 2002, Dislocation microstructure and phase distribution in a lower crustal shear zone - an example from the Ivrea-Zone, Italy: International Journal of Earth Sciences, v. 91, no. 3, p. 445-458.

Pfiffner, O., and Ramsay, J., 1982, Constraints on geological strain rates: arguments from finite strain states of naturally deformed rocks: Journal of Geophysical Research, v. 87, no. B1, p. 311-321.

Van der Pluijm, B. A., and Marshak, S., 2003, Earth Structure: An Introduction to Structural Geology and Tectonics (Second Edition), W. W. Norton & Company, 672 p.: